Universidad Autónoma de Madrid
Escuela Politécnica Superior
Departamento de Tecnología Electrónica y de las Comunicaciones

Tesis Doctoral

CONTRIBUTION TO THE EFFICIENT MODELING AND DESIGN OF PASSIVE WAVEGUIDE DEVICES THROUGH METHODS BASED ON MODAL DECOMPOSITIONS OF ELECTROMAGNETIC FIELDS IN UNCONVENTIONAL GEOMETRIES

Autora: Ana Morán López
Director: Juan Córcoles Ortega
Codirector: Jorge Alfonso Ruiz Cruz
Mayo 2019

DEPARTAMENTO:	Tecnología Electrónica y de las Comunicaciones Escuela Politécnica Superior Universidad Autónoma de Madrid, España
TESIS DOCTORAL:	Contribution to the efficient modeling and design of passive waveguide devices through methods based on modal decompositions of electromagnetic fields in unconventional geometries
AUTORA:	**Ana Morán López** Ingeniero de Telecomunicación
DIRECTOR:	**Juan Córcoles Ortega** Doctor Ingeniero de Telecomunicación Profesor Contratado Doctor de Universidad
CODIRECTOR:	**Jorge Alfonso Ruiz Cruz** Doctor Ingeniero de Telecomunicación Profesor Titular de Universidad

El Tribunal de Calificación, compuesto por:

PRESIDENTE:

SECRETARIO:

VOCALES:

VOCALES SUPLENTES:

Realizado el acto de defensa y lectura de la Tesis en la Escuela Politécnica Superiorde la Universidad Autónoma de Madrid. El Tribunal acuerda otorgarle la CALIFICACIÓN de:

Madrid, a de de 20

El trabajo desarrollado en esta tesis doctoral ha sido realizado en el grupo Radiofrecuencia: Circuitos, Antenas y Sistemas (RFCAS) del Tecnología Electrónica y de las Comunicaciones (TEC) de la Escuela Politécnica Superior (EPS) de la Universidad Autónoma de Madrid (UAM). Ha sido cofinanciado por el Ministerio de Economía, Industria y Competitividad (MINECO) del Gobierno de España a través de los proyectos TEC2013-47106-C3-2-R (TECOAMP) y TEC2016-76070-C3-1-R (AEI/FEDER, UE) (ADDMATE); el Gobierno de la Comunidad de Madrid a través del proyecto S2013/ICE-3000 (SPADERADAR-CM).

A mi familia, mi eterno apoyo.
A ti Juanjo, mi luz cada día.
A mis amigos, vuestro calor en mis pasos.

Hay almas a las que uno tiene ganas de asomarse,
como a una ventana llena de sol.
Federico García Lorca

Cuando creíamos que teníamos todas las respuestas,
de pronto cambiaron todas las preguntas.
Mario Benedetti

Agradecimientos

Quisiera dedicar este espacio a las personas que estos años han formado parte de esta Tesis.

A Juan y a Jorge, por la oportunidad de realizar este trabajo, y por los buenos momentos en los que compartimos el entusiasmo de una idea que nacía o la euforia de un trabajo publicado.

A Joserra y a Rebo, por tener siempre la puerta abierta y la mano tendida, habéis sido fundamentales en este trabajo.

A mis compañeros del C-116, porque es difícil no quereros con lo que me hacéis reír, gracias por ser como sois y por vuestro apoyo, me llevo conmigo muy buen recuerdo de estos tres años.

A José Luis y a Chema, por vuestra implicación conmigo a lo largo de este camino, es una suerte contar con vosotros.

A mis amigos, por escucharme y regalarme tantas tardes, sóis una pieza fundamental en mi particular puzle. En relación con esta Tesis quisiera dar las gracias especialmente a Roci, porque contigo todo fue más fácil en Alemania y siempre te voy a estar agradecida; a Luis y a Pascu, porque habéis sido los mejores compañeros de viaje y una gran fuente de apoyo; y a Celia, Cris y Álex, porque siempre habéis tenido palabras de aliento y una tarde para mí en el bolsillo.

A mi familia, porque siempre encuentro en vosotros ese cariño y afecto de quienes son felices viéndote feliz.

A Quini, por acompañarme no sólo estos 3 años sino estos 28, porque contigo no importa el color del día, siempre vistes nuestras conversaciones con risas y buenos consejos.

A Jimmy, por tus palabras de ánimo y por ese sentido tuyo del humor que te hace único, las mejores sobremesas son contigo y mi tío juntos, ¡sin duda!.

A Rebe, por creer en mí y darme ese empujón que a veces me falta, porque en estos años me has ayudado a crecer como persona. De ti me llevo muy buenos momentos estos tres años, momentos de auténticas carcajadas y de retos superados.

A mis padres y hermanas, mis cuatro estrellas polares, no me faltéis nunca porque en vosotros encuentro mis fuerzas y mi norte.

A ti Juanjo, por tu apoyo incondicional, porque los momentos más difíciles de este trabajo los he vivido contigo y contigo los he superado. Eres mi luz cada día, me llenas de esa paz que sólo se siente cuando uno es feliz.

Gracias a todos una vez más por hacer esto posible.

Acknowledgements

I would like to express my gratitude to Michael Höft and Daniel Miek for their support during my stay in Kiel, at the Lehrstuhl für Hochfrequenztechnik. Thank you for such a fruitful collaboration, both in Germany and during the last year of my Thesis. Working with you and being part of your team has been a great honour.

Resumen

La creciente demanda de mayor calidad de servicio ya es una realidad en los sistemas de telecomunicaciones. Con la llegada del 5G, la red de redes, esta tendencia es aún mas marcada. En general, los sistemas de telecomunicaciones han supuesto siempre un reto para los ingenieros de microondas, siendo los sistemas por satélite especialmente exigentes. Dichos sistemas no solo han de utilizar de forma eficiente el espectro disponible, sino que, además, deben lidiar con la limitada potencia disponible en el espacio o con fenómenos físicos propios del vacío como el conocido fenómeno de *multipactor*.

En este contexto, los ingenieros de microondas necesitan herramientas de diseño asistido por ordenador potentes y eficientes, capaces de predecir en un tiempo de ejecución razonable el comportamiento de los dispositivos que diseñan. Hay dispositivos que han de analizarse por medio de métodos numéricos, siendo estos menos eficientes pero más genéricos que los analíticos. Los métodos de análisis modal pertenecen a este último grupo: son más eficientes que los numéricos y, por tanto, preferibles siempre que se apliquen a geometrías cuyos modos pueden expresarse de forma analítica o cuasianalítica. El objetivo de esta Tesis doctoral es contribuir al análisis electromagnético eficiente de geometrías poco convencionales. En particular, las guías estudiadas en este trabajo son la triangular equilátera y la parabólico-cilíndrica, presentes en la literatura desde hace varias décadas. Sin embargo, ambas fueron relegadas a un segundo plano en el diseño de dispositivos, probablemente debido a la falta del conjunto completo de modos en la guía triangular equilátera y a la ausencia de un método analítico y sistemático de resolución de modos en la guía parabólico-cilíndrica.

En esta Tesis se aborda la aplicación del método de ajuste modal (*Mode-Matching*) para problemas electromagnéticos formados por bloques de guías triangulares equiláteras, para lo cual se ha hecho uso del conjunto completo de modos de esta guía publicado recientemente. Ademas, gracias a la formulación basada en ondas planas, la integración de la guía triangular equilátera en problemas de discontinuidades donde aparecen otras guías clásicas (como la circular, la rectangular o la elíptica) se resuelve de forma sencilla y homogénea. Asimismo, se han calculado las expresiones analíticas del factor de calidad Q típico de los filtros de microondas, lo que constituye una extensión a las expresiones ya existentes en la literatura para las cavidades clásicas (rectangular y circular) para el caso de la cavidad triangular equilátera.

En lo que respecta al análisis electromagnético de la guía parabólico-cilíndrica, las herramientas existentes de caracterización analítica estaban menos desarrolladas que en el caso de la guía triangular equilátera. Tanto es así que, para la resolución analítica de su espectro modal, hasta ahora era necesario recurrir a métodos de intersección gráfica de curvas. Gracias al trabajo desarrollado en esta Tesis, se puede resolver por primera vez el

conjunto completo de modos de esta geometría de forma plenamente robusta, con precisión y de forma sistematizada en una herramienta de diseño asistido por ordenador.

Además de las dos geometrías estudiadas en esta Tesis, resulta evidente la posibilidad de que otras no convencionales lleguen a formar parte de los futuros dispositivos de comunicaciones. En aras de la exhaustividad, se propone una formulación eficiente para hibridar los métodos de elementos finitos en 2D y ajuste modal (*2D Finite Element* y *Mode-Matching*), basada en el uso de espacios anidados de funciones base de elementos finitos que reduce el número necesario de operaciones. De esta manera, cualquier dispositivo formado por secciones de guía (con solución modal analítica o numérica) puede ser analizado con el software que se ha desarrollado en esta Tesis.

Las herramientas de análisis electromagnético diseñadas en esta Tesis permiten caracterizar una gran variedad de dispositivos de microondas y ondas milimétricas. En concreto, la segunda parte del trabajo realizado se centra en el diseño de filtros. Los filtros de microondas son los dispositivos que seleccionan los canales de información en los sistemas de telecomunicaciones, sistemas que, en el sector espacial concretamente, están sujetos a complejas restricciones de diseño. En esta Tesis se han diseñado dos prototipos *inline* en cavidades equiláteras triangulares y parabólico-cilíndricas, con resultados que demuestran la viabilidad de la integración en futuros dispositivos de estas geometrías poco convencionales. También se ha diseñado, fabricado, sintonizado y medido un prototipo *dual-mode* basado en cavidades triangulares equiláteras. Presentado como prueba de concepto, constituye una alternativa a los prototipos *dual-mode* clásicos de cavidades circulares, los cuales permiten alcanzar la misma selectividad que los dispositivos monomodo con la mitad de resonadores.

Además del uso de resonadores multimodo, existen otras técnicas que permiten reducir el tamaño de los filtros de microondas sin renunciar a la respuesta objetivo requerida por el sistema de comunicaciones. En la última parte de esta Tesis se presentan dos estrategias: el uso de acoplos dispersivos y el uso de geometrías de sección transversal reducida. Los acoplos dispersivos se caracterizan por presentar una variación significativa en frecuencia, lo que permite generar ceros de transmisión adicionales fuera de la banda de paso. De esta manera, se consiguen niveles de rechazo de frecuencias indeseadas similares a los alcanzables mediante el uso de un mayor número de resonadores. En concreto, esta Tesis se centra en la aplicación de acoplos fuente-carga dispersivos en las topologías *folded* clásicas debido a su fácil implementación. Se han fabricado y medido dos prototipos en plano E y plano H en banda W con resultados muy prometedores.

Finalmente, se propone el uso de la forma triangular equilátera en otro contexto: el de los resonadores dieléctricos. Debido a su limitada capacidad para manejar altas potencias, este tipo de filtros normalmente se emplea en los multiplexores de entrada de los sistemas de comunicaciones por satélite. A cambio, los filtros en resonadores dieléctricos ofrecen un tamaño y un peso reducidos. En ese contexto, en las últimas décadas se ha realizado una importante inversión en desarrollar resonadores dieléctricos multimodo que reducen más si cabe el volumen de los filtros. En esta Tesis, se proponen varias topologías que, aun siendo monomodo, se benefician de la reducida sección transversal inherente al resonador dieléctrico de forma triangular equilátera. Entre todas ellas, se ha elegido la toplogía hexagonal para mostrar un diseño a modo de prueba de concepto en la banda Ku, que es, además, el primer filtro de microondas en esta geometría hasta donde el autor sabe.

Palabras clave

Método de ajuste modal, método de elementos finitos en 2D, guía de onda triangular equilátera, filtro *inline* en cavidades triangulares equiláteras, guía parabólico-cilíndrica, filtro *inline* en cavidades parabólicas asimétricas, filtro *dual-mode* en cavidades triangulares equiláteras, factor Q, búsqueda de raíces, continuación analítica, acoplo fuente carga dispersivo, filtros *folded* canónicos, circuitos equivalentes, inversor dispersivo, filtro plano E, filtro plano H, filtros en resonadores dieléctricos, resonador dieléctrico en guía triangular equilátera.

Abstract

Telecommunication systems have experienced an increasing demand in the quality of service over the recent years. With the arrival of 5G, the network of networks, this trend is even more significant. Systems have always posed a challenge for microwave engineers, especially in satellite communications. Even though these systems seek the efficient utilization of the electromagnetic spectrum as in any other communication systems, they must also manage the limited availability of power or the effects related to the vacuum environment such as the multipactor phenomenon. For all of the above, on-board devices are designed making use of the latest advances. One of the popular trends nowadays is the use of 3D printing techniques, which paves the way for the use of unconventional geometries different to those traditionally (and still currently) used.

In this context, microwave practitioners demand robust Computer-Aided-Design tools capable of predicting the behavior of devices designed with an affordable computational burden. Numerical techniques are sometimes required, as they enable analyzing complex arbitrary geometries. However, the use of analytical or quasi-analytical techniques offers multiple advantages where this kind of analysis is feasible as they are highly efficient. In this scenario, this Thesis aims to contribute to the efficient electromagnetic analysis of waveguide devices made up of unconventional cross-sections. In particular, two geometries are addressed: the equilateral triangular and the parabolic cylinder waveguides. Both geometries were reported in the literature a long time ago, but the lack of the complete set of modes in the former and a systematic procedure to find the analytical modal spectra in the latter had made them not be usually considered for microwave design.

A flexible formulation based on plane waves is proposed in this Thesis to address the resolution of waveguide devices made up of equilateral triangular blocks by means of the Mode-Matching method. The recently published complete modal set is here used. Furthermore, the integration of this specific waveguide with other canonical ones (*i.e.* rectangular, circular, elliptical) has been successfully solved in a unified manner. The derivation of the analytical closed-form expressions of the Q-factor in the equilateral triangular resonator has been developed as well. The obtained formulas extend the well-known classic expressions found in the literature for rectangular and circular cavities to the case of equilateral triangular cavities.

In the case of the parabolic cylinder waveguide, its analytical resolution had not been subject of a thourough development, as in the case of the equilateral triangular waveguide. In fact, the analytical methods available to solve its modal spectra resorted to graphical intersections. The work developed in this Thesis makes it possible to carry out its analytical modal analysis for the first time in a systematic way, so that it can be embedded into modern Computer-Aided-Design tools.

In addition to equilateral triangular and the parabolic cylinder waveguides, other unconventional cross-sections may also become part of prospective devices. For the sake of completeness, an efficient formulation for hybridizing the 2D-Finite Element and the Mode-Matching methods is proposed. Based on the use of nested finite-element function spaces, devices made up of cascaded arbitrary cross-sectional waveguide steps are efficiently analyzed reducing the total computations.

The analysis tools developed in this Thesis can be applied to a wide variety of microwave and and millimeter-wave devices. In particular, the second part of this dissertation focuses on microwave filters. These devices select frequency channels and are usually designed fulfilling very stringent specifications in the space sector. Two inline prototypes made up of equilateral triangular and asymmetric parabolic cavities are presented, thus proving the good performance of these unconventional geometries. A dual-mode prototype of equilateral triangular cavities has also been designed, manufactured, tuned and measured. This prototype, which is presented as a proof of concept and as an alternative to the classical TE_{113} dual-mode filters typical of satellite systems, allows to implement the desired electromagnetic response with half the number of resonators required by a single-mode prototype.

Compactness can also be achieved following other strategies apart from the use of multimode resonators. In particular, two of them are developed in the last section of this Thesis: the implementation of dispersive couplings and the use of reduced footprint topologies. Dispersive couplings are characterized by their strong variation over frequency, and allow the generation of additional out of band transmission zeros. Hence, the stopband behavior of the filter can be improved without increasing the number of resonators, which is strongly desirable at high frequency bands. This Thesis has focused on dispersive source to load couplings in the well-known waveguide folded topology due to the ease of implementation. Two prototypes at the W-band have been manufactured and measured: an E-plane filter with phase equalization and and H-plane filter of mixed TE_{101} and TE_{102} cavities, showing promising results.

Finally, the proposal of novel dielectric resonator filters is addressed. Due to their limited power handling capability, these filters are usually placed at input multiplexers of satellite communication systems. Although it is well-known that dielectric resonators offer a significant size reduction compared to waveguide cavities, huge efforts have been made in recent decades to obtain more compact designs. In this context, several topologies benefiting from equilateral triangular dielectric resonators are proposed. Among all of them, the hexagonal topology has been selected to show a proof-of-concept design in the Ku-band. To the best of the author's knowledge, this filter is the first one made up of equilateral triangular dielectric resonators reported in the literature, showing very good performance and overall reduced size.

Key words

Mode-Matching method, 2D-Finite Element method, equilateral triangular waveguide, inline equilateral triangular filter, parabolic cylinder waveguide, inline asymmetric parabolic filter, dual-mode equilateral triangular filter, analytical Q-factor, root-finding, analytic continuation, dispersive source to load coupling, fully canonical folded filters, equivalent circuits, dispersive source to load inverter, E-plane filter, H-plane filter, dielectric resonator filters, equilataral triangular dielectric resonator.

Contents

List of Figures

List of Tables

1 Introduction

1.1 Motivation

The world is connected nowadays. Behind this reality there are modern telecommunication systems, completely transparent to the final user, which have evolved to provide a wide variety of services with increasing quality. Among all the available systems, in the recent years one has attracted the attention of the industry with the emerging concept of the Internet of Things (IoT) [1]: the satellite communication systems.

The IoT concept refers to the connection of the everyday devices with each other, sharing information through 5G. The first live demonstration of 5G by satellite has been recently held in the Berlin 5G week 2018 [2]. In this scenario 5G becomes more than the next generation of mobile services that provides greater bandwidth and reduced latency, as it requires the creation of a network of networks where satellite links play a major role. In fact, the European Space Agency (ESA) and 16 satellite industry leaders recently signed a Join Statement in their collaboration in the area of Satellite for 5G on the 21st of June 2017 at the Paris and Space show [3]. Moreover, a week later the ESA and the European Space Policy Institute (ESPI) co-hosted a conference in Brussels to discuss about policy and the technology aspects related to 5G and the future space-base solutions [4]. In this context satellites are presented as a cost-effective solution that must coexist with the terrestrial mobile networks providing added value in terms of security, resilience, coverage, mobility and delivery of broadband.

In order to comply with all the Key Performance Indicators (KPIs) that 5G requires, the communication systems must meet increasingly stringent specifications. This poses a challenge for engineers especially in the space sector, where the environment is particularly hostile. The devices sought to make up the whole satellite system must deal with the thermal stress associated to wide variations of temperature, the launching vibration and the problems associated to the vacuum condition such as the multipactor phenomenon, among others [5–7]. These demanding requirements have led over the last decades to the significant development of robust Computer Aided Design (CAD) tools capable of analyzing all these effects with affordable computational burden [8–16]. Furthermore, a huge effort has been made to improve the manufacturing techniques and the search of materials with desirable properties. Among all the available technologies for passive devices, in this scenario waveguide technology has long been widely used due to its power-handling capability and low insertion losses [17]. Waveguide polarizers, orthomode transducers, cavity filters or transformers are typically designed with the canonical rectangular, circular or elliptical cross-sections [18–25]. With the revolution of 3D printers [26–29], however, the design possibilities have been undoubtedly widened.

The first 3D printer dates back to the 80's decade [30]. However the recent advances in additive manufacturing in the last decade have made it possible to bring cumbersome prototypes to reality [31]. Novel prototypes for satellite communications can be found in [32–35]. The use of the 3D printing technology is beyond the scope of this work, however, it is considered a valuable tool that may boost the future use of non-canonical cross-sections such as the equilateral triangular and the asymmetric parabolic cross-sections treated in this Thesis. This work aims to contribute to the use of these unconventional waveguides for the design of microwave devices. The first step taken towards this end is to achieve their efficient analysis, and the second one is to integrate such geometries in prototypes of real application using the tools developed in the first step.

1.2 Efficient modeling of the equilateral triangular and the parabolic cylinder waveguides and their integration in mixed discontinuities

The resolution of waveguide geometries through methods based on analytical modal decompositions [11] helps to understand the electromagnetic problem under study. In this context, the work developed for the equilateral triangular and the parabolic cross-sections is oriented to the use of modal decompositions, although it addresses different stages of their electromagnetic resolution. For an electromagnetic solver of this type the first step is to solve the complete set of modes that makes up the electromagnetic field, and in the case of the equilateral triangular waveguide this problem was successfully addressed before the beginning of this Thesis. In the case of the parabolic cylinder waveguide, the lack of a systematic procedure integrable in a modern CAD tool has made it imperative to focus this contribution on the systematic resolution of its modes.

The origin of the resolution of the electromagnetic field inside an equilateral triangular waveguide dates back to the XIXth century, when Gabriel Lamé solved the eigenvalues and eigenfunctions of the Laplace equation in the equilateral triangular geometry [36]. Although this work was carried out in the context of heat transfer, the eigenvalue problem that Lamé faced was the same as the one described by the scalar Helmholtz equation in electromagnetism. Later on, expressions referred to the electromagnetic field were gathered in [37] without any derivation. Renewed attention was given to this problem in [38], where superposition of plane waves was used to find suitable modal solutions of several triangular contours, of which the equilateral triangular contour was one of the case studies. However, [38] claimed that the derived analytical solution did not provide the complete set of modes. The search of this set, essential for any solver based on modal decomposition, has been a topic of interest in the scientific community [39], where the expressions obtained in [40, 41] were the ones that brought the complete solution. An interesting derivation based on the work of Lamé and on [40, 41] has been recently published in [42], where a plane wave reconstruction technique is used to shed light on the mode symmetries and on how triangular patch antennas are excited.

Since the complete set of modes of the equilateral triangular waveguide is known, the contribution of the present work is focused on the applicability of such mathematical set. Given the great efficiency associated to solvers based on analytical closed-form expressions, this work has found of great interest to develop the Mode-Matching method formulation [8] over the proposed non-canonical geometry, with the idea of having a robust and efficient

tool available to carry out its electromagnetic analysis for microwave design [18, 20, 43–45].

On the other hand, the resolution of the parabolic cylinder waveguide, the second unconventional geometry addressed in this Thesis, was at an earlier stage of development in contrast to the equilateral triangular geometry The theory of its analytical resolution from the scalar Helmholtz equation was already known, but in the final steps of the electromagnetic problem its modal spectra was obtained resorting to graphical intersections. The derivation followed from the 2D-Helmholtz equation in parabolic cylinder coordinates leads to the parabolic cylinder equation, where the Weber parabolic functions can be used to find the modal solutions [46]. These functions were tabulated in [47], but their integration into modern CAD tools is currently far from being trivial [48, 49]. The strategy shown in [50], however, allows to avoid these cumbersome functions by means of a 1D-analytic continuation technique. This strategy is followed in this Thesis due to its simplicity and great performance.

Once these functions are successfully computed, a bivariate system of equations must be solved. The difficulty of finding the modal spectra of the parabolic cylinder waveguide precisely lies in this system of equations, where the two sought variables belong to the real domain. Up until now the modes of the parabolic cylinder waveguide were analytically solved by means of graphical intersections [46, 50, 51]. The contribution of this work in regard to this non-canonical geometry is the search of a suitable mathematical method [52] that enables to find its modal spectra and its integration into a modern CAD-tool.

Both the parabolic cylinder and the equilateral triangular waveguides are unconventional geometries of interest for engineering as prospective candidates that may take part of future satellite devices. However, other canonical geometries or even other non-analytical ones can be present in such designs as well. Among all the possible topologies, a large class of waveguide devices are made up of waveguide steps cascaded along the propagation direction. If their cross-sections are analytical, then their computation can be efficiently addressed by the Mode-Matching method [8, 11]. In fact, thanks to the formulation based on plane waves used in this Thesis, the corresponding full-wave analysis can be carried out in a unified manner when equilateral triangular, rectangular, circular and/or elliptical sections take part of the electromagnetic problem under consideration.

In contrast to the Mode-Matching method, there are other methods extremely flexible when coping with electromagnetic problems that involve arbitrary cross-sections. This is the case of the Finite Element method, a popular numerical technique in electromagnetic engineering whose capability for the computation of numerical modes in waveguides of irregulary-shaped cross-section is long known and used [8, 53, 54]. Its hybridation with the Mode-Matching method was developed in the mid-1990's [55–58], and constitutes a powerful tool to efficiently analyze devices made up of mixed analytical and numerical cascaded cross-sections. In this context the goal of this work is to complement all these previous works providing a formulation that minimizes the number of operations needed and thus reducing the overall computational cost. With this contribution the part of the Thesis devoted to the improvement of the electromagnetic analysis of unconventional geometries and its integration with other available ones (canonical or numerical) comes to its end.

1.3 Towards prospective filters integrable in future satellite systems

Once the full-wave analysis has been addressed, the second step to contribute to the use of the equilateral triangular and the parabolic cylinder waveguides is to face their suitability for microwave devices. In particular, this Thesis has focused on filters, which are key devices for the selection of frequency channels in current telecommunication systems. Besides the selection of channels, these elements contribute to reduce the noise and therefore to improve the Signal to Noise Ratio (SNR) of the system.

The design of filters for satellite communications encompasses very diverse analyses. The electromagnetic study carried out for the realization of the desired S-parameter response is the one that may be similar to other waveguide components in communication systems. However, the analysis of the multipaction phenomenon, or the study of the thermal stability are critical for the particular case of the space environment. Besides, filters devoted to satellite communications are subjected to restrictive specifications in terms of light-weight, selectivity, group delay, low losses and power handling [5]. Compact designs of reduced weight are desirable as the size of their footprint has a direct impact on the launching cost [59]. The achievement of high selectivity is mandatory to isolate the channels preventing the wastage of the available bandwidth with the use of wide guard-bands. Linear group delay behaviour is desired to reduce signal distortion. Low losses are a priority since the available power is ultimately limited by the solar cells, and also because of the well-known problem of heat dissipation. Finally, good capabilities of power handling are sought for the output multiplexers that follow the High Power Amplifiers (HPA). The technologies preferred to accomplish these requirements depend on the frequency band and on the filter location within the whole chain of communication. Waveguides have been traditionally used in output multiplexers due to their low losses and power handling capability. In fact, the waveguide manifold made up of TE_{113} circular cavities became one of the most popular schemes [60–62]. On the other hand, dielectric-loaded cavity filters have been widely used for input multiplexers due to the significant size reduction achievable with this technology [63].

The analysis and attainment of all the requirements for a real on-board filter are not goals of this work. Instead, this Thesis aims at presenting proof-of-concept designs that open the door for the future integration of non-conventional geometries in satellite communications. For that purpose the classical charts of analysis applied to the presented unconventional geometries are given, and the formulation of the analytical quality factor (Q-factor) in the equilateral triangular waveguide is developed. All the designs are inline prototypes that can be analyzed by the electromagnetic software developed in the first chapters of this dissertation. Among them, one corresponds to a dual-mode filter, whose design and manufacture were considered of great relevance as the size reduction achieved by this technique is nowadays fully-exploited by modern satellite systems.

The race on compactness is not limited to the use of multimode resonators. One of the current trends is the use of dispersive (*i.e.*, frequency dependent) couplings in waveguide structures [64–66], conceived to enhance the filter performance in demanding scenarios [63, 67]. With this strategy finite transmission zeros can be generated, reducing the required number of resonators for a given level of selectivity. Another current trend is the development of dielectric resonators. The significant mass and volume reduction that

they offer make them attractive for the growth of satellite communications. In this kind of systems dielectric resonators have been traditionally used in input multiplexers due to their limited power handling capability, while their application in output multiplexers is relegated to low frequency bands [68–70]. Nowadays the increased investment in materials of high quality factor, low loss and high power handling capabilities has changed this reality [71].

In this context the last part of this work is devoted to the improvement of filter compactness in two of the current areas of concern in the satellite industry. In particular, this Thesis aims at the improvement of the out-of-band rejection in fully canonical folded topologies throughout the dispersive behaviour of certain source to load couplings in waveguide technology. This strategy is specially suited for this topology in comparison to others due to the associated ease of implementation. Two prototypes are designed and manufactured at the W frequency band, where increased interest has been recently shown for future high capacity satellite communications [72, 73]. Finally, this work intends to contribute to mitigate the absolute reliance on dielectric materials of high permittivity that may limit the power handling capacity in favor of size reduction. Towards that end, several novel compact dielectric topologies based on the equilateral triangular dielectric resonator are proposed, one of which has given rise to a novel prototype that evidences the compactness of the proposed approach.

1.4 Text organization

The content of this Thesis is divided into seven chapters, including this first one devoted to the presentation of the addressed topics and the last one where the main conclusions and contributions of this work are gathered.

Chapter 2 addresses the efficient modeling of equilateral triangular waveguide. The corresponding analytical modal expressions are reviewed and the well-known Mode-Matching method is introduced. Then, a formulation based on the use of plane waves is developed and validated with several case studies of equilateral triangular discontinuities. The proposed formulation is tested as well with waveguide steps where the discontinuity involves an equilateral triangular waveguide and other canonical cross-sections (*i.e.* rectangular, circular or elliptical).

Chapter 3 deals with the challenging resolution of the parabolic cylinder waveguide, whose modal spectra was up to date analytically solved resorting to graphic intersections. A worthy strategy to obtain the suitable functions by means of analytic continuation is reviewed and followed. Then, a recently published algorithm for the resolution of bivariate systems of equations is proposed and integrated with the previous technique to give rise to a modern CAD tool where this waveguide is for the first time systematically solved.

Chapter 4 presents a novel formulation for the hybridation between the Finite Element and the Mode-Matching methods. The proposed formulation is based on the use of nested function spaces, which enable the use of the already computed matrices from the Finite Element method to build the inner-cross products of the Mode-Matching method, thus reducing the overall computational cost. An efficient orthonormalization procedure is also given, and several case studies are analyzed using already published or measured prototypes as a source of validation.

Chapter 5 shows the application of the two unconventional geometries addressed in this Thesis for their prospective integration in the design of on-board satellite filters . Both the asymmetric parabolic and the equilateral triangular resonators make up inline single mode prototypes, conceived following the classical design charts. Among them, the Q-chart is analytically derived for the equilateral triangular cavity. The design, manufacture and measurement of a dual mode equilateral triangular prototype is also carried out exploiting the degeneracy inherent to this particular geometry.

Chapter 6 focuses on the contribution to the design of filters from the point of view of compactness, since this feature is of great relevance in satellite communications. The use of dispersive source to load couplings in the well-known fully canonical folded waveguide filters is proposed to reduce the required number of resonators. In this context two designs are manufactured and measured in the W-band, and several equivalent circuits are proposed as well. Finally, novel compact topologies based on the use of the equilateral triangular dielectric resonator are presented. The design of a prototype using one of these topologies of reduced footprint is carried out as a proof of concept.

Finally, *Chapter 7* describes the main conclusions derived from the work developed in this Thesis along the different chapters. The contributions of this dissertation are outlined as well, and the corresponding list of publications is detailed.

Appendix A is included at the end of this document to clarify the derivation of TE, TM and TEM modes in homogeneous waveguides for arbitrary cross-section geometry since this is used throughout the whole text.

2 The equilateral triangular waveguide

2.1 Introduction

The equilateral triangular waveguide is an unconventional geometry used in microwave devices when compared with other geometries as the rectangular, circular or elliptical cross-sections. However, its resolution by separation of variables is far from being new.

The resolution of the eigenvalues and eigenfunctions of the Laplacian in the equilateral triangular geometry under Dirichlet and Neumann conditions dates back to the XIXth century, when Gabriel Lamé carried out studies in the context of heat transfer [36]. The eigenvalue problem that Lamé faced was the same described by the 2D-Helmholtz wave equation present in electromagnetism. Later work [37] based on Lamé provided the corresponding expressions for this geometry in the context of miscellaneous waveguide cross-sections. Nevertheless, those expressions were not deduced in the text.

Some derivations of the modal expressions in the equilateral triangular waveguide have been carried out [38, 39], but it is in the recent work [40, 41] where Brian J. McCartin has given a complete derivation of Lame's formulas and proved that they were a complete set of orthonormal eigenfunctions, which is essential for the application of electromagnetic methods based on modal decomposition. One of those is the Mode-Matching method [8], developed some decades ago and extensively used to speed-up the electromagnetic analysis of microwave devices made up of the connection of cross-sections with analytical or quasi-analytical modal solution.

The contribution of this chapter is the application of this method to the equilateral triangular waveguide, allowing to efficiently design microwave devices in this technology. First, the modal expressions are reviewed using a convenient coordinate system. A normalized mode-chart is shown, where the main features of this waveguide for microwave design are evidenced: its modal degeneracy and the wider bandwidth compared to other waveguides, under a proper excitation. Then, a brief overview of the Mode-Matching method is given and a formulation based on plane waves is proposed for this kind of waveguide to ease the resolution of the integrals associated to this method. Several case studies for equilateral triangular waveguide steps are validated. Finally the usefulness of the proposed flexible formulation is shown when this waveguide is connected to other classical cross-sections (*i.e.*, rectangular, circular, elliptical). Some examples are given for validation purposes showing very good agreement.

2.2 Modal expressions and mode chart

The electric and magnetic fields of a homogeneous waveguide with translation symmetry along the propagation axis can be described as orthogonal series of modes:

$$\vec{E} = \sum_{p=1}^{\infty} \left(a_p e^{-\gamma_p z} + b_p e^{\gamma_p z}\right)\vec{e}_p + \left(a_p e^{-\gamma_p z} - b_p e^{\gamma_p z}\right)e_{zp}\hat{z} \tag{2.1}$$

$$\vec{H} = \sum_{p=1}^{\infty} \left(a_p e^{-\gamma_p z} - b_p e^{\gamma_p z}\right)\vec{h}_p + \left(a_p e^{-\gamma_p z} + b_p e^{\gamma_p z}\right)h_{zp}\hat{z}. \tag{2.2}$$

In the preceding expressions, the terms $a_p e^{-\gamma_p z}$ and $b_p e^{\gamma_p z}$ are complex variables that represent the modal amplitudes at an arbitrary z-plane, where a_p and b_p depend on the source and load of the waveguide imposed by the radiofrequency system. On the other hand, the geometrical cross-section and the particular mode identified by subindex p determine the propagation constant (γ_p) and the transversal ($\vec{e}_p$, $\vec{h}_p$) and longitudinal (e_{zp}, h_{zp}) components of the field.

In order to determine all these components dependent on the geometry under consideration the Helmholtz equation must be solved. In the case of waveguides made up of an enclosing metallic conductor filled with homogeneous dielectric material, the problem of characterizing the Transversal Electric (TE) and Transversal Magnetic (TM) waveguide modes becomes scalar:

$$\Delta_t \Phi_p + k_{cp}^2 \Phi_p = 0, \tag{2.3}$$

which must be satisfied in all the points of the inner cross-section surface. This function Φ represents the longitudinal electric or magnetic field component for TM and TE modes, respectively, conveniently normalized. Two types of boundary conditions must be imposed to solve the previous equation, the Dirichlet and Neumann conditions, from which the two possible mode families arise:

- TE modes, where Φ_p must satisfy $\frac{\partial \Phi_p}{\partial n}|_\zeta = 0$ (Neumann-type boundary conditions) ,
- TM modes, where Φ_p must satisfy $\Phi_p|_\zeta = 0$ (Dirichlet-type boundary conditions),

with ζ being the metallic contour of the waveguide. After solving the differential equation with the corresponding boundary conditions, the eigenfunctions Φ_p and eigenvalues k_{cp} of (2.3) are obtained, where each one corresponds to the p-th mode of (2.1)-(2.2). The expressions of these functions are specific to each cross-section geometry, whereas the derivation of γ_p, $\vec{e}_p$, $\vec{h}_p$, e_{zp} and h_{zp} from Φ_p can be addressed in general for any homogeneous waveguide of arbitrary cross-section as it is indicated in Appendix A. The two main unconventional waveguides studied in this Thesis have equilateral triangular and parabolic cross-sections, with a single conductor. For waveguides with more than one conductor, Transversal Electro-Magnetic (TEM) modes would be also needed in (2.1)-(2.2).

In the equilateral triangular waveguide each of the previous two mode families (TE and TM) is split into two more, one symmetric (S) and another one asymmetric (A), giving rise to four mode families (TE^A, TE^S, TM^A and TM^S respectively). This classification is

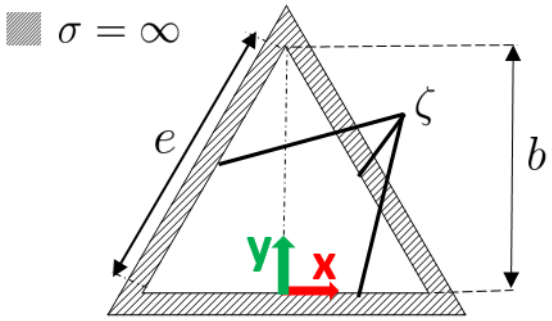

Figure 2.1: Equilateral triangular cross-cross section, with contour ζ, side e and height b, with the reference system set in the proposed formulation.

due to the symmetry of the cross-section with respect to the y-axis, as it can be seen in Figure 2.1, which gives rise to solutions with even/odd symmetry with respect to this axis. Their complete resolution is given in [40, 41]. According to the position of the center of coordinates shown in Figure 2.1, chosen for the development of an in-house software, the expressions of the eigenfunctions (mode families) in [40, 41] are changed into:

$$\begin{aligned}\Phi^{S}_{TE} &= \cos(\tilde{k}_{y1}(y-b))\cos(\tilde{k}_{x1}x) + \cos(\tilde{k}_{y2}(y-b))\cos(\tilde{k}_{x2}x) + \\ &\quad \cos(\tilde{k}_{y3}(y-b))\cos(\tilde{k}_{x3}x) \end{aligned} \tag{2.4}$$

$$\begin{aligned}\Phi^{A}_{TE} &= \cos(\tilde{k}_{y1}(y-b))\sin(\tilde{k}_{x1}x) + \cos(\tilde{k}_{y2}(y-b))\sin(\tilde{k}_{x2}x) + \\ &\quad \cos(\tilde{k}_{y3}(y-b))\sin(\tilde{k}_{x3}x) \end{aligned} \tag{2.5}$$

$$\begin{aligned}\Phi^{S}_{TM} &= \sin(\tilde{k}_{y1}(y-b))\cos(\tilde{k}_{x1}x) + \sin(\tilde{k}_{y2}(y-b))\cos(\tilde{k}_{x2}x) + \\ &\quad \sin(\tilde{k}_{y3}(y-b))\cos(\tilde{k}_{x3}x) \end{aligned} \tag{2.6}$$

$$\begin{aligned}\Phi^{A}_{TM} &= \sin(\tilde{k}_{y1}(y-b))\sin(\tilde{k}_{x1}x) + \sin(\tilde{k}_{y2}(y-b))\sin(\tilde{k}_{x2}x) + \\ &\quad \sin(\tilde{k}_{y3}(y-b))\sin(\tilde{k}_{x3}x) \end{aligned} \tag{2.7}$$

where $\tilde{k}_{y1} = \frac{(-m-n)\pi}{b}$, $\tilde{k}_{y2} = \frac{m\pi}{b}$, $\tilde{k}_{y3} = \frac{n\pi}{b}$, $\tilde{k}_{x1} = \frac{(m-n)\pi}{\sqrt{3}b}$, $\tilde{k}_{x2} = \frac{(2n+m)\pi}{\sqrt{3}b}$, $\tilde{k}_{x3} = \frac{(-2m-n)\pi}{\sqrt{3}b}$. Variable b is the height of the equilateral triangular cross-section depicted in Figure 2.1, related to its side e through $b = e\sqrt{3}/2$. Variables m and n in the previous expressions adopt values whose range depend on the mode family under consideration $m \geq n \geq 0$ for symmetric TE modes (TE^S), $m > n \geq 0$ for asymmetric TE modes (TE^A), $m \geq n > 0$ for symmetric TM modes (TM^S) and $m > n > 0$ for asymmetric TM modes (TM^A).

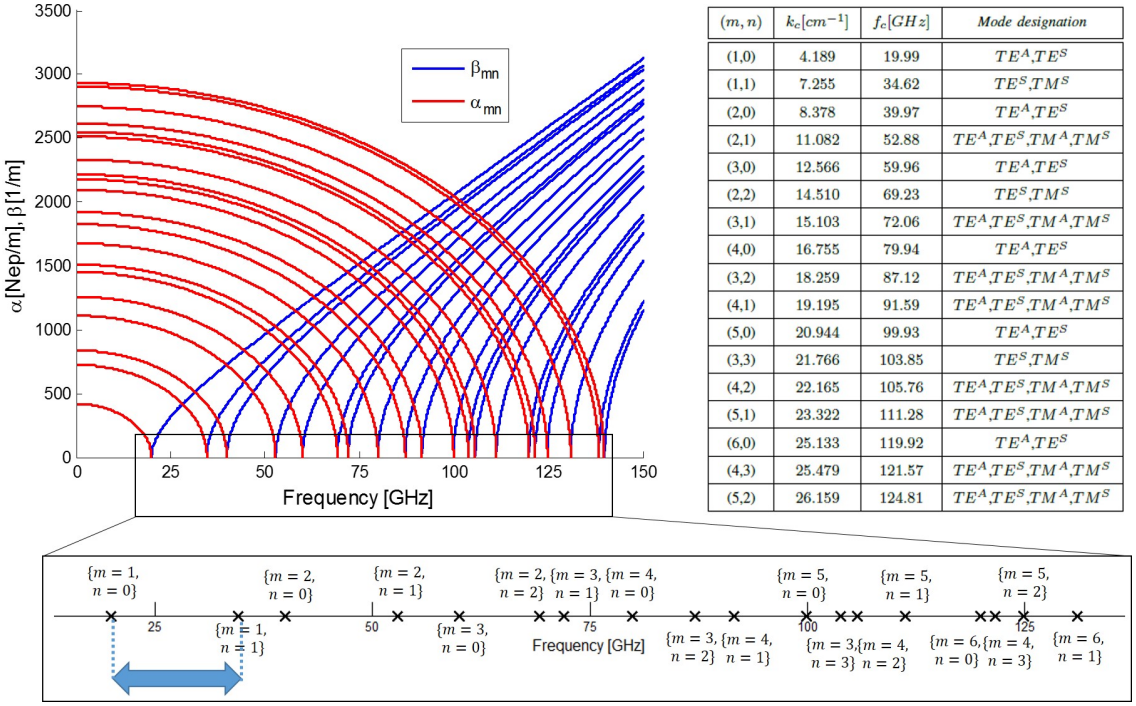

(m,n)	$k_c[cm^{-1}]$	$f_c[GHz]$	*Mode designation*
(1,0)	4.189	19.99	TE^A,TE^S
(1,1)	7.255	34.62	TE^S,TM^S
(2,0)	8.378	39.97	TE^A,TE^S
(2,1)	11.082	52.88	TE^A,TE^S,TM^A,TM^S
(3,0)	12.566	59.96	TE^A,TE^S
(2,2)	14.510	69.23	TE^S,TM^S
(3,1)	15.103	72.06	TE^A,TE^S,TM^A,TM^S
(4,0)	16.755	79.94	TE^A,TE^S
(3,2)	18.259	87.12	TE^A,TE^S,TM^A,TM^S
(4,1)	19.195	91.59	TE^A,TE^S,TM^A,TM^S
(5,0)	20.944	99.93	TE^A,TE^S
(3,3)	21.766	103.85	TE^S,TM^S
(4,2)	22.165	105.76	TE^A,TE^S,TM^A,TM^S
(5,1)	23.322	111.28	TE^A,TE^S,TM^A,TM^S
(6,0)	25.133	119.92	TE^A,TE^S
(4,3)	25.479	121.57	TE^A,TE^S,TM^A,TM^S
(5,2)	26.159	124.81	TE^A,TE^S,TM^A,TM^S

Figure 2.2: Dispersion diagram of an equilateral triangular waveguide with side $e = 1$ cm.

In fact, the values of m and n determine the eigenvalue k_{cp} associated to each eigenfunction Φ_p in (2.3). It is important to emphasize here that each single index p is refered to a mode uniquely identified by its type, symmetry and pair of subindexes (*i.e.*, TE^A_{mn},TE^S_{mn},TM^A_{mn},TM^S_{mn}). The eigenvalues k_{cp} are commonly known in electromagnetism as cut-off wavenumbers of the waveguide, and are directly related to the propagation constant γ_p through the formula $\gamma_p^2 = k_{cp}^2 - \omega^2\mu\varepsilon$ (μ and ε are the magnetic permeability and the electric permittivity of the medium enclosed by the perfect conductor of the waveguide, respectively). According to [40, 41], k_{cp} is obtained in the equilateral triangular waveguide as:

$$k_{cp} = \frac{4\pi}{3e}\sqrt{m^2 + n^2 + mn}. \tag{2.8}$$

It can be also computed from the previous variables of (2.4)-(2.7) as:

$$k_{cp}^2 = \tilde{k}_{xi}^2 + \tilde{k}_{yi}^2\,, \text{ for } i = 1, 2, 3. \tag{2.9}$$

The cut-off wavenumbers k_{cp} of any waveguide homogeneously filled are related to the cut-off frequencies by $f_{cp} = \frac{k_{cp}}{2\pi\sqrt{\mu\varepsilon}}$, from which the corresponding modes start to propagate. Such frequencies are represented in the abscissa axis of the dispersion diagram plotted in Figure 2.2 at the points where β and α become zero and thus the propagation constant as well (given $\gamma = \alpha + j\beta$). This diagram has been generated for a hollow equilateral triangular waveguide of side $e = 1$ cm. The corresponding cut-off frequencies are shown in detail in the rectangular box below, where the m and n subindexes are specified. The table given next to the diagram shows in detail the k_c and f_c values. What is more, in the table it is evidenced the degeneracy present in this particular waveguide since each pair

	Square	**Circular**	**Equilateral Triangular**
f_{c2}/f_{c1}	$\sqrt{2} \approx 1.41$	≈ 1.31	$\sqrt{2} \approx 1.41$
f_{c3}/f_{c1}	2	≈ 1.66	2
f_{c4}/f_{c1}	$\sqrt{5} \approx 2.24$	≈ 2.08	$\sqrt{7} \approx 2.65$
f_{c5}/f_{c1}	$\sqrt{8} \approx 2.83$	≈ 2.28	3

Table 2.1: Mode chart comparison: cut-off frequencies of higher order modes with respect to the degenerated fundamental modes for waveguides having different canonical cross-sections.

(m, n) gives rise to several degenerated modes. In particular, when $n = 0$ or $m = n$, a pair of degenerated modes arise. When $m \neq n \neq 0$, four degenerated modes are present.

Finally it is worth to point out that the division by symmetry of the four mode families facilitates the identification of modes in the design of a microwave device. In particular, Perfect Electric Wall (PEW) symmetry is shown by symmetric TE modes (TE^{S}_{mn}) and asymmetric TM modes (TM^{A}_{mn}), whereas Perfect Magnetic Wall (PMW) symmetry is shown in asymmetric TE modes (TE^{A}_{mn}) and symmetric TM modes (TM^{S}_{mn}).

The field patterns and corresponding symmetries for the first modes are shown in the examples of Figure 2.3. The classification done in this figure with the PEW/PMW symmetry is very important for microwave devices, in order to understand its modal behavior. For instance, if an equilateral triangular waveguide is excited with a mode of certain symmetry aligning the axis of symmetry between waveguide steps, not all the mode families of the mode chart will be present (only the ones of the same symmetry).

One of the attractive features of the equilateral triangular waveguide is its inherent modal degeneracy, which can be exploited by resonant devices to generate more compact designs, as it will be shown later in this Thesis in Section 5.4.2. However, there is another feature even more interesting: the separation between the fundamental degenerated modes and the immediately higher ones is wider compared to conventional waveguides as Table 2.1 evidences.

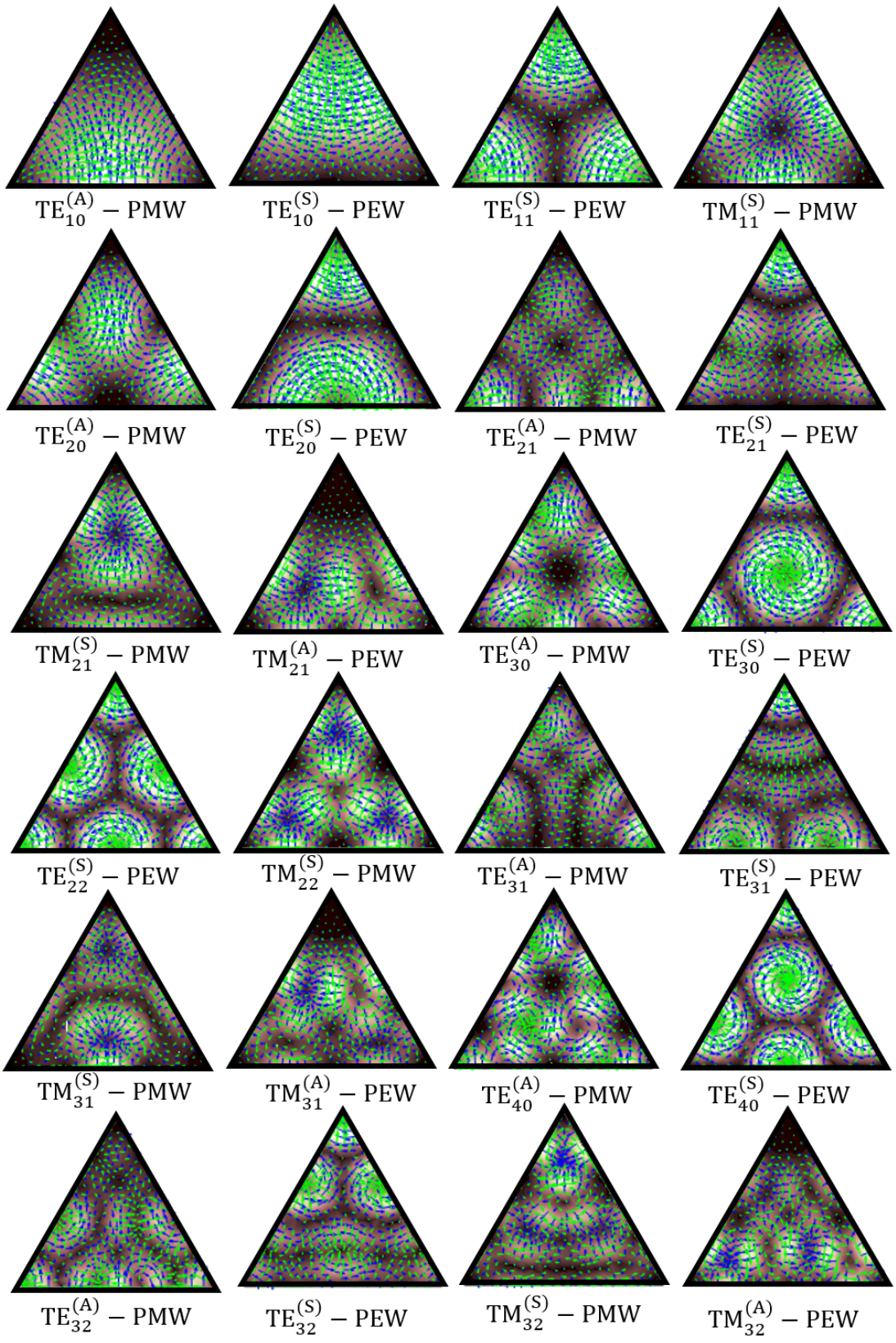

Figure 2.3: Mode pattern of the first 24 modes in the equilateral triangular waveguide.

2.3 Overview of the Mode-Matching method

Now that the modes of the electromagnetic field in (2.1) and (2.2) have been fully characterized for the equilateral triangular waveguide through (2.4)-(2.8), and the equations in Appendix A, the Mode-Matching method can be applied. This method, introduced long ago in [8], is nowadays almost standard for the analysis of devices made up of cascaded blocks of analytical modal spectrum [11, 74]. A great variety of devices designed using canonical waveguides such as the rectangular, circular or elliptical ones benefit from the efficiency of this method [75–82]. However, prior to this Thesis it had not been applied to the equilateral triangular waveguide yet.

This Section outlines the formulation of the Mode-Matching method, which is given in detail in the aforementioned literature [8, 11, 74]. Thus, the purpose is to introduce the method to facilitate the comprehension of the formulation proposed in the next Section, where the specific case of the equilateral triangular geometry is addressed.

Figure 2.4a) represents two cascaded waveguides of arbitrary cross-section, where the waveguide (w) is connected with the smaller waveguide (s). In the waveguide step, the larger waveguide has been ended with a perfect conductor wall except in the intersected area with the smaller waveguide (s). Both waveguides are depicted without conductor thickness. According to the Mode-Matching method the total transversal fields must be continuous across the intersected area in the waveguide step under consideration. If such intersection is placed at plane $z = 0$, the expressions (2.1) and (2.2) lead to:

$$\vec{E}_t^{(w)}\Big|_{A_w, z=0^-} = \sum_{j=1}^{N_w} \big(a_j^{(w)} + b_j^{(w)}\big)\vec{e}_j^{(w)} \tag{2.10}$$

$$\vec{E}_t^{(s)}\Big|_{A_s, z=0^+} = \sum_{i=1}^{N_s} \big(b_i^{(s)} + a_i^{(s)}\big)\vec{e}_i^{(s)} \tag{2.11}$$

$$\vec{H}_t^{(w)}\Big|_{A_w, z=0^-} = \sum_{j=1}^{N_w} \big(a_j^{(w)} - b_j^{(w)}\big)\vec{h}_j^{(w)} \tag{2.12}$$

$$\vec{H}_t^{(s)}\Big|_{A_s, z=0^+} = \sum_{i=1}^{N_s} \big(b_i^{(s)} - a_i^{(s)}\big)\vec{h}_i^{(s)}, \tag{2.13}$$

where superscripts (w) and (s) refer to each waveguide of the generic intersection shown in Figure 2.4a) , and the series of (2.1) and (2.2) have been truncated to N_w and N_s terms (modes) in order to formulate an affordable computational problem.

Now both modal series at each waveguide ($\vec{E}_t^{(w)}$ and $\vec{H}_t^{(w)}$ on one side, and $\vec{E}_t^{(s)}$ and $\vec{H}_t^{(s)}$ on the other side) are linked through the following boundary conditions:

$$\begin{cases} \textit{EFBC} \text{ in } A_w : \hat{z} \times \vec{E}_t^{(w)} = \begin{cases} 0, & \text{in } A_c,\ z = 0 \\ \hat{z} \times \vec{E}_t^{(s)} & \text{in } A_s,\ z = 0 \end{cases} \\ \\ \textit{MFBC} \text{ in } A_s : \hat{z} \times \vec{H}_t^{(w)} = \hat{z} \times \vec{H}_t^{(s)} \quad \text{in } A_s,\ z = 0 \end{cases} \tag{2.14}$$

where EFBC stands for *Electric Field Boundary Condition* , MFBC stands for *Magnetic Field Boundary Condition*, and A_w, A_s and A_c are the areas shown in Figure 2.4. These

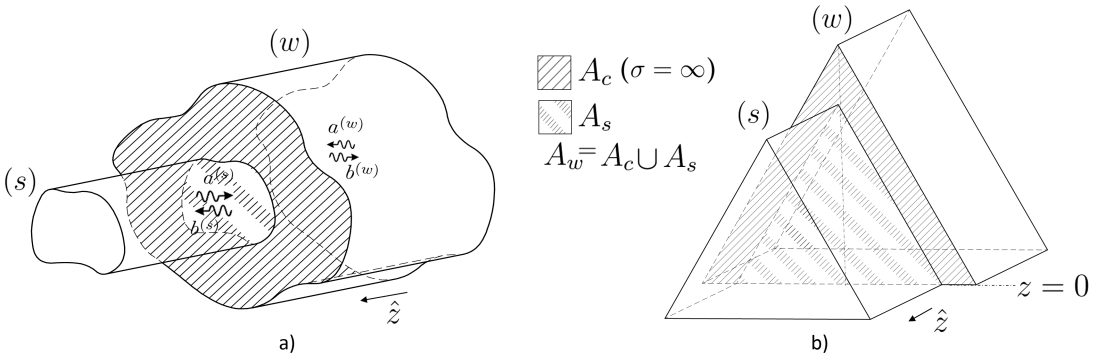

Figure 2.4: Step between a) generic and b) equilateral triangular waveguides.

boundary conditions are imposed using a Galerkin method [74] where the modal magnetic fields of waveguide (w) test the EFBC (*i.e.* $h_j^{(w)}$), whereas the electric fields of waveguide (s) test the MFBC (*i.e.* $e_i^{(s)}$). The following system of equations arise:

$$\begin{cases} EFBC\text{:} & (\mathbf{a}_w + \mathbf{b}_w) = \mathbf{X}^t(\mathbf{a}_s + \mathbf{b}_s) \quad (N_w \text{ eqs.}) \\ MFBC\text{:} & \mathbf{X}(\mathbf{a}_w - \mathbf{b}_w) = (\mathbf{b}_s - \mathbf{a}_s) \quad (N_s \text{ eqs.}) \end{cases} \tag{2.15}$$

where the modal amplitudes have been arranged in column vectors ($\mathbf{a}_g = [...a_p^{(g)}...]^T$, $\mathbf{b}_g = [...a_p^{(g)}...]^T$, with $g = w, s$) and the term $\mathbf{X}$ is known as the inner product matrix, defined as:

$$[X_{ij}] = Y_j^{(w)} \iint_{A_s} \vec{e}_i^{(s)} \cdot \vec{e}_j^{(w)}\, dS = Z_i^{(s)} \iint_{A_s} \vec{h}_i^{(s)} \cdot \vec{h}_j^{(w)}\, dS, \tag{2.16}$$

where $Y_j^{(w)}$ and $Z_i^{(s)}$ are the mode admittance and impedance in each waveguide respectively, obtained according to the mode family from expressions (A.9) or (A.17) of Appendix A, and $Y_j(\vec{e}_i \cdot \vec{e}_j) = Z_i(\vec{h}_i \cdot \vec{h}_j)$ holds. The elements X_{ij} of the inner cross-product matrix $\mathbf{X}$, expressed in (2.16) in terms of the modal fields, can be written in terms of the function Φ solution of (2.3) as:

$$X_{ij} = \frac{\sqrt{Y_j^{(w)}}}{\sqrt{Y_i^{(S)}}} \iint_{A_s} \vec{\Phi}_{E_i}^{(s)} \times \vec{\Phi}_{H_j}^{(w)} \cdot \hat{z} dS = \frac{\sqrt{Y_j^{(w)}}}{\sqrt{Y_i^{(S)}}} \cdot \bar{X}_{ij}, \tag{2.17}$$

where $\bar{X}_{ij}$ is the corresponding element of the so-called normalized inner cross-product matrix $\bar{\mathbf{X}}$, independent of frequency and of the material filling the waveguide, and:

$$\left.\begin{aligned} \vec{\Phi}_{E_i}^{(s)} &= \nabla_t \Phi_i \times \hat{z} \\ \vec{\Phi}_{H_j}^{(w)} &= \nabla_t \Phi_j \end{aligned}\right\} \text{for TE modes,} \tag{2.18}$$

$$\left.\begin{aligned} \vec{\Phi}_{E_i}^{(s)} &= \nabla_t \Phi_i \\ \vec{\Phi}_{H_j}^{(w)} &= \hat{z} \times \nabla_t \Phi_j \end{aligned}\right\} \text{for TM modes.} \tag{2.19}$$

Equation (2.17) can be written in matrix form as $\mathbf{X} = \mathbf{Z_s^{1/2}} \cdot \bar{\mathbf{X}} \cdot \mathbf{Y_w^{1/2}}$. Besides, the matrix elements $\bar{X}_{ij}$ can be further developed in terms of the sort of modes that make up the cross-products [83]:

$$\bar{X}_{ij} = 0 \text{ for TEM}^{(s)}\text{-TE}^{(w)}, \text{TM}^{(s)}\text{-TEM}^{(w)}, \text{TM}^{(s)}\text{-TE}^{(w)} \tag{2.20}$$

$$\bar{X}_{ij} = \iint_{A_s} \nabla_t \Phi_i^{(s)} \times \nabla_t \Phi_j^{(w)} \cdot \hat{z}\, dS \text{ for TE}^{(s)}\text{-TEM}^{(w)}, \text{TE}^{(s)}\text{-TM}^{(w)} \tag{2.21}$$

$$\bar{X}_{ij} = \iint_{A_s} \nabla_t \Phi_i^{(s)} \cdot \nabla_t \Phi_j^{(w)}\, dS \text{ for the remaining cases.} \tag{2.22}$$

The objective of the Mode-Matching method is to obtain the modal amplitudes in both waveguides at each side of the discontinuity by the resolution of the system of equations shown in (2.15). In fact, in order to design microwave devices we are interested not in their specific values but in their relationship, giving rise to the dispersion parameters (also known as S-parameters). In particular, the matrix that relates the modal amplitudes is called the Generalised Scattering Matrix (GSM) of the discontinuity:

$$\mathbf{S} = \begin{bmatrix} \mathbf{X}^T\mathbf{F}\mathbf{X} - \mathbf{I}_w & \mathbf{X}^T\mathbf{F} \\ \mathbf{F}\mathbf{X} & \mathbf{F} - \mathbf{I}_s \end{bmatrix}, \quad \begin{bmatrix} \mathbf{b}_w \\ \mathbf{b}_s \end{bmatrix} = \mathbf{S} \begin{bmatrix} \mathbf{a}_w \\ \mathbf{a}_s \end{bmatrix} \tag{2.23}$$

where $\mathbf{F} = 2(\mathbf{I}_s + \mathbf{X}\mathbf{X}^T)^{-1}$ (where superscript T stands for the transpose operation), and $\mathbf{I}_w$, $\mathbf{I}_s$ is the identity matrix of the corresponding size (N_w or N_s). The analysis of two or more discontinuities or steps is carried out cascading GSM matrices as in [9, 11, 74, 76, 84, 85]. In order to obtain the GSM in (2.23) it can be seen at a quick glance that it is essential to compute the inner cross-product matrix defined in (2.16) or equivalently in (2.17).

2.4 Mode-Matching method applied to equilateral triangular discontinuities

The purpose of this Section is to provide a suitable formulation that greatly simplifies the surface integrals associated to the inner cross products matrix whose definition is given in (2.17). In the proposed formulation equations (2.4)-(2.7) are each rewritten as a sum of plane waves using elementary conversions of the trigonometric functions to complex exponentials:

$$\Phi_{TE/TM}^{S,A/S,A} = \sum_{u=1}^{12} A_u e^{j(k_{xu}x + k_{yu}y)}, \tag{2.24}$$

where the values of A_u, k_{xu} and k_{yu} depend on each mode family and are all gathered in Table 2.2. Equation (2.24) can be written as well as follows, resembling a plane-wave expansion:

$$\Phi_{TE/TM}^{S,A/S,A} = \sum_{u=1}^{12} A_u e^{j(\vec{r}\cdot\vec{k}_u)}, \tag{2.25}$$

where $\vec{r}$ is the position vector defined as $\vec{r} = x\hat{x} + y\hat{y}$ and $\vec{k}_u$ is the so-called wave vector defined as $\vec{k}_u = k_{xu}\hat{x} + k_{yu}\hat{y}$.

In order to compute the surface integral defined in (2.16), the normalized fields $\vec{e}_i^{(s)}$, $\vec{e}_j^{(w)}$ computed as in (A.7) and (A.15) of Appendix A must be solved in each waveguide. To that end the first step is to calculate the normalization constants defined in expression (A.10), whose values are already given in [40, 41]:

$$N_p = \begin{cases} \frac{16}{3\sqrt{3}e^2k_{cp}^2} & \text{if } m \neq n \text{ and } n \neq 0 \\ \\ \frac{8}{3\sqrt{3}e^2k_{cp}^2} & \text{if } m = n \text{ or } n = 0. \end{cases} \tag{2.26}$$

The second step according to (A.7) and (A.15) in the Appendix is to obtain the transversal gradients of the eigenfunctions Φ. With such eigenfunctions written as proposed in (2.24) each term X_{ij} of the inner cross product matrix $\mathbf{X}$ in (2.17) is computed as:

$$X_{ij} = \left(\bar{X}_{ij,x} + \bar{X}_{ij,y}\right)\frac{\sqrt{Y_j^{(w)}}}{\sqrt{Y_i^{(s)}}}, \tag{2.27}$$

where the terms $\bar{X}_{ij,x}$ and $\bar{X}_{ij,y}$ are independent of the frequency and the material filling the waveguide, and refer to the surface integrals associated with the transversal fields in $\hat{x}$ and $\hat{y}$:

$$\bar{X}_{ij,x} = \sum_{r=1}^{12}\sum_{q=1}^{12} A_{sr}^{(s)}A_{sq}^{(w)} \iint_{A_s} e^{j(k_{xr}^{(s)}+k_{xq}^{(w)})x}e^{j(k_{yr}^{(s)}+k_{yq}^{(w)})y}dS, \tag{2.28}$$

$$\bar{X}_{ij,y} = \sum_{r=1}^{12}\sum_{q=1}^{12} A_{tr}^{(s)}A_{tq}^{(w)} \iint_{A_s} e^{j(k_{xr}^{(s)}+k_{xq}^{(w)})x}e^{j(k_{yr}^{(s)}+k_{yq}^{(w)})y}dS. \tag{2.29}$$

In the above expressions A_s is the intersected area between both equilateral waveguides as it can be seen in Figure 2.4b). The variables k_{xr}, k_{xq}, k_{yr}, and k_{yq} are the wavenumbers shown in (2.24) for each respective waveguide, and therefore their values are the ones gathered in Table 2.2. In particular, subindex u has been replaced by r to refer to the smaller waveguide (s) and by q to refer to the greater one (w). Only the new amplitudes A_{sr},A_{sq}, A_{tr} and A_{tq} must be computed according to the involved gradients shown in Appendix A. The results of these amplitudes, dependent on each mode family, are given in Table 2.3.

The two previous equations (2.28) and (2.29) evidence that one advantage of this formulation is that all the surface integrals involved in the calculation of the inner cross product matrix $\mathbf{X}$ can be reduced to the following simple analytical exponential integral over a triangle surface:

$$I = \iint_{A_s} e^{jB_1x}e^{jB_2y}dS, \tag{2.30}$$

where B_1 and B_2 represent the additions of the corresponding wavenumbers.

u	k_{xu}	k_{yu}	A_u
1	$\tilde{k}_{x1}$	$\tilde{k}_{y1}$	$\frac{1}{4}e^{j(-\tilde{k}_{y1}b-\Psi-\Omega)}$
2	$-\tilde{k}_{x1}$	$\tilde{k}_{y1}$	$\frac{1}{4}e^{j(-\tilde{k}_{y1}b-\Psi+\Omega)}$
3	$\tilde{k}_{x1}$	$-\tilde{k}_{y1}$	$\frac{1}{4}e^{j(\tilde{k}_{y1}b+\Psi-\Omega)}$
4	$-\tilde{k}_{x1}$	$-\tilde{k}_{y1}$	$\frac{1}{4}e^{j(\tilde{k}_{y1}b+\Psi+\Omega)}$
5	$\tilde{k}_{x2}$	$\tilde{k}_{y2}$	$\frac{1}{4}e^{j(-\tilde{k}_{y2}b-\Psi-\Omega)}$
6	$-\tilde{k}_{x2}$	$\tilde{k}_{y2}$	$\frac{1}{4}e^{j(-\tilde{k}_{y2}b-\Psi+\Omega)}$
7	$\tilde{k}_{x2}$	$-\tilde{k}_{y2}$	$\frac{1}{4}e^{j(\tilde{k}_{y2}b+\Psi-\Omega)}$
8	$-\tilde{k}_{x2}$	$-\tilde{k}_{y2}$	$\frac{1}{4}e^{j(\tilde{k}_{y2}b+\Psi+\Omega)}$
9	$\tilde{k}_{x3}$	$\tilde{k}_{y3}$	$\frac{1}{4}e^{j(-\tilde{k}_{y3}b-\Psi-\Omega)}$
10	$-\tilde{k}_{x3}$	$\tilde{k}_{y3}$	$\frac{1}{4}e^{j(-\tilde{k}_{y3}b-\Psi+\Omega)}$
11	$\tilde{k}_{x3}$	$-\tilde{k}_{y3}$	$\frac{1}{4}e^{j(\tilde{k}_{y3}b+\Psi-\Omega)}$
12	$-\tilde{k}_{x3}$	$-\tilde{k}_{y3}$	$\frac{1}{4}e^{j(\tilde{k}_{y3}b+\Psi+\Omega)}$

Mode designation	Ψ	Ω
TE^S	0	0
TE^A	0	$\frac{\pi}{2}$
TM^S	$\frac{\pi}{2}$	0
TM^A	$\frac{\pi}{2}$	$\frac{\pi}{2}$

Table 2.2: Values of parameters k_{xu}, k_{yu} and A_u, where $\tilde{k}_{y_{1,2,3}}$ and $\tilde{k}_{x_{1,2,3}}$ are described immediately after (2.4)-(2.7), and Ψ and Ω, are defined on the right side for each mode family.

r, q	$A_{sr,sq}$[TE]	$A_{sr,sq}$[TM]	$A_{tr,tq}$[TE]	$A_{tr,tq}$[TM]
1	$j\tilde{k}_{y1}A_u$	$j\tilde{k}_{x1}A_u$	$-j\tilde{k}_{x1}A_u$	$j\tilde{k}_{y1}A_u$
2	$j\tilde{k}_{y1}A_u$	$-j\tilde{k}_{x1}A_u$	$j\tilde{k}_{x1}A_u$	$j\tilde{k}_{y1}A_u$
3	$-j\tilde{k}_{y1}A_u$	$j\tilde{k}_{x1}A_u$	$-j\tilde{k}_{x1}A_u$	$-j\tilde{k}_{y1}A_u$
4	$-j\tilde{k}_{y1}A_u$	$-j\tilde{k}_{x1}A_u$	$j\tilde{k}_{x1}A_u$	$-j\tilde{k}_{y1}A_u$
5	$j\tilde{k}_{y2}A_u$	$j\tilde{k}_{x2}A_u$	$-j\tilde{k}_{x2}A_u$	$j\tilde{k}_{y2}A_u$
6	$j\tilde{k}_{y2}A_u$	$-j\tilde{k}_{x2}A_u$	$j\tilde{k}_{x2}A_u$	$j\tilde{k}_{y2}A_u$
7	$-j\tilde{k}_{y2}A_u$	$j\tilde{k}_{x2}A_u$	$-j\tilde{k}_{x2}A_u$	$-j\tilde{k}_{y2}A_u$
8	$-j\tilde{k}_{y2}A_u$	$-j\tilde{k}_{x2}A_u$	$j\tilde{k}_{x2}A_u$	$-j\tilde{k}_{y2}A_u$
9	$j\tilde{k}_{y3}A_u$	$j\tilde{k}_{x3}A_u$	$-j\tilde{k}_{x3}A_u$	$j\tilde{k}_{y3}A_u$
10	$j\tilde{k}_{y3}A_u$	$-j\tilde{k}_{x3}A_u$	$j\tilde{k}_{x3}A_u$	$j\tilde{k}_{y3}A_u$
11	$-j\tilde{k}_{y3}A_u$	$j\tilde{k}_{x3}A_u$	$-j\tilde{k}_{x3}A_u$	$-j\tilde{k}_{y3}A_u$
12	$-j\tilde{k}_{y3}A_u$	$-j\tilde{k}_{x3}A_u$	$j\tilde{k}_{x3}A_u$	$-j\tilde{k}_{y3}A_u$

Table 2.3: Values of parameters A_{sr}, A_{sq}, A_{tr} and A_{tq}.

Another significant advantage is that once the problem has been formulated for aligned equilateral triangular waveguides such as in Figure 2.4b), an offset for one of the waveguides can be easily introduced. As the following equation shows, any offset introduced in the reference coordinate system results again in plane waves with the same wave vector as in (2.25) and just a change in their associated amplitudes:

$$\Phi'^{S,A/S,A}_{TE/TM} = \sum_{u=1}^{12} A_u e^{j(k_{xu}(x'+\Delta x)+k_{yu}(y'+\Delta y))} = \sum_{u=1}^{12} A'_u e^{j(k_{xu}x'+k_{yu}y')}, \tag{2.31}$$

where $A'_u = A_u e^{j(k_{xu}\Delta x+k_{yu}\Delta y)}$. This means that the same simple integrals as shown in (2.30) hold.

The way of sorting the modes to compute each surface integral in (2.28) and (2.29) can be arbitrary. However, it is usual to sort the inner cross-products by mode family, organising matrix $\bar{\mathbf{X}}$ as a set of sub-matrices:

$$\bar{\mathbf{X}} = \begin{bmatrix} \bar{\mathbf{X}}^{(s)-(w)}_{\mathrm{TE}^S-\mathrm{TE}^S} & \bar{\mathbf{X}}^{(s)-(w)}_{\mathrm{TE}^S-\mathrm{TE}^A} & \bar{\mathbf{X}}^{(s)-(w)}_{\mathrm{TE}^S-\mathrm{TM}^S} & \bar{\mathbf{X}}^{(s)-(w)}_{\mathrm{TE}^S-\mathrm{TM}^A} \\ \bar{\mathbf{X}}^{(s)-(w)}_{\mathrm{TE}^A-\mathrm{TE}^S} & \bar{\mathbf{X}}^{(s)-(w)}_{\mathrm{TE}^A-\mathrm{TE}^A} & \bar{\mathbf{X}}^{(s)-(w)}_{\mathrm{TE}^A-\mathrm{TM}^S} & \bar{\mathbf{X}}^{(s)-(w)}_{\mathrm{TE}^A-\mathrm{TM}^A} \\ \bar{\mathbf{X}}^{(s)-(w)}_{\mathrm{TM}^S-\mathrm{TE}^S} & \bar{\mathbf{X}}^{(s)-(w)}_{\mathrm{TM}^S-\mathrm{TE}^A} & \bar{\mathbf{X}}^{(s)-(w)}_{\mathrm{TM}^S-\mathrm{TM}^S} & \bar{\mathbf{X}}^{(s)-(w)}_{\mathrm{TM}^S-\mathrm{TM}^A} \\ \bar{\mathbf{X}}^{(s)-(w)}_{\mathrm{TM}^A-\mathrm{TE}^S} & \bar{\mathbf{X}}^{(s)-(w)}_{\mathrm{TM}^A-\mathrm{TE}^A} & \bar{\mathbf{X}}^{(s)-(w)}_{\mathrm{TM}^A-\mathrm{TM}^S} & \bar{\mathbf{X}}^{(s)-(w)}_{\mathrm{TM}^A-\mathrm{TM}^A} \end{bmatrix}. \tag{2.32}$$

Having the submatrices of $\bar{\mathbf{X}}$ arranged by mode-families avoids the computation of some of them since their associated surface integrals are zero, as indicated by (2.20) [83]. Thereby (2.32) becomes:

$$\bar{\mathbf{X}} = \begin{bmatrix} \bar{\mathbf{X}}^{(s)-(w)}_{\mathrm{TE}^S-\mathrm{TE}^S} & \bar{\mathbf{X}}^{(s)-(w)}_{\mathrm{TE}^S-\mathrm{TE}^A} & \bar{\mathbf{X}}^{(s)-(w)}_{\mathrm{TE}^S-\mathrm{TM}^S} & \bar{\mathbf{X}}^{(s)-(w)}_{\mathrm{TE}^S-\mathrm{TM}^A} \\ \bar{\mathbf{X}}^{(s)-(w)}_{\mathrm{TE}^A-\mathrm{TE}^S} & \bar{\mathbf{X}}^{(s)-(w)}_{\mathrm{TE}^A-\mathrm{TE}^A} & \bar{\mathbf{X}}^{(s)-(w)}_{\mathrm{TE}^A-\mathrm{TM}^S} & \bar{\mathbf{X}}^{(s)-(w)}_{\mathrm{TE}^A-\mathrm{TM}^A} \\ 0 & 0 & \bar{\mathbf{X}}^{(s)-(w)}_{\mathrm{TM}^S-\mathrm{TM}^S} & \bar{\mathbf{X}}^{(s)-(w)}_{\mathrm{TM}^S-\mathrm{TM}^A} \\ 0 & 0 & \bar{\mathbf{X}}^{(s)-(w)}_{\mathrm{TM}^A-\mathrm{TM}^S} & \bar{\mathbf{X}}^{(s)-(w)}_{\mathrm{TM}^A-\mathrm{TM}^A} \end{bmatrix}. \tag{2.33}$$

Furthermore, having these submatrices arranged by mode-families as well allows to discard the cross-products between modes of different perfect wall symmetry when the

waveguide step is made up of triangular equilateral waveguides of aligned symmetry axis (as in Figure 2.4b)):

$$\bar{\mathbf{X}} = \begin{bmatrix} \bar{\mathbf{X}}^{(s)-(w)}_{\mathrm{TE}^S-\mathrm{TE}^S} & 0 & 0 & \bar{\mathbf{X}}^{(s)-(w)}_{\mathrm{TE}^S-\mathrm{TM}^A} \\ 0 & \bar{\mathbf{X}}^{(s)-(w)}_{\mathrm{TE}^A-\mathrm{TE}^A} & \bar{\mathbf{X}}^{(s)-(w)}_{\mathrm{TE}^A-\mathrm{TM}^S} & 0 \\ 0 & 0 & \bar{\mathbf{X}}^{(s)-(w)}_{\mathrm{TM}^S-\mathrm{TM}^S} & 0 \\ 0 & 0 & 0 & \bar{\mathbf{X}}^{(s)-(w)}_{\mathrm{TM}^A-\mathrm{TM}^A} \end{bmatrix} \tag{2.34}$$

It is important to bear in mind that these simplifications not only speed up the computation process but also prevent from having numerical errors associated to very low values in the order of machine precision.

2.5 Validation cases for Section 2.4

Three case studies are proposed to validate the formulation based on plane waves presented in Section 2.4. All of them are represented in Figure 2.5, where the first case is made up of two aligned waveguides, the second case of two misaligned waveguides and the third case represents a double step where two GSM are cascaded. In all these cases the smallest waveguides have a side of $e = \sqrt{3}$ mm, and the largest ones a side of $e = 2\sqrt{3}$ mm.

Once the case studies have been selected, the first decision is to choose the number of modes of each waveguide (N_w in the larger waveguide and N_s in the smaller waveguide at each step), since the series in (2.1) and (2.2) must be truncated to be computationally affordable. If the number of modes is very high, the computational cost is increased and the efficiency of the Mode-Matching method is compromised. Moreover, when two modal series are matched the problem of relative convergence arises [9]. In order to overcome this problem a well-known strategy has been followed:

(i) a reference frequency f_c^{ref} is set and the modes whose cut-off frequency is below it in each waveguide are chosen,

(ii) this reference is increased until the obtained results are nearly the same as the ones obtained with the previous f_c^{ref}.

Three thresholds have been set to analyze each of the three case studies. For a low number of modes, $f_c^{ref} = 6\, f_{c10}^{(w)}$, where $f_{c10}^{(w)}$ is the cut-off frequency of the two degenerated fundamental modes in the largest waveguide (denoted as (w) in Figure 2.5). Afterwards, a second threshold of $f_c^{ref} = 11\, f_{c10}^{(w)}$ has been considered. Finally the last threshold is increased to $f_c^{ref} = 16\, f_{c10}^{(w)}$ for the highest number of modes.

According to the selected criterion based on a cut-off frequency threshold to truncate the theoretically infinite series, three pairs of mode relationships are used for the case

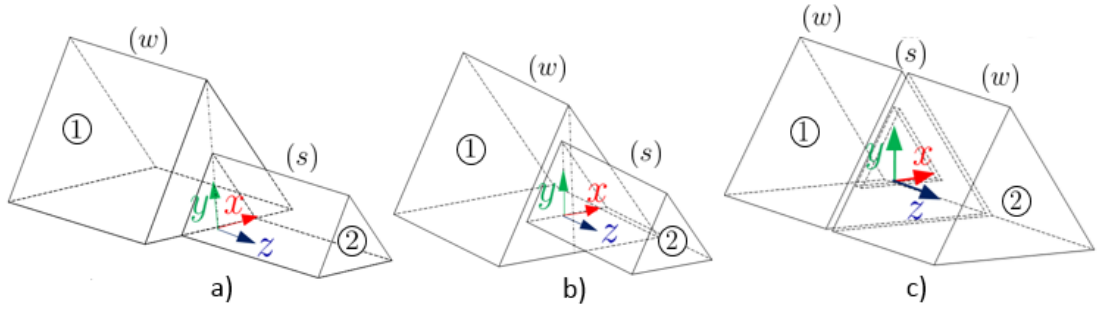

Figure 2.5: Case studies: single step a) without offset, b) with offset, and c) double step with offset.

study a), then for the case study b), and finally for the case study c). The selected relationships are 34-10, 106-34 and 214-58, where the first number indicates the number of modes considered in the largest waveguide, and the second number the modes considered in the smallest one (denoted as (w) and (s) respectively in Figure 2.5). In the first case study, however, the inner cross-product matrix $\mathbf{X}$ is simplified due to symmetry as in (2.34) and therefore half of the modes are required for the three pairs of relationships used.

Each case study analyzed with the Mode-Matching method gives rise to a GSM defined as in (2.23), where the relationship between the reflected and transmitted power waves of all the modes considered at the waveguide step is stored. In particular, this matrix has a size of $(N_s + N_w) \times (N_s + N_w)$, but in this Section we are only interested in the two fundamental degenerated modes, that is, in the $\mathrm{TE}_{10}^{(A)}$ and the $\mathrm{TE}_{10}^{(s)}$ modes. Thus, a problem of two physical ports is solved in each of the three cases of Figure 2.5, and 16 entries of the Generalized Scattering Matrix are analyzed. These entries are plotted as signal paths in Figure 2.6.

Figure 2.7 compares the results obtained with the proposed formulation using the Mode-Matching method and those obtained with a numerical approach from CST Microwave Studio (CST MWS) for the case study depicted in Figure 2.5a). The frequency range has been selected from 117 to 122 GHz for the two first case studies to ensure the propagation of the fundamental pair of degenerate modes at the waveguide ports so that a better comparison with the commercial software is guaranteed.

In particular, Figures 2.7a) and 2.7b) show the magnitude and phase of the reflection parameters of the mode TE_{10}^{A}, which correspond to the signal paths (or power wave relationships) depicted in Figure 2.6b). The magnitude and phase of the transmission parameters that correspond to the signal paths of Figure 2.6a) are shown in Figures 2.7c) and 2.7d) respectively. The same information is given for the TE_{10}^{S} mode in Figures 2.7e) to 2.7h), associated to the signal paths shown in 2.6c) and 2.6d).

If the results achieved for the TE_{10}^{A} mode are compared to the ones obtained for the TE_{10}^{S} mode, it can be seen that in this first case study the TE_{10}^{s} mode requires more modes in the series to achieve the results given by the numerical method in CST MWS in general. In the TE_{10}^{A} mode only the magnitude of the S_{11} parameter and the phase of the transmission parameters require a larger number of modes to converge.

Figure 2.8 analyzes the second case study given in 2.5b), where a vertical offset of 0.08 mm and a horizontal offset of 0.02 mm is introduced. The signal paths shown in Figures 2.6a) to 2.6d) are shown in Figures 2.8a) to 2.8h) in terms of their associated power waves. Compared to the first case study, the single step with misaligned waveguides requires a higher number of modes to obtain similar results as those obtained by the commercial software. This is caused by the presence of higher order modes that were not present in the previous case due to the simplification of the $\mathbf{X}$ matrix for symmetry reasons.

In the third and last case study the double step between misaligned waveguides shown in Figure 2.5c) is considered. This case is interesting to evaluate the interaction between high order modes and thus to test the formulation in a more robust way. In order to test the evanescent modes (i.e. those whose cut-off frequency is below the analyzed range of frequencies), a range of frequencies is selected where none of the modes in the smallest waveguide placed in between propagates (*i.e.* $90 - 95$ GHz). Moreover, in order to allow significant higher-order mode interaction between the two discontinuities the thickness of waveguide (s) is set to 0.3 mm, limiting the attenuation of its first three pairs of modes to 3.9 dB, 10 dB and 11.5 dB respectively.

Figures 2.9a) to 2.9h) show the power reflected and the power transfer related to the signal paths of Figure 2.6a) to 2.6d). The notation used in the legend in this case refers to the number of modes of each of the three waveguides present. It can be seen that the results obtained using a very low number of modes (*i.e.* 34-10-34, corresponding to the lowest threshold) and those with a higher number show greater differences than in the previous two case studies. Yet the achieved results finally converge once the number of modes is increased, as it is expected.

The power wave transfer between the TE_{10}^{A} and the TE_{10}^{S} modes is shown in Figures 2.6e) to h). Since both modes belong to mode families of dual symmetry, this transference is zero when the symmetry axis of the cross-sections is aligned, as in the first case study of Figure 2.5a). In the case studies of Figures 2.5b) and 2.5c) those axis are no longer aligned. Therefore there is a non zero transference, as it is evidenced in Figures 2.10 and 2.11 respectively.

The achieved results for the three analyzed cases have shown good agreement with the commercial software CST Microwave Studio, and therefore the proposed formulation is validated for discontinuities made up of equilateral triangular waveguides.

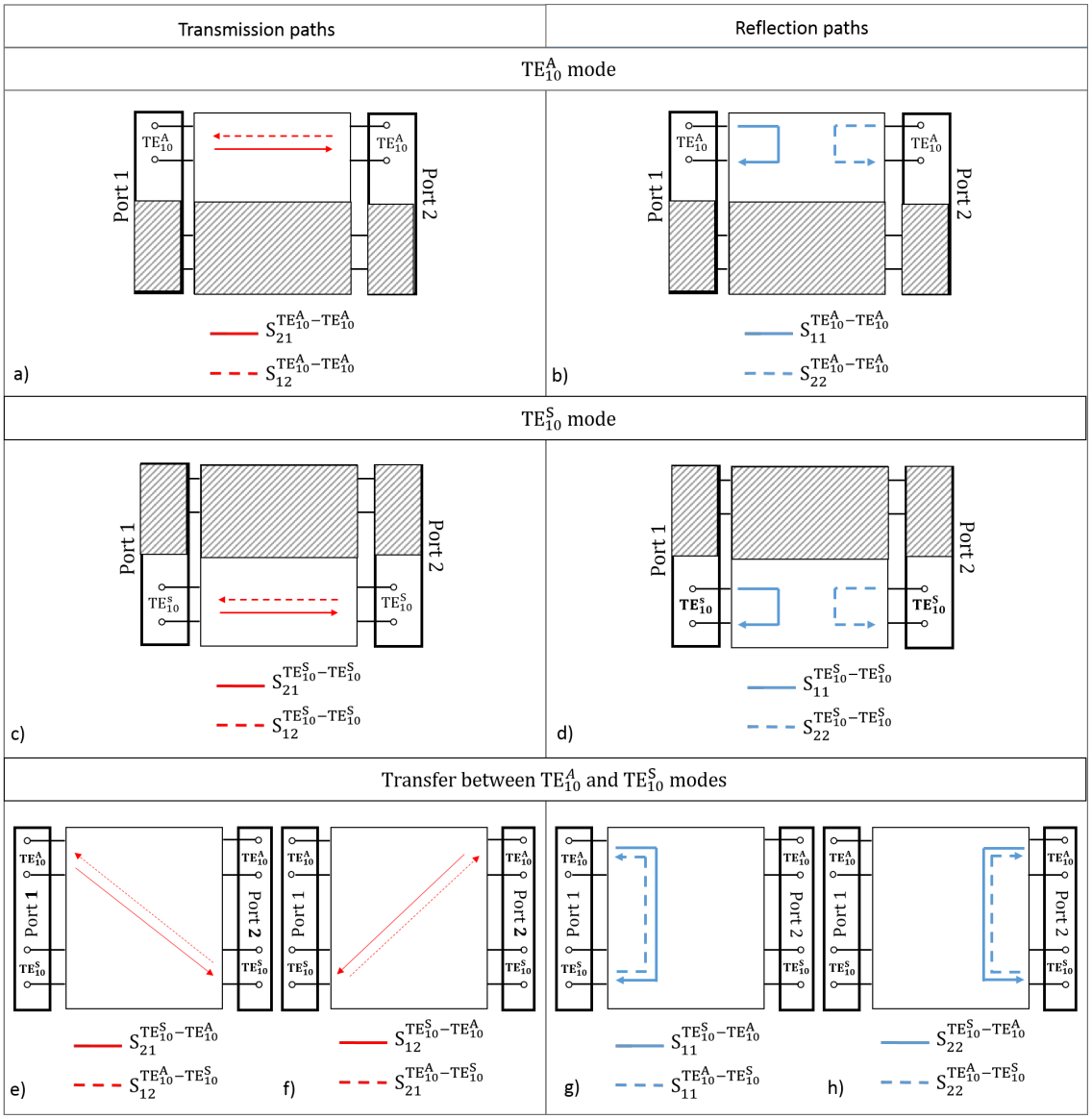

Figure 2.6: Signal paths in the equilateral triangular waveguides with TE_{10}^{A} and TE_{10}^{S} as fundamental propagating modes in the physical ports 1 and 2. .

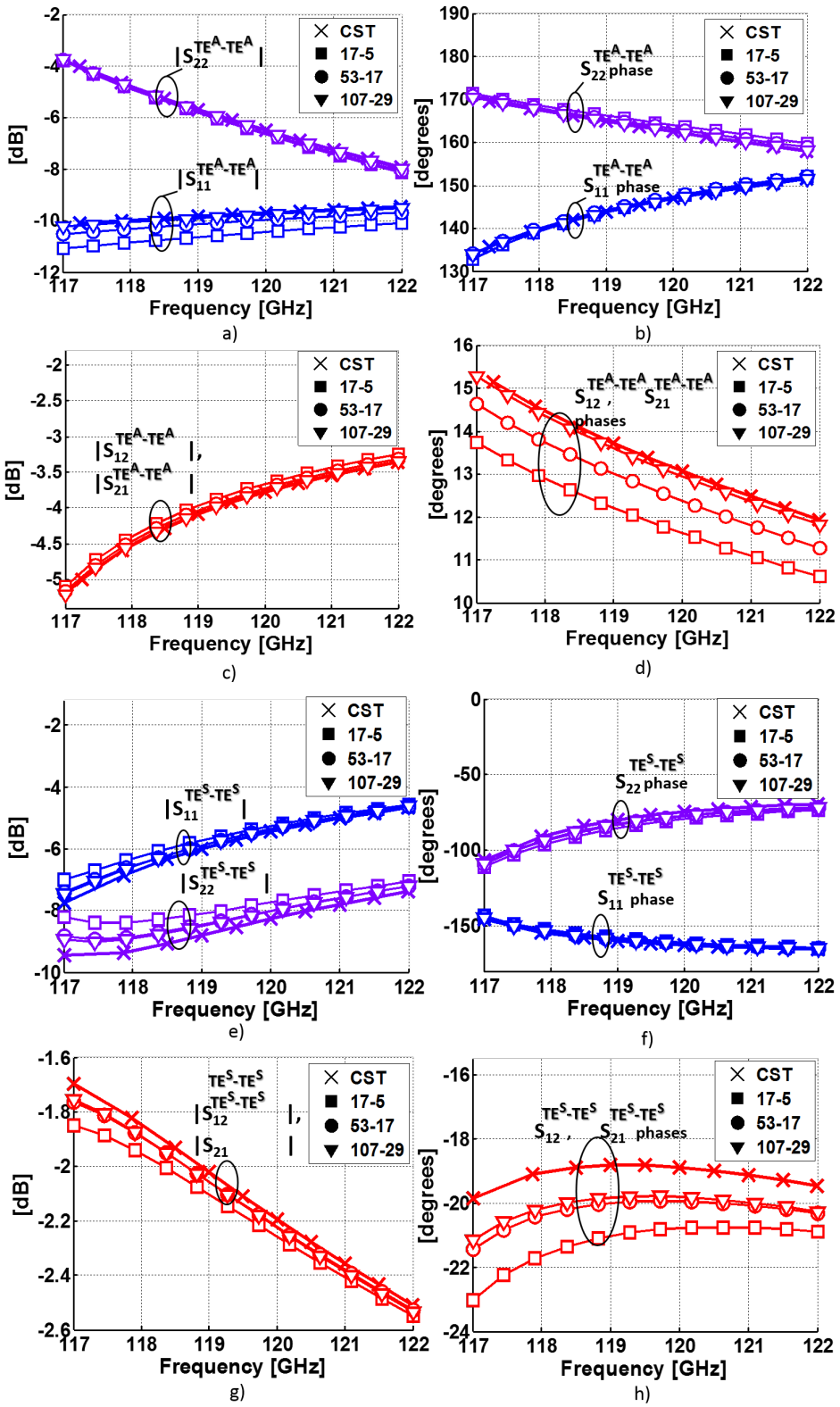

Figure 2.7: Case study a) in Figure 2.5. Mode TE_{10}^{A} in waveguide 1 to mode TE_{10}^{A} in waveguide 2: a) reflection magnitude, b) reflection phase, c) transmission magnitude and d) transmission phase. Mode TE_{10}^{S} in waveguide 1 to mode TE_{10}^{S} in waveguide 2: e) reflection magnitude, f) reflection phase, g) transmission magnitude and h) transmission phase.

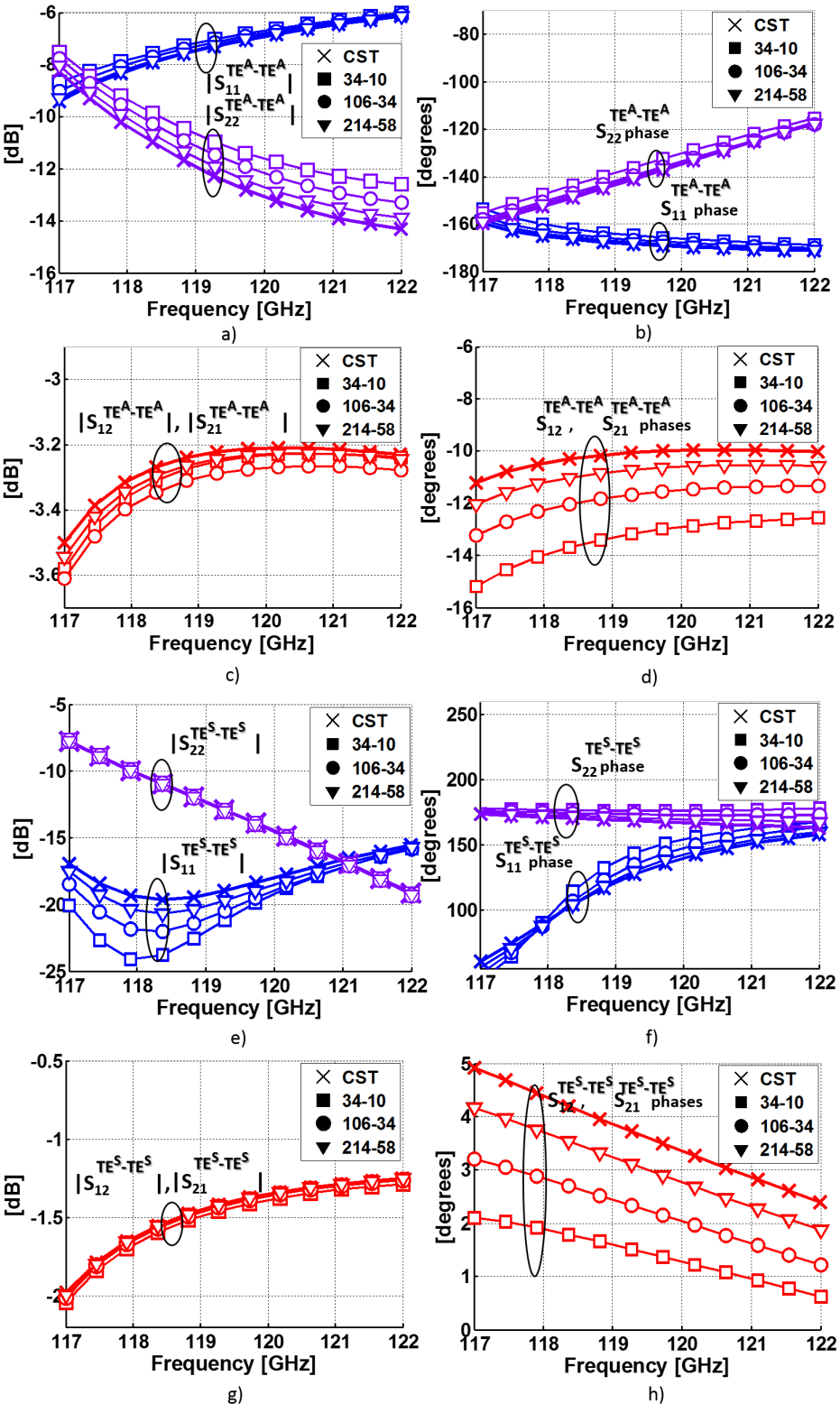

Figure 2.8: Case study b) in Figure 2.5. Mode TE_{10}^{A} in waveguide 1 to mode TE_{10}^{A} in waveguide 2: a) reflection magnitude, b) reflection phase, c) transmission magnitude and d) transmission phase. Mode TE_{10}^{S} in waveguide 1 to mode TE_{10}^{S} in waveguide 2: e) reflection magnitude, f) reflection phase, g) transmission magnitude and h) transmission phase.

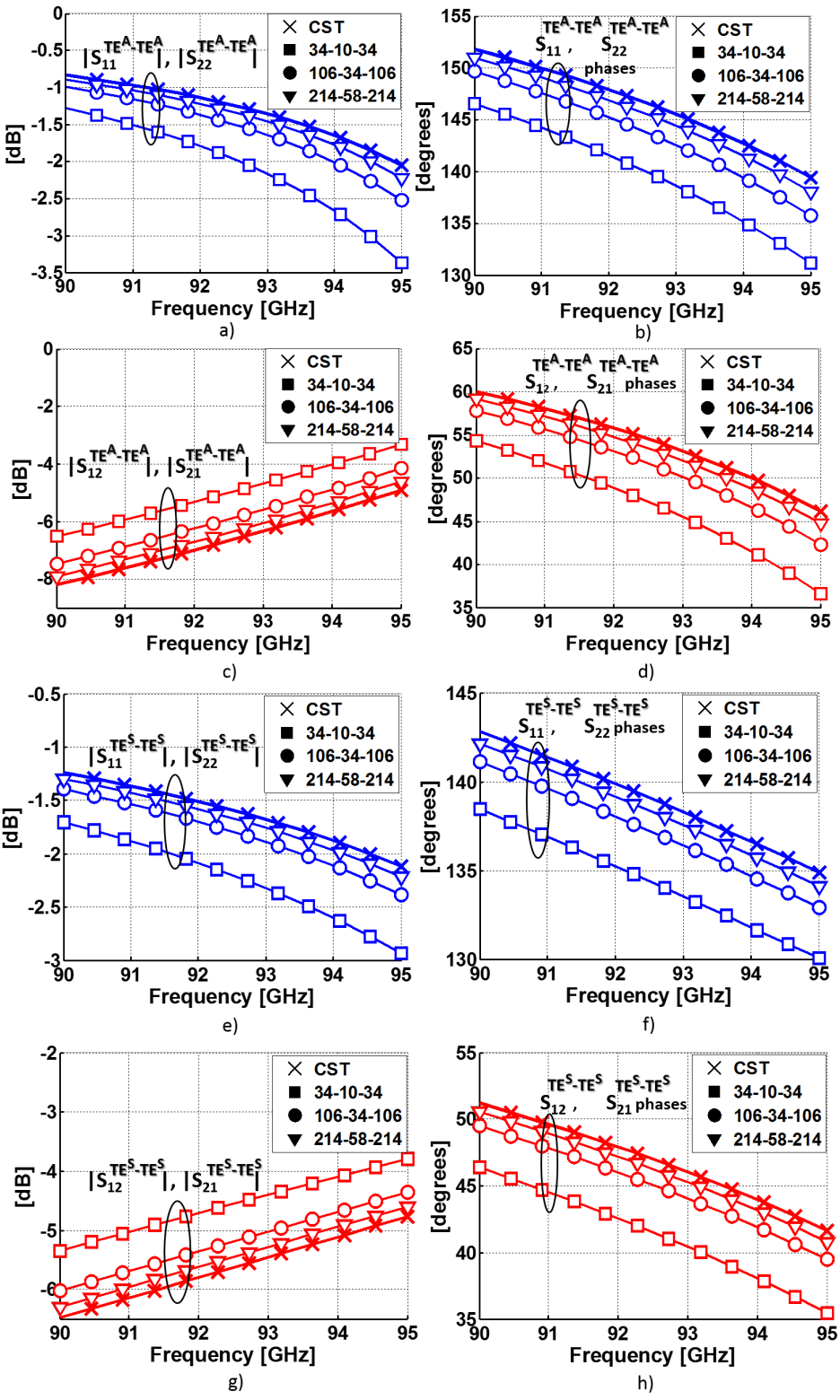

Figure 2.9: Case study c) in Figure 2.5. Mode TE_{10}^{A} in waveguide 1 to mode TE_{10}^{A} in waveguide 2: a) reflection magnitude, b) reflection phase, c) transmission magnitude and d) transmission phase. Mode TE_{10}^{S} in waveguide 1 to mode TE_{10}^{S} in waveguide 2: e) reflection magnitude, f) reflection phase, g) transmission magnitude and h) transmission phase.

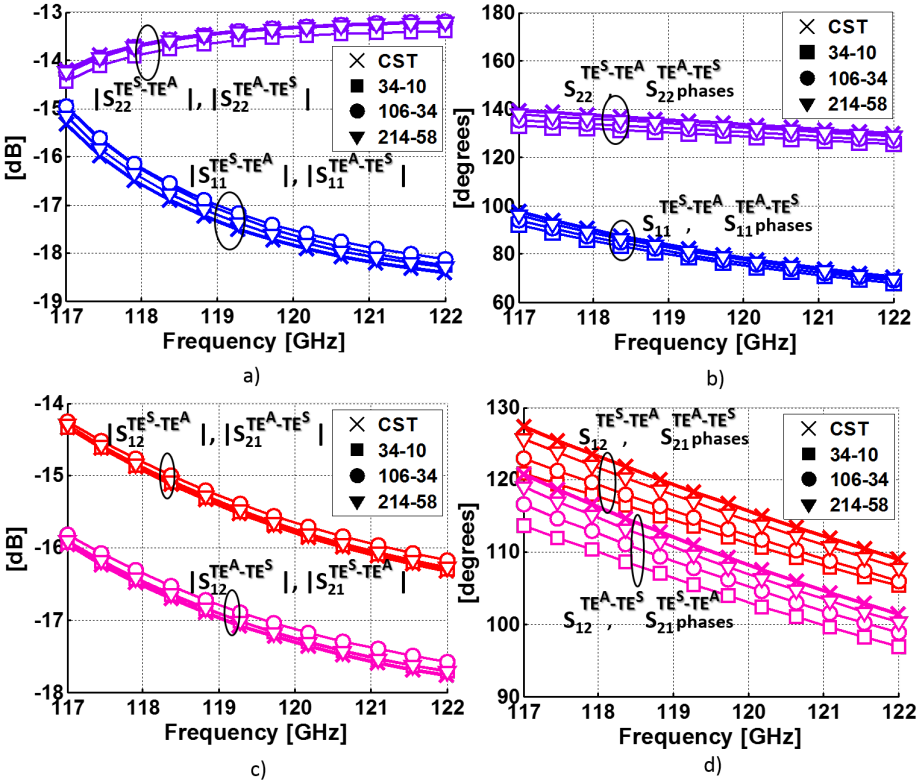

Figure 2.10: Case study b) in Figure 2.5. Mode TE_{10}^{A} in waveguide 1 to mode TE_{10}^{S} in waveguide 2: a) reflection magnitude, b) reflection phase, c) transmission magnitude and d) transmission phase.

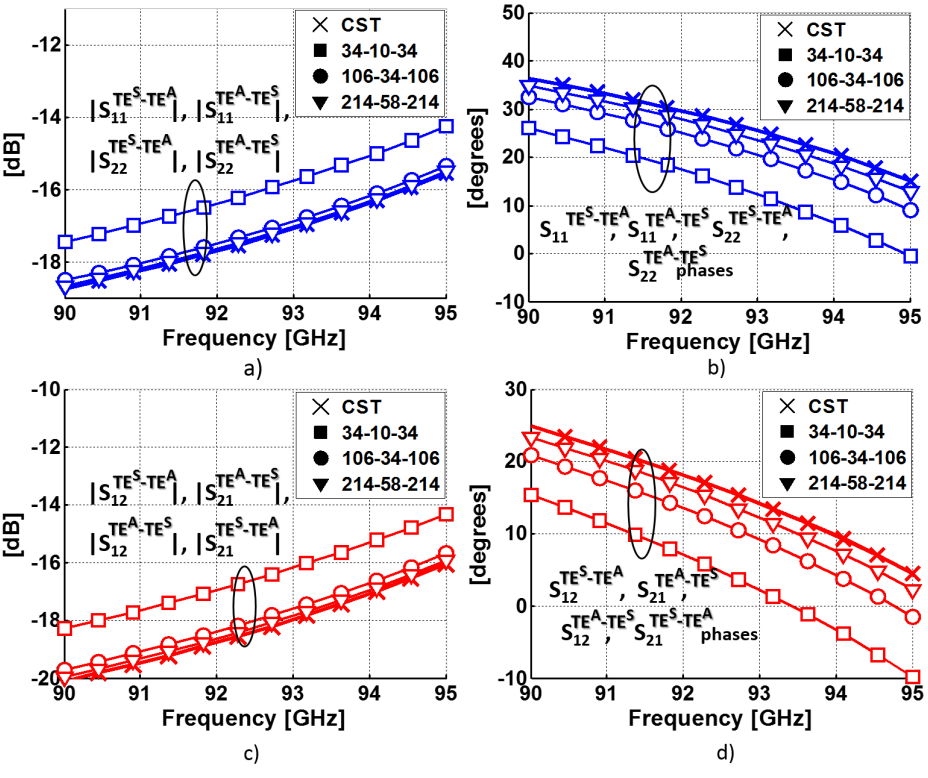

Figure 2.11: Case study c) in Figure 2.5. Mode TE_{10}^{A} in waveguide 1 to mode TE_{10}^{S} in waveguide 2: a) reflection magnitude, b) reflection phase, c) transmission magnitude and d) transmission phase.

2.6 Mode-Matching method applied to mixed discontinuities

As previously described in this Chapter, the Mode-Matching method has been extensively used so far for the efficient analysis of waveguide devices such as filters, directional couplers, transformers or polarizers [75, 79, 86–88]. Those devices are typically made up of rectangular, circular, or elliptical cross-sections, which are studied in this Section. This Chapter aims at providing a unified formulation for electromagnetic problems that include not only these classical canonical geometries but the equilateral triangular cross-section as well. Thereby the range of problems where the Mode-Matching method can be applied is broadened, contributing to the efficient design of novel devices that can benefit from this unconventional geometry.

To that end, the goal is to express the modes of canonical cross-sections as a finite sum of plane waves:

$$\Phi_{\text{TE/TM}} = \sum_u A_u e^{j(\vec{r}\cdot\vec{k}_u)}, \tag{2.35}$$

where the complex amplitudes A_u and real wave vectors $\vec{k_u}$ are the ones specific to each geometry. In all the cases Φ will belong to a TE or TM mode family since the canonical waveguides under consideration (*i.e.*, rectangular, circular and elliptic) are made up of one single conductor.

In the rectangular waveguide the eigenfunctions of (2.3) are products of trigonometric functions:

$$\Phi_{\substack{\text{TE}\\\text{TM}}} = \begin{matrix}\cos\\\sin\end{matrix}(k_x x)\begin{matrix}\cos\\\sin\end{matrix}(k_y y), \tag{2.36}$$

where a and b are the width and height of the cross-section respectively and $k_x = \frac{m\pi}{a}$, and $k_y = \frac{n\pi}{b}$. Hence, its associated plane wave expression is:

$$\Phi_{\text{TE/TM}} = \frac{e^{j(-\Psi-\Omega)}}{4}e^{j(k_x x+k_y y)} + \frac{e^{j(-\Psi+\Omega)}}{4}e^{j(k_x x-k_y y)} + \frac{e^{j(\Psi-\Omega)}}{4}e^{j(-k_x x+k_y y)} + \frac{e^{j(\Psi+\Omega)}}{4}e^{j(-k_x x-k_y y)}, \tag{2.37}$$

where the complex amplitudes A_u according to (2.35) are $A_u = \frac{e^{j(\pm\Psi\pm\Omega)}}{4}$ with $\Psi = \Omega = 0$ for TE modes and $\Psi = \Omega = \frac{\pi}{2}$ for TM modes.

In the circular waveguide these functions expressed in terms of circular coordinates (ρ, φ) are:

$$\Phi_{\text{TE/TM}} = J_m(k_c\rho)\begin{cases}\cos(m\varphi)\\\sin(m\varphi)\end{cases}, \tag{2.38}$$

where $k_c = \frac{p'_{mn}}{a}$ for TE modes and $k_c = \frac{p_{mn}}{a}$ for TM modes, with a the radius of the waveguide, p_{mn} the n-th zero of the bessel function J_m and p'_{mn} the n-th zero of its derivative J'_m. This function has an integral representation [78, 89, 90] that can be approximated in cartesian coordinates (x,y) by:

$$\begin{aligned}\Phi_{\text{TE/TM}} = {} & \frac{1}{2\pi}j^{-m}\int_0^{2\pi} e^{jk_c(x\cos u + y\sin u)}\begin{cases}\cos(mu)\\\sin(mu)\end{cases} du \approx \\ & \frac{j^{-m}}{P}\sum_{p=0}^{P-1} e^{jk_c(x\cos u_p + y\sin u_p)}\begin{cases}\cos(mu_p)\\\sin(mu_p)\end{cases},\end{aligned} \tag{2.39}$$

where $u_p = p\frac{2\pi}{P}$ and P is a large integer [78] that ensures enough accuracy in the truncation of the infinite series and k_c would be the same ones as defined in (2.38) for TE and TM modes. Therefore the complex amplitudes A_u and the real wave vector $\vec{k_u}$ of (2.35) are respectively: $A_u = \frac{j^{-m}}{P}\begin{Bmatrix}\cos(mu)\\ \sin(mu)\end{Bmatrix}$ and $\vec{k_u} = k_c\cos(u)\hat{x} + k_c\sin(u)\hat{y}$.

Finally the eigenfunctions Φ for the elliptical waveguide in elliptical coordinates (η, φ) are [51]:

$$\Phi_{\text{TE/TM}} = \begin{cases}\text{Mc}_m(\eta, q_{mn})\text{ce}_m(\varphi, q_{mn})\\ \text{Ms}_m(\eta, q_{mn})\text{se}_m(\varphi, q_{mn})\end{cases}, \tag{2.40}$$

where se_m and ce_m are the elliptic sine and cosine respectively, Mc_m and Ms_m are the modified Mathieu functions [91, 92] and q_{mn} is the n-th zero of these functions for TM modes and the n-th zero of the derivative of modified Mathieu functions Mc_m' and Ms_m' for TE modes. The cut-off wavenumber is given by $k_c = \frac{2\sqrt{q_{mn}}}{f}$, where f is the focal distance of the ellipse. The same type of approximation as in (2.39) can be carried out:

$$\begin{aligned}\Phi_{\text{TE/TM}} = \quad & \tfrac{1}{2\pi}j^{-m}\int_0^{2\pi} e^{jk_c(x\cos u + y\sin u)}\begin{cases}\text{ce}_m(u, q_{mn})\\ \text{se}_m(u, q_{mn})\end{cases} du \approx \\ & \tfrac{j^{-m}}{P}\sum_{p=0}^{P-1} e^{jk_c(x\cos u_p + y\sin u_p)}\begin{cases}\text{ce}_m(u_p, q_{mn})\\ \text{se}_m(u_p, q_{mn})\end{cases}.\end{aligned} \tag{2.41}$$

Therefore the complex modal amplitudes A_u in (2.35) are $A_u = \frac{j^{-m}}{P}\begin{Bmatrix}\text{ce}_m(u,q_{mn})\\ \text{se}_m(u,q_{mn})\end{Bmatrix}$ and the real wave vectors are $\vec{k_u} = k_c\cos(u)\hat{x} + k_c\sin(u)\hat{y}$.

The inner cross-product matrix $\mathbf{X}$ of a discontinuity holds the same definition as in (2.16), where the fields and the admittance are the ones associated to the corresponding type of waveguide. Therefore, having the expressions (2.37), (2.39) and (2.41), all the surface integrals related to the discontinuities of Figure 2.12 have the form of (2.30). This way, they can be solved analytically in a unified manner, even if the reference systems are shifted and/or rotated.

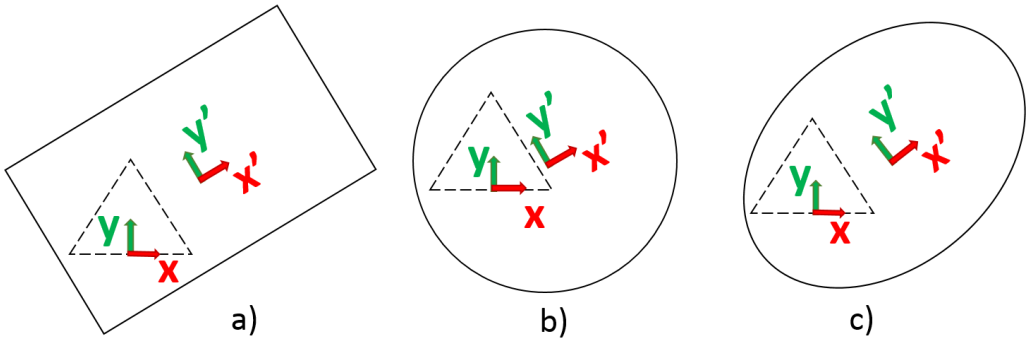

Figure 2.12: Transversal view of the discontinuities that can be analyzed by the presented unified formulation based on plane waves, with shifted and rotated reference systems: a) equilateral triangular-rectangular; b) equilateral triangular-circular; c) equilateral triangular-elliptical.

2.7 Validation cases for Section 2.6

Three case studies have been selected to validate the proposed formulation, from which the Mode-Matching method benefits. The relative reference systems of the corresponding waveguides have been shifted and rotated in order to analyze generic discontinuities. The first case is a waveguide junction where an equilateral triangular waveguide is place between two circular ones. In the second case study the circular waveguides have been replaced by elliptical waveguides. Finally, the third case study analyzes a waveguide junction where an equilateral triangular waveguide has been placed between an elliptical and a rectangular waveguide. Figure 2.13 shows the perspective views and the cross-sections of the analyzed structures.

The results attained by the Mode-Matching method using the plane wave formulation are presented in Figures 2.14, 2.15 and 2.16, together with the ones obtained by the Finite Element Method of the commercial software HFSS. The frequency threshold is set to 115 GHz, enough for convergence as the results attest. The excellent agreement between the approach of plane waves and the numerical commercial software validates the unified formulation where the equilateral triangular waveguide takes part of generic junctions where other conventional geometries such as the rectangular, circular and elliptical waveguides are present.

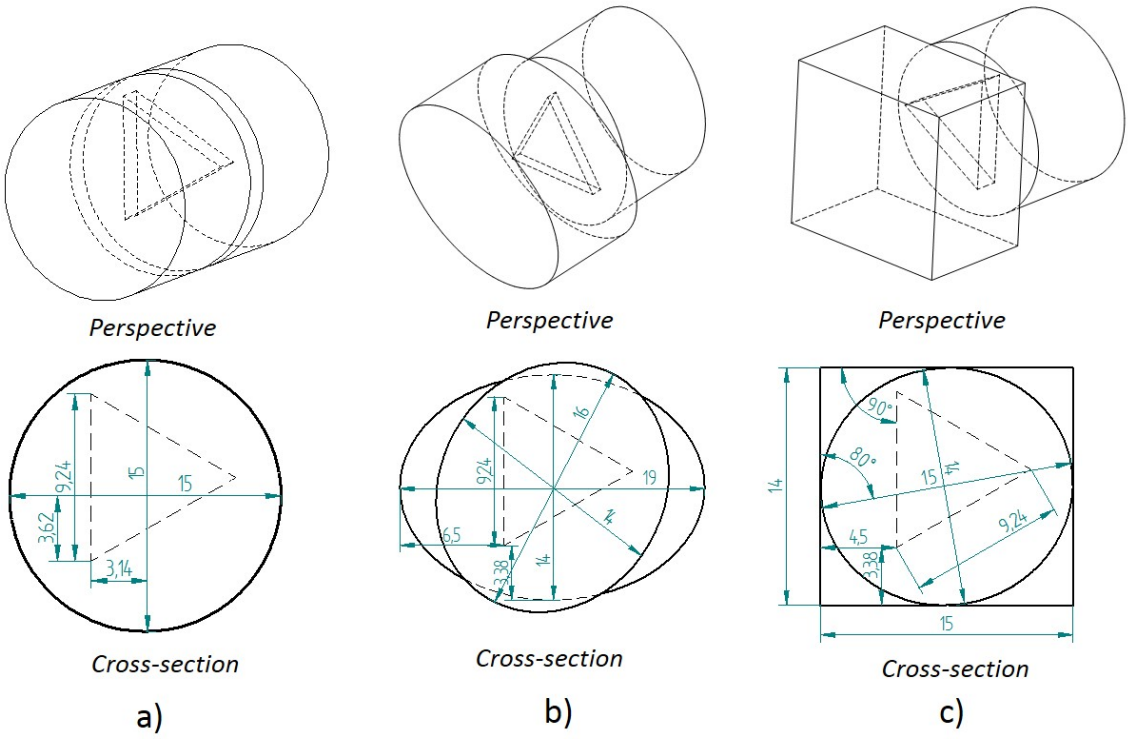

Figure 2.13: Case studies: junction with an equilateral triangular waveguide places between a) two circular waveguides, b) two elliptical waveguides and c) a rectangular and an elliptical waveguides.

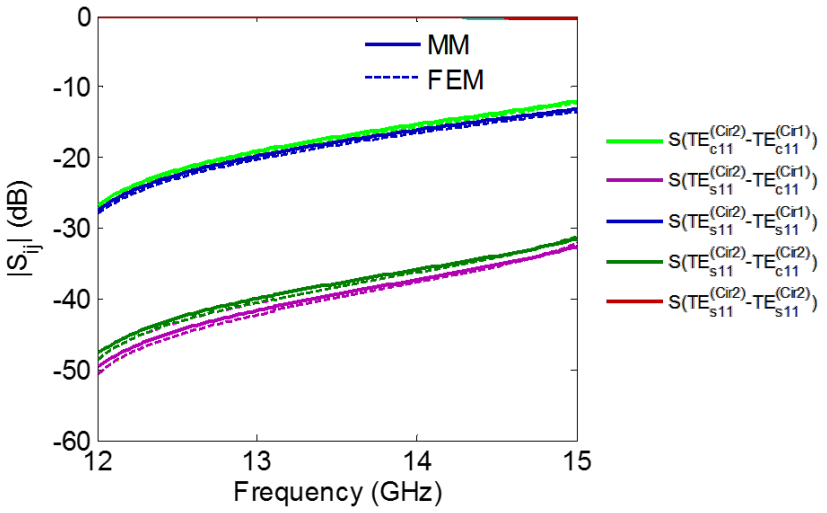

Figure 2.14: Results for case study a): waveguide junction made up of an equilateral triangular waveguide placed between circular waveguides.

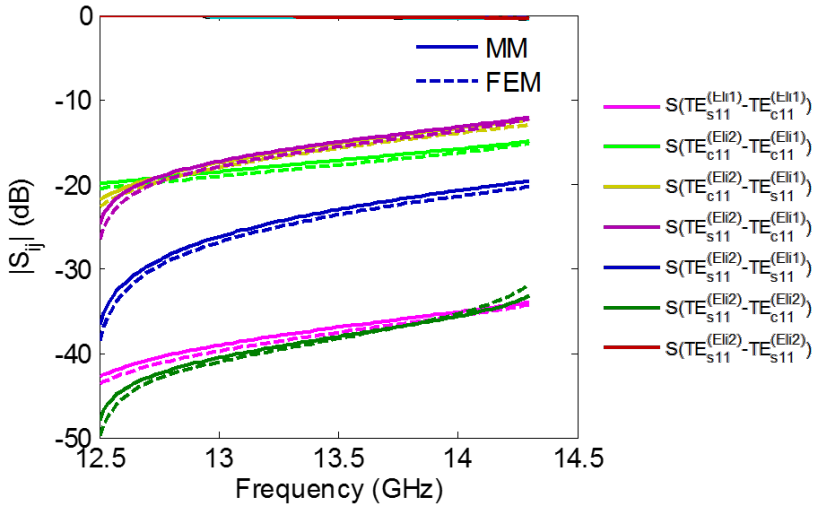

Figure 2.15: Results for case study b): waveguide junction made up of an equilateral triangular waveguide placed between elliptical waveguides.

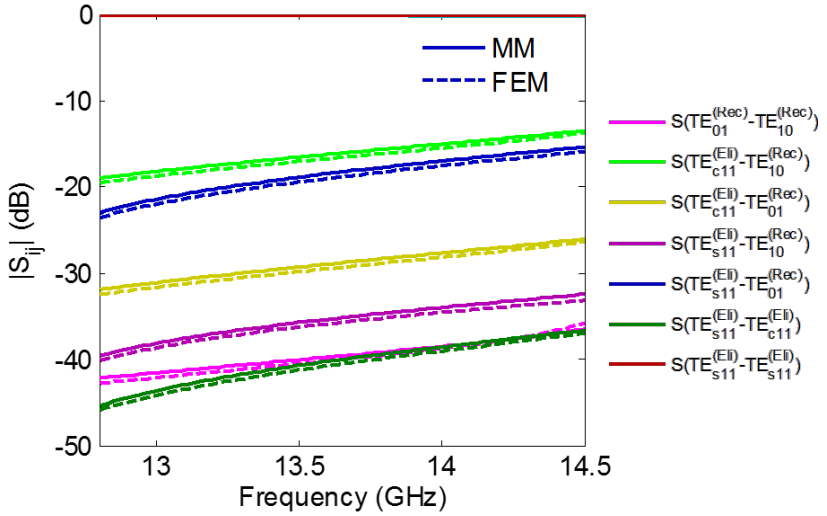

Figure 2.16: Results for case study c): waveguide junction made up of an equilateral triangular waveguide placed between a rectangular and an elliptical waveguide.

3 The parabolic cylinder waveguide

3.1 Introduction

The parabolic cylinder waveguide is the other unconventional geometry studied in this Thesis. As it happened with the equilateral triangular waveguide, its resolution by the method of variable separation was addressed some decades ago. In particular, in this electromagnetic problem another curvilinear coordinate system with translational symmetry different from the rectangular, circular or elliptical is needed to keep the solution quasi-analytical: the parabolic cylinder coordinates [93].

In the context of its modal resolution, pioneering work was developed in [94], where closed form expressions were given for the specific cases where the modal solutions can be reduced to the Bessel functions. However, the difficulty lies in the search of modal solutions in the remaining cases, where the problem cannot be reduced to a univariate root-finding problem as it happens in the circular or elliptical waveguides. In contrast, its resolution constitutes a cumbersome problem where a non-linear system of equations with two variables in the real domain must be solved.

The challenge of solving the complete set of modes of the parabolic cylinder waveguide was faced decades ago in [46] and [50], where graphical intersections were used as it was first suggested by [51]. Such strategy, however, is far from being practical since it cannot exploit the computational resources that are nowadays available.

The contribution of this Chapter is the systematic computation of the modes in the parabolic cylinder waveguide avoiding graphical means, so that the proposed procedure can be integrated into modern CAD tools. Towards that end the parabolic cylinder differential equation is presented in first place. Then, the combination of analytic continuation [50] with a recently published algorithm for bivariate systems of equations [52] is proposed. Some validation cases are given at the end of the Chapter, where results with proven high accuracy are achieved.

In contrast to the equilateral triangular waveguide, the practical utility of this waveguide has been addressed a number of times in the literature. In fact, the parabolic cylinder waveguide has already been used in a circular to rectangular mode converter [95]. Besides, its inherent stability of polarization has been reported in [96], where it has been suggested as an alternative to the circular waveguide. Furthermore, contour plots for loss estimation have been recently reported in [97]. Despite these references, it is evident that this geometry is not among the most popular ones for the design of microwave devices. In this sense, the purpose of this work is to boost its relevance in microwave engineering providing an efficient tool to carry out the corresponding designs with improved efficiency.

3.2 The parabolic cylinder differential equation

The procedure to solve the electromagnetic field of any waveguide with translation symmetry, homogeneously filled and surrounded by perfect conductor walls was described in the previous Chapter and detailed in the Appendix A. It starts with the resolution of the scalar Helmholtz equation given in (2.3), where the choice of a suitable coordinate system greatly simplifies the problem. In the case of the parabolic cylinder waveguide, its modal spectra can be quasi-analytically described if the parabolic cylinder coordinates are exploited to face the problem of variable separation.

The parabolic cylinder coordinates belong to a curvilinear orthogonal coordinate system whose curves along the xy plane are confocal parabolas which share a common focus placed at the cartesian origin $(0,0)$. The coordinates u, v and z are related to the cartesian coordinates by:

$$x = \frac{1}{2}(u^2 - v^2), \tag{3.1}$$

$$y = uv, \tag{3.2}$$

$$z = z, \tag{3.3}$$

where $0 \leq u < \infty$ and $-\infty < v < \infty$ [51]. An arbitrary parabolic cross-section is uniquely defined by the intersection of two confocal parabolas of coordinates ($u = u_0$, $v = v_0$). Figure 3.1a) shows an example with $u_0 \neq v_0$ that defines an asymmetric contour. On the other hand, a symmetric contour is defined choosing $u_0 = v_0$.

The position vector in parabolic cylinder coordinates is defined as:

$$\vec{r} = \frac{1}{2}(u - v)\hat{x} + uv\hat{y} + z\hat{z}, \tag{3.4}$$

and the associated scale factors are [51]:

$$h_u = \left|\frac{\partial \vec{r}}{\partial u}\right| = \sqrt{u^2 + v^2}, \quad h_v = \left|\frac{\partial \vec{r}}{\partial v}\right| = \sqrt{u^2 + v^2}, \quad h_z = 1. \tag{3.5}$$

Therefore, the relationship between the unitary cartesian vectors and the parabolic cylindrical ones is:

$$\hat{u} = \frac{\partial \vec{r}/\partial u}{h_u} = \frac{u\hat{x} + v\hat{y}}{\sqrt{u^2 + v^2}}, \quad \hat{v} = \frac{\partial \vec{r}/\partial v}{h_v} = \frac{-v\hat{x} + u\hat{y}}{\sqrt{u^2 + v^2}}, \quad \hat{z} = \hat{z}. \tag{3.6}$$

The Helmholtz equation, required to compute the modes as described in Appendix A, $\Delta\Phi + k_c^2\Phi = 0$ is written for any orthogonal curvilinear coordinate system as:

$$\frac{1}{h_u h_v h_z}\left[\frac{\partial}{\partial u}\left(\frac{h_v h_z}{h_u}\frac{\partial \Phi}{\partial u}\right) + \frac{\partial}{\partial v}\left(\frac{h_u h_z}{h_v}\frac{\Phi}{\partial v}\right)\right] + k_c^2\Phi = 0, \tag{3.7}$$

Using the scale factors defined in (3.5), the Helmholtz equation in parabolic cylinder coordinates is simplified to:

$$\frac{1}{u^2 + v^2}\left[\frac{\partial^2 \Phi}{\partial u^2} + \frac{\partial^2 \Phi}{\partial v^2}\right] + k_c^2\Phi = 0. \tag{3.8}$$

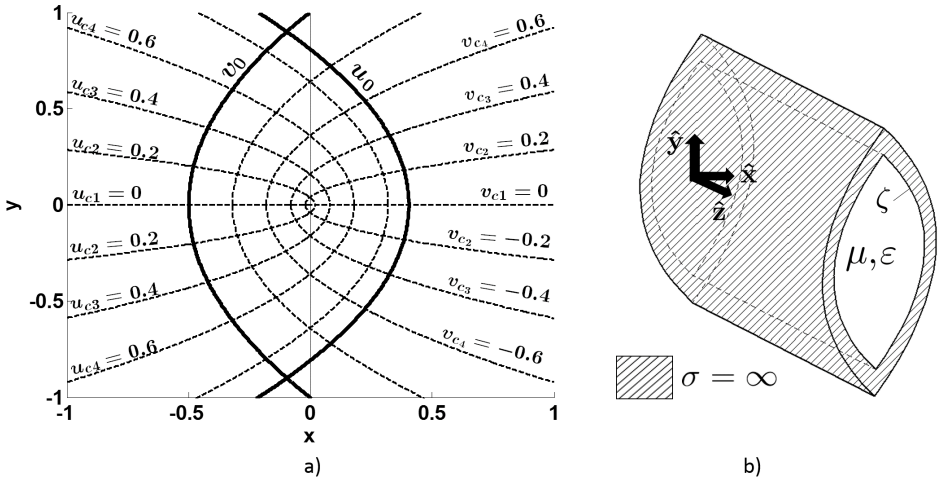

Figure 3.1: a) Parabolic cylinder coordinates with a remarked arbitrary contour ($u = u_0$, $v = v_0$) and b) 3D example of a parabolic cylinder waveguide.

In order to find the modal spectrum of the parabolic cylinder waveguide it is assumed that Φ can be written as a product of separated variables $\Phi(u, v) = F(u)G(v)$ and hence (3.8) becomes:

$$\left[\frac{F^{"}(u)}{F(u)} + \frac{G^{"}(v)}{G(v)}\right] + k_c^2(u^2 + v^2) = 0. \tag{3.9}$$

The previous expression leads to two ordinary differential equations with c an arbitrary separation constant:

$$\frac{F^{"}(u)}{F(u)} + k_c^2 u^2 = c \;\leftrightarrow\quad F^{"}(u) + (k_c^2 u^2 - c)F(u) = 0 \tag{3.10}$$

$$\frac{G^{"}(v)}{G(v)} + k_c^2 v^2 = c \;\leftrightarrow\quad G^{"}(v) + (k_c^2 v^2 - c)G(v) = 0. \tag{3.11}$$

At this point the next particular standard form of the parabolic cylinder equation is sought:

$$\frac{d^2y(x)}{dx^2} + \left(\frac{x^2}{4} - \alpha\right)y(x) = 0. \tag{3.12}$$

To that end, the variables $h = \sqrt{2k_c}u$ and $t = \sqrt{2k_c}v$ are defined. Thus, $F(u) = f(h(u))$ and $G(v) = g(t(v))$ hold, and equations (3.10) and (3.11) change into the following expressions:

$$f^{"}(h)2k_c + \left(k_c^2 \tfrac{h}{2k_c} - c\right)f(h) = 0 \tag{3.13}$$

$$g^{"}(t)2k_c + \left(k_c^2 \tfrac{t}{2k_c} + c\right)g(t) = 0. \tag{3.14}$$

In order to achieve the expression given in (3.12), equations (3.13) and (3.14) must be

rewritten in terms of the separation constants $a = \frac{c}{2k_c}$ and $a' = -a$, leading to:

$$f^{"}(h) + \left(\frac{h^2}{4} - a\right) f(h) = 0, \tag{3.15}$$

$$g^{"}(t) + \left(\frac{t^2}{4} - a'\right) g(t) = 0, \tag{3.16}$$

which can be directly compared with (3.12). Once the expressions are identified with a well-known ordinary differential equation, the same procedure as in Chapter 2 must be followed, that is, the corresponding boundary conditions must be imposed.

Thus, Neumann and Dirichlet boundary conditions must be fulfilled by TE and TM modes respectively (please refer to Appendix A):

$$\left.\frac{\partial \Phi}{\partial n}\right|_{\zeta} = 0, \quad \text{for TE modes (Neumann-type)}, \tag{3.17}$$

$$\Phi\big|_{\zeta} = 0 \quad \text{for TM modes (Dirichlet-type)}, \tag{3.18}$$

where ζ is the external contour of the cross-section of the parabolic cylinder waveguide shown in Figure 3.1b).

The usage of a particular coordinate system provides the so-called implicit boundary conditions as well. This happens in classical waveguides such as the circular or the elliptical one, and so does in the parabolic cylinder waveguide.

In the parabolic cylinder coordinate system these conditions are referred to the continuity of the scalar function Φ. This function is defined in terms of the transformed functions $f(h)$ and $g(t)$ as the product:

$$\Phi(u, v) = f(h)g(t). \tag{3.19}$$

On the other hand, any function can be decomposed into its even and odd parts ($f_e(h)$, $f_o(h)$, $g_e(t)$, and $g_o(t)$ respectively). Applying this decomposition to (3.19) it becomes evident that only the products between even functions ($f_e(h)g_e(t)$) or between odd functions ($f_o(h)g_o(t)$) correspond to real physical solutions [51]. The mixed products $f_e(h)g_o(t)$ and $f_o(h)g_e(t)$ do not ensure the continuity of a maximum or a minimum along the axis of symmetry associated with the parabolic cylinder waveguide and must be discarded.

Therefore the Φ function from which the complete set of modes arise is simplified to:

$$\Phi(u, v) = f_e(h)g_e(t) + f_o(h)g_o(t), \tag{3.20}$$

where the application of (3.17) leads to the modal expressions for TE modes and the application of (3.18) provides the corresponding expressions for TM modes. Furthermore, thanks to this subdivision the boundary conditions can be applied separately to:

$$\Phi_e(u, v) = f_e(h)g_e(t), \tag{3.21}$$

$$\Phi_o(u, v) = f_o(h)g_o(t), \tag{3.22}$$

giving rise to four mode families: even TE (TE_e), even TM (TM_e), odd TE (TE_o), and odd TM (TM_o). As it happened with the symmetric and asymmetric mode families in the equilateral triangular waveguide of Chapter 2 with respect to the y-axis, these even and

odd families in the parabolic cylinder waveguide also present different symmetries along the cartesian x-axis ($u_{c1} = 0$ and $v_{c1} = 0$ in parabolic cylinder coordinates). In fact, the TE_e and TM_o modes present a PEW symmetry, whereas the TE_o and TM_e modes present a PMW symmetry. This behaviour will be evidenced in Section 3.4 once the fields have been solved and some mode patterns are given.

3.3 Systematic resolution of the modes

In the previous Section the scalar Helmholtz equation is transformed into one of the well-known standard forms of the parabolic cylinder differential equation. After applying all the boundary conditions, the Φ eigenfunctions are simplified to the product of even and odd functions of the transformed functions $f(h)$ and $g(t)$.

In this Section there are two main objectives:

(i) Find the suitable even and odd functions whose product satisfy the Helmholtz equation, the implicit boundary conditions and the Neumann or Dirichlet conditions (for TE or TM modes respectively).

(ii) Find a systematic way to solve the corresponding eigenvalue k_c, also known as the cut-off wavenumber, for each eigenfunction Φ_e or Φ_o, so that the modal spectra can be uniquely defined.

Regarding the first goal of this Section, several expressions are found in the literature as the linear independent solutions to (3.12), such as the summatories of even and odd powers of x obtained following the Frobenius method or the parabolic cylinder functions [92]. The parabolic cylinder functions shown in [92] are better suited for the asymptotic expansions to have a desired behaviour, but they are neither even nor odd as it is required by (3.20)-(3.22). The Weber parabolic functions (or parabolic cylinder functions) can be combined to provide an even and odd solution to (3.12) following the derivation shown in [46]. These functions were tabulated in [47]. However, it has become evident that the generation of a reliable algorithm to obtain their values in current CAD tools is cumbersome [48, 49]. In fact, the routine included in [92] is only valid for a very limited range where $\alpha, x \in [0, 5]$ in (3.12) [49], and its extension to other ranges is far from being trivial. Several techniques must be combined to guarantee accuracy as it is shown in [48, 49], where Maclaurin and Chebychev series, asymptotic expansions or integrating the differential with local Taylor series are used depending on the range of $|\alpha|$ and $|x|$.

In this Thesis another strategy is followed due to its simplicity and great performance, with a relative error of the computed results only limited by the machine round-off. The method is based on the use of a 1D-analytic continuation technique, also known as a constant-step variable-order Taylor method [50]. It will be proven in the next Section that this strategy allows to obtain accurate results for a wide range of variables x and α in (3.12), in fact more than enough to obtain a large number of modes to be used in any solver based on modal decomposition.

The constant-step variable-order Taylor method computes the function $y(x)$ that satisfies equation (3.12) by a Taylor expansion carried out about an arbitrary point x_0 rather than about $x_0 = 0$. This function $y(x)$ represents $f(h)$ and $g(h)$ of equations (3.13)

and (3.14) as it was shown earlier in Section 3.2. Each term of the series is obtained recursively as [50]:

$$y^{(n)}(x) = -\left(\frac{x^2+4\alpha}{4}\right)y^{(n-2)}(x) - \frac{n-2}{2}xy^{(n-3)}(x) - \frac{(n-2)(n-3)}{4}y^{(n-4)}(x) \quad (3.23)$$

where the argument is $x = \sqrt{2k_c}u$ with $\alpha = a$ for $f(h)$ and $x = \sqrt{2k_c}v$ with $\alpha = -a$ for $g(t)$. In fact, (3.23) provides the complete Taylor series and we are not interested in $f(h)$ or in $g(h)$, but in their associated even and odd functions $f_e(h)$, $f_o(h)$, $g_e(t)$ and $g_o(t)$. These functions, denoted as $y_e(x)$ for $f_e(h)$, $g_e(t)$ and $y_o(x)$ for $f_e(h)$, $g_e(t)$, are obtained using different starting points in (3.23):

$$y_e(x) = \begin{cases} y^{(0)}(x_i = 0) = 1 \\ y^{(1)}(x_i = 0) = 0 \end{cases}, \quad y_o(x) = \begin{cases} y^{(0)}(x_i = 0) = 0 \\ y^{(1)}(x_i = 0) = 1 \end{cases}, \quad (3.24)$$

where x_i denotes the initial point of the series, $y^{(0)}(x) = y(x)$ and $y^{(1)}(x) = y'(x)$.

For a given contour (u_0, v_0) variable x varies in small intervals of width $|s| \leq 0.15$ from $x = 0$ to $x = \sqrt{2k_c}u_0$ for (3.13), and between $x = 0$ and $x = \sqrt{2k_c}v_0$ for (3.14). The first interval uses the initial points given in (3.24). The rest of the intervals use the last calculated value of the function and its derivative in the preceding interval as the starting values for the recursion formula (*i.e.*, $y(0)$ and $y(1)$).

Once $f_{e,o}$ and $g_{e,o}$ have been approximated by (3.23), the even and odd functions Φ_e and Φ_o of (3.21) and (3.22) can be obtained. The next step is to apply the boundary conditions defined in (3.17),(3.18). Since each condition is applied to both functions four mode families arise:

$$\Phi_e^{\mathrm{TE}_e}(u,v) \quad : \left.\frac{\partial \Phi_e(u,v)}{\partial n}\right|_\zeta = 0, \quad (3.25)$$

$$\Phi_o^{\mathrm{TE}_o}(u,v) \quad : \left.\frac{\partial \Phi_o(u,v)}{\partial n}\right|_\zeta = 0, \quad (3.26)$$

$$\Phi_e^{\mathrm{TM}_e}(u,v) \quad : \Phi_e\big|_\zeta = 0, \quad (3.27)$$

$$\Phi_o^{\mathrm{TM}_o}(u,v) \quad : \Phi_o\big|_\zeta = 0. \quad (3.28)$$

For an arbitrary parabolic contour (u_0,v_0), where $h_0 = \sqrt{2k_c}u_0$, $t_0 = \sqrt{2k_c}v_0$, expressions (3.25)-(3.28) lead to four non-linear bivariate systems of equations:

$$\text{TE modes} \begin{cases} \mathrm{TE}_{\mathrm{even}} \begin{cases} f_e'(h_0)g_e'(t) = 0 \ \forall t \\ f_e'(h)g_e'(t_0) = 0 \ \forall h \end{cases} \begin{cases} f_e'(h_0) = 0 \\ g_e'(t_0) = 0 \end{cases} \\ \mathrm{TE}_{\mathrm{odd}} \begin{cases} f_o'(h_0)g_o'(t) = 0 \ \forall t \\ f_o'(h)g_o'(t_0) = 0 \ \forall h \end{cases} \begin{cases} f_o'(h_0) = 0 \\ g_o'(t_0) = 0 \end{cases} \end{cases}, \quad (3.29)$$

$$\text{TM modes} \begin{cases} \mathrm{TM}_{\mathrm{even}} \begin{cases} f_e(h_0)g_e(t) = 0 \ \forall t \\ f_e(h)g_e(t_0) = 0 \ \forall h \end{cases} \begin{cases} f_e(h_0) = 0 \\ g_e(t_0) = 0 \end{cases} \\ \mathrm{TM}_{\mathrm{odd}} \begin{cases} f_o(h_0)g_o(t) = 0 \ \forall t \\ f_o(h)g_o(t_0) = 0 \ \forall h \end{cases} \begin{cases} f_o(h_0) = 0 \\ g_o(t_0) = 0. \end{cases} \end{cases}, \quad (3.30)$$

where each modal solution is uniquely identified by a fixed pair (a, k_c) and $a, k_c \in \mathbb{R}$. The previous systems of equations, written in terms of the Taylor series derived in (3.23) are:

$$\text{TE even} \begin{cases} y'_e(x_0 = \sqrt{2k_c}u_0; \ \ \alpha = a) = 0, \\ y'_e(x_0 = \sqrt{2k_c}v_0; \ \ \alpha = -a) = 0, \end{cases} \tag{3.31}$$

$$\text{TE odd} \begin{cases} y'_o(x_0 = \sqrt{2k_c}u_0; \ \ \alpha = a) = 0, \\ y'_o(x_0 = \sqrt{2k_c}v_0; \ \ \alpha = -a) = 0, \end{cases} \tag{3.32}$$

$$\text{TM even} \begin{cases} y_e(x_0 = \sqrt{2k_c}u_0; \ \ \alpha = a) = 0, \\ y_e(x_0 = \sqrt{2k_c}v_0; \ \ \alpha = -a) = 0, \end{cases} \tag{3.33}$$

$$\text{TM odd} \begin{cases} y_o(x_0 = \sqrt{2k_c}u_0; \ \ \alpha = a) = 0, \\ y_o(x_0 = \sqrt{2k_c}v_0; \ \ \alpha = -a) = 0, \end{cases} \tag{3.34}$$

where $y_e(x, \alpha)$ and $y_o(x, \alpha)$ are the Taylor approximations for the even and odd part of the solution $y(x)$ to (3.12) for a given α.

Figure 3.2 shows several examples of the above systems of equations where the values of the separation constant a are obtained from [50], and only the argument x is varied in the real domain. These functions have been drawn using the constant-step variable-order Taylor approach followed in this Thesis. The curves have been drawn dependent on variable x to show their even or odd behavior with respect to $x = 0$.

The first row contains roots that belong to the TE odd mode family, whereas the second one shows fixed pairs (a, k_c) for the TE even solutions. The appearance of the curves drawn associated to the TE even family is odd since the derivative of the function is represented to find the roots, as it is given in (3.31). On the other hand, the curves of the odd family are even for the same reason (see (3.32)). The third and fourth rows show examples of odd and even TM modes respectively. In this case even TM modes are solved with the intersection of even functions according to (3.33), and odd TM modes with the intersection of odd functions according to (3.34).

It is important to notice that, although in Figure 3.2 the argument x has been depicted from real negative numbers to positive ones to see the symmetries of the functions that make up the systems, only one root per case is valid, in particular the one with $x > 0$ since $k_c, u_0, v_0 > 0$. When variable a is plotted in the abscissa axis, a suitable numeration where two subindexes uniquely identify a mode arises from the curve intersections [46, 50].

The previous systems of equations are difficult to be faced in general [50] taking into account that both a and x are unknown and belong to the real domain. Only the cases where $a = 0$, present in both symmetric ($u_0 = v_0$) and asymmetric contours ($u_0 \neq v_0$), are reduced to the roots of the well-known Bessel functions [47, 51].

In other classical waveguides finding the modal spectra can be reduced to a 1D-problem, since the modes can be found by seeking sequentially the zeros of a function where the order, in the integer space, is varied. This is the case of the circular waveguide,

where the Bessel functions (or their derivatives) are involved, or the elliptical one, where the modified Mathieu functions (or their derivatives) are used. In the parabolic cylinder waveguide, however, the intersection of two functions dependent upon two parameters in the real domain, a and k_c, are sought. This can be seen in (3.31) to (3.34). Thus, the modal spectra of the parabolic cylinder waveguide constitutes a cumbersome 2D-problem.

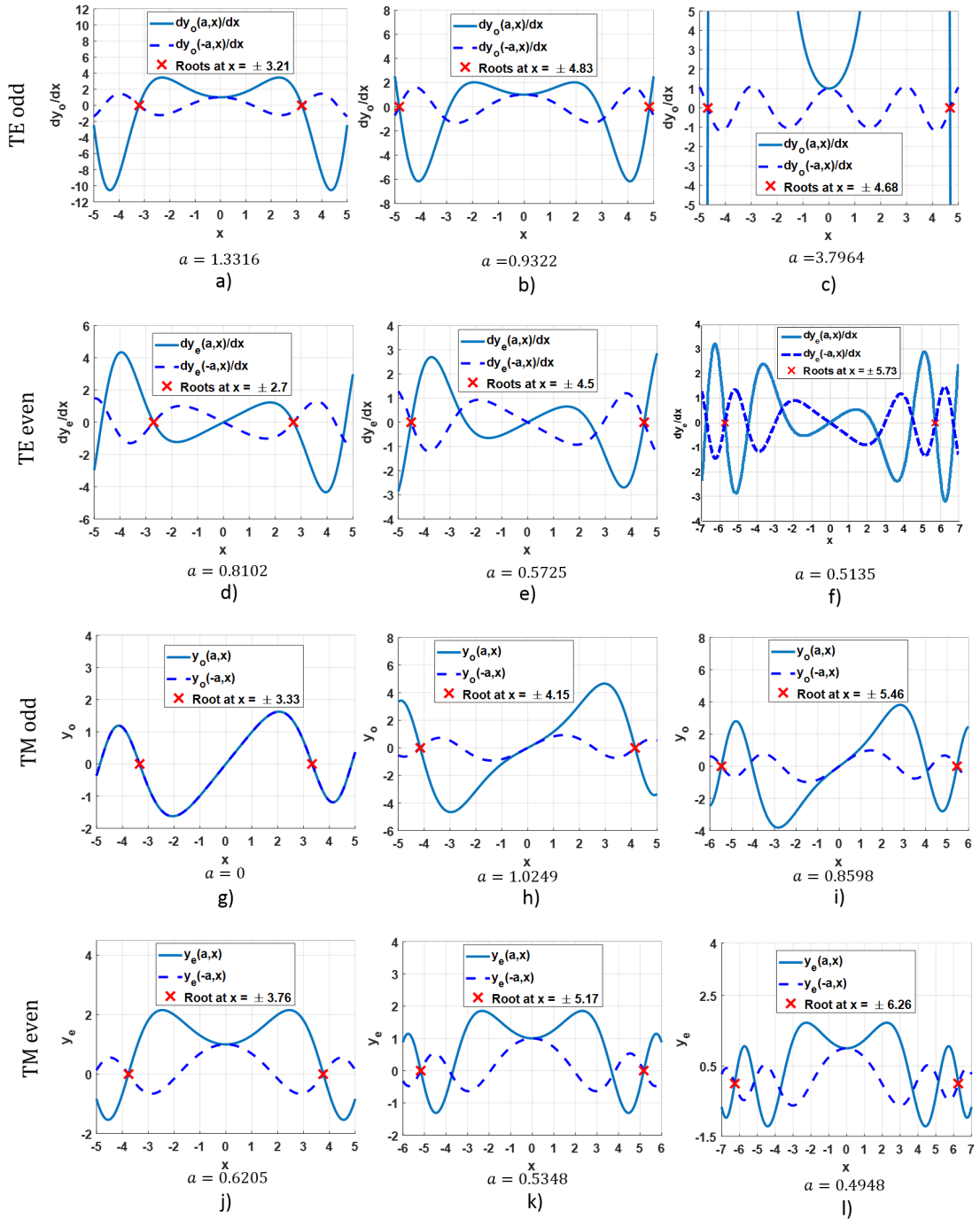

Figure 3.2: Examples of the systems of equations defined in (3.31), (3.32), (3.33) and (3.34) for the search of modal solutions in a parabolic waveguide of $u_0 = v_0 = 1$, where the functions have been obtained by the method proposed in [50].

The difficulty was highlighted in [51], where a graphical method to solve intersections as the solutions to the systems of equations was suggested. This strategy was followed by [46] for the first modes in a symmetrical waveguide contour. A significant improvement in the accuracy of the solutions was achieved in [50], where the obtained values were compared to others from different sources [46, 51, 94, 98]. This enhancement was due to the use of a root-finding algorithm based on the Newton-Poisson shooting method. However, the method presented in [50] has some disadvantages that makes it unfeasible to its application in current CAD tools. The main disadvantage is that it resorts to graphical intersections to provide starting points close enough to the solutions to the root-finding algorithm, at least in the symmetric contour. Once the roots of the proposed symmetric contour have been found, [50] suggests to combine the Newton-Poisson root-finding method with homotopy to provide new starting points for any other desired contour. Thus, another evident disadvantage is the iterative behavior of the proposed procedure for asymmetrical contours, which can compromise efficiency in a modal solver where significant speed is expected. Besides, its performance depends on the good selection of the homotopy functions.

The main progress of the method proposed in [50] over the graphical intersections of [46] is that the modal solutions are found with high precision. What makes them accurate is the use of a numerical root-finding algorithm that refines the graphical results together with a good mechanism to approach the functions that are solution to the parabolic cylinder differential equation, that is, the constant-step variable-order Taylor method.

In this Thesis the limitations of [50] are overcome. Towards that end, the focus is on the root-finding algorithm. A recent method based on the hidden variable resultant method and Bezout matrices for two bivariate functions is proposed [52], where the graphical means are completely avoided and thus the method can be fully integrated in any solver based on modal decomposition.

This algorithm separates the dependence of both variables a and k_c by using Chebychev polynomials as interpolants of the functions that make up the bivariate system in (3.31)–(3.34), which is convenient for the hidden variable resultant method that is used. Thus, the four bivariate systems are defined accordingly in our problem as:

$$p(\sqrt{2k_c}u_0, a) = \sum_{i=0}^{m_p}\sum_{j=0}^{n_p} P_{ij}T_i(\sqrt{2k_c}u_0)T_j(a), \tag{3.35}$$

$$q(\sqrt{2k_c}v_0, -a) = \sum_{i=0}^{m_q}\sum_{j=0}^{n_q} Q_{ij}T_i(\sqrt{2k_c}v_0)T_j(-a) \tag{3.36}$$

where P_{ij} and Q_{ij} are suitable coefficients for the approximation and the Chebychev polynomials $T_j(x)$ take the following usual form:

$$T_j(x) = \cos(j\cos^{-1}(x)). \tag{3.37}$$

The degrees of the polynomials (m_p, n_p, m_q and n_q) in (3.35) and (3.36) are in close relation with the search domain subdivision of the algorithm, and the use of the Chebychev basis allows to employ fast transforms based on the fast Fourier transform and prevents numerical instability [52]. A Bezout resultant matrix is built from (3.35) and (3.36), and the fixed pairs (a, k_c) are found by solving a generalized eigenvalue problem combined with a univariate root-finding algorithm based on the colleague matrix.

Since its strategy is based on solving eigenvalues, the proposed algorithm has another significant advantage apart from its feasibility to be integrated in CAD tools. For a given contour (u_0, v_0) it finds all the roots at once within a limited range $[a_{\text{init}}, a_{\text{end}}] \times [k_{c\,\text{init}}, k_{c\,\text{end}}]$, eliminating the dependence on good starting points from which to iterate as it happens in the Newton-Poisson shooting method.

Once the fixed pairs are found the four mode families in the parabolic cylinder waveguide $\Phi_e^{\text{TE}_e}(u,v)$, $\Phi_o^{\text{TE}_e},(u,v)$, $\Phi_e^{\text{TM}_e}(u,v)$ and $\Phi_o^{\text{TM}_o},(u,v)$ are calculated as:

$$\Phi_e^{\text{TE}_e}(u,v) = y_e(\sqrt{2k_c^{\text{TE}_e}}u, a)y_e(\sqrt{2vk_c^{\text{TE}_e}}v, -a), \tag{3.38}$$

$$\Phi_e^{\text{TM}_e}(u,v) = y_e(\sqrt{2k_c^{\text{TM}_e}}u, a)y_e(\sqrt{2k_c^{\text{TM}_e}}v, -a), \tag{3.39}$$

$$\Phi_o^{\text{TE}_o}(u,v) = y_o(\sqrt{2k_c^{\text{TE}_o}}u, a)y_o(\sqrt{2k_c^{\text{TE}_o}}v, -a), \tag{3.40}$$

$$\Phi_o^{\text{TM}_o}(u,v) = y_o(\sqrt{2k_c^{\text{TM}_o}}u, a)y_o(\sqrt{2k_c^{\text{TM}_o}}v, -a). \tag{3.41}$$

The two objectives presented at the beginning of this Section have been accomplished. On the one hand, the even and odd functions $f_{e,o}(h)$ and $g_{e,o}(t)$ have been solved by using the accurate derivation presented in [50] based on the constant-step variable-order Taylor method. On the other hand, a systematic procedure based on a recently published algorithm [52] has been proposed to find the fixed pairs (a, k_c) that uniquely identify the eigenfunctions Φ_e and Φ_o. Therefore at the end of this Section the modal spectra of the parabolic cylinder waveguide has been fully characterized in a systematic way allowing for the first time to be integrated into modern CAD tools based on modal decomposition.

3.4 Validation cases

In this Section the proposed method to systematically solve the modal spectra of the parabolic cylinder waveguide is tested and validated. The first step to be taken is to compare the quasi-analytical results with the available ones given in [50] for a symmetrical contour. This reference claims to have an impressive relative error in the order of the machine round-off, and compares its results with previous references justifying the improvement achieved. Thus, [50] can be considered a reliable source.

In particular, the symmetrical contour in [50] has $u_0 = v_0 = 1$. The fixed pairs (a, k_c) are found for the four mode families of equations (3.38)-(3.41), and then are sorted according to the cut-off wavenumber (from lower to higher values up to 80 modes). Figure 3.3 shows the achieved results together with the ones given in [50] used here as a reference. From now on in this Section the values of u and v are given without dimensions (their actual dimensions would be square root of length), and therefore the values of k_c (whose actual dimension would be inverse of length) are shown normalized without dimensions in the figures and tables.

Apart from the graphical validation of Figure 3.3, where it can be qualitatively seen that there is a good agreement between results, we define the relative difference Δ to compare the obtained values quantitatively as:

$$\Delta = \frac{\left|k_c - k_c^{\text{ref}}\right|}{k_c^{\text{ref}}}, \tag{3.42}$$

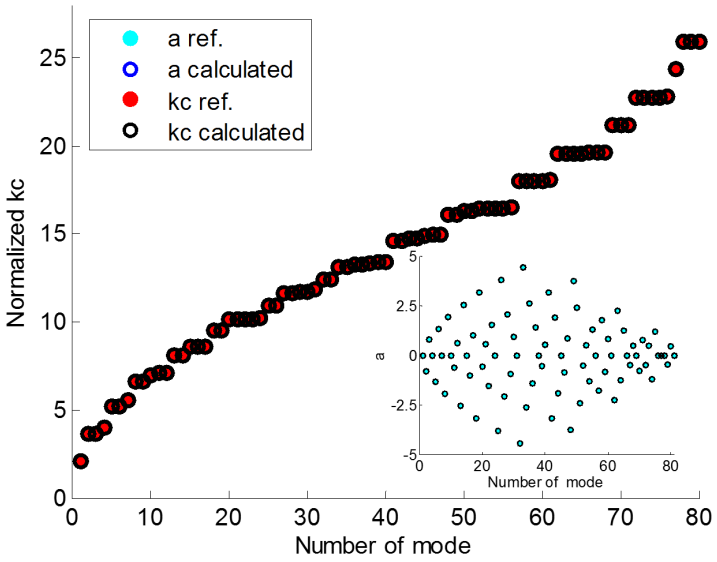

Figure 3.3: Comparison of the computed pairs (a, k_c) for each mode for $u_0 = 1$, $v_0 = 1$ with [50]: normalized cut-off wavenumber and associated separation constant.

where k_c is each solution obtained by the proposed algorithm in this paper, whereas k_c^{ref} is each solution given in [50]. The maximum obtained relative difference regarding the cut-off wavenumbers is $1.7 \cdot 10^{-5}$ for mode number 32.

It is important to highlight that [50] used one graphical intersection for each one of the 80 modes calculated, which in turn is a starting point to be refined with a Newton–Poisson shooting method. The strategy addressed in this Thesis does not solve each root individually, and it uses neither starting points nor graphical means: it solves systematically the 80 roots at once in the suitable 2-D domain ($[a_{\text{init}}, a_{\text{end}}] \times [k_{c\,\text{init}}, k_{c\,\text{end}}] = [-5, 5] \times [2, 26]$).

Finally, this first validation is ended with Table 3.1, which is included for completeness. It shows the cut-off wavenumbers of the first and last modes of Figure 3.3 obtained not only from [50] from an in-house implementation (based on [99] of the Finite Element method (FEM) for homogeneous waveguides [54] using second-order Lagrange triangular elements).

At this point the proposed method is tested for asymmetrical contours, since it is reasonable to think that u_0 may be chosen with a different value from v_0 to have an additional degree of freedom in the design of microwave devices. However, to the best of the author's knowledge, there are not references in the literature with enough number of modes for a test validation in the asymmetric cases. In fact, a wide range of asymmetric contours can be found in [50], but the values are only solved for ten or twenty modes depending on the case.

For that reason three test case studies are proposed: one symmetric contour with $u_0 = v_0 = 0.5$, another one asymmetric with $u_0 = 0.8$ and $v_0 = 1$, and finally one also asymmetric with $u_0 = 0.15$ and $v_0 = 0.5$. Figure 3.4 shows the selected cases. With this choice of contours this Thesis addresses two objectives: on the one hand it tests the stability of the proposed algorithm in terms of the achieved relative difference between values and on the other hand a guideline for the choice of the domains of search is revealed.

Mode number	Mode family	k_c	k_c^{ref} [50]	k_c^{ref} FEM
1	TE_o	2.117016	2.117017	2.116986
2*	TE_e	3.647922	3.647921	3.647989 3.648105
3	TM_e	4.012599	4.012598	4.011785
4*	TE_o	5.163531	5.163532	5.163424 5.163458
5	TM_o	5.561775	5.561776	5.561780
...	...	...	...	...
77	TM_e	22.792935	22.792935	22.786287
78	TM_o	24.362683	24.362684	24.362836
79	TE_e	25.894069	25.89072	25.895568
80*	TM_e	25.928333	25.928338	25.913881 25.926654

* *Degenerate modes.*

Table 3.1: Normalized Cut-Off Wavenumber for $u_0 = 1$, $v_0 = 1$.

In the first place the relative difference defined in (3.42) should be measured over a large number of modes since any modal solver that can benefit from the proposed procedure may use hundreds of modes until convergence is ensured. To that end more than 1600 modes have been successfully computed for each contour. Each of the bivariate non-linear systems of (3.31)-(3.34) are solved giving rise to four groups of solutions: the ones that correspond to the even and odd TE modes of (3.38) and (3.40), and the ones that belong to the even and odd TM modes of (3.39) and (3.41). Once the modal solutions have been separately found for each family the results are sorted according to their k_c values (from the lowest k_c associated to the first mode to the highest k_c of the last one computed). The corresponding fixed pairs (a, k_c) are shown in Figure 3.5. Some of the first and last values of the two analyzed asymmetrical contours are also given in Tables 3.2 and 3.3.

Once the modal solutions have been found, the relative difference defined in (3.42) is computed as a source of validation. The aforementioned in-house implementation based on the purely numerical Finite Element method is used to obtain the k_c^{ref} values since there are not reference values available in the literature. In order to guarantee the accuracy of such a high number of eigenvalues in the Finite Element method, the number of degrees of freedom has been set as 129388 (using 64053 triangular elements). A significant time reduction has been found with the methodology proposed in this Thesis. In fact, our developed proof-of-concept code is approximately five times faster than the specialized Finite Element method software using the Arnoldi solver from [100] and placing the corresponding symmetry walls.

The maximum relative difference obtained for each mode family is gathered in Table 3.4, where it can be seen that its magnitude is in the order of $10^{-4} - 10^{-5}$ and occurs at very high order modes. In particular the total mean relative difference is $1.4 \cdot 10^{-5}$ for the case $u_0 = v_0 = 0.5$, $1.6 \cdot 10^{-5}$ for the case $u_0 = 0.8$ and $v_0 = 1$, and $1.9 \cdot 10^{-5}$ for the case $u_0 = 0.15$ and $v_0 = 0.5$. Thus, the good performance of the proposed algorithm in this electromagnetic problem has been proven. The evolution of the relative difference in detail is given in the first column of Figure 3.6.

The second goal of the three proposed test case studies is to provide a guideline for the choice of the domain of search. Giving the suitable limits of search $[a_{\text{init}}, a_{\text{end}}] \times$

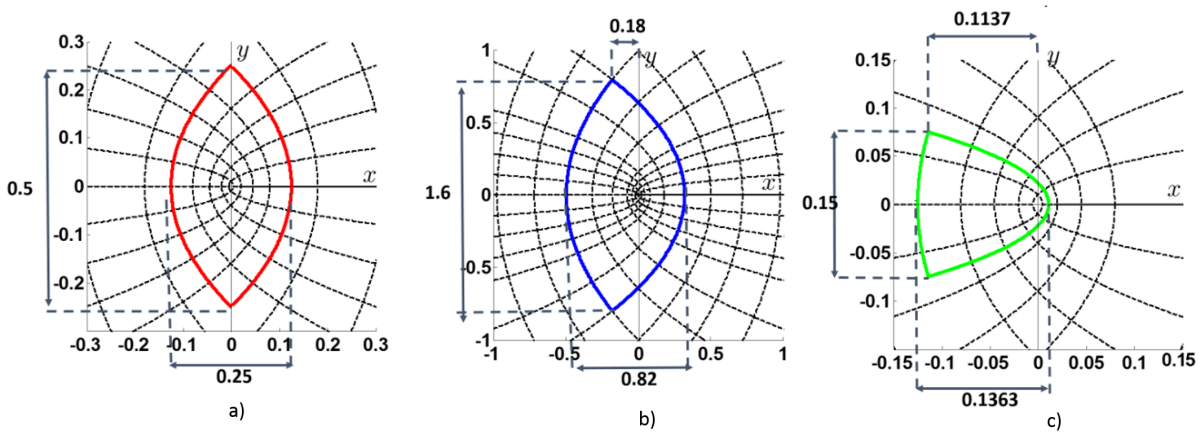

Figure 3.4: Parabolic cross sections of values: a) $u_0 = 0.5$, $v_0 = 0.5$; b) $u_0 = 0.8$, $v_0 = 1$ and c) $u_0 = 0.15$, $v_0 = 0.5$.

$[k_{c\,\mathrm{init}}, k_{c\,\mathrm{end}}]$ to the algorithm is crucial to ensure efficiency. Domains where the lowest k_c value is not present or where the associated a values are missing lead to a significant time increase.

The representation of the a separation constants in Figure 3.5b), d) and f) shows that the range of this variable widens as the mode number increases. However, from this representation it is difficult to observe the asymmetrical distribution of this parameter in the asymmetric contour ($u_0 = 0.8$, $v_0 = 1$). To that end the histograms of Figure 3.6b), d) and f) show the number of expected roots found over the different ranges of a. In the case of the symmetric contour depicted in Figure 3.6b) it can be seen that the histogram is symmetric with respect to zero. From this information it is deduced that in a symmetrical case only half of the range of variable a is required (*i.e.*, either the positive or negative range), speeding up the overall search process. Figures 3.6d) and f) evidence that the more asymmetric the waveguide contour is, the more asymmetry will be found in the distribution of the values for the separation constant a. Therefore, the domain of search must be selected considering this effect for an efficient root-finding process.

The good selection of the input domain of search is indeed a core feature, but also the choice of the parameters that control the accuracy and convergence in the algorithm. The authors in [52] have set all the parameters giving priority to the accuracy. However, in this Thesis the very diverse tolerances for each of the many steps involved in the algorithm have been adjusted for an enhancement of the efficiency without compromising the accuracy needed for the specific problem here solved.

The case study $u_0 = 0.15$, $v_0 = 0.5$ is selected to compare the efficiency between the standard settings proposed in [52] and the new selected ones. Table 3.5 gathers the time spent in both cases using MATLAB in a 64-bit virtual machine based on CentOS 7 with 4 GB of RAM and an i7-4790 @3.60GHz processor.

It is evident that the achieved time reduction must not be at expense of poor accuracy. For that reason the relative difference between the roots obtained with the default implementation of the algorithm and the experimental tuned one is computed, getting a maximum value in the order of 10^{-10}, which is negligible for the electromagnetic problem under study.

The computation time can be compared as well with other numerical techniques. Table 3.6 compares the time spent by the Boundary Contour Mode-Matching method (BCMM) [101] and the commercial software CST MWS for the first 40 modes in the same waveguide. The former method is run using a contour of 75 points (45 for the curve $u_0 = 0.15$ and 30 for the curve $v_0 = 0.5$) and the following number of base functions: 28 for even TE modes, 22 for odd TM modes, 10 for odd TE modes and 22 for even TM modes. On the other hand in CST Microwave Studio the time-domain solver is run for the 2D problem (*i.e.* the modes are solved solely in the port) with 20 cells per wavelength.

The proposed algorithm was executed again in MATLAB in the aforementioned virtual machine based on CentOS and the same selected settings, whereas both BCMM and CST MWS were executed in Windows with 32 GB of available RAM, in the same physical machine i7-4790 @3.60 GHz. Table 3.6 shows a significant time reduction, which is obtained although the other methods were not meant for high accuracy as Table 3.7 evidences.

Finally the first mode patterns divided by symmetries are shown in Figure 3.7 for a parabolic cylinder waveguide of $u_0 = 4.04$ and $v_0 = 1.68$. For the sake of simplicity, in this Thesis, the mode ordering has been set according to k_c (from lower to higher values), which, together with the mode family, uniquely identifies a mode. Alternatively, two subscripts (m and n) related to the nodal lines along the u and v curves can be used [97], or a generic mode-classifying system can be adopted based on the pattern of the corresponding mode in a rectangular waveguide [102]. The numeration used in [46, 50, 51] is here impractical since graphical intersections would be needed to properly define the m and n subindexes.

The previous examples have validated the proposed procedure to obtain the modal spectra of the parabolic cylinder waveguide, which is the basis to understand the principle of operation of microwave devices made up of this geometry. A practical example will be presented in Chapter 5, where an inline prototype in parabolic cylinder cavities will be designed taking into account a mode chart derived from the procedure here proposed.

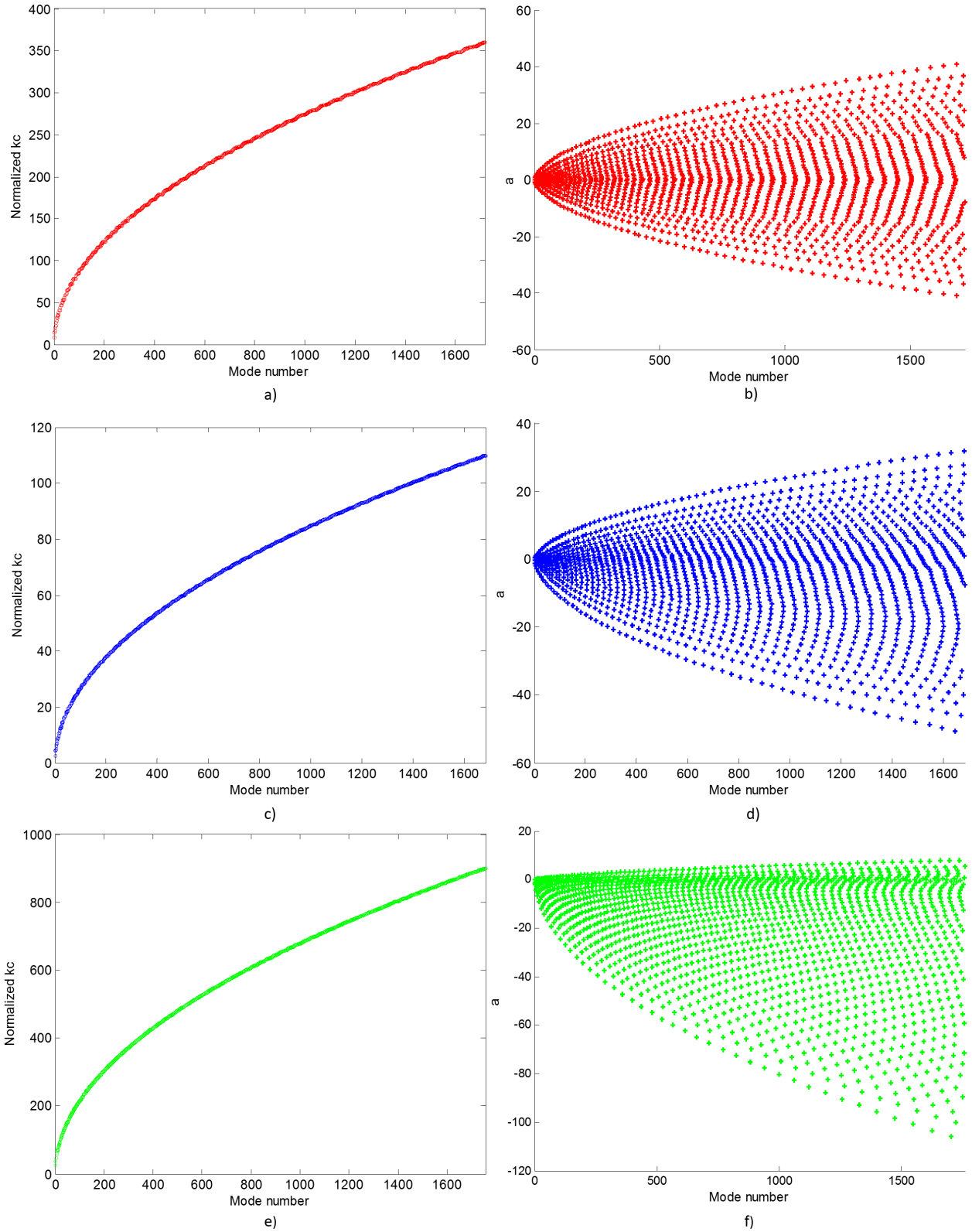

Figure 3.5: Root pairs (a, k_c) for the three proposed test case studies for a), b) $u_0 = 0.5$, $v_0 = 0.5$; c), d) $u_0 = 0.8$, $v_0 = 1$; e), f) $u_0 = 0.15$, $v_0 = 0.5$.

Mode number	**Mode family**	a	k_c	k_c^{ref} **FEM**
1	TE_o	-0.2695	2.6399	2.6399
2	TE_e	0.5541	4.3323	4.3325
3	TE_e	-1.1656	4.6735	4.6736
4	TM_e	-0.1637	4.9336	4.9337
5	TE_o	0.8409	6.1832	6.1831
...	...	...	...	...
1678	TM_o	-39.9810	109.8174	109.8195
1679	TE_o	24.9592	109.8306	109.8351
1680	TE_e	31.8748	109.8558	109.8550
1681	TE_o	0.9959	109.8602	109.8630
1682	TE_e	-7.6107	109.8892	109.8916

Table 3.2: Normalized Cut-Off Wavenumber and Separation Constant for $u_0 = 0.8$, $v_0 = 1$.

Mode number	**Mode family**	a	k_c	k_c^{ref} **FEM**
1	TE_e	0.0967	25.5757	25.5770
2	TE_o	-1.9196	26.3742	26.3741
3	TM_e	-1.3694	38.4429	38.4425
4	TE_o	-0.9017	46.3487	46.3484
5	TE_e	0.1867	48.3180	48.3217
...	...	...	...	...
1753	TE_o	-41.1201	899.3626	899.3862
1754	TM_o	-59.0797	899.5714	899.5946
1755	TM_e	0.6117	899.6471	899.6851
1756	TM_e	-71.3019	899.8382	899.8496
1757	TM_e	5.4317	899.9614	899.9661

Table 3.3: Normalized Cut-Off Wavenumber and Separation Constant for $u_0 = 0.15$, $v_0 = 0.5$.

$\mathbf{u_0 = 0.5}$, $\mathbf{v_0 = 0.5}$				
	TE even	TE odd	TM even	TM odd
Max diff.	$1.5 \cdot 10^{-4}$	$5.7 \cdot 10^{-5}$	$7.6 \cdot 10^{-5}$	$2.7 \cdot 10^{-5}$
Mode num.	1561	1025	862	1710
$\mathbf{u_0 = 0.8}$, $\mathbf{v_0 = 1}$				
	TE even	TE odd	TM even	TM odd
Max diff.	$9.0 \cdot 10^{-5}$	$7.6 \cdot 10^{-5}$	$5.4 \cdot 10^{-5}$	$3.1 \cdot 10^{-5}$
Mode num.	1630	1020	1626	1672
$\mathbf{u_0 = 0.15}$, $\mathbf{v_0 = 0.5}$				
	TE even	TE odd	TM even	TM odd
Max diff.	$1.7 \cdot 10^{-4}$	$2.0 \cdot 10^{-4}$	$5.2 \cdot 10^{-5}$	$1.0 \cdot 10^{-4}$
Mode num.	266	1696	1505	1718

Table 3.4: Relative Differences of Normalized Cut-Off Wavenumbers with respect to the Finite Element method (FEM) used as a reference.

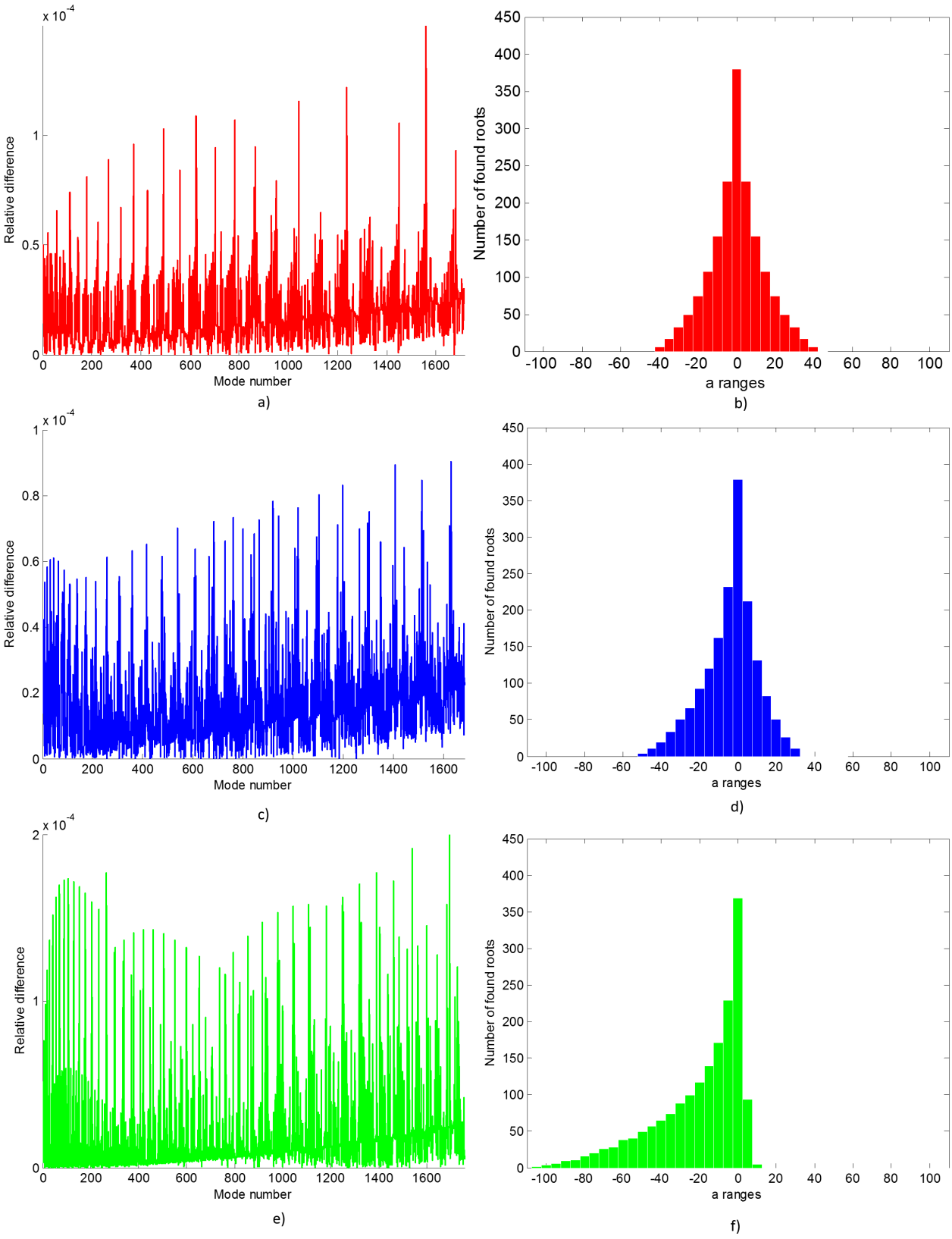

Figure 3.6: Evolution of the relative difference for the three case studies: a) $u_0 = 0.5$, $v_0 = 0.5$; c) $u_0 = 0.8$, $v_0 = 1$; e) $u_0 = 0.15$, $v_0 = 0.5$, and histograms of the separation constant a for: b) $u_0 = 0.5$, $v_0 = 0.5$; d) $u_0 = 0.8$, $v_0 = 1$; f) $u_0 = 0.15$, $v_0 = 0.5$.

Time spent with [52] [seg.]			
TE even	TE odd	TM even	TM odd
13.42	12.05	11.19	9.81
Time spent with our settings [seg.]			
TE even	TE odd	TM even	TM odd
4.68	4.78	4.42	3.71

Table 3.5: Comparison of the time spent by the proposed algorithm with the settings proposed in [52] and with the proposed settings in this Thesis for efficiency enhancement.

Time consumption [seg.]					
Prop. method		**BCMM**		**CST MWS**	
PEW	**PMW**	**PEW**	**PMW**	**PEW**	**PMW**
3.75	3.87	22.43	26.84	16.66	17.32

Table 3.6: Comparison of the time consumption of the proposed algorithm with the enhanced settings and other numerical methods.

Mode number	**Mode family**	k_c **prop. method**	k_c **BCMM**	k_c **CST MWS**
1	TE even	25.5757	25.5781	25.59
2	TE odd	26.3742	36.3755	26.36
3	TM even	38.4429	38.4456	38.47
4	TE odd	46.3487	46.3519	46.31
5	TE even	48.3180	48.3224	48.39
...	...	...	...	...
36	TE odd	128.0938	128.1920	127.97
37	TE even	130.4312	130.4418	130.48
38	TE odd	132.6409	132.6170	132.60
39	TE even	134.0221	134.0290	133.98
40	TE even	135.7780	135.7867	135.78

Table 3.7: Comparison of the results obtained with the proposed algorithm and other numerical methods.

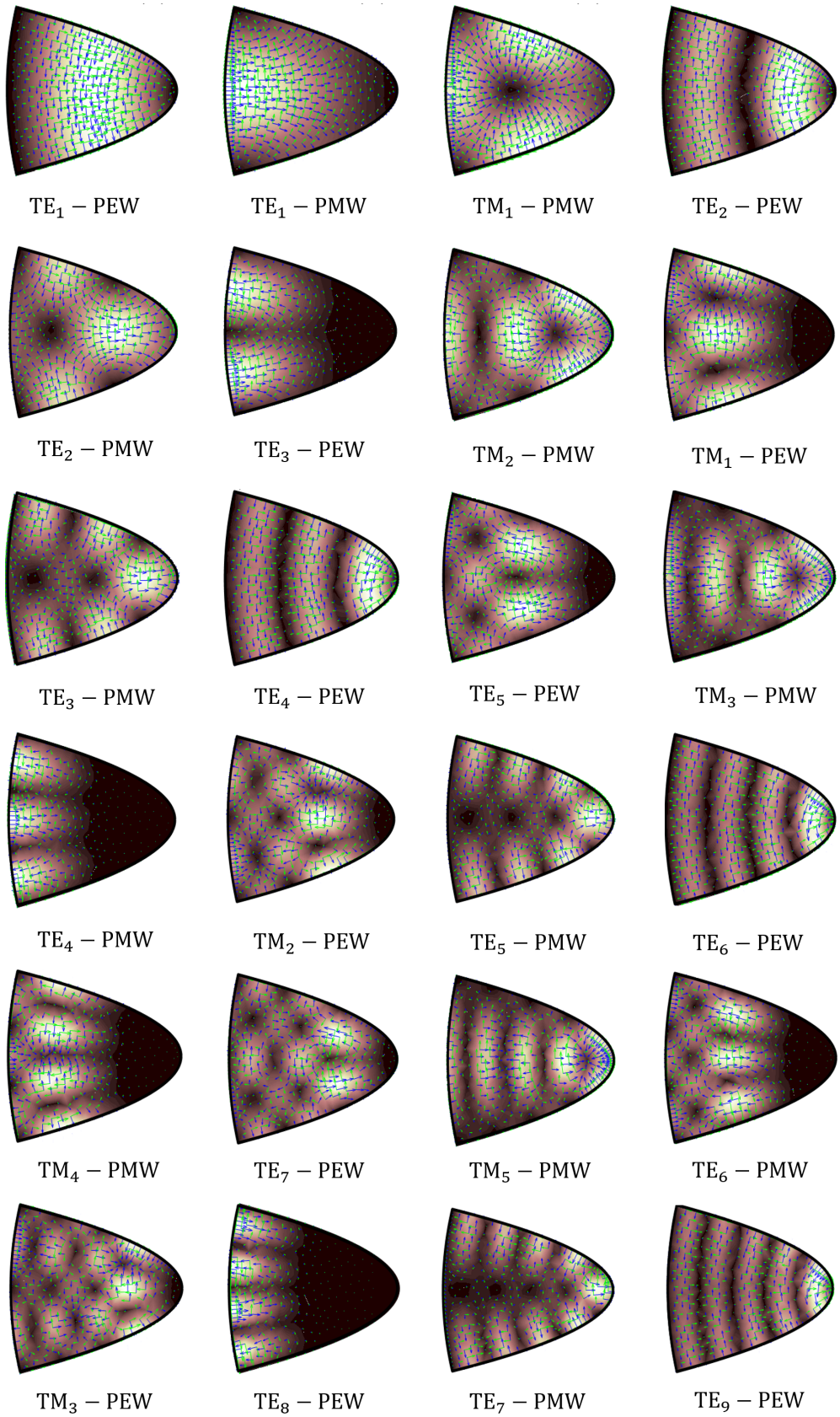

Figure 3.7: Mode pattern of the first 24 modes in a parabolic cylinder waveguide of $u_0 = 4.04$ and $v_0 = 1.68$.

4 Efficient analysis of waveguide devices by a hybrid 2D-Finite Element and Mode-Matching method

4.1 Introduction

In the previous chapters the equilateral triangular and the parabolic cylinder waveguides were introduced. In particular, their efficient electromagnetic analysis was addressed so that the design of microwaves devices based on such unconventional geometries is fast and accurate. However, these are not the only prospective geometries to be used in future satellite communications. The arrival of sophisticated 3D-printing techniques has undoubtedly widened the spectrum of possible geometries. In this context, it is evident that the analytical cross-sections represent particular cases of the possible set of hypothetical geometries.

One of the most popular topologies used in waveguide devices is the so-called inline [103, 104], where hollow waveguides are cascaded making up sequential building blocks. When the cascaded cross-sections are analytical, such topology can be efficiently analyzed by the Mode-Matching method. However, when arbitrary geometries take part of the electromagnetic problem, or even in the case of some quasi-analytical cross-sections such as the parabolic one of Chapter 3, the Mode-Matching method needs to be hybridated with a robust and accurate 2D numerical method. One of the possible numerical techniques is the Finite Element method, whose hybridation with the Mode-Matching method was researched in the mid-1990's [55–58].

The contribution of this Chapter is to improve the overall efficiency of the hybridation between the two well-known methods. To that end, a novel formulation is proposed, where the modal fields are expressed in terms of 2D nested functions spaces made up of Finite Element basis functions. This leads to Finite Element matrices that can be directly used to build the inner cross-product matrices inherent to the Mode-Matching method, speeding up the analysis as the number of required computations is reduced. Besides, an efficient orthonormalization procedure is shown, which is needed for a correct hybridation between the two methods when multiconductor problems are addressed. Several examples are analyzed with the proposed formulation, achieving results that are in good agreement with measured ones and from commercial software.

4.2 Proposed formulation

The scalar Helmholtz equation $\nabla_t^2\Phi + k_c^2\Phi = 0$, whose solution provides the TE and TM modes in hollow waveguides filled with a homogeneous dielectric, or the Laplace equation $\nabla_t^2\Phi = 0$ for TEM modes in multiconductor waveguides (see Appendix A), can be discretized for those geometries that do not lead to analytic or quasi-analytic solutions. To that end, the Finite Element method approximates the scalar function Φ over a mesh through a proper set of basis functions ϕ_n and the corresponding N weighting coefficients v_n (also known as degrees of freedom):

$$\Phi = \sum_{n=1}^{N} v_n \phi_n. \tag{4.1}$$

In this Thesis the chosen mesh is made up of triangular elements and the scalar Lagrange functions are selected as the basis functions. The discretized matrix version of the Helmholtz or Laplace equations using (4.1) are respectively [53, 54]:

$$\mathbf{K}\mathbf{v} - k_c^2\mathbf{M}\mathbf{v} = \mathbf{0}, \tag{4.2}$$

$$\mathbf{K}\mathbf{v} = \mathbf{0}, \tag{4.3}$$

where $\mathbf{v}$ is a column vector that contains the N weighting coefficients and the i, j elements of matrices $\mathbf{K}$ and $\mathbf{M}$ are computed over the area A_s of the cross-section in the following way:

$$K_{ij} = \iint_{A_s} \nabla_{\mathrm{t}}\phi_i \cdot \nabla_{\mathrm{t}}\phi_j dS, \tag{4.4}$$

$$M_{ij} = \iint_{A_s} \phi_i \phi_j dS. \tag{4.5}$$

At this point it is convenient to introduce another matrix useful for a later stage, where each element (i, j) is computed as:

$$R_{ij} = \iint_{A_s} \nabla_{\mathrm{t}}\phi_i \times \nabla_{\mathrm{t}}\phi_j \cdot \hat{z} dS. \tag{4.6}$$

The goal of this Chapter is to provide a formulation where the 2D-Finite Element and Mode-Matching methods are efficiently hybridated to solve problems made up of cascaded waveguide sections having arbitrary transversal shapes as in Figure 4.1. To that end, it will be shown how the previous expressions are not only valid for the 2D-problem of computing the modes but also for the analysis of 3D waveguide devices if they are properly combined with other methods that take advantage of translational symmetry, as it is the case of the Mode-Matching method presented in Chapter 2.

In first place, the computation of the normalized inner cross-product matrix $\bar{\mathbf{X}}$ was presented in Section 2.3 according to the type of modes. Expressions (2.20)-(2.22) are repeated here for convenience:

$$\bar{X}_{ij} = 0 \text{ for TEM}^{(s)}\text{-TE}^{(w)}, \text{TM}^{(s)}\text{-TEM}^{(w)}, \text{TM}^{(s)}\text{-TE}^{(w)} \tag{4.7}$$

$$\bar{X}_{ij} = \iint_{A_s} \nabla_t \Phi_i^{(s)} \times \nabla_t \Phi_j^{(w)} \cdot \hat{z} dS \text{ for TE}^{(s)}\text{-TEM}^{(w)}, \text{TE}^{(s)}\text{-TM}^{(w)} \tag{4.8}$$

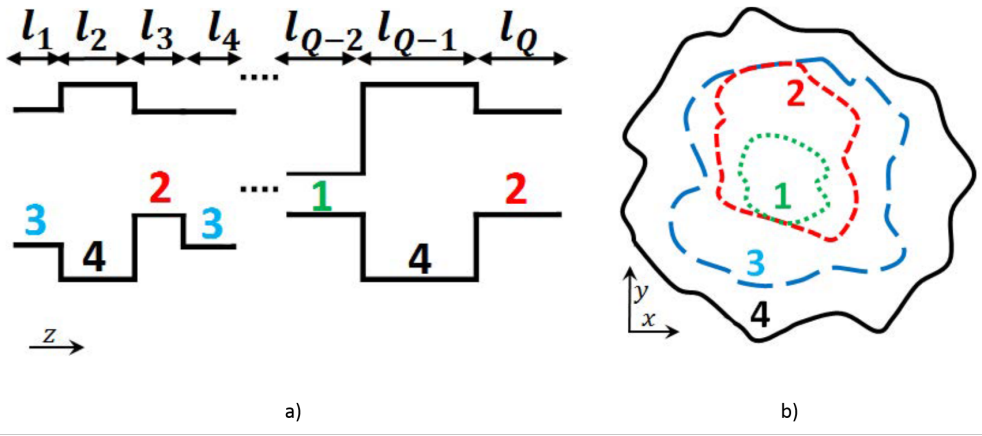

Figure 4.1: Schematic structure of a problem made up of arbitrary cross-section waveguides cascaded along the longitudinal direction a) longitudinal cut and b) transversal cut, showing an example with four different arbitrary cross-sections.

$$\bar{X}_{ij} = \iint_{A_s} \nabla_t \Phi_i^{(s)} \cdot \nabla_t \Phi_j^{(w)} dS \quad \text{for the remaining cases.} \tag{4.9}$$

If the previous expressions are hybridated with the 2D Finite Element method, then (4.1) must be inserted in (4.8) and (4.9). At this point, let us assume that the device under analysis has Q different waveguide cross-sections, which are all projected onto the transverse plane (*i.e.* the xy-plane), as the example of Figure 4.2 made up of $Q = 4$ cross-sections. In this example at each discontinuity one cross-section lies inside the other one, which simplifies the explanation without loss of generality. This way, the cross-sections are numbered according to their sizes from #1 (smallest) to #Q (biggest).

Now the N_1 basis functions of the smallest cross section (#1 in this example) are used as part of the function space in the next cross-section (#2) made up of N_2 functions, and so on. This leads to a set of nested function spaces as it is shown in Table 4.1. In order to follow this procedure the mesh of the cross-section q must be a sub-mesh of cross-section $q+1$. This can be achieved with the aforementioned projection of all cross-sections onto the transverse plane and the subsequent generation of an inter-cross-section conforming mesh, as shown in Figure 4.2.

Then, with the previous considerations, when (4.1) is inserted in (4.8) and (4.9), the use of the linearity property of the sum, the integral and the transverse gradient operators leads to:

$$\begin{aligned}
\bar{X}_{ij} &= \iint_{A_s} \nabla_t \Phi_i^{(s)} \times \nabla_t \Phi_j^{(w)} \cdot \hat{z} dS = \\
&= \iint_{A_s} \nabla_t \sum_{a=1}^{N_s} v_{i,a}^{(s)} \phi_a \times \nabla_t \Big(\sum_{b=1}^{N_s} v_{j,b}^{(w)} \phi_b + \sum_{b=N_s+1}^{N_w} v_{j,b}^{(w)} \phi_b \Big) \cdot \hat{z} dS, \qquad (4.10) \\
\bar{X}_{ij} &= \iint_{A_s} \nabla_t \Phi_i^{(s)} \cdot \nabla_t \Phi_j^{(w)} dS = \\
&= \iint_{A_s} \nabla_t \sum_{a=1}^{N_s} v_{i,a}^{(s)} \phi_a \cdot \nabla_t \Big(\sum_{b=1}^{N_s} v_{j,b}^{(w)} \phi_b + \sum_{b=N_s+1}^{N_w} v_{j,b}^{(w)} \phi_b \Big) dS, \qquad (4.11)
\end{aligned}$$

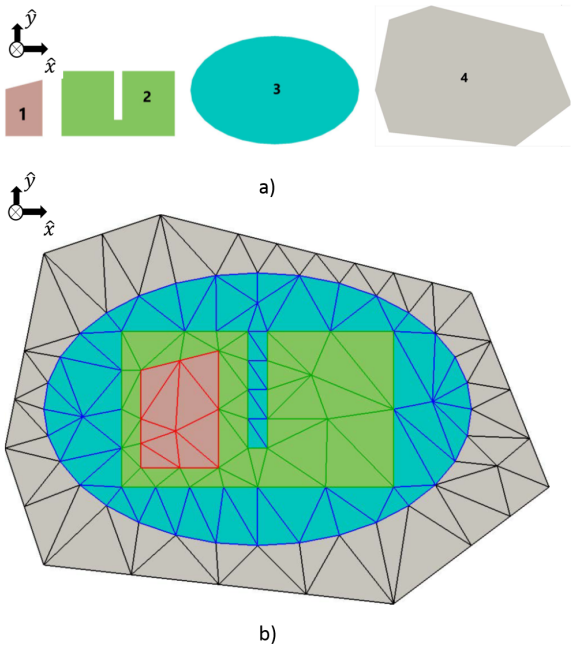

Figure 4.2: a) Set of consecutive waveguides along the $\hat{z}$ axis of different cross-section : quadrangular (1), ridge (2), elliptical (3) and polygonal (4). b) Example of inter-cross-section conforming mesh of the projection onto the xy-plane.

where N_w and N_s are the basis functions of the method used for the waveguide with larger (w) and smaller (s) cross-sections at each discontinuity respectively. Thus, in the previous example of Figure 4.2, the first waveguide step would involve $N_s = N_1$ basis functions for the smaller waveguide numbered as 1 and $N_w = N_2$ basis functions for the larger waveguide numbered as 2. Then, in the second waveguide step the waveguide numbered as 2 is the smaller one, and hence in the proposed formulation $N_s = N_2$ basis functions when (4.10) and (4.11) are computed, whereas the third waveguide would have $N_w = N_3$ basis functions, and so on. Furthermore, because of the nested nature of the function spaces, the overall computational cost is greatly simplified since any integral over A_s that contains a basis function ϕ_b, with $\forall b = N_{s+1}, ..., N_w$ has a null value. That is, $\iint_{A_s} \nabla_t\phi_a \times \nabla_t\phi_b \cdot \hat{z}dS = 0, \quad \iint_{A_s} \nabla_t\phi_a \cdot \nabla_t\phi_b dS = 0, \quad \forall b = N_{s+1}, ...N_w$. Therefore equations (4.10) and (4.11) are respectively simplified to:

$$\bar{X}_{ij} = \sum_{a=1}^{N_s}\sum_{b=1}^{N_s} v_{i,a}^{(s)} \left(\iint_{A_s} \nabla_t\phi_a \times \nabla_t\phi_b \cdot \hat{z}dS \right) v_{j,b}^{(w)}, \tag{4.12}$$

$$\bar{X}_{ij} = \sum_{a=1}^{N_s}\sum_{b=1}^{N_s} v_{i,a}^{(s)} \left(\iint_{A_s} \nabla_t\phi_a \cdot \nabla_t\phi_b dS \right) v_{j,b}^{(w)}. \tag{4.13}$$

At this point the two previous expressions must be compared with those of equations (4.4) and (4.6) for the smaller waveguide (s), so that the $\bar{\mathbf{X}}$ matrix can be written in the

Cross-section:	1-st	2-nd	...	q-th	...	$(Q-1)$-th	Q-th
Function Space:	$\phi^{(1)}$ $\phi^{(2)}$ $\phi^{(N_1)}$	$\phi^{(1)}$ $\phi^{(2)}$ $\phi^{(N_1)}$ $\vdots$ $\phi^{(N_1+1)}$ $\vdots$ $\phi^{(N_2)}$	... ... $\ddots$	$\phi^{(1)}$ $\phi^{(2)}$ $\phi^{(N_1)}$ $\vdots$ $\phi^{(N_1+1)}$ $\vdots$ $\phi^{(N_2)}$ $\phi^{(N_2+1)}$ $\vdots$ $\vdots$ $\phi^{(N_{q-1}+1)}$ $\vdots$ $\phi^{(N_q)}$	... ... $\ddots$	$\phi^{(1)}$ $\phi^{(2)}$ $\phi^{(N_1)}$ $\vdots$ $\phi^{(N_1+1)}$ $\vdots$ $\phi^{(N_2)}$ $\phi^{(N_2+1)}$ $\vdots$ $\vdots$ $\phi^{(N_{q-1}+1)}$ $\vdots$ $\phi^{(N_q)}$ $\phi^{(N_q+1)}$ $\vdots$ $\vdots$ $\phi^{(N_{Q-2}+1)}$ $\vdots$ $\phi^{(N_{Q-1})}$	$\phi^{(1)}$ $\phi^{(2)}$ $\phi^{(N_1)}$ $\vdots$ $\phi^{(N_1+1)}$ $\vdots$ $\phi^{(N_2)}$ $\phi^{(N_2+1)}$ $\vdots$ $\vdots$ $\phi^{(N_{q-1}+1)}$ $\vdots$ $\phi^{(N_q)}$ $\phi^{(N_q+1)}$ $\vdots$ $\vdots$ $\phi^{(N_{Q-2}+1)}$ $\vdots$ $\phi^{(N_{Q-1})}$ $\phi^{(N_{Q-1}+1)}$ $\vdots$ $\phi^{(N_Q)}$

Table 4.1: Overall set of nested function spaces from the smallest (1-st) to the biggest (Q-th) waveguide cross-section.

following compact closed-form:

$$\bar{\mathbf{X}} = \begin{pmatrix} \bar{\mathbf{X}}_{\mathrm{TEM},s-\mathrm{TEM}w} & \bar{\mathbf{X}}_{\mathrm{TEM},s-\mathrm{TE},w} & \bar{\mathbf{X}}_{\mathrm{TEM},s-\mathrm{TM},w} \\ \bar{\mathbf{X}}_{\mathrm{TE},s-\mathrm{TEM},w} & \bar{\mathbf{X}}_{\mathrm{TE},s-\mathrm{TE},w} & \bar{\mathbf{X}}_{\mathrm{TE},s-\mathrm{TM},w} \\ \bar{\mathbf{X}}_{\mathrm{TM},s-\mathrm{TEM},w} & \bar{\mathbf{X}}_{\mathrm{TM},s-\mathrm{TE},w} & \bar{\mathbf{X}}_{\mathrm{TM},s-\mathrm{TM},w} \end{pmatrix} = \tag{4.14}$$

$$= \begin{pmatrix} \mathbf{V}_{\mathrm{TEM},s}^T \mathbf{K}_s \mathbf{V}_{\mathrm{TEM},w\rfloor_s} & \mathbf{0} & \mathbf{V}_{\mathrm{TEM},s}^T \mathbf{K}_s \mathbf{V}_{\mathrm{TM},w\rfloor_s} \\ \mathbf{V}_{\mathrm{TE},s}^T \mathbf{R}_s \mathbf{V}_{\mathrm{TEM},w\rfloor_s} & \mathbf{V}_{\mathrm{TE},s}^T \mathbf{K}_s \mathbf{V}_{\mathrm{TE},w\rfloor_s} & \mathbf{V}_{\mathrm{TE},s}^T \mathbf{R}_s \mathbf{V}_{\mathrm{TM},w\rfloor_s} \\ \mathbf{0} & \mathbf{0} & \mathbf{V}_{\mathrm{TM},s}^T \mathbf{K}_s \mathbf{V}_{\mathrm{TM},w\rfloor_s} \end{pmatrix}$$

where superscript T stands for the transpose operation, while each matrix symbol denoted in the form $\mathbf{V}_{\cdot,w]_s}$ stands for a matrix consisting of the first N_s rows of $\mathbf{V}_{\cdot,w}$.

Once the inner cross-product matrices are obtained, the generalized scattering matrix $\mathbf{S}$ of each discontinuity can be easily obtained as in (2.23). The cascading of the generalized scattering matrices of the different steps to characterize the full structure is done in the usual way [9, 11].

It is not the objective of this work to report how $\mathbf{V}$, $\mathbf{K}$ or $\mathbf{R}$ are computed and assembled, as this is a standard procedure in the Finite Element framework and can be found in many textbooks [53, 54]. In fact, what it is relevant in this Thesis is that matrices $\mathbf{K}$ and $\mathbf{V}$ have already been computed whenever a non-analytical cross-section has been solved by the 2D-Finite Element Method. Therefore, at the same time the modes are numerically solved, the matrices required to build the inner cross-product matrix for this formulation are computed. Besides, the computation of these matrices can be highly efficient due to their proposed structure of blocks where the mathematical operations carried out for a nested cross-section q are extracted from the next one $q+1$ as in Figure 4.3. Furthermore, the multiplication of matrices shown in (4.14) benefits from the sparsity properties of $\mathbf{R}$ and $\mathbf{K}$ [54].

Finally, it should be noted that the use of matrices which were initially built to characterize modes to compute waveguide steps has been also used in the Boundary Integral Resonant-Mode Expansion (BI-RME) context [11]. However, in this work the computation of the normalized inner-product matrix $\bar{\mathbf{X}}$ in (4.14) for all the steps is straightforward within the presented Finite Element framework since it is directly built from pre-computed Finite Element solution matrices, without the need for further interpolation or quadrature, as well as already assembled Finite Element matrices.

$$\begin{pmatrix}
K_{1,1} & \cdots & K_{1,N_1} & \cdots & K_{1,N_q} & \cdots & K_{1,N_Q} \\
\vdots & \ddots & \vdots & \ddots & \vdots & \ddots & \vdots \\
K_{N_1,1} & \cdots & K_{N_1,N_1} & \ddots & K_{N_1,N_q} & \ddots & K_{N_1,N_Q} \\
\vdots & \vdots & \vdots & \ddots & \vdots & \ddots & \vdots \\
K_{N_q,1} & \cdots & K_{N_q,N_1} & \cdots & K_{N_q,N_q} & \ddots & K_{N_q,N_Q} \\
\vdots & \vdots & \vdots & \vdots & \vdots & \ddots & \vdots \\
K_{N_Q,1} & \cdots & K_{N_Q,N_1} & \cdots & K_{N_Q,N_q} & \cdots & K_{N_Q,N_Q}
\end{pmatrix}$$

Figure 4.3: Partitioning of the overall $\mathbf{K}$ matrix obtained from the FE method with nested function spaces in Table 4.1 for the inter-cross-section conformal single mesh of the whole waveguide device. The blocks provide the respective $\mathbf{K}$ matrix of the different cross-sections. Other FE matrices in the problem are also partitioned in the same exact manner.

4.3 Orthonormalization

The derivations carried out in the previous Section have been made under the assumption that the set of modes computed by the Finite Element Method in each q-th cross-section where orthonormal, which means that [53]:

$$\iint_{A_q} \nabla_{\mathrm{t}}\Phi_i^{(q)} \cdot \nabla_{\mathrm{t}}\Phi_j^{(q)} \mathrm{d}S = \begin{cases} 1, \text{ for } i = j \\ 0, \text{ for } i \neq j \end{cases} . \tag{4.15}$$

This condition in terms of the Finite Element matrices of (4.14) implies that:

$$\mathbf{V}_{\mathrm{TEM}}^T \mathbf{K} \mathbf{V}_{\mathrm{TEM}} = \mathbf{I}_{\mathrm{TEM}}, \tag{4.16}$$

$$\mathbf{V}_{\mathrm{TE}}^T \mathbf{K} \mathbf{V}_{\mathrm{TE}} = \mathbf{I}_{\mathrm{TE}}, \tag{4.17}$$

$$\mathbf{V}_{\mathrm{TM}}^T \mathbf{K} \mathbf{V}_{\mathrm{TM}} = \mathbf{I}_{\mathrm{TM}}, \tag{4.18}$$

where the size of the identity matrices on the right hand side $\mathbf{I}_{\mathrm{TEM}}$, $\mathbf{I}_{\mathrm{TE}}$ and $\mathbf{I}_{\mathrm{TM}}$ is equal to the number of modes present of each kind, and all the expressions found in this Section are referred to every single cross-section q.

The orthonormal property of the computed modes must be ensured for the hybridation with the Mode-Matching method. However, the modal solutions found in the previous Section may not comply with (4.16)-(4.18) since degenerate modes may arise among other reasons.

Most matrix eigensolvers provide orthogonal solutions for positive definite generalized eigenvalue problems as the one presented in (4.2). In particular, such solutions fulfil $\tilde{\mathbf{V}}^T \mathbf{M} \tilde{\mathbf{V}} = \mathbf{I}$, where $\tilde{\mathbf{V}}$ are the corresponding (*a priori* non-orthonormal) matrices found for TE and TM modes respectively ($\tilde{\mathbf{V}}_{\mathrm{TE}}, \tilde{\mathbf{V}}_{\mathrm{TM}}$). Thus, in order to turn them into orthonormal a simple scaling process must be carried out, where each column of the solution matrix (which corresponds to a mode) is multiplied by the inverse of its associated cut-off wavenumber. Therefore, if $\mathbf{k}_{c,\mathrm{TE}}$ and $\mathbf{k}_{c,\mathrm{TM}}$ are the vectors that store the associated real positive cut-off wavenumbers, then the orthonormal solutions are obtained as:

$$\mathbf{V} = \begin{cases} \tilde{\mathbf{V}}(\mathbf{diag}\{\mathbf{k}_{\mathbf{c},\mathrm{TE}}\})^{-\mathbf{1}} \text{ for TE modes,} \\ \tilde{\mathbf{V}}(\mathbf{diag}\{\mathbf{k}_{\mathbf{c},\mathrm{TM}}\})^{-\mathbf{1}} \text{ for TM modes.} \end{cases} \tag{4.19}$$

In the case of the resolution of TEM modes, orthogonality is not ensured by the usual Finite Element process [53, 54]. For that reason an orthonormalization procedure that takes advantage of the proposed formulation is here shown. In a multiconductor waveguide where there are L indepent perfect electric contours, it suffices to ensure the linear independence of all $L-1$ computed modes [105, p. 251]. Thus, the new base of orthonormal solutions (Φ_i) is obtained from a linear combination of the already computed $L-1$ non-orthonormal solutions ($\tilde{\Phi}_j$):

$$\Phi_i = \sum_{j=1}^{L-1} T_{ij} \tilde{\Phi}_j = \sum_{j=1}^{L-1} T_{ij} \sum_{n=1}^{N} \tilde{v}_{j,n} \phi_n, \tag{4.20}$$

where T_{ij} is the coordinate of Φ_i with respect to $\tilde{\Phi}_j$. Then, if (4.20) is inserted into (4.15) and (4.4) is used, it can be seen that a mode transformation matrix $\mathbf{T}$ must be sought, which fulfils:

$$\mathbf{T} \tilde{\mathbf{V}}_{\mathrm{TEM}}^T \mathbf{K} \tilde{\mathbf{V}}_{\mathrm{TEM}} \mathbf{T}^T = \mathbf{I}. \tag{4.21}$$

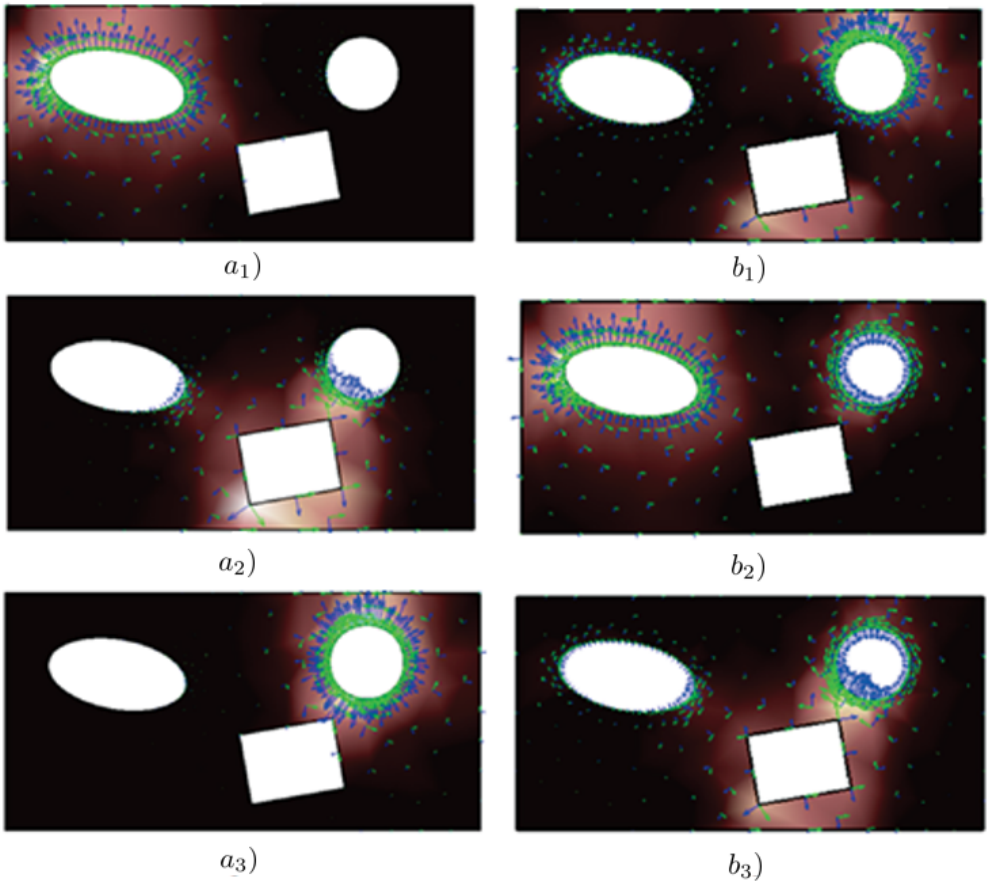

Figure 4.4: Each of the three TEM mode fields for an arbitrary waveguide cross-section with four conductors; blue: electric field, green: magnetic field; background: power density. a_i) Computed with a unitary voltage value at each PEC. b_i) Orthonormalized TEM modes. Subscript indicates mode number.

To that end an eigendecomposition is carried out, where the following standard eigenvalue problem of size equal to the number of TEM modes $(L-1)$ is solved :

$$\left(\tilde{\mathbf{V}}_{\mathrm{TEM}}^{T}\mathbf{K}\tilde{\mathbf{V}}_{\mathrm{TEM}} - \lambda\mathbf{I}_{\mathrm{TEM}}\right)\mathbf{e} = \mathbf{0}, \tag{4.22}$$

where the eigenvalues λ_n are real and the eigenvectors $\mathbf{e}_n$ form an orthonormal basis since $\tilde{\mathbf{V}}_{\mathrm{TEM}}^{T}\mathbf{K}\tilde{\mathbf{V}}_{\mathrm{TEM}}$ is symmetric [106]. These solutions can be written in matrix form as:

$$\mathbf{\Lambda} = \mathrm{diag}\{(\lambda_1 \quad \lambda_2 \quad \cdots \quad \lambda_{L-1})\}, \tag{4.23}$$

$$\mathbf{E} = (\mathbf{e}_1 \quad \mathbf{e}_2 \quad \cdots \quad \mathbf{e}_{L-1}). \tag{4.24}$$

Given the fact that $\mathbf{E}^T\mathbf{E} = \mathbf{I}$ and $\mathbf{E}\mathbf{\Lambda}\mathbf{E}^T = \mathbf{V}_{\mathrm{TEM}}^{T}\mathbf{K}\mathbf{V}_{\mathrm{TEM}}$, it can be shown from (4.21) that the required transformation matrix $\mathbf{T}$ takes the form $\mathbf{T} = \mathbf{\Lambda}^{-1/2}\mathbf{E}^T$, and thus the orthonormalized matrix solution can be computed as:

$$\mathbf{V}_{\mathrm{TEM}} = \tilde{\mathbf{V}}_{\mathrm{TEM}}\mathbf{E}\mathbf{\Lambda}^{-1/2}. \tag{4.25}$$

Finally, it must be highlighted that the orthonormalization procedure is required for a correct hybridation between the 2D Finite Element and Mode-Matching methods for TEM modes, and that with the formulation proposed in this Thesis the computations can be efficiently carried out. On the one hand, the standard eigenvalue problem that needs to be solved in (4.22) is directly constructed from a double product of the already available matrices $\mathbf{K}$, $\tilde{\mathbf{V}}$. Furthermore, the high sparsity inherent to $\mathbf{K}$ allows very efficient matrix multiplications [53, 54]. And last but not least, this eigenvalue problem is usually small since its size solely depends on the number of TEM modes present in the cross-section under analysis, which tends to remain low in practical microwave devices.

Figure 4.4 shows an example of the application of the proposed approach, where an arbitrary waveguide cross-section with four conductors having three TEM modes is analyzed. The TEM mode fields with a unitary voltage at each conductor and thus without orthonormal properties are plotted in Figure 4.4 denoted by a), whereas in Figure 4.4 denoted by b) presents the results of applying the orthonormalization procedure presented in this Section.

4.4 Validation cases

The proposed formulation has been implemented on a proof-of-concept basis with the aid of the high-level Python interface of the Finite Element platform FEniCS [99]. This platform is combined with the SLEPc package [100], which is used to solve the aforementioned eigenvalue problems through the same high-level Python interface.

In the first place the formulation is validated with three sets of cascaded analytical cross-sections of different type. Thereby this would be the typical scenario where analytical closed-form expressions are useful to test a numerical solver. In particular, the first case analyzed consists of two equilateral triangular cross-sections, whose analytical modal expressions were presented in Chapter 2. These waveguides are placed keeping aligned their symmetry axis, and therefore half of the structure can be analyzed as in Figure 4.5a), where the inter-cross-section conforming mesh is also shown.

The symmetry axis (on the right side as drawn in Figure 4.5a) is set to Perfect Electric Conductor (PEC) and then to Perfect Magnetic Conductor (PMC), and only the modes whose cut-off frequency is below 15 GHz are taken into account, which corresponds to $M = 6$ and $N = 3$ modes in each cross-section respectively. The Finite Element analysis resulted in 4152 basis functions for the biggest cross-section, 1888 of which made up the function space for the smallest one. The analytical results obtained with the formulation presented in Chapter 2 are compared to those obtained by the numerical procedure proposed in this Chapter by means of the normalized inner cross-product matrix. Table 4.2 shows the analytical matrix $\bar{\mathbf{X}}_{\mathrm{AN}}$, which constitutes the reference for the validation, as well as the one numerically obtained $\bar{\mathbf{X}}$ for this case study.

Besides, in order to provide a formal way of comparison, three figures of merit are used to estimate the difference with respect to $\bar{\mathbf{X}}_{\mathrm{AN}}$: the L_2 matrix norm, the maximum absolute error and the maximum relative error. In the latter case the terms that are almost zero for a typical accuracy of 10^{-6} are discarded. The good results obtained for the equilateral triangular case are gathered in the two first rows of Table 4.3.

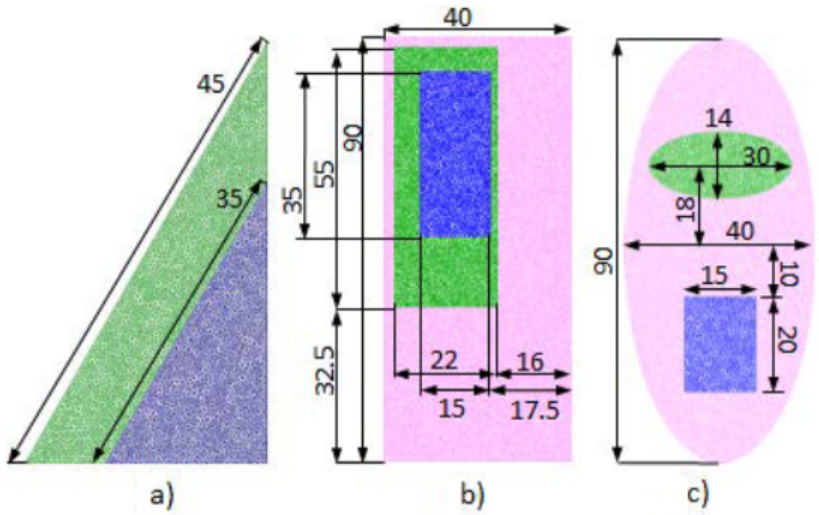

Figure 4.5: Cross-sections of the waveguide steps involved in Table 2 , showing the single mesh used for the computation for a) triangular, b) rectangular and c) elliptical-rectangular geometries. Dimensions in mm.

$$\bar{\mathbf{X}}_{\mathrm{AN}} = \begin{pmatrix} 7.9498\text{E-}1 & 3.4196\text{E-}1 & 6.3791\text{E-}3 & -3.2489\text{E-}1 & -5.6025\text{E-}2 & 2.2797\text{E-}1 \\ 0 & 5.1290\text{E-}1 & 0 & 0 & -4.1614\text{E-}1 & 0 \\ 1.1005\text{E-}1 & -5.6447\text{E-}17 & 5.3241\text{E-}1 & -1.0355\text{E-}1 & 3.2419\text{E-}1 & -1.6523\text{E-}1 \end{pmatrix}$$

$$\bar{\mathbf{X}} = \begin{pmatrix} 7.9503\text{E-}1 & 3.4117\text{E-}1 & 6.3708\text{E-}3 & -3.2482\text{E-}1 & -5.4847\text{E-}2 & 2.2791\text{E-}1 \\ 0 & 5.1305\text{E-}1 & 0 & 0 & -4.1668\text{E-}1 & 0 \\ 1.1009\text{E-}1 & -1.9688\text{E-}4 & 5.3253\text{E-}1 & -1.0357\text{E-}1 & 3.2404\text{E-}1 & -1.6523\text{E-}1 \end{pmatrix}$$

Table 4.2: Normalized inner product matrix for the triangular discontinuity with PMC at the right side wall.

The second example is made up of three rectangular cross-sections placed with different offsets, and it is shown in 4.5b) together with the single inter-cross-section conforming mesh that is used. The number of basis functions obtained for the largest cross-section is 9504, 3228 of which made up the function space for the medium-sized rectangular cross-section. Regarding the smallest cross-section, 1452 basis functions are obtained, which belong to the two larger cross-sections as well due to the nested nature of the set of function spaces. The modes taken into consideration are the ones whose cut-off frequency is below or equal to 10 GHz. This corresponds to $M = 24$ modes in the largest cross-section, $N = 3$ in the smallest one, and to 8 modes in the medium sized (denoted with letter M or N depending on its relative size with respect to the other two), as it is shown in the third and fourth rows of Table 4.3.

Finally, the third example of this initial stage of validation involves two elliptical cross-sections (one of them rotated) together with a rectangular one. This case study is shown in 4.5c) where the conforming mesh can be seen as well. The biggest elliptical cross-section leads to 6837 basis functions in the Finite Element analysis, 771 of which are used for the smallest elliptical cross-section and 836 for the rectangular cross-section. All the modes whose cut-off frequency is below 12 GHz are considered for the computation of the

Case	N	M	$\|\bar{\mathbf{X}}-\bar{\mathbf{X}}_{\mathrm{AN}}\|$	$\max\left\|\bar{X}^{(n,m)}-\bar{X}_{\mathrm{AN}}^{(n,m)}\right\|$	$\max\left\|\frac{\bar{X}^{(n,m)}-\bar{X}_{\mathrm{AN}}^{(n,m)}}{\bar{X}_{\mathrm{AN}}^{(n,m)}}\right\|^{*}$
Tri. Small - Tri. Big, PEC	3	6	2.00E-4	1.45E-4	0.15 %
Tri. Small - Tri. Big, PMC	3	6	1.52E-3	5.34E-4	2.10 %
Rect. Medium- Rect. Big	8	24	4.22E-4	1.90E-4	0.91 %
Rect. Small - Rect. Medium	3	8	3.54E-4	3.02E-4	0.11 %
Ellip. Small - Ellip. Big	3	29	4.42E-3	1.47E-3	2.93 %
Rectangular - Ellip. Big	2	29	3.29E-3	1.49E-3	3.63 %

*: excluding all entries $\left|\bar{X}_{\mathrm{AN}}^{(n,m)}\right| \leq$ 1E-6

Table 4.3: Accuracy in the computation of the $N \times M$ normalized inner-product matrix $\bar{\mathbf{X}}$ with the approach based on nested function spaces with analytical results $\bar{\mathbf{X}}_{\mathrm{AN}}$.

normalized inner cross-product matrix, which is translated into 29 modes for the biggest elliptical cross-section, 3 for the smallest one and 2 modes for the rectangular cross-section, as it is shown in the last two rows of Table 4.3. The computed figures of merit are also in this table and evidence a good agreement between computed matrices.

After this first level of validation where the normalized inner cross-product matrices are compared, the effectiveness of the proposed formulation is now tested with some complete advanced devices whose full-wave simulation by other methods as well as their measurements are available in the technical literature. The steps that are going to be followed according to the proposed formulation for the complete full-wave analysis are summarized in Table 4.4. In particular, five devices are going to be used as a source of validation.

The first device used as a reference is a wide-band filter designed in ridge technology filled with dielectric of a relative permittivity of 5.9 [107]. The structure of this device is shown in Figure 4.6a). The corresponding projection of the cross-sections onto the xy-plane for the generation of the inter-cross-section conforming mesh is given in Figure 4.6b), together with its dimensions, where it can be seen that only the half of the structure suffices for the electromagnetic analysis. In particular 4390 and 2872 basis functions have been used for the Finite Element mesh and sub-mesh respectively. Its full-wave response obtained by CST Microwave Studio (CST MWS) is given in Figure 4.6c), which is in good agreement with the response achieved by the proposed procedure in the Thesis using 159 and 105 modes in the ridge waveguides.

The next device is a double grooved circular polarizer described in [108], where the grooved sections placed along a circular waveguide provide the desired phase shift for the two polarizations. The whole structure is given in Figure 4.6d). The corresponding inter-cross-section conforming mesh, shown in Figure 4.6e) has an overall number of 4513 basis functions. The structure shown in Figure 4.6e) is only a quarter of the cross-section of the double grooved circular polarizer since the whole simulation can be carried out by placing PEW-PMW at the symmetry planes (left and bottom sides respectively in Figure 4.6e)) and then PMW-PEW in these symmetry planes. Figure 4.6f) shows the obtained return-loss level on top of the phase shift between polarizations compared to the results achieved by the commercial software CST MWS. The largest number of modes involved in the calculation with the proposed formulation has been 146 for this device.

1. Project all cross-sections of the device onto the $x-y$ plane and generate an inter-cross-section conforming mesh
2. Assemble matrices $\mathbf{K_Q}$ and $\mathbf{M_Q}$ by using (4.4) and (4.5)
3. For each different cross-section q:
   (a) Extract submatrices $\mathbf{K_q}$ and $\mathbf{M_q}$ from $\mathbf{K_Q}$ and $\mathbf{M_Q}$
   (b) Solve (4.2) with corresponding boundary conditions for TE and TM modes and store $\mathbf{V}_{\mathrm{TE},\mathbf{q}}$ and $\mathbf{V}_{\mathrm{TM},\mathbf{q}}$
   (c) If there are TEM modes, solve (4.3) and store $\mathbf{V}_{\mathrm{TEM},q}$ (if necessary, orthonormalize using (4.25))
4. For each discontinuity in the device:
   (a) Compute $\bar{\mathbf{X}}$ straightforwardly from (4.14)
   (b) Compute $\mathbf{S}$ at the discontinuity from (2.23)
5. Compute the response for the device by cascading the generalized scattering matrices in the usual way [9, 11].

Table 4.4: Self-contained algorithm which summarizes the application of the proposed formulation to analyze a waveguide device.

Now a transformer with octagonal sections is used as a source of validation [109]. This structure, given in Figure 4.6g), has a rectangular and a circular waveguide in each of the two device ports and four intermediate octagonal cross-sections. The used mesh is shown in Figure 4.6h) , which is a quarter of the whole structure, together with its dimensions. This mesh is very partitioned and has an overall number of 4557 basis functions. In order to have an accurate full-wave response the selected modes must have a cut-off frequency lower than 100 GHz, since the return loss levels are in the order of 40 dB. Figure 4.6i) shows the corresponding simulation results compared to those of CST MWS.

The fourth example is an interdigital filter from [110], whose structure is shown in Figure 4.6j). The corresponding mesh and dimensions are given in Figure 4.6k). In this kind of filters it is well-known that an initial analysis based exclusively on TEM modes provides a full-wave response close to the final one achieved when higher order modes are taken into consideration. Thus, the initial dimensions of the device can be obtained with a lower computational cost at the early stages of the design, and then they can be refined later in a full-wave optimization where higher order modes are taken into account. In fact, [110] presents the analysis involving only TEM modes using the Generalized Transverse Resonance method. In this Thesis this analysis is carried out with the proposed formulation. In our first simulation only TEM modes are considered, which are orthonormalized following the process explained in Section 4.3. Then, the rigorous full-wave computation where higher order modes are present is done. Both responses are presented in Figure 4.6l) together with the response obtained by the commercial software CST MWS. The rigorous full-wave simulation is almost superimposed to this latter one used as a reference. On the other hand, it can be seen that the response with TEM modes approximates very well the final response. Only 8 modes are considered in this simulation, which is much lower compared to the 328 modes used in the largest waveguide for the final simulation using a cut-off limit of 150 GHz. In both cases 9118 basis functions were used for the overall single mesh presented in Figure 4.6k).

The last example used to validate the proposed formulation is a bow-tie waveguide polarizator rotator from [111]. This structure is placed between two standard WR75 waveguides, where one is rotated 90 degrees with respect to the other. This structure of unconventional shape is shown in Figure 4.6m), whose single mesh used in the application of the proposed formulation is given in Figure 4.6n), with 3678 basis functions. From these basis functions 3108 are used in the bow-tie cross-section, while the remaining ones are used to account for the non-overlapping regions that belong to both rectangular waveguides. The result of this analysis is given in Figure 4.6o), where all the modes up to 160 GHz have been taken into account in order to get an accurate response even below -40 dB. This result is compared to the measurements given in [111] with great agreement as it is evidenced in the same Figure.

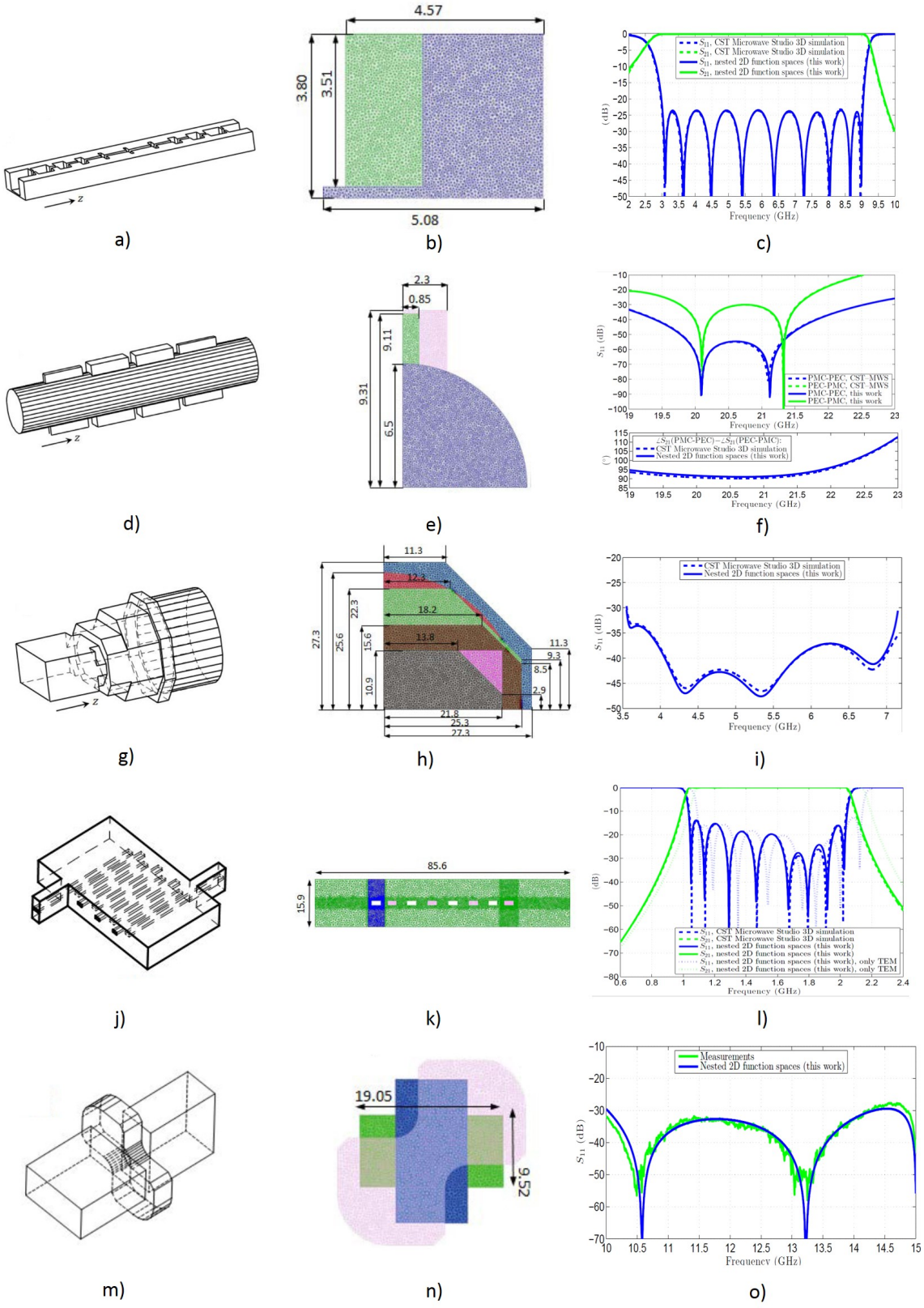

Figure 4.6: Analyzed devices by the hybridation procedure between the 2D Finite Element and the Mode-Matching methods: a) wideband filter in ridge technology , d) double grooved circular polarizer, g) octagonal transformer, j) interdigital filter and m) bow-tie waveguide polarizator rotator. The meshes used for their analysis are shown in subfigures b), e), h), k), and n) respectively. The corresponding full-wave responses are given in subfigures c), f), i), l), and o).

5 Contribution to the design of filters (Part I)

5.1 Introduction

Chapters 2 and 3 have addressed the electromagnetic analysis of two unconventional geometries that can widen the possibilities for the design of passive devices at microwave frequencies: the equilateral triangular and the parabolic cylinder waveguides. Furthermore, Chapter 4 addressed the efficient analysis of inline topologies where arbitrary cross-sections may also take part. This Chapter is focused on the use of the unconventional geometries presented in this Thesis for the design of microwave filters, using all the modal decompositions already studied in previous chapters. To that end, some guidelines are given to choose the suitable dimensions for the resonators that make up the filters.

The resonant frequency, the spurious-free window and the quality factor (Q-factor) are three fundamental parameters for the design of a cavity resonator [5–7]. Cavities with larger volume usually provide greater Q-factor, however, the spurious-free window is usually reduced. Filter designers must pursue a trade-off between these two parameters, so that a good out-of band rejection and low insertion losses in the passband are achieved. To that end, resonant mode charts and Q-charts are usually used to design the physical dimensions of the resonators.

The resonant frequency and the spurious-free window are usually studied together, as the spurious-free window directly depends on the bandwidth available between the different resonant frequencies present in the cavity. The quality factor is studied separately but taking into account the impact of the selected dimensions on the spurious-free window. The corresponding normalized resonant chart for the equilateral triangular resonator is given in this Chapter, together with the complete derivation of the analytical expressions of a universal Q-chart. Such expressions, still undeveloped to the best of the author's knowledge, extend the well-known classic formulas for rectangular and circular cavities [18, 43]. The derivation of a mode chart normalized to the aspect ratio is also given for the parabolic cylinder geometry, where different regions of interest are described.

Three designs based on these guidelines are presented in this Chapter to prove that these unconventional geometries are suitable for filter design as promising results are achieved. In particular, the equilateral triangular dual-mode prototype has been manufactured and measured. The electromagnetic simulation of this structure has been carried out with the software presented in Chapter 2 and by commercial software as well, showing very good agreement also with the measurements.

5.2 Guidelines for the equilateral triangular resonator

The resonant mode chart of the equilateral triangular cavity is shown in this Section. Several points are analyzed to provide practical examples of the achievable bandwidth by this type of resonator. Besides, since mode degeneracy is one of the particular features of this geometry, some of the design possibilities for multimode resonators are here outlined. In addition, this Section addresses the solution of the unloaded Q-factor (Q_u) of the resonant modes in this cavity. Closed-form expressions are for the first time derived and validated with commercial software.

5.2.1 Normalized resonant mode chart

An example of an equilateral triangular resontor of side e and length d is shown in Figure 5.1. The resonant frequency f_0 obtained from a waveguide mode with cut-off wavenumber k_c, defined as in (2.8) for the equilateral triangular geometry for both TE and TM modes, and with q variations along z is [43]:

$$f_0 \equiv f_{0,mnq} = \frac{c}{2\pi}\sqrt{k_c^2 + \left(\frac{q\pi}{d}\right)^2} = \frac{c}{2e}\sqrt{\frac{16}{9}(m^2+n^2+mn) + q^2\left(\frac{e}{d}\right)^2}, \tag{5.1}$$

where m and n are the mode subindexes, e and d are the side of the equilateral triangle and the cavity length respectively, and $c = 1/\sqrt{\mu\varepsilon}$, with μ the magnetic permeability and ε the electric permittivity. From the previous expression, it is easy to see that a normalized frequency $\bar{f}_0 = f_{0,mnq} \cdot e$ can be defined. This parameter only depends on the aspect ratio of the cavity e/d, and thus, a normalized resonant chart can be computed. This type of chart is shown in Figure 5.2, where $\bar{f}_0^2$ is plotted with respect to the square of the aspect ratio to have in the graph straight lines whose slope is determined by the resonant mode variation index. Given the resonant frequency f_0 imposed by the system specifications, the filter designer will usually choose the resonant mode and obtain according to the ordinate axis of the previous chart the side of the resonator since $\bar{f}_0^2 = f_{0,mnq}^2 \cdot e^2$. Once the side is chosen, the cavity length is set by the abscissa axis.

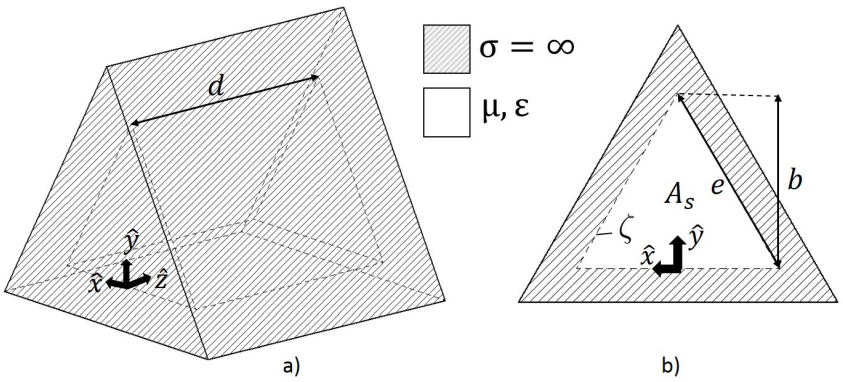

Figure 5.1: a) Example of an equilateral triangular cavity homogeneously filled with electric permittivity ε and magnetic permeability μ closed by a perfect conductor ($\sigma = \infty$). b) Transversal cut of the cavity at $z = z_0, 0 < z_0 < d$, with contour ζ, with cross-section A_s, side e and height $b = e\sqrt{3}/2$.

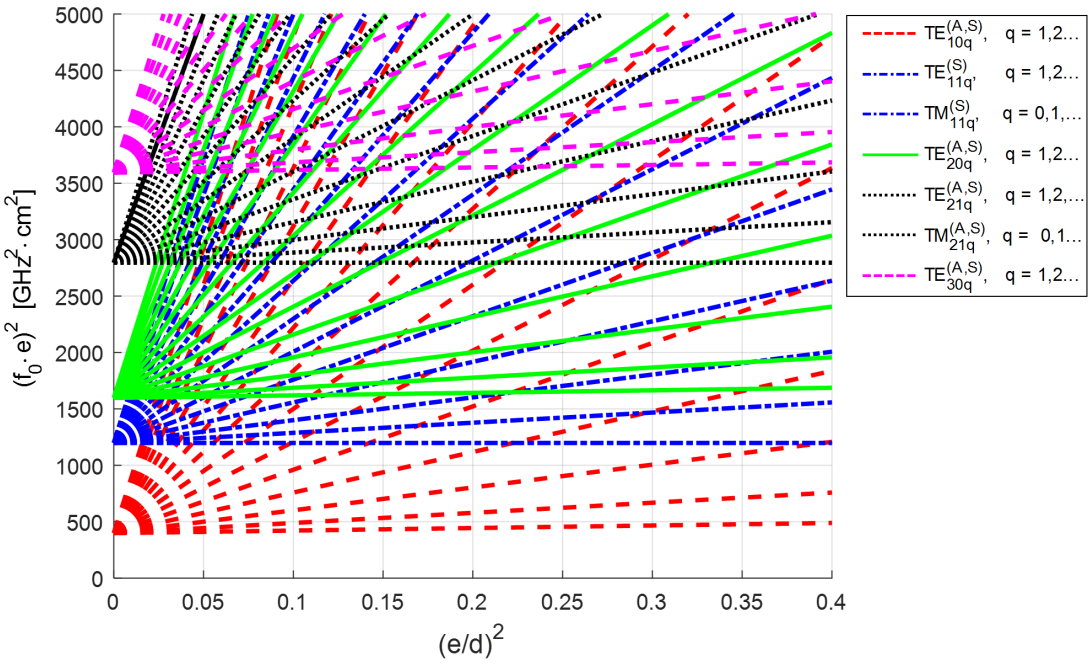

Figure 5.2: Normalized resonant chart for the first resonant modes of the equilateral triangular cavity of side e and length d.

Before the quality factor is taken into account, the choice of the most convenient point in the normalized resonant mode chart depends on the desired spurious free window. An example of analysis is given in this Section for the first three resonances of the fundamental modes, that is, the modes $\mathrm{TE}_{10q}^{(A)}$ and $\mathrm{TE}_{10q}^{(S)}$, which are degenerate, with $q = 1, 2, 3$. Several points of analysis are marked in Figure 5.3, denoted by a cross. For each cross, the immediately lower and higher resonances are denoted by two circles named with the same letter of the alphabet, one with a tilde and one without it (*i.e.*, A-A', or B-B', or C-C' and so on).

The degenerate modes $\mathrm{TE}_{101}^{(A)}$ and $\mathrm{TE}_{101}^{(S)}$ correspond to the lower red dashed line of Figure 5.3. In the first example, the spurious free window is analyzed at $(\frac{e}{d})^2 = 0.9039$. The lower spurious resonance is denoted as p_A and is placed at zero, whereas the first higher spurious resonance is marked at point $p_{A'} = 1198\ \mathrm{GHz}^2 \cdot \mathrm{cm}^2$, where three resonant modes are present: the couple of degenerated modes $\mathrm{TE}_{102}^{(A)}$ and $\mathrm{TE}_{102}^{(S)}$ and the mode $\mathrm{TM}_{110}^{(S)}$. Then, for a given side e, chosen from the center frequency of the filter f_0 at $(\frac{e}{d})^2 = 0.9039$, the total bandwidth $\Delta_{\text{free-spur}}$ free of spurious resonances is computed as $\Delta_{\text{free-spur}}\,[\mathrm{GHz}] = \sqrt{1198}/e$.

The choice of the resonant mode the filter designer must bear in mind that two degenerated modes of the same resonant frequency can present different spurious-free windows if the well-known symmetries (PEW, PMW) are exploited. If we have a look at the same degenerated mode families $\mathrm{TE}_{101}^{(A,S)}$ at a higher aspect ratio $(\frac{e}{d})^2 = 1.783$, we can see that both are free from lower spurious resonances and thus the point p_B is placed at zero. However, the first higher spurious resonance is located at different points for the two mode families. In fact, if symmetry is kept, the horizontal blue dashed line that belongs to

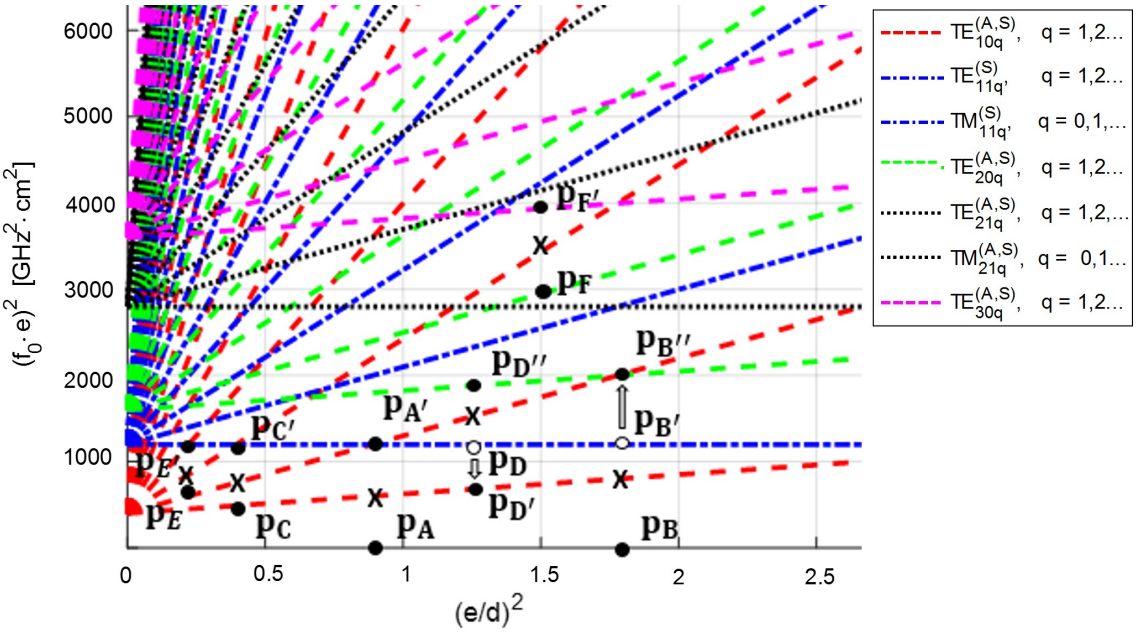

Figure 5.3: Some suggested points for improved spurious-free window for different aspect ratios for the $\mathrm{TE}_{10q}^{(A,S)}$ modes with $q = 1, 2, 3$.

mode	$\mathrm{TE}_{101}^{(A,S)}$	$\mathrm{TE}_{101}^{(A)}$	$\mathrm{TE}_{101}^{(S)}$	$\mathrm{TE}_{102}^{(A,S)}$	$\mathrm{TE}_{102}^{(A)}$	$\mathrm{TE}_{102}^{(S)}$	$\mathrm{TE}_{102}^{(A)}$	$\mathrm{TE}_{102}^{(S)}$
p_1-p_2	p_A-$p_{A'}$	p_B-$p_{B'}$	p_B-$p_{B''}$	p_C-$p_{C'}$	p_D-$p_{D''}$	$p_{D'}$-$p_{D''}$	p_E-$p_{E'}$	p_F-$p_{F'}$
p_1	0	0	0	487.9	1198	685	607.6	2941
p_2	1198	1198	1998	1198	1883	1883	1198	3931
e/d	0.90	1.78	1.78	0.39	1.27	1.27	0.23	1.49
$\Delta_{\mathrm{fs}} \cdot e$	34.61	34.61	44.69	26.64	26.17	34.61	24.29	31.46

Table 5.1: Normalized free of spurious bandwidth for points p_A-$p_{A'}$ to p_F-$p_{F'}$ in Figure 5.3. Points p_1 and p_2 are measured in [$\mathrm{GHz}^2 \cdot \mathrm{cm}^2$], the ratio e/d is adimensional and $\Delta_{\mathrm{fs}} \cdot e$ is measured in [$\mathrm{GHz} \cdot \mathrm{cm}$].

the $\mathrm{TM}_{110}^{(S)}$ mode, with PMW symmetry, only represents a spurious resonance at point $p_{B'}$ for the $\mathrm{TE}_{101}^{(A)}$ mode, which has the same symmetry. In contrast, the first higher spurious resonances for the $\mathrm{TE}_{101}^{(S)}$ mode, of PEW symmetry, are the $\mathrm{TE}_{102}^{(S)}$ and the $\mathrm{TE}_{201}^{(S)}$ modes, of the same symmetry, at point $p_{B''}$.

In the next Section it will be evidenced that the previous consideration is of great importance, since modes $\mathrm{TE}_{mnq}^{(A)}$ and $\mathrm{TE}_{mnq}^{(S)}$ mode of the same m, n and q present the same Q-factor. This means that, sometimes, the simple choice of one of the two degenerate resonant modes can lead to a cavity of better performance in absolute sense, that is, with the same dimensions, same Q-factor but improved spurious-free window.

The spurious improvement due to the use of symmetries can also be exploited in the $\mathrm{TE}_{102}^{(S)}$ mode. In particular, Figure 5.3 shows that the lower limit of the spurious free window can be improved with respect to the $\mathrm{TE}_{102}^{(A)}$ mode at the aspect ratios 1.271, where the limit for this mode is set at $p_{D'}$ instead of p_D. Table 5.1 provide the detailed information associated to these presented points, plus some additional examples. The last

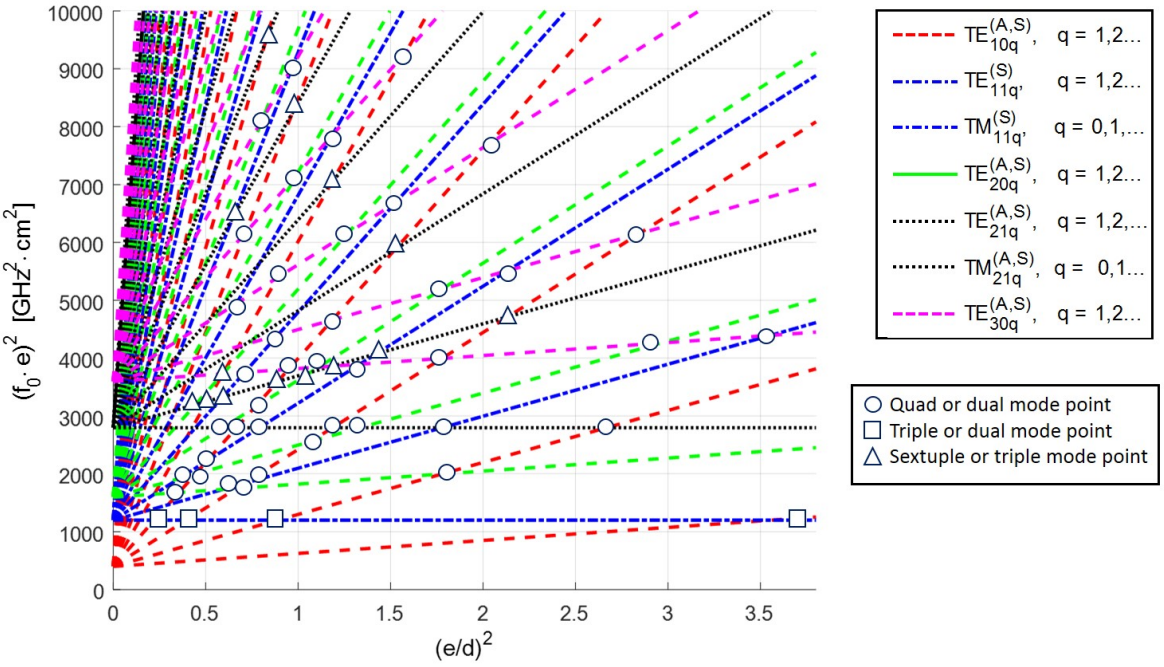

Figure 5.4: Points where mode families with different cut-off frequencies hold the same resonant frequency.

row of the table allows to compute the available free spurious window Δ_{fs} for a cavity of side e by dividing the given quantities by the side e in cm.

One significant aspect of the equilateral triangular resonator is the mode degeneracy for each pair (m, n) and thus for each associated resonance q. This feature can be used to design very compact filters. Each line in Figures 5.2 and 5.3 represents at least two modes with the same resonant frequency, or even up to four modes with the same resonant frequency. The only exception are the lines that belong to TM modes with $m = n$ and $q = 0$, such as the horizontal blue line at $(f_0 \cdot e)^2 = 1198$, where a single resonant mode is present.

The points where these lines intersect represent points where there is degeneracy for the same resonant frequency, apart from the one inherent to each pair (m, n). The combination of different mode families can give rise up to six degenerated resonant modes. Figure 5.4 identifies some of these intersections, where the legend indicates that half of the degenerated modes can be used if a certain symmetry is kept. The points that represent six or three degenerated modes can only be obtained combining mode families with different cut-off frequencies (*i.e.*, different (m, n)).

5.2.2 Analytical computation of the unloaded quality factor

This subsection aims at providing the closed-form expressions for the unloaded Q-factor in metallic cavities with equilateral triangular cross-section. To the best of the author's knowledge, these analytical expressions are for the first time developed and therefore extend the well-known classic formulas for rectangular and circular cavities present in the literature

[18, 43]. The computation of this parameter, which is directly related with the insertion losses in the passband, can also be carried out with numerical techniques [9, 54]. However, if the cavity is very large compared to the wavelength the efficiency of this computation can be compromised, while analytical Q-factors are only limited by machine precision and provide a physical insight into the electromagnetic problem.

In order to begin the derivation, the expressions of a resonant field inside a cavity are here given [105]:

$$\vec{E}^{(res)} = A(\sin(\beta_p z)\vec{e}_p + j\cos(\beta_p z)e_{zp}\hat{z}), \tag{5.2}$$

$$\vec{H}^{(res)} = A(j\cos(\beta_p z)\vec{h}_p + \sin(\beta_p z)h_{zp}\hat{z}), \tag{5.3}$$

where β is the phase constant of a TE or TM mode of the corresponding equilateral triangle waveguide fulfilling $\beta d = 2\pi d/\lambda_g = q\pi$ at the resonant frequency f_0, and A is an arbitrary complex amplitude constant. The transverse electric and magnetic fields ($\vec{e}_p$, $\vec{h}_p$) of each waveguide mode are normalized without loss of generality to:

$$\iint_{A_s} \vec{e}_p \times \vec{h}_p \cdot \hat{\mathbf{z}}\, dS = 1, \tag{5.4}$$

where A_s is the waveguide cavity cross-section as in Figure 5.1 for the equilateral triangular resonator. Secondly, the definition of the quality factor is [5, 7, 43]:

$$Q = 2\pi f_0 \frac{(W_E + W_H)}{P_{\text{dis}}}, \tag{5.5}$$

where W_E and W_H are the mean electric and magnetic energies stored in the cavity, respectively, at the resonant frequency. Using the expressions (5.2), (5.3) and the normalization of (5.4), the mean stored electric and magnetic energies in the volume cavity are both equal at resonance and computed as:

$$W_E = W_H = \frac{\mu}{4}\iiint_V |\vec{H}^{(res)}|^2 dV = |A|^2\mu\varepsilon\frac{d^2}{4}\frac{f_0}{p}. \tag{5.6}$$

The total amount of dissipated power in the cavity resonator is equal to the sum of the power dissipated at the lateral walls of the cavity (the contour of the equilateral triangular geometry in our case) plus the one dissipated at the short-circuited ends ($P_{\text{dis}} = P_{\text{dis,walls}} + P_{\text{dis,sc}}$). The first addend, *i.e.*, the power at the lateral walls, is computed as:

$$P_{\text{dis,walls}} = \frac{R_s}{2}\int_{z=0}^{d}\oint_C |\vec{H}^{(res)}|^2 \text{dl dz} = |A|^2\frac{R_s}{2Z_p}, \tag{5.7}$$

where Z_p is the modal wave impedance defined in (A.9) and (A.17), $|\vec{H}^{(res)}|^2 = |A|^2\cos^2(\beta_p z)\cdot |\vec{h}_p|^2 + |A|^2\sin^2(\beta_p z)|h_{zp}|^2$ according to (5.3), and R_s is the surface resistivity related to the conductivity σ and the skin depth of the conductor $\delta = \frac{1}{\sqrt{\pi f\mu\sigma}}$ as $R_s = \frac{1}{\sigma\delta}$. Therefore:

$$\begin{aligned} P_{\text{dis,walls}} &= \frac{R_s}{2}\int_{z=0}^{d}|A|^2\cos^2(\beta_p z)\text{dz}\oint_C|\vec{h}_p|^2\text{dl} + \frac{R_s}{2}\int_{z=0}^{d}|A|^2\sin^2(\beta_p z)\text{dz}\oint_C|h_{zp}|^2\text{dl} = \\ &\frac{R_s}{2}|A|^2\frac{\epsilon_{q0}d}{2}\left(\oint_C\{|\vec{h}_p|^2 + |h_{zp}|^2\}\text{dl}\right), \end{aligned} \tag{5.8}$$

where $\epsilon_{q0} = 2$ when $q = 0$ (which is only allowed for resonant TM modes) and $\epsilon_{q0} = 1$ otherwise. The previous expression contains the dissipated power per unit length p_{dis} :

$$p_{\text{dis}} = \frac{R_s}{2} \oint_C \{|\vec{h}_p|^2 + |h_{zp}|^2\} \text{dl}, \tag{5.9}$$

which must be computed separately for TE and TM modes. On the one hand, TE modes have both transversal and longitudinal magnetic field. According to the longitudinal expression of (A.6):

$$\oint_C |h_{zp,\text{TE}}|^2 \text{dl} = \oint_C h_{zp,\text{TE}} \cdot h^*_{zp,\text{TE}} \text{dl} = \oint_C \sqrt{Y_p \cdot Y_p^*} \sqrt{N_p \cdot N_p^*} \frac{k_{cp}^2 \cdot k_{cp}^{*\,2}}{\gamma_p \cdot \gamma_p^*} \Phi_p \cdot \Phi_p^* \text{dl}. \tag{5.10}$$

In the preceding equation the cut-off wavenumber k_{cp}, defined as in (2.8), is a real number. Moreover, under propagation conditions, the mode admittance Y_p is real and the propagation constant is purely imaginary and equal to $\gamma_p = j\beta_p$. In addition, since Φ is a real quantity, N_p, the normalization constant computed as in (A.10) and (A.18), is also real positive. Thus:

$$\oint_C |h_{zp,\text{TE}}|^2 \text{dl} = N_p Y_p \frac{k_{cp}^4}{\beta_p^2} \oint_C |\Phi_p|^2 \text{dl}. \tag{5.11}$$

Now, according to the transversal equation (A.8), and taking into account the previous considerations about propagation:

$$\oint_C |\vec{h}_p|^2 \text{dl} = N_p \cdot Y_p \oint_C |\nabla_t \Phi_p|^2 dl. \tag{5.12}$$

Therefore, the dissipated power per unit length in TE modes is:

$$p_{\text{dis,TE}} = N_p \cdot \frac{R_s}{2} Y_p \left(\frac{k_{cp}^4}{\beta_p^2} \oint_C |\Phi_p|^2 \text{dl} + \oint_C |\nabla_t \Phi_p|^2 dl \right). \tag{5.13}$$

On the other hand, TM modes only have transversal magnetic field and thus only one of the addends of (5.9) must be computed. According to (A.16) and under propagation conditions:

$$\oint_C |\vec{h}_p|^2 \, dl = N_p \cdot Y_p \oint_C |\nabla_t \Phi_p|^2 dl. \tag{5.14}$$

Thus, the dissipated power per unit length in TM modes is:

$$p_{\text{dis,TM}} = N_p \cdot \frac{R_s}{2} Y_p \oint_C |\nabla_t \Phi_p|^2 dl. \tag{5.15}$$

Up to this point there has been no mention to any particular coordinate system. In order to preserve this advantageous notation, two orthonormal vectors that go along the contour are defined: $\hat{\nu}$ perpendicular and $\hat{\tau}$ tangential to the contour, as in Figure 5.5. The curve integral of p_{dis} is defined in the contour of the waveguide, where the next relationship holds:

$$|\nabla_t \Phi_p|^2 = |\frac{\partial \Phi_p}{\partial \tau} \hat{\tau} + \frac{\partial \Phi_p}{\partial \nu} \hat{\nu}|^2 = \begin{cases} |\frac{\partial \Phi_p}{\partial \tau}|^2 \text{ for TE modes,} \\ |\frac{\partial \Phi_p}{\partial \nu}|^2 \text{ for TM modes.} \end{cases} \tag{5.16}$$

I_c	$I_{c\tau}$	$\oint_C \lvert\frac{\partial\Phi_p}{\partial\tau}\rvert^2 dl$
	I_{cz}	$\oint_C \lvert\Phi_p\rvert^2 dl$
	$I_{c\nu}$	$\oint_C \lvert\frac{\partial\Phi_p}{\partial\nu}\rvert^2 dl$

Table 5.2: Definition of contour integrals.

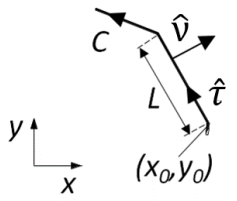

Figure 5.5: Normal and tangential vectors ($\hat{\nu}$,$\hat{\tau}$ respectively) to a segment of length L that belongs to the contour of a waveguide.

Therefore the power dissipated at the lateral walls can be written in a unified manner as:

$$P_{\text{dis,walls}} = |A|^2 \frac{e_{q0} d}{2} \cdot p_{\text{dis}} = |A|^2 \frac{e_{q0} d}{2} \cdot \frac{R_s Y_p}{2} \cdot N_p \cdot I_c, \tag{5.17}$$

where the I_c factor is defined as:

$$I_c = I_{c\tau} + \frac{k_{cp}^4}{\beta_p^2} I_{cz} \quad \text{for TE modes,} \tag{5.18}$$

$$I_c = I_{c\nu} \quad \text{for TM modes,} \tag{5.19}$$

and $I_{c\tau}$, I_{cz} and $I_{c\nu}$ are three contour integrals whose definition is gathered in Table 5.2. These integrals can be solved for the equilateral triangular cavity. Although the integration involves simple trigonometric functions, the function to be integrated is the square of a sum of three trigonometric functions, integrated over the contour of the equilateral triangle. At the end, however, very simple expressions have been obtained:

$$I_{c\tau}^{\text{TE}} = I_{c\nu}^{\text{TM}} = N_p k_c^2 e_s 3 \times \begin{cases} 1, & n = 0 \\ 3/2, & m = n \\ 3/4, & \text{otherwise} \end{cases}, \tag{5.20}$$

$$I_{cz}^{\text{TE}} = N_p e_s \frac{9}{2} \times \begin{cases} 5/3, & n = 0 \\ 2, & m = n \\ 1, & \text{otherwise} \end{cases}, \tag{5.21}$$

where N_p is the normalization constant used along this Section computed as in equations (A.10) and (A.18) of Appendix A, whose particular value for the equilateral triangular waveguide was seen in Chapter 2 in equation (2.26). Finally the power dissipated at the short-circuited ends is easily computed as:

$$P_{\text{dis,sc}} = \iint_{S,z=0,d} |\vec{H}^{(res)}|^2 dS = \frac{|A|^2 R_s Y_p}{2}. \tag{5.22}$$

Expressions (5.20) and (5.21) are then replaced in (5.18) and (5.19), and hence, with the computed $P_{\text{dis,walls}}$ and $P_{\text{dis,sc}}$ defined in (5.17) and (5.22) the total amount of dissipated power is obtained. Then, using (5.5),(5.6), (5.17) and (5.22), the sought simple and analytical closed-form expression for the unloaded Q-factor of an equilateral triangular

cavity of side e and length d is obtained:

$$Q = \frac{\lambda_0}{\delta_s} \times \begin{cases} \dfrac{\frac{2}{q^2}\frac{d^3}{\lambda_0^3}}{(u_{n0}+v_{n0}\frac{k_c^2 d^2}{q^2\pi^2})\sqrt{3}\frac{d}{e}+1}, & \mathrm{TE}_{\binom{S}{A},mnq} \\ \dfrac{\frac{1}{2}\frac{d}{\lambda_0}}{\sqrt{3}\frac{d}{e}+\frac{1}{\epsilon_{q0}}}, & \mathrm{TM}_{\binom{S}{A},mnq} \end{cases}, \tag{5.23}$$

where $(u_{n0}, v_{n0}) = (1, 2)$ for TE modes with $n \neq 0$, whereas $(u_{00}, v_{00}) = (\frac{2}{3}, \frac{5}{3})$ for TE modes with $n = 0$.

In order to compute a universal Q-chart valid for any equilateral triangular resonator, (5.23) is rewritten in terms of the aspect ratio $r = e/d$ and $\overline{k_{cp}} = k_{cp} \cdot e$ (recall equation (2.8)):

$$F^{\mathrm{TE}}_{\binom{S}{A},mnq}(r) = Q^{\mathrm{TE}} \cdot \frac{\delta_s}{\lambda_0} = \frac{\frac{1}{4\pi^3 q^2} \cdot \left(\sqrt{\left(\overline{k_c}/r\right)^2 + \left(q\pi\right)^2}\right)^3}{\left(u_{n0} + v_{n0}\frac{(\overline{k_c}/r)^2}{q^2\pi^2}\right)\frac{\sqrt{3}}{r} + 1}, \tag{5.24}$$

$$F^{\mathrm{TM}}_{\binom{S}{A},mnq}(r) = Q^{\mathrm{TM}} \cdot \frac{\delta_s}{\lambda_0} = \frac{\frac{1}{4\pi} \cdot \sqrt{\left(\overline{k_c}/r\right)^2 + \left(q\pi\right)^2}}{\frac{\sqrt{3}}{r} + \frac{1}{\epsilon_{q0}}}. \tag{5.25}$$

The analytical closed-form expressions presented in (5.23), or its normalized version in (5.24) and (5.25), are the counterpart of the expressions found in [18], [43] for the rectangular and circular cavities. To conclude this Section they are now validated with commercial software. Table 5.3 gathers the results obtained for an equilateral triangular cavity of side $e = 28$ mm and length $d = 4e$ ("long" cavity), $2e$ ("normal" cavity) , $e/2$ ("short" cavity).

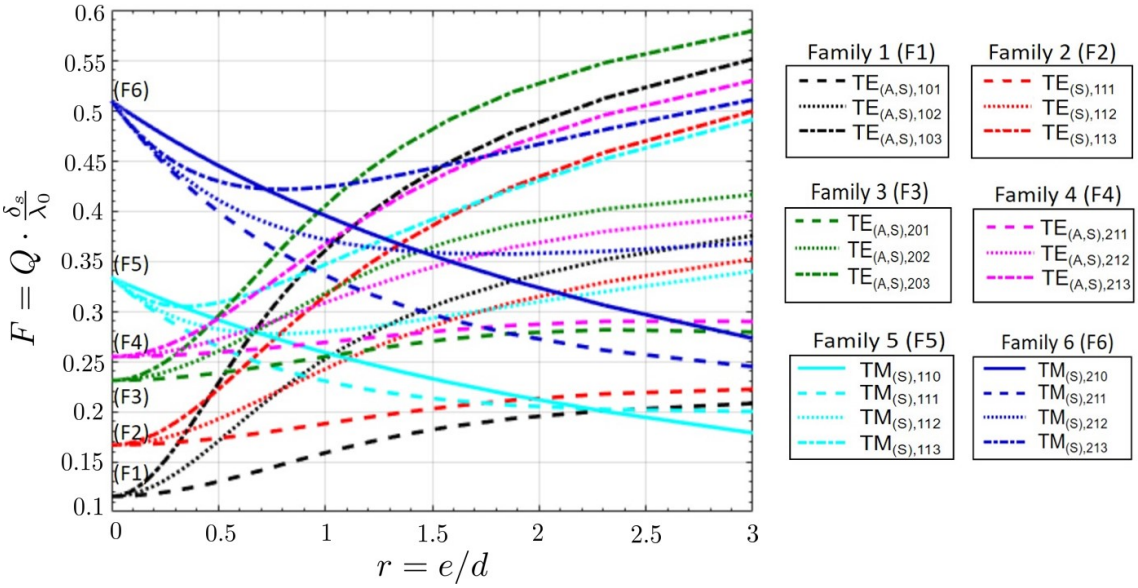

Figure 5.6: Universal chart for the normalized unloaded Q-factor for the first resonant modes in an equilateral triangular cavity, only dependent on the mode type and the aspect ratio of the cavity.

Cavity length $d = 56$ mm						
	Analytical Closed-forms		**CST**		**HFSS**	
	f_0 [GHz]	**Q-factor**	**f_0 [GHz]**	**Q-factor**	**f_0 [GHz]**	**Q-factor**
$TE_{A,101}$	7.6233	6763	7.6232	6759	7.6228	6762
$TE_{S,101}$			7.6232	6759	7.6229	6762
$TE_{A,102}$	8.9224	8190	8.9223	8185	8.9222	8188
$TE_{S,102}$			8.9223	8185	8.9223	8188
$TE_{A,103}$	10.7440	9988	10.7439	9980	10.7445	9980
$TE_{S,103}$			10.7439	9980	10.7449	9980
$TM_{S,110}$	12.3632	11884	12.3632	11858	12.3641	11868
$TM_{S,111}$	12.6497	10675	12.6496	10653	12.6511	10659
$TE_{S,111}$	12.6497	6989	12.6496	6978	12.6509	6985
$TE_{A,104}$	12.8681	11816	12.8680	11804	12.8702	11795
$TE_{S,104}$			12.8680	11803	12.8709	11800
$TM_{S,112}$	13.4725	11016	13.4725	10993	13.4747	11000
$TE_{S,112}$	13.4725	7521	13.4725	7508	13.4756	7512
$TE_{A,201}$	14.5246	8974	14.5246	8950	14.5266	8966
$TE_{S,201}$			14.5246	8953	14.5279	8968
$TM_{S,113}$	14.7422	11524	14.7422	11496	14.7460	11506
$TE_{S,113}$	14.7422	8301	14.7422	8287	14.7469	8286
$TE_{A,105}$	15.1681	13536	15.1680	13536	15.1730	13488
$TE_{S,105}$			15.1680	13515	15.1768	13505
Cavity length $d = 14$ mm						
$TM_{S,110}$	12.3632	8622	12.3632	8607	12.3626	8620
$TE_{A,101}$	12.8681	7822	12.8680	7811	12.8674	7821
$TE_{S,101}$			12.8680	7811	12.8673	7821
$TM_{S,111}$	16.3550	7259	16.3550	7240	16.3545	7258
$TE_{S,111}$	16.3550	7570	16.3550	7558	16.3541	7569
$TE_{A,201}$	17.8447	9486	17.8448	9462	17.8445	9481
$TE_{S,201}$			17.8448	9465	17.8441	9484
Cavity length $d = 112$ mm						
$TE_{A,101}$	7.2623	6365	7.2623	6360	7.2618	6364
$TE_{S,101}$			7.2623	6361	7.2619	6364
$TE_{A,102}$	7.6233	6840	7.6232	6836	7.6228	6839
$TE_{S,102}$			7.6232	6836	7.6230	6839
$TE_{A,103}$	8.1897	7576	8.1896	7571	8.1893	7575
$TE_{S,103}$			8.1896	7571	8.1895	7574
$TE_{A,104}$	8.9223	8504	8.9224	8498	8.9221	8501
$TE_{S,104}$			8.9223	8498	8.9224	8500

Table 5.3: Unloaded Q-factor for the first resonant modes in an equilateral triangular cavity with side $e = 28\,\text{mm}$, conductivity $\sigma = 58\,\text{MS/m}$ (copper) and different cavity lengths.

A good agreement between the numerical results of CST Microwave Studio and Ansys HFSS with those obtained by the analytical expressions is achieved. Once the derived expressions have been checked, the universal Q-chart is shown in Figure 5.6 for the first resonant modes of the equilateral triangular resonator.

5.3 Guidelines for the parabolic resonator

This Section is devoted to the analysis of the modal spectra of the parabolic resonator, which is the other unconventional geometry addressed in this Thesis. Compared to the equilateral triangular resonator, the computation of the core parameters for filter design is more intricate. As it has been shown in Chapter 3, the cut-off wavenumbers are not found by closed-form expressions but from the resolution of four non-linear bivariate systems of equations. Besides, the symmetric contour is the one that has mainly attracted the attention in the literature. For these reasons the generation of a mode chart where the first cut-off wavenumbers are shown as a function of the aspect ratio deserves special attention. Once this mode chart is given, the parabolic resonator can be conveniently studied, as it will be remarked at the end of this Section.

In first place a suitable definition of the aspect ratio must be chosen. This ratio must provide the relationship between the degrees of freedom that the parabolic cross-section presents, that is, the relationship between u_0 and v_0 from a given contour. However, the use of the direct relation between parameters u_0 and v_0 as a ratio, such as u_0/v_0 or v_0/u_0, does not give a clear idea of how the parabolic cross-section is. Since we are more used to other types of coordinates, such as the cartesian ones, in this Thesis it has been considered convenient to define the aspect ratio r of the parabolic cylinder waveguide in terms of the equivalent rectangular enclosing waveguide.

Figure 5.7 shows an arbitrary parabolic cross-section made up of the intersection between the curves $u = u_0$ and $v = v_0$. A rectangular contour of height b and width w surrounding the theoretical parabolic waveguide is also plotted. For a ratio definition of $r = b/w$, its relationship with the pair of values (u_0, v_0) is obtained from the coordinates x_1, x_2, y_1 and y_2. On the one hand, point x_1 is placed on the negative x-semiaxis, as it is shown in Figure 5.7, where $u = 0$ according to Figure 5.7 . Thus, the $v = v_0$ curve crosses the negative x-semiaxis in $x_1 = \frac{1}{2}(u^2 - v_0^2)\big|_{u=0} = -\frac{v_0^2}{2}$ according to (3.1). Likewise, the point x_2 is placed on the positive x-semiaxis, where $v = 0$ and thus for the $u = u_0$ curve the point x_2 is $x_2 = \frac{1}{2}(u_0^2 - v^2)\big|_{v=0} = \frac{u_0^2}{2}$. Therefore, the width of the equivalent rectangular waveguide is:

$$w = x_2 - x_1 = \frac{1}{2}(u_0^2 + v_0^2). \tag{5.26}$$

Regarding the height b of the rectangular enclosing cross-section, due to symmetry only one of the points y_1 or y_2 of Figure 5.7 is needed ($y_1 = -y_2$). Point y_2 satisfies $y_2 = \frac{b}{2}$, and at the same it is the intersection between curves $(u = u_0, v = v_0)$. Thus, according to (3.2) $y_2 = u_0 v_0 = \frac{b}{2}$ and therefore the height b is defined in terms of u_0 and v_0 as:

$$b = 2u_0 v_0. \tag{5.27}$$

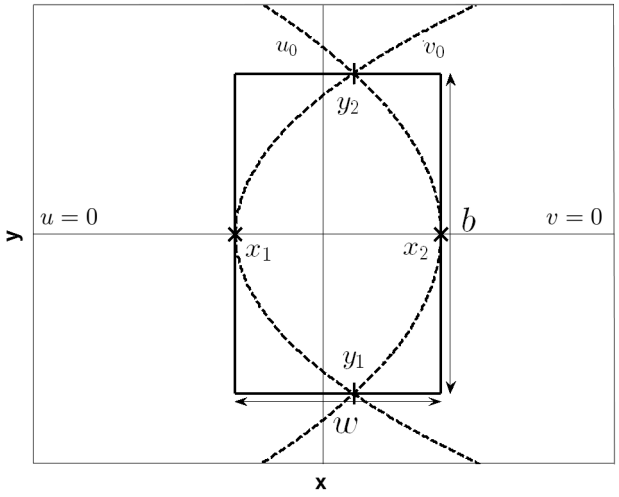

Figure 5.7: Equivalent enclosing rectangular waveguide for the definition of the aspect ratio $r = b/w$ in the parabolic cylinder waveguide.

The parabolic cylinder coordinates (u_0, v_0) written in terms of the ratio r can be obtained replacing $u_0 = \frac{b}{2v_0}$ from (5.27) into (5.26) leading to the biquadratic equation $v_0^4 - 2wv_0^2 + b^2/4 = 0$, whose solution for this problem is:

$$v_0 = \sqrt{w + \sqrt{w^2 - \frac{b^2}{4}}}. \tag{5.28}$$

Now (5.28) is reorganized in terms of the r factor as:

$$v_0 = \sqrt{w}\sqrt{1 + \sqrt{1 - \frac{(b/w)^2}{4}}} = \sqrt{w}\sqrt{1 + \sqrt{1 - \frac{r^2}{4}}}, \tag{5.29}$$

and u_0 accordingly as:

$$u_0 = \frac{b}{2v_0} = \sqrt{w}\frac{\sqrt{b/w}\sqrt{b/w}}{2\sqrt{1 + \sqrt{1 - \frac{(b/w)^2}{4}}}} = \sqrt{w}\frac{r}{2\sqrt{1 + \sqrt{1 - \frac{r^2}{4}}}}. \tag{5.30}$$

With the defined parameter $r = b/w$ as the aspect ratio of any parabolic cross-section the sought mode chart for the TE and TM modes of the parabolic waveguide can be conveniently plotted. Figure 5.8 shows the normalized cut-off wavenumbers of the first modes multiplied by the aforementioned width w for different aspect ratios r. The variation of r is carried out for the range $0 < r \leq 2$, since this parametric study leads to the same (flipped) parabolic contours once larger values are used. As it can be seen, with this representation the symmetric contour is a particular case within a continuous spectra of ratios where $r = 2$. In this Figure each mode labelled as "1" is the first of its family, "2" is the second, and so on regardless of its pattern (since the mode pattern will change at certain points as it can be seen in Fig. 5.7).

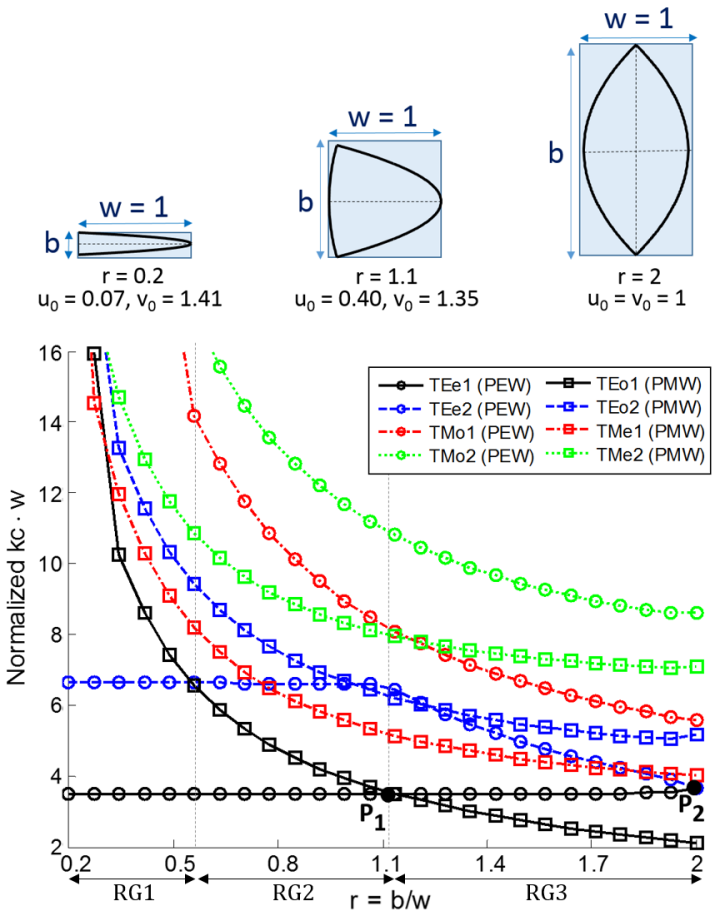

Figure 5.8: Variation of the cut-off wavenumber with the aspect ratio of the parabolic cylinder waveguide, for the first two modes per mode family. The symmetry of each mode with respect to the x-axis of the parabolic waveguide is shown in the legend.

According to the two first modes, which are in principle more likely to be the ones chosen for filter design, Figure 5.8 can be divided into three regions RG:

RG1: The first region, where the aspect ratio is $r < 0.5$, presents a constant fractional monomode bandwidth of $B_{\text{frac}} = 2(w \cdot k_{c2} - w \cdot k_{c1})/(w \cdot k_{c2} + w \cdot k_{c1}) = 2(k_{c2} - k_{c1})/(k_{c2} + k_{c1}) \approx 0.622$, where $w \cdot k_{c1} = 3.49$ and $w \cdot k_{c2} = 6.65$ belong to the first and second propagating even TE modes according to the legend (TE_{e1} and TE_{e2} with PEW symmetry respectively).

RG2: In the second region, where $0.5 < r < 1.1$, the first even TE mode (the TE_{e1}) is still the fundamental mode, but the first higher order mode has changed to an odd TE mode (the TE_{o1}), which has a PMW symmetry instead. In this region the fractional monomode bandwidth decreases from $B_{\text{frac}} \approx 0.622$ at $r = 0.5$ to $B_{\text{frac}} = 0$ at $r = 1.1$. This latter point is marked as P_1 in Figure 5.8, and in fact it is a point of interest since the two modes are degenerate with $w \cdot k_{c1} = w \cdot k_{c2} = 3.48$ and could be used to implement a dual-mode filer.

RG3: Finally the ratio r adopts values $1.1 < r < 2$ in the third and last region. Within these ratios the fundamental mode (TE_{o1}) and the first higher order mode (TE_{e1}) are exchanged with respect to the second region. B_{frac} can be redefined considering the TE_{o1} mode as the fundamental mode in this region and, taking this observation into account, it can be seen that it increases gradually with a maximum of $B_{\mathrm{frac}} = 0.531$ reached for $r = 2$. At this ratio it can be seen point $P2$, where $w \cdot k_c = 3.64$ and again two pairs of modes are degenerate (the first and second TE even modes, TE_{e1} and TE_{e2} respectively, none of them are the fundamental ones in this case).

In order to use Figure 5.8 to obtain the cut-off wavenumbers of a particular parabolic cross-section one must proceed in the following way. For a given aspect ratio r_i the point that belongs to one of the modal curves in Figure 5.8 has a value in the ordinate axis $y_i = k_c \cdot w$, where y_i is the corresponding coordinate in the ordinate axis and k_c stands for the normalized cut-off wavenumber (normalized in terms of units as it was mentioned in Chapter 3). Therefore, the cut-off wavenumber related to the cut-off frequencies of the waveguide as $f_c = k_c/(2\pi)$ is obtained as $k_c = y_i/w$, where w is the particular width of the theoretical enclosing rectangular waveguide. Two examples relating the validation cases of Chapter 3 with the practical mode chart presented in this Section are given:

(i) For the parabolic contour $u_0 = 0.8$ and $v_0 = 1$, the surrounding rectangular contour has $w = 0.5 \cdot (0.8^2 + 1^2) = 0.82$ and $b = 2 \cdot 0.8 \cdot 1 = 1.6$ according to (5.26) and (5.27). Therefore $r = b/w = 1.6/0.82 = 1.95$. The corresponding value of the fundamental mode in the ordinate axis is $k_c \cdot w = 2.1647$, and thus the cut-off wavenumber is finally $k_c = 2.1647/0.82 = 2.6399$, which is the same value as the one that can be found in Table 3.2 on page 46.

(ii) For the parabolic contour $u_0 = 0.15$ and $v_0 = 5$, the surrounding rectangular contour has a width of $w = 0.5 \cdot (0.15^2 + 0.5^2) = 0.1362$ and a height of $b = 2 \cdot 0.15 \cdot 0.5 = 0.15$. Therefore the aspect ratio is $r = b/w = 0.15/0.1362 = 1.1$. For such aspect ratio the fundamental mode has a value of $k_c \cdot w = 3.4834$, and thus the cut-off wavenumber is finally $k_c = 3.4834/0.1362 = 25.5757$, which is the same value as the one that can be found in Table 3.3 on page 46.

The derivation of a resonant chart for the parabolic cylinder resonator is not as direct as in the equilateral triangular one. However, Figure 5.8 can also be used to analyze the free-spurious window as it was done in the previous Section since, for a given cavity length d, the resonant frequency f_{res} is defined as $f_{\mathrm{res}} = \frac{c}{2\pi}\sqrt{k_c^2 + (\frac{q\pi}{d})^2}$, where q is the number of resonance ($q \geq 0$ for TM modes and $q > 0$ for TE modes). Section 5.4.3 will provide a practical example of design.

Finally, the quality factor in the parabolic cylinder waveguide can be obtained from any numerical commercial software such as CST MWS or HFSS. A Q-chart is not derived in this Section since the associated integrals (5.18) and (5.19) are not analytical in this kind of waveguide.

5.4 Designs

In this Section some designs based on the presented unconventional geometries addressed in this Thesis are presented. The purpose of this Section is to validate the CAD tools developed in Chapters 2 and 3 and at the same time to present this geometries as innovative candidates in the design of passive devices. In particular the guidelines given in this Chapter for their application to filter design are followed, and three different prototypes have been successfully designed. The most ambitious of them made up of dual-mode cavities has been also manufactured.

5.4.1 Inline equilateral triangular filter

An inline equilateral triangular filter of 7-th order of 25 dB of return loss and 2% of relative bandwidth at $f_0 = 25$ GHz (*i.e.*, 500 MHz) is designed. The TE^{A}_{101} mode is selected as the resonant mode, and therefore for a waveguide side of $e = 1$ cm the corresponding cavity length would be, without the loading effect of the irises, $d = \frac{\lambda_g}{2} = \frac{1}{2}\lambda_0/\sqrt{1-(\frac{f_c}{f_0})^2} = 0.9981$ cm. The normalized coupling matrix for this design based on the well-known Chebychev response is [5]: $\mathrm{M}_{S1} = \mathrm{M}_{7L} = 1.0938$, $\mathrm{M}_{12} = \mathrm{M}_{67} = 0.9220$, $\mathrm{M}_{23} = \mathrm{M}_{56} = 0.6311$, $\mathrm{M}_{34} = \mathrm{M}_{45} = 0.5852$.

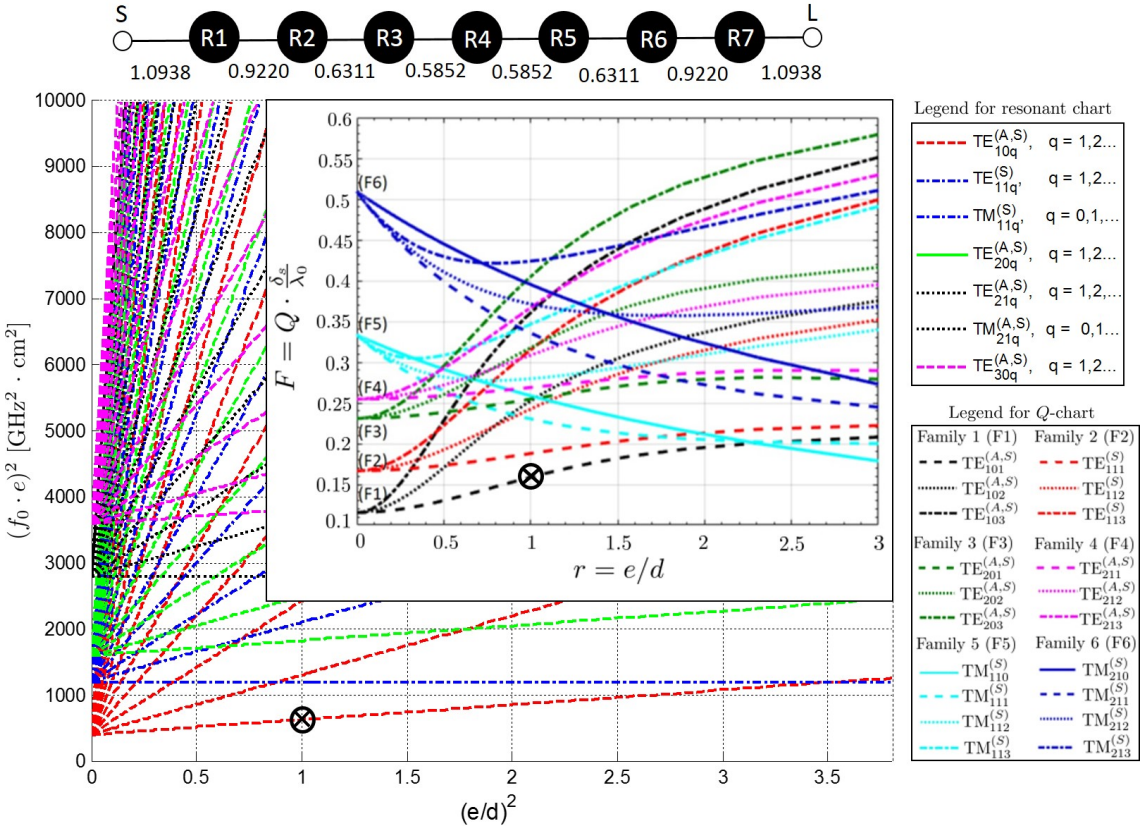

Figure 5.9: Design point (black circle with cross inside) for an all-pole equilateral triangular filter based on the TE^{A}_{101} mode.

Thus, the selected design point in terms of the spurious-free window and the unloaded Q-factor is shown in Figure 5.9 and its inset, where $(\frac{e}{d})^2 = 1.003$ and $\frac{e}{d} = 1.0019$ respectively. The same figure above shows the topology with the corresponding coupling scheme. The 3D filter structure is given in Figure 5.10a). Figure 5.10b) evidences that the resonant mode is the TE^A_{101} mode. The final dimensions can be found in Figure 5.10c) and its associated caption. The narrowband response is presented in Figure 5.10d), where the electromagnetic (EM) and circuital (circ.) responses have been drawn together showing very good agreement. Finally the wideband response is presented in Figure 5.10e). According to the chart of mode resonances the next spurious would be the TE^A_{102} resonance at $f_{\mathrm{res}} = 34.6$ GHz. This quantity can slightly vary due to the loading effect of the irises. It is important to notice that neither the TE^S_{101} mode nor the TE^S_{102} are present since it is assumed that the filter will operate under PMW symmetry. If the unloaded Q-factor is denormalized for the selected fundamental mode and a conductivity of $\sigma = 5.8 \cdot 10^7$ S/m (corresponding to copper) a value of $Q_u = 4561.9$ is achieved.

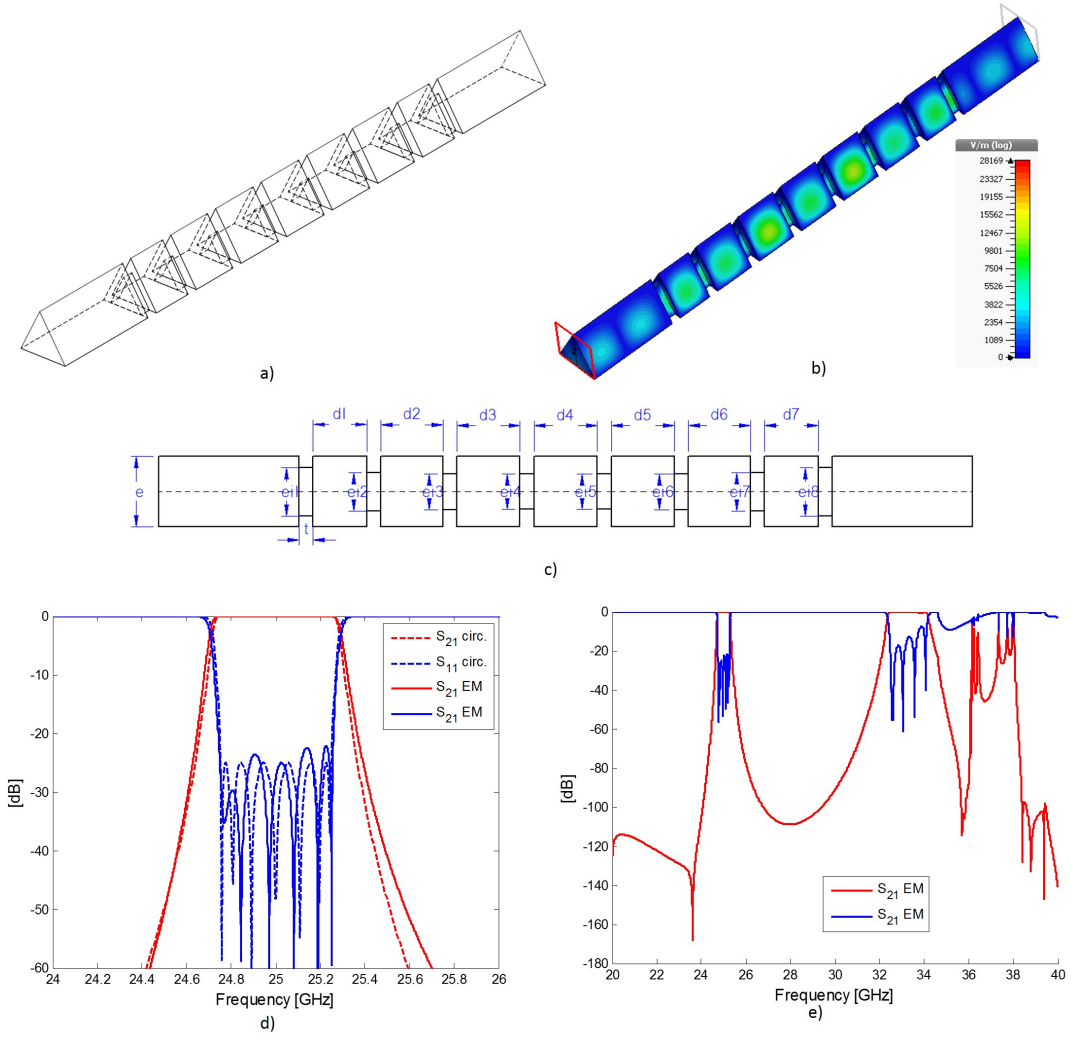

Figure 5.10: Equilateral triangular inline filter. a) Perspective view. b) Absolute value of the electric field pattern of the TE^A_{101} mode. c) Top view with dimensions (in cm): $e = 1$, $e_{i1} = e_{i8} = 0.6886$, $e_{i2} = e_{i7} = 0.5453$, $e_{i3} = e_{i6} = 0.5085$, $e_{i4} = e_{i5} = 0.5011$, $t = 0.2$, $d_1 = d_7 = 0.7672$, $d_2 = d_6 = 0.8817$, $d_3 = d_5 = 0.8999$, and $d_4 = 0.9027$. d) Narrowband response. e) Wideband response.

5.4.2 Dual mode equilateral triangular filter

Dual-mode filters are used when the specifications demand high selectivity and at the same time a reduced volume is required. In particular, this is a typical scenario in satellite communications. The operating principle of this kind of filters is based on the use of two degenerated resonant modes per cavity. Thus, each cavity provides two resonators in the equivalent filter circuit. In such scheme half of the resonators is needed to guarantee the same selectivity, and besides, cross-couplings can be easily implemented by breaking the orthogonality between the resonant modes.

Section 5.2 showed that mode degeneracy is the inherent property of the equilateral triangular resonator. In this section this property is exploited and a dual-mode prototype is designed, manufactured and measured. The prototype proposed as a proof of concept is centered at 11.8 GHz with a fractional bandwidth of 0.85% (*i.e.*, 100 MHz) with 20 dB of return loss. Following the design in [112], the normalized coupling matrix is: $M_{S1} = M_{4L} = 1.0349$, $M_{12} = M_{34} = 0.8038$, $M_{14} = -0.4270$. In this case the $\mathrm{TE}^{(A)}_{103}$ mode will implement the first and fourth resonators, whereas the $\mathrm{TE}^{(S)}_{103}$ will implement the second and third resonators (R_1 and R_2 in the first cavity and R_3 and R_4 in the second cavity). This scheme is shown in Figure 5.11 above.

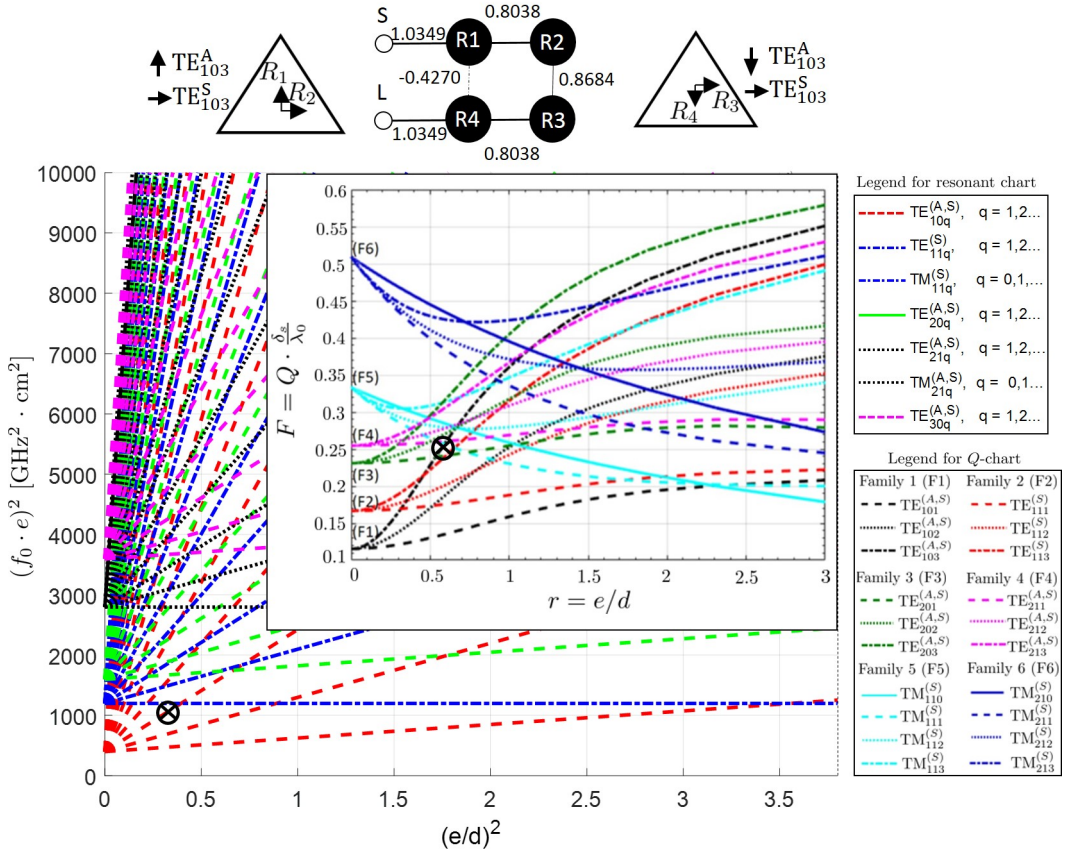

Figure 5.11: Design point (black cross) for a dual mode equilateral triangular filter based on the TE^{A}_{103} mode.

The selected side for the proposed dual-mode prototype is $e = 28$ mm, and since the third resonance is used the cavity lengths are around $d = \frac{3\lambda_g}{2} = 47.858$ mm. The chart of resonant frequencies of Figure 5.11 shows the corresponding design point $(\frac{e}{d})^2 = 0.3423$ at the the $\mathrm{TE}_{103}^{A/S}$ modes. According to this value the first higher resonance is theoretically present at 12.36 GHz and belongs the TM_{110}^{S} resonance, while the lower one is placed at 9.49 GHz and belongs to the $\mathrm{TE}_{102}^{A/S}$ resonances. The Q_u chart present in the inset of the same Figure also shows the associated design point $\frac{e}{d} = 0.5851$. If the associated value is denormalized for a cavity working at the $\mathrm{TE}_{103}^{A/S}$ modes and made up of $\sigma = 5.8 \cdot 10^7 S/m$, the unloaded quality factor is of $Q_u = 10660$ per mode.

Figure 5.12a) shows several views of the prototype with the associated dimensions given in the caption. The stanard WR-75 waveguides are coupled to the equilateral triangular cavities with normalized M_{S1} and M_{4L} values respectively throughout rectangular irises of width a_1 and height b_1. The input waveguide only excites the TE_{103}^{A} mode because it has the same symmetry as the TE_{10} mode that is propagating along the rectangular waveguide (PMW).

The TE_{103}^{S} mode is generated with a discontinuity that breaks the symmetry in the middle of both cavities and implements couplings M_{12} and M_{34}. This discontinuity is made up of an equilateral triangle of side e_g, which means that the whole filter structure is completely analytic and can be efficiently simulated by the Mode-Matching method of Chapter 2. Finally the inter-cavity couplings M_{14} and M_{23} are implemented by a rectangular iris of width a_2 and height b_2 placed in between. It is important to notice that the equilateral triangular section of the discontinuity in the first cavity is shifted in the opposite direction to the one in the second cavity in order to implement the negative sign of the coupling M_{14}.

The simulated narrowband results are given in Figure 5.12b) compared to the ideal circuital ones associated to the selected coupling matrix. The electromagnetic simulation has been carried out using two different techniques: one purely numerical using the HFSS commercial software (FEM), and the other one analytical using the Mode-Matching (MM) formulation presented in Chapter 2. The good agreement between results constitutes again a validation of the software developed in this Thesis. The wideband response is provided in Figure 5.12c) and has been obtained with the Mode-Matching technique for efficiency reasons (the inner-cross products which constitute the core computation do not depend on frequency).

The theoretical first higher spurious resonance due to the TM_{110} mode is just slightly excited and the spurious-free window is enlargened up to 14 GHz. Figure 5.12d) shows photographs of the manufactured prototype and the measurement set-up.

In the manufactured prototype the two equilateral triangular discontinuities of side e_g have been replaced by three screws in the middle of each face to enable tuning to correct the tolerances to which a waveguide filter at the Ku band is usually subjected. The filter is manufactured in aluminium ($\sigma = 3.8 \cdot 10^7 S/m$), but the insertion losses of the measurement are poorer for this material as it can be seen in Figure 5.12e), where $|S_{21}| = -1.085$ dB. The response has been also slightly shifted from the desired 11.8 GHz to 11.768 GHz (a total shift of 32 MHz). The measured wideband response is given in Figure 5.12f).

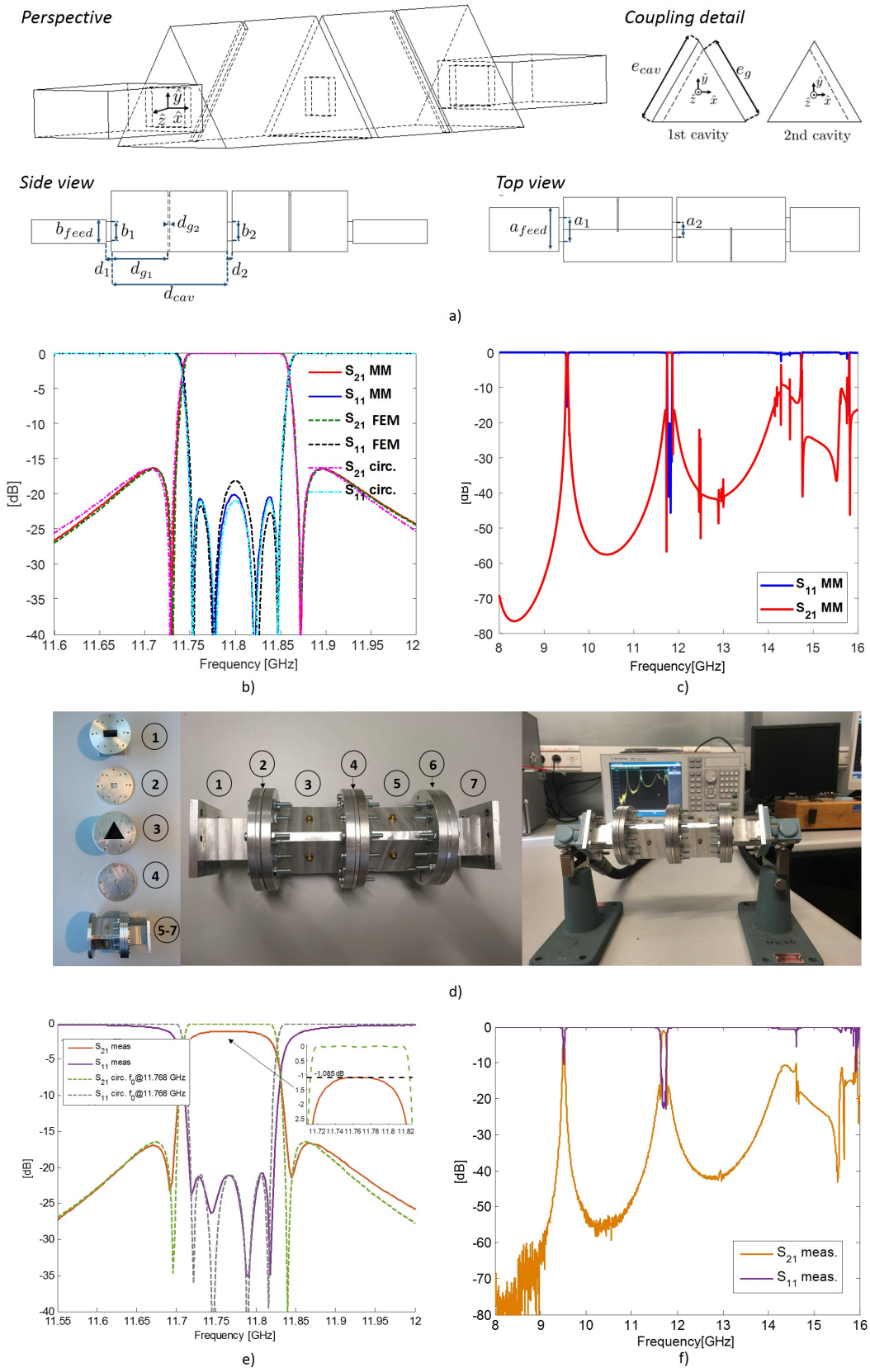

Figure 5.12: Equilateral triangular dual mode filter. a) Views with dimensions (in mm): $a_{\text{feed}} = 19.05$, $b_{\text{feed}} = 9.525$, $a_1 = 10$, $a_2 = 6.12$, $b_1 = 7.90$, $b_2 = 7.65$, $d_{\text{cav}} = 46.53$, $d_{g1} = 22.86$, $d_{g2} = 0.80$, $e_{\text{cav}} = 28$, $e_g = 26.23$. b) Simulated narrowband responses (MM, FEM) together with the ideal response (circ.). c) Simulated wideband response (MM). d) Photographs of the manufactured prototype and the measurement set-up. e) Measured response together with the ideal response shifted to 11.768 GHz. f) Measured wideband response.

5.4.3 Asymmetrical parabolic inline filter

Charts of resonant frequencies are useful in filter design since one mode with lower cut-off frequency can resonate before or after another one with higher cut-off frequency once the one with higher cut-off frequency starts to propagate. This depends on the number of variations q along the longitudinal dimensions of the cavity for a given physical length d. However, if the resonant mode with lowest k_c and the lowest number of variations q is chosen to implement the desired response of the filter, then the chart of Figure 5.8 suffices to analyze the spurious free-window.

A parabolic filter of order $N = 9$ has been designed with $f_0 = 20$ GHz, 20 dB of return loss and a fractional bandwidth of 4% (800 MHz). The classical all-pole response is pursued, and therefore the inline topology has been selected. This filter will have a symmetry plane at $y = 0$ and will be excited by the TE_{10} mode of a waveguide. Thus only the modes of Figure 5.8 with PEW symmetry will be present. Such modes are depicted in Figure 5.13, where the coupling scheme together with the corresponding normalized values are shown as well. In particular, the first resonance of the TE_{e1} mode of Figure 5.13 is chosen to implement the desired response, that is, the $\mathrm{TE}_{e1,q=1}$ mode.

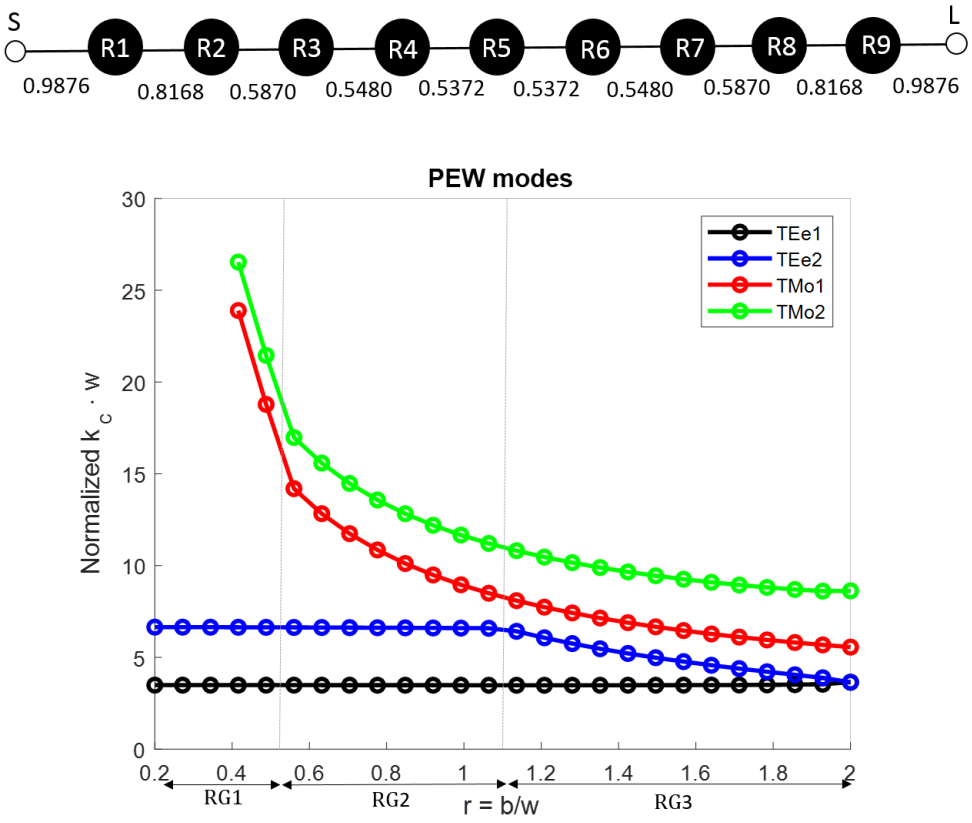

Figure 5.13: Variation of the cut-off wavenumber with the aspect ratio of the parabolic cylinder waveguide, for the first modes of PEW symmetry with respect to the x-axis of the parabolic waveguide. Above: coupling topology with normalized coupling values.

The choice of the aspect ratio r for this design depends on two factors: the realizability and the spurious-free window. In first place, for a given cut-off frequency $f_c < f_0$ ($f_c < 20$ GHz) and a chosen ratio r_i, the dimensions w and b are fixed since $w = y_i/k_c$ and

$b = r_i \cdot w$, where y_i is the ordinate value of the modal curve chosen as fundamental (in this design the first resonance of the structure).

The question now is what mode is the fundamental one in Figure 5.13 along all the possible aspect ratios r. In principle the mode that provides the first resonance would be the one with lowest k_c and lowest q. Thus the lowest line of Figure 5.13 is a good candidate to provide the first resonant frequency $f_{\mathrm{r1}} = \sqrt{A_1^2 + B_1^2}$, where $A_1 = f_{\mathrm{c1}}$ and $B_1 = \frac{q_1 c}{2d_1}$ with $q_1 = 1$. With this selection, $d_1 = \lambda_{g,1}/2$.

Indeed, for a given cut-off frequency f_c and a chosen aspect ratio r any curve placed above the lowest one in Figure 5.13 leads to a higher resonant frequency $f_{\mathrm{r2}} = \sqrt{A_2^2 + B_2^2}$ if it belongs to a TE mode since, for a chosen physical length $d = d_1$. This can be easily deduced since $B_2 > B_1$ for the minimum variation $q_2 = 1$; and $A_2 > A_1$ as $k_{c2} = y_2/w$, where $y_2 > y_1$ as the curve is placed above and w has been fixed as it was mentioned two paragraphs ago.

However, if the curve above belongs to a TM mode it can resonate first since for this mode family the value $q = 0$ is allowed. In fact, if we refer to f_{r3} as the resonant frequency associated to the curve of the mode $\mathrm{TM_{o1}}$, $f_{\mathrm{r3}} = \sqrt{A_3^2 + B_3^2}$, where $A_3 > A_1$ as $y_3 > y_1$ but $B_3 < B_1$ since for the same given cavity length $d = d_1$ it happens that $q_3 < q_1$ ($q_3 = 0$ and $q_1 = 1$). Hence, there can be some values where the $\mathrm{TM_{o1}}$ mode resonates first than the $\mathrm{TE_{e1}}$ mode. Regarding the next TM mode, the $\mathrm{TM_{o2}}$, it will present a higher resonant frequency than the $\mathrm{TM_{o1}}$ and therefore there is no need to consider it as a candidate for the fundamental mode ($A_4 > A_3$ and $B_4 = B_3 = 0$, with $f_{\mathrm{r4}} = \sqrt{A_4^2 + B_4^2}$) .

Bearing in mind the previous observations, the $\mathrm{TE_{e1}}$ with $q_1 = 1$ is selected as the fundamental mode for the filter structure, and therefore it will be checked that for the selected aspect ratio r and cut-off frequency f_c the $\mathrm{TM_{o1}}$ mode has a higher resonant frequency.

The choice of a suitable aspect ratio r follows the next reasoning:

(i) For a wider spurious-free window a wider space between curves is sought, since the next cut-off wavenumber $k_{\mathrm{c,1st\ sup}}$ will have a higher value. This is easy to prove since $k_{\mathrm{c,1st\ sup}} = y_{\mathrm{1st\ sup}}/w$, where w has been fixed once r has been selected ($w = y/k_c$, with y and k_c being the ordinate value and the cut-off wavenumber that belong to the fundamental mode).

(ii) According to (i), the ratios of regions RG1 and RG2 of Figure 5.13 should be preferred.

(iii) However, a trade-off between realizability and a wide spurious-free window is pursued. If two points of different ratios r_i, r_j are compared for the $\mathrm{TE_{e1}}$ mode, for the selected k_c the dimension w will be nearly the same for both cases since the ordinate value y remain more or less constant and hence $w_i = w_j = w = y/k_c$. However, the height b will be lower for the case of the lowest ratio r_i since $b_i = w \cdot r_i$, $b_j = w \cdot r_j$, with $r_i < r_j$, and the realizability turns out to be more complicated. This was already shown in Figure 5.8.

(iv) In order to take both factors (realizability and wide spurious-free window) into account a ratio on the left side of region RG3 is selected. In particular, the choice for this design is $r = 1.14$.

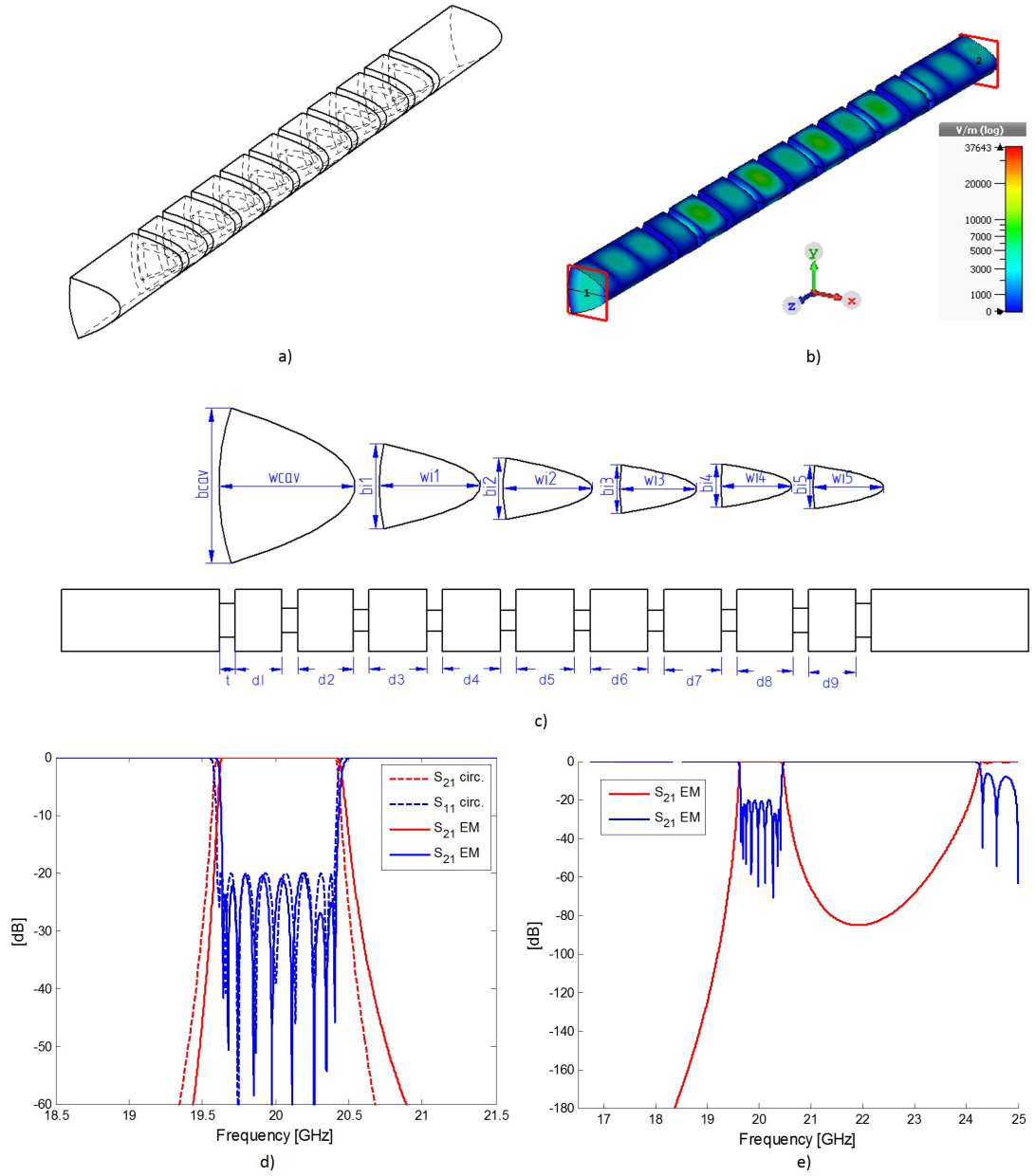

Figure 5.14: Asymmetric parabolic inline filter. a) Perspective view. b) Absolute value of the electric field pattern of the TE_{e1} mode with $q = 1$. c) Top view of the structure and front view of the separated contours of the cavity and the irises, with dimensions (in mm): $b_{\text{cav}} = 11.83$, $w_{\text{cav}} = 10.37$, $b_{i1} = b_{i10} = 6.45$, $w_{i1} = w_{i10} = 7.68$, $b_{i2} = b_{i9} = 4.69$, $w_{i2} = w_{i9} = 6.8$, $b_{i3} = b_{i8} = 4.1$, $w_{i3} = w_{i8} = 6.5$, $b_{i4} = b_{i7} = 3.95$, $w_{i4} = w_{i7} = 6.43$, $b_{i5} = b_{i6} = 3.91$, $w_{i5} = w_{i6} = 6.41$, $t = 3$, $d_1 = d_9 = 8.95$, $d_2 = d_8 = 10.57$, $d_3 = d_7 = 10.97$, $d_4 = d_6 = 11.06$ and $d_7 = 11.07$. d) Narrowband response. e) Wideband response.

Regarding the choice of the cut-off frequency f_c, it must be fulfilled that $f_c < 20$ GHz. For a desired aspect ratio r, a lower value of f_c leads to a larger value of w and b since $w = y/k_c$ and $b = r{\cdot}w$. Apart from having a larger cross-section, another implication is that the spurious-free window is reduced. This can be easily seen since $k_{\text{c,1st sup}} = y_{\text{1st sup}}/w$.

For this particular design a cut-off frequency $f_c = 16$ GHz has been chosen, which corresponds to $k_c = 335.33$ m^{-1} , $w = y/k_c = 10.36$ mm and $b = r \cdot w = 11.82$ mm.With the selected dimensions the $\mathrm{TM}_{o1,q=1}$ mode resonates at a higher frequency of around 36.8 GHz. On the other hand, the spurious-free window will be limited by the $\mathrm{TE}_{e2,q=1}$ mode with a resonant frequency of approximately 29.5 GHz.

The proposed prototype is shown in Figure 5.14a), where the fundamental resonating mode is the $\mathrm{TE}_{e1,q=1}$ and whose absolute value of the electric field is shown in Figure 5.14b). The dimensions of the structure are given in Figure 5.14c), with the specific values gathered in the caption. Figure 5.14d) shows the narrowband response obtained by the electromagnetic simulator (EM) compared to the ideal circuital response (circ.) obtained from the coupling values of Figure 5.13, while the wideband response of the filter is given in Figure 5.14e).

Finally the input and output waveguides of this prototype are changed to standard ones, in particular to WR-51 models, where the TE_{10} mode guarantees that only the modes with PEW symmetry are excited (to that end the whole symmetry of the filter is kept). The corresponding structure and response are given in Figure 5.15.

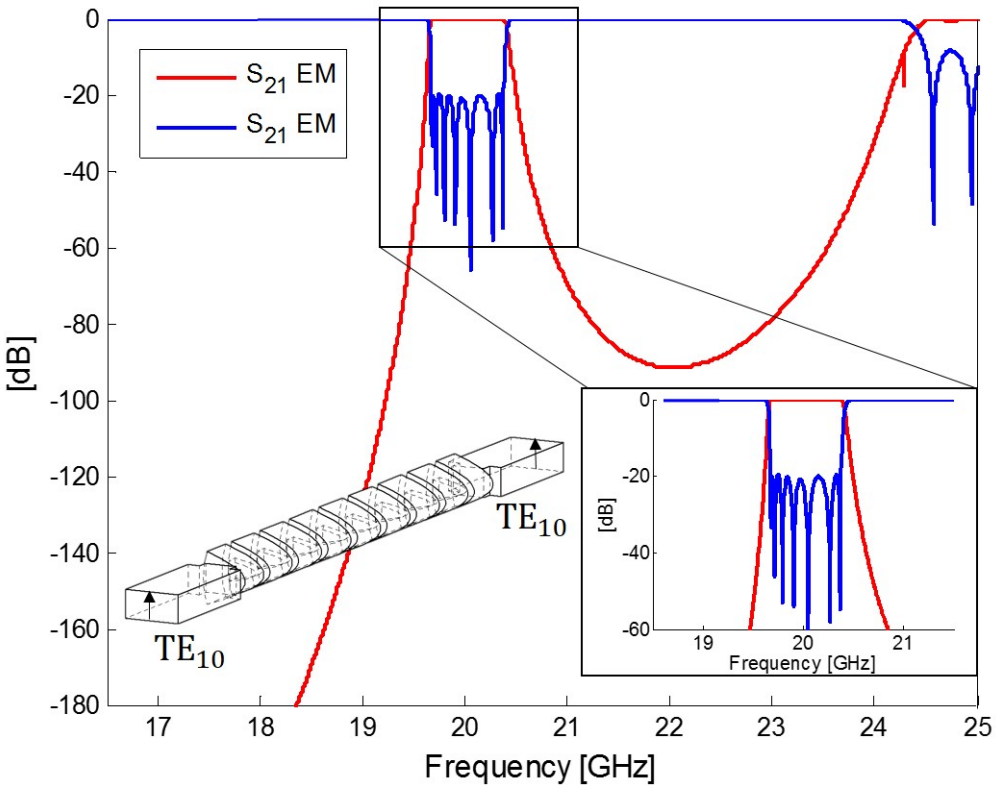

Figure 5.15: Structure and response of the asymmetric parabolic inline filter of Figure 5.14 fed with with standard WR51 working at the TE_{10} mode.

6 Contribution to the design of filters (Part II)

6.1 Introduction

In the previous Chapter the two unconventional geometries addressed in this Thesis were used for the design of novel inline filters. Two prototypes that implement the classical all-pole Chebychev response introduced the equilateral triangular and the asymmetric parabolic resonators as good candidates for filter design. Another prototype working in dual-mode operation was designed, manufactured and measured, providing an alternative to the classic TE_{113} dual-mode filters in circular cavities used in satellite communications. Filters working on dual-mode operation require half of the resonators to implement the same single-mode full-wave response, at the expense of an increased complexity in the design process. Other alternatives for size reduction will be discussed in this Chapter.

Compactness is a desired feature, specially in the space sector where larger filters raise the cost. In this context, the use of multiple resonant modes in a single cavity is only one of the possible strategies used for size reduction. Another possibility is to use dispersive couplings, irises of strong frequency-dependent behaviour that allow the generation of additional out-of-band transmission zeros [113–115]. Thus, the limit of the maximum number of achievable transmission zeros is overcome [116] and the stopband behaviour is enhanced without increasing the number of resonators. This is relevant at high frequency bands, as in W-band applications [72, 73], where obtaining resonators with high quality factors becomes a challenging task.

In this Thesis the dispersive behaviour of source to load couplings is studied in the well-known folded fully canonical filters made up of rectangular waveguides. Two designs exploiting this feature are presented, and several equivalent circuits are proposed for the generation of up to two additional transmission zeros. This part of the Chapter arises from the collaboration with the group Lehrstuhl für Hochfrequenztechnik from the Christian Albrechts University of Kiel in the context of a three-month research stays during the three-year PhD period. Finally, the last part of the Chapter is devoted to the improvement of compactness using dielectric resonator filters, which are well-known for the significant size reduction that they can offer compared to the empty waveguide technology. Very diverse shapes working in multi-mode schemes have been proposed in the literature to improve the achievable compactness [117–125]. However, to the best of the author's knowledge, the equilateral triangular dielectric resonator has not been reported yet in the context of microwave filters. In this Chapter several topologies are researched and a designed prototype is presented as a proof of concept showing very good results.

6.2 Dispersive couplings in well-known topologies

The coupling matrix is a useful design tool used for the synthesis of the desired responses in microwave filters [126]. In fact, one of the strengths of this tool is that it can be used regardless of the technology used (microstrip, waveguide, stripline, and so on). However, the coupling matrix model was initially conceived assuming frequency-invariant couplings, and thus it was only valid for the design of narrowband filters.

In the recent years couplings dependent on frequency have drawn the attention of filter designers to produce responses that a priori were not predictable by the narrowband classical model. This is the case of responses where additional transmission zeros allow to improve the selectivity without increasing the number of resonators. The integration of the so-called dispersive couplings into the coupling matrix theory was recently presented in [114]. The main advantage of the formulation proposed in [114] is that the synthesis method is generic for any user defined topology. However, only one extra transmission zero can be synthesized with the given procedure.

In [113] a simpler process was followed for the synthesis of the coupling matrix of trisections with a single dispersive coupling. The proposed synthesis procedure only affected one circuit element (*i.e.*, a single coupling), and the admittance matrix was directly used to determine the coupling coefficients. Again, the reported filter examples of order N provided up to $N+1$ transmission zeros. Besides, the mathematical condition associated to the generation of the transmission zeros was quite simple.

In this Section several equivalent circuit models for the generation of additional transmission zeros are researched. In particular, two of the three advantages presented in [113] are sought. In first place, the mathematical analysis must remain simple. Secondly, the dispersive behaviour must be associated to a single coupling structure to make the design process simpler than in any of the prototypes shown in [114], where several dependent couplings were needed. In particular, the dispersive structure considered in this Chapter will be the source to load coupling (referred as SL coupling later in the text), which is easy to be implemented in folded structures. The third advantage of [113], which is the possibility to synthesize the coupling matrix directly from the admittance matrix, is not exploited here.

Taking all these considerations into account, several equivalent circuits are proposed to replace the ideal (*i.e.*, frequency independent) source to load coupling of the traditional

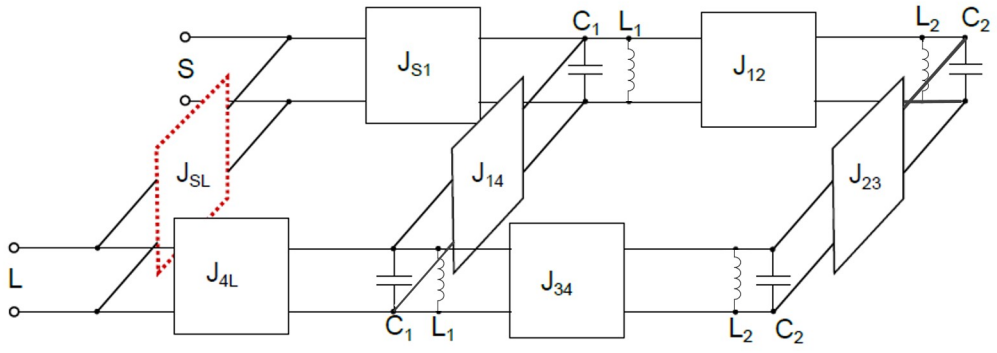

Figure 6.1: Discrete equivalent circuit for a band-pass folded network made up of ideal inverters.

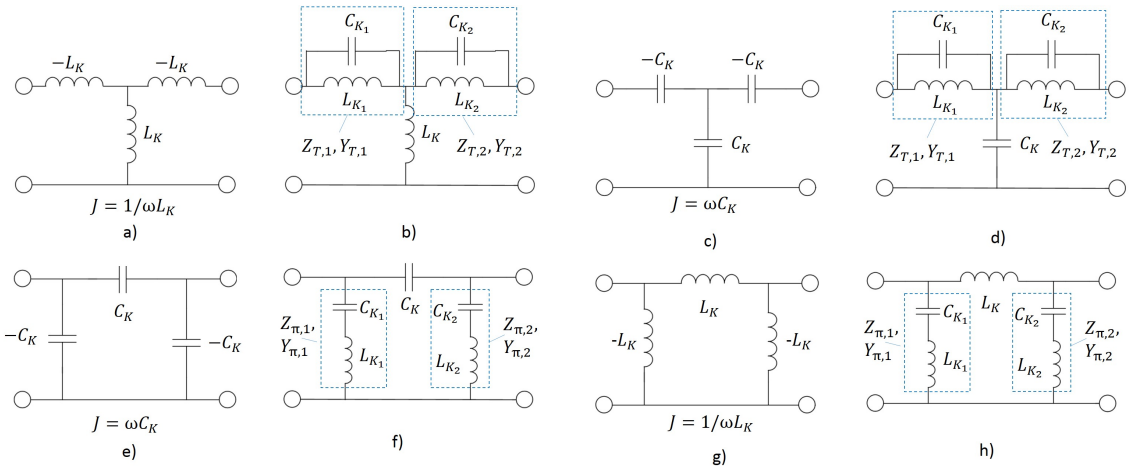

Figure 6.2: a), c), e) and g): Classic equivalent T- and Π-networks for inverters. b), d) f) and h): Proposed equivalent circuit models for the generation of up to two transmission zeros.

folded structure shown in Figure 6.1, which is directly related to the narrowband coupling matrix model. In particular, four equivalent circuits shown in Figure 6.2 are proposed, with which up to $N+2$ transmission zeros can be achieved, one extra apart from the one achievable in [114] and [113].

The choice of the equivalent circuit depends on the sign of the coupling value modelled by the ideal inverter J_{SL} of Figure 6.1. Furthermore, the out-of-band behaviour of the four proposed circuit models differs as it will be shown in the design examples of the next section.

I- Dispersive T-network developed from inductors

A typical T-network made up of inductors is shown in Figure 6.2a). The value of the inductor can be calculated as $L_k = \frac{1}{J_{\mathrm{SL}}\omega_0}$, where ω_0 is the angular central frequency of the filter. The proposed equivalent circuit for the generation of up to two additional transmission zeros is shown in Figure 6.2b), where each inductor placed on the series branches is replaced by a shunt resonator, giving rise to $Z_{T,1}$ and $Z_{T,2}$ respectively. Now, these series branches made up of shunt resonators must satisfy the following two conditions:

(i) At the central frequency ω_0 the circuit must behave as the ideal T-inverter, that is $Z_{T,1} = Z_{T,2} = -j\omega_0 L_k$. Thus, each shunt resonator must fulfill:

$$Y_{T,i} = \frac{1}{Z_{T,i}} = j(\omega_0 C_{K_i} - \frac{1}{\omega_0 L_{K_i}}) = j\frac{1}{\omega_0 L_K} \quad \text{with } i = 1, 2. \tag{6.1}$$

(ii) Each branch must behave as an open circuit at the frequency of one of the two possible transmission zeros (t_{z1},t_{z2}), so that the signal transmission between the source and load is prevented:

$$Y_{T,i} = \frac{1}{Z_{T,i}} = j(\omega_{tz_i} C_{K_i} - \frac{1}{\omega_{tz_i} L_{K_i}}) = 0 \quad \text{with } i = 1, 2. \tag{6.2}$$

This is equivalent to say that each branch resonates at the frequency of one of the two possible transmission zeros.

Now, from (6.1) and (6.2) it is derived that, on the one hand:

$$C_{K_i} = \frac{1}{\omega_0^2 L_{K_i}} + \frac{1}{\omega_0^2 L_K}, \tag{6.3}$$

and on the other hand:

$$C_{K_i} = \frac{1}{\omega_{tz_i}^2 L_{K_i}}, \tag{6.4}$$

for $i = 1, 2$ and $\omega_{tz_i}^2$ being the angular frequency where each transmission zero is located. If equation (6.4) is replaced in (6.3), the value of the inductors L_{K_1} and L_{K_2} can be found as:

$$L_{K_i} = L_K\big(\frac{\omega_0^2}{\omega_{tz_i}^2} - 1\big), \quad \text{for } i = 1, 2. \tag{6.5}$$

Then, from (6.4) and (6.5):

$$C_{K_i} = \frac{1}{L_K(\omega_0^2 - \omega_{tz_i}^2)}, \quad \text{for } i = 1, 2. \tag{6.6}$$

II- Dispersive T-network developed from capacitors

The next proposed circuit is based on the ideal T inverter shown in Figure 6.2c) and it is shown in Figure 6.2d), where the value of the capacitors can be computed as $C_K = \frac{J_{SL}}{\omega_0}$. Thus:

(i) At the central frequency ω_0 it holds:

$$Y_{T,i} = \frac{1}{Z_{T,i}} = j(\omega_0 C_{K_i} - \frac{1}{\omega_0 L_{K_i}}) = -j\omega_0 C_K \quad \text{with } i = 1, 2. \tag{6.7}$$

so that the circuit behaves as an ideal inverter.

(ii) At each transmission zero the condition is the same as in the previous circuit, each branch must behave as an open circuit and thus:

$$Y_{T,i} = \frac{1}{Z_{T,i}} = j(\omega_{tz_i} C_{K_i} - \frac{1}{\omega_{tz_i} L_{K_i}}) = 0 \quad \text{with } i = 1, 2. \tag{6.8}$$

From the first of the two above conditions it is deduced that:

$$C_{K_i} = -C_K + \frac{1}{\omega_0^2 L_{K_i}}, \quad \text{with } i = 1, 2. \tag{6.9}$$

and, on the other hand from the second condition the value of the inductors L_{K_i} is:

$$L_{K_i} = \frac{1}{\omega_{tz_i}^2 C_{K_i}}, \tag{6.10}$$

for $i = 1, 2$. Then, if (6.10) is replaced in (6.9), then the value of the capacitors C_{K_i} is found as:

$$C_{K_i} = C_K \frac{\omega_0^2}{\omega_{tz_i}^2 - \omega_0^2} \quad \text{for } i = 1, 2. \tag{6.11}$$

Finally, from (6.10) and (6.11):

$$L_{K_i} = \frac{\omega_{tz_i}^2 - \omega_0^2}{\omega_{tz_i}^2 \omega_0^2 C_K} \quad \text{for } i = 1, 2. \tag{6.12}$$

III- Dispersive π-network developed from capacitors

If the shunt branches of the π-network shown in Figure 6.2e) are replaced by series resonators as in Figure 6.2f), the following conditions must be satisfied taking into account that $C_K = \frac{J_{SL}}{\omega_0}$:

(i) Again, at the central frequency ω_0 the circuit must act as an the corresponding ideal inverter of Figure 6.2e):

$$Z_{\pi,i} = j\left(\omega_0 L_{K_i} - \frac{1}{\omega_0 C_{K_i}}\right) = \frac{j}{\omega_0 C_K} \quad \text{with } i = 1, 2. \tag{6.13}$$

(ii) On the other hand, in order to prevent the signal transmission between the source and load each branch must behave as a short circuit at the frequency of one of the two possible transmission zeros (t_{z1},t_{z2}):

$$Z_{\pi,i} = j\left(\omega_{tz_i} L_{K_i} - \frac{1}{\omega_{tz_i} C_{K_i}}\right) = 0 \quad \text{with } i = 1, 2. \tag{6.14}$$

Hence, from (6.13) and (6.14) it can be deduced that:

$$L_{K_i} = \frac{1}{\omega_0^2 C_{K_i}}, + \frac{1}{\omega_0^2 C_K}, \tag{6.15}$$

$$L_{K_i} = \frac{1}{\omega_{tz_i}^2 C_{K_i}}, \tag{6.16}$$

for $i = 1, 2$. Then, if (6.16) is replaced in (6.15) the value of the capacitor C_{K_i} is obtained as:

$$C_{K_i} = C_K\left(\frac{\omega_0^2}{\omega_{tz_i}^2} - 1\right) \quad \text{for } i = 1, 2. \tag{6.17}$$

In order to obtain the values of the inductors L_{K_i} the equation (6.17) is replaced in (6.15) leading to:

$$L_{K_i} = \frac{1}{C_K(\omega_0^2 - \omega_{tz_i}^2)} \quad \text{for } i = 1, 2. \tag{6.18}$$

IV- Dispersive π-network developed from inductors

Finally the π network of Figure 6.2g) made up of inductors is analyzed, where $L_K = \frac{1}{J_{SL}\omega_0}$. The proposed equivalent circuit is shown in Figure 6.2h), where the shunt branches are replaced by series resonators. A similar reasoning as in the previous cases is followed, being in this case $L_K = \frac{1}{J_{SL}\omega_0}$:

(i) Again, at the central frequency ω_0 the circuit must act as an the corresponding ideal inverter of Figure 6.2g):

$$Z_{\pi,i} = j\left(\omega_0 L_{K_i} - \frac{1}{\omega_0 C_{K_i}}\right) = -j\omega_0 L_K \quad \text{with } i = 1, 2. \tag{6.19}$$

(ii) On the other hand at each transmission zero the condition is the same as in the previous circuit, that is, each branch must behave as an open circuit:

$$Z_{\pi,i} = j(\omega_{tz_i} L_{K_i} - \frac{1}{\omega_{tz_i} C_{K_i}}) = 0 \quad \text{with } i = 1, 2. \tag{6.20}$$

From the two previous conditions it is deduced that:

$$L_{K_i} = -L_K + \frac{1}{\omega_0^2 C_{K_i}}, \tag{6.21}$$

$$C_{K_i} = \frac{1}{\omega_{tz_i}^2 L_{K_i}}, \tag{6.22}$$

for $i = 1, 2$. Finally, if equation (6.22) is replaced in (6.21), the value of the inductors in Figure 6.2h) is obtained as:

$$L_{K_i} = L_K \frac{\omega_0^2}{\omega_{tz_i}^2 - \omega_0^2} \quad \text{for } i = 1, 2. \tag{6.23}$$

Regarding the capacitors C_{K_i}, their values are obtained replacing (6.23) in (6.21):

$$C_{K_i} = \frac{\omega_{tz_i}^2 - \omega_0^2}{\omega_{tz_i}^2 \omega_0^2 L_K} \quad \text{for } i = 1, 2. \tag{6.24}$$

6.3 Designs with source to load dispersive couplings

Nowadays a good out of band rejection is an important issue in the design of microwave filters for demanding satellite communications. In order to improve this feature without increasing the number of resonators one of the well-known techniques is to resort to topologies that allow to place transmission zeros near the passband, as in folded configurations [126]. This technique is particularly useful in higher bands, such as the W-band, where the complexity to obtain high quality factors is increased and a high number of resonators would indeed penalize the in-band insertion loss.

According to the classical coupling matrix theory, in a filter of order N a maximum number of $N-2$ transmission zeros are achievable in a folded configuration without source

to load coupling. This amount can be increased to N if the convenient source to load coupling is implemented [126]. In the recent years the dispersive behaviour of some coupling structures has been used to overcome this limit. In this Thesis this behaviour is exploited for the source to load coupling, easy to be implemented in folded waveguide structures.

Two designs with folded topology are presented in this Section as a proof of concept for E-plane and H-plane configurations. Both of them are filters of fourth order, centered at $f_0 = 87.7$ GHz with a bandwidth of 1 GHz (1.14% of fractional bandwidth) and 20 dB of return-loss level. The coupling scheme together with the normalized coupling matrix is presented in Figure 6.3.

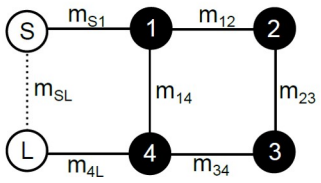

a)

Normalized coupling values	
E-plane prototype	*H-plane prototype*
$m_{SL} = -0.0267$ $m_{14} = 0.3149$ $m_{23} = 0.5808$ $m_{s1} = m_{4L} = 1.0586$ $m_{12} = m_{34} = 0.9387$	$m_{SL} = 0.049$ $m_{14} = -0.3122$ $m_{23} = 0.8014$ $m_{s1} = m_{4L} = 1.0107$ $m_{12} = m_{34} = 0.8407$

b)

Figure 6.3: a) Topology used for the two designed filters, b) normalized coupling matrix values for 20 dB of return-loss and transmission zeros at $\omega = \pm j, \pm 4$ (E-plane) and $\omega = \pm 1.722, \pm 2.387$ (H-plane).

Notice that the previous coupling matrix does not account for the dispersive couplings as it will be used to design the initial dimensions for all the couplings except for the source to load coupling. This latter coupling is designed by means of a parametric study in the commercial full-wave solver CST MWS.

6.3.1 E-plane phase equalized filter

This filter is designed to pursue a trade-off between good levels of selectivity and group delay distortion at the band-pass edges. The transmission zeros in charge of the equalization are symmetrically placed in the imaginary axis at the normalized angular frequencies $w_{tz} = \pm j$, while the two ones devoted to the improvement of selectivity are placed at the normalized angular frequencies $w_{tz} = \pm 4$. According to the classical coupling matrix theory [126], this filter already presents the maximum number of finite transmission zeros (four, which is equal to the order of the filter).

The sliced structure simulated in CST Microwave Studio is shown in Figure 6.4a), where it can be seen that all the mainline couplings are implemented by inductive windows, except for the m_{23} coupling, which is implemented by a hole located at the side wall of the structure due to its positive sign, which is the same as the remaining mainline couplings and is here considered as magnetic. The coupling hole designed for m_{14} is also located at the side walls of the corresponding cavities for the same reason.

The location of the source to load coupling deserves special attention. According to the value of m_{SL} in Figure 6.3b), the corresponding hole should be positioned in the middle of the feedlines to couple electric energy (as in Figure 6.4a)). However, in the feedlines an additional degree of freedom can be exploited to design apart from the diameter of the hole

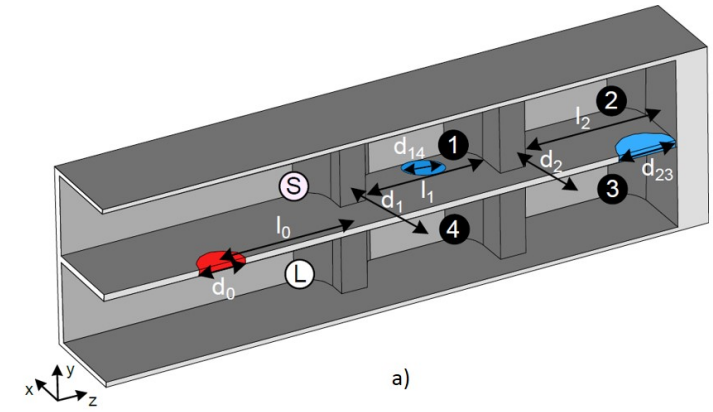

Filter dimensions [mm]	
l_0	3.2
l_1	1.937
l_2	2.196
d_0	0.85
d_1	1.218
d_2	0.759
d_{14}	0.55
d_{23}	0.75

b)

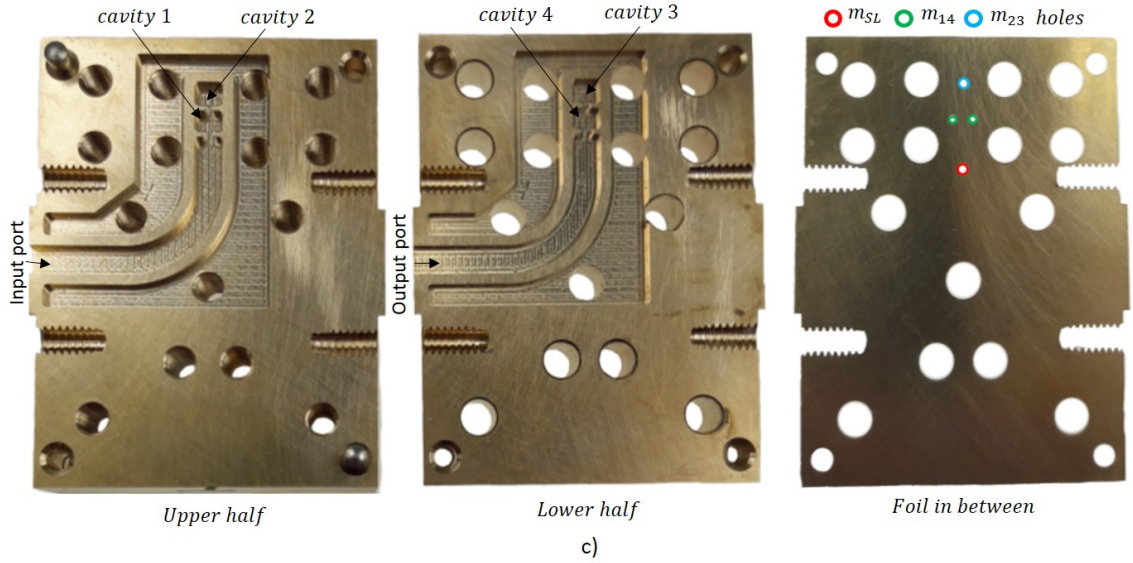

Figure 6.4: a) Sliced folded filter structure for the E-plane phase equalized filter, b) filter dimensions and c) photographs of the manufactured parts (courtesy of the group Lehrstuhl für Hochfrequenztechnik from the Christian Albrechts University of Kiel).

and its distance to the side walls: its distance to the input and output irises (parameter l_0 of Figure 6.4a)). A parametric study is carried out and the selected final dimensions are gathered in Figure 6.4b).

Figure 6.4c) shows a photograph of the manufactured prototype made up of three parts milled in brass. The lower and upper parts are identical due to the symmetry of the structure. It can be seen that two 90-degree curves are included to get a better access to the waveguide ports to measure the filter. A foil of 0.1 mm thickness is placed in between to implement the couplings m_{SL}, m_{14} and m_{23} (drawn in red, green and blue colors respectively on the right side of Figure 6.4c)). Notice that two holes implement the m_{14} coupling since a perfect magnetic wall was placed at the yz-plane in Figure 6.4a) to speed-up the simulations.

Figure 6.5 shows the measured results together with the achievable ones by the coupling matrix shown on the left column of Figure 6.3b). It can be seen that the designed filter achieves two additional transmission zeros at around 80 and 95 GHz that overcome the limit of the order of the filter. With them it is evident that the out-of band rejection

far away from the passband is improved for almost the whole W-band. Figure 6.6 shows the expected measurement results for the equalization: the group delay is worse than a filter without any transmission zeros, but it is improved with respect to a filter with all the theoretically predicted transmission zeros devoted to selectivity (four in this design).

Finally an equivalent circuit from the previous Section is used to model the obtained full-wave response. In first place, the ideal source to load inverter of the folded network of Figure 6.1 is replaced by the standard T-network of Figure 6.2c), as it is indicated in Figure 6.7a). Then, this source to load inverter is replaced by the proposed network of Figure 6.2d), as it is shown in Figure 6.7b). According to Section 6.2 the circuit values of the source to load circuits in Figure 6.7 are: $J_{SL} = -0.0275$S for the ideal inverter, $C_K = -4.9982 \cdot 10^{-14}$F for the standard network, and finally $C_1 = 3.2 \cdot 10^{-13}$F, $C_2 = -2.85 \cdot 10^{-13}$F, $L_1 = 1.22 \cdot 10^{-11}$H and $L_1 = -9.81 \cdot 10^{-12}$H.

A comparison of the ideal inverter, the standard one and the proposed network is carried out with the circuital solver ADS. The results are shown in Figure 6.8, where it can be seen that the three inverters have approximately the same behaviour in the band-pass region, but in the out of band the only circuit that it is capable of modeling the two additional transmission zeros is the proposed one. Then, the full-wave results of the filter are compared to the circuital ones achieved with the proposed equivalent circuit model. The comparison is carried out with the full-wave response since the loss in the passband or the manufacturing tolerances are not taken into account. The good agreement between responses is shown in Figure 6.9.

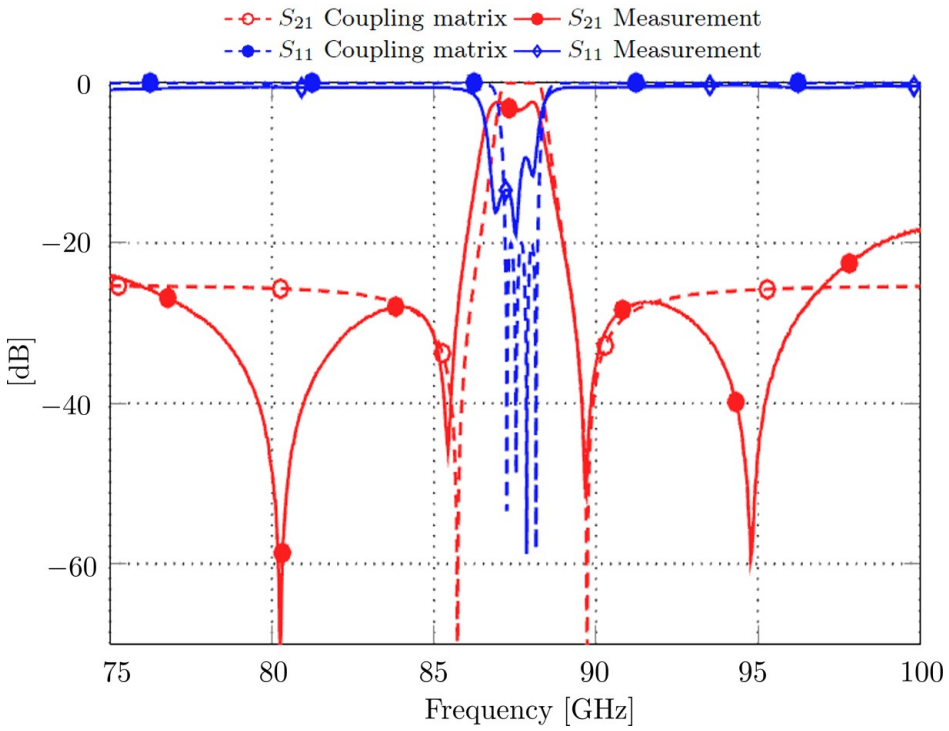

Figure 6.5: Comparison of the S-parameters from the coupling matrix on the left column of Figure 6.3b) and the measured ones (courtesy of the group Lehrstuhl für Hochfrequenztechnik from the Christian Albrechts University of Kiel).

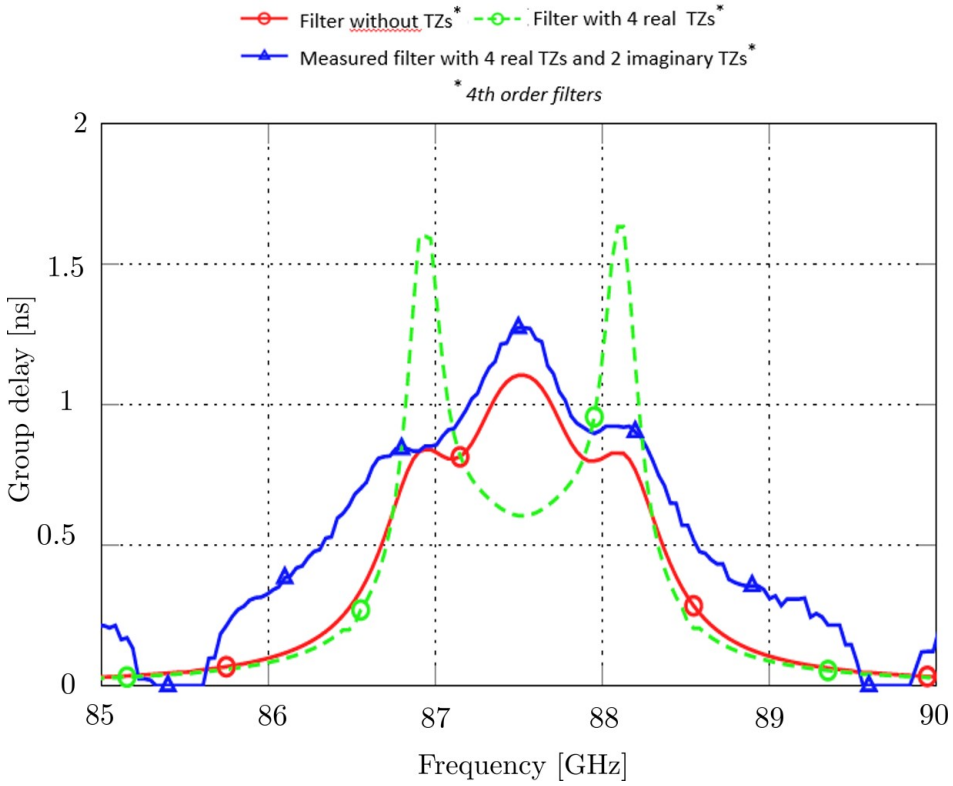

Figure 6.6: Comparison of the measured group delay of the manufactured prototype with other possible 4-th order filter responses (courtesy of the group Lehrstuhl für Hochfrequenztechnik from the Christian Albrechts University of Kiel).

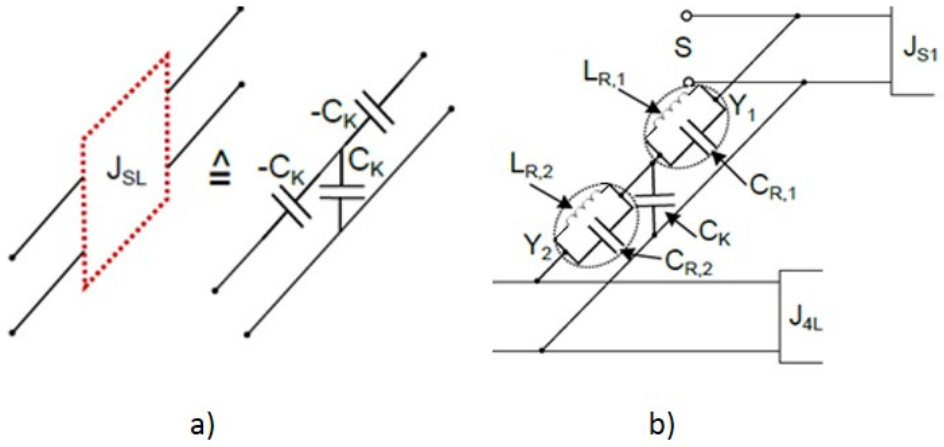

Figure 6.7: a) Replacement of the SL ideal inverter by a standard T-network, b) replacement by the proposed T-network shown in Figure 6.2d).

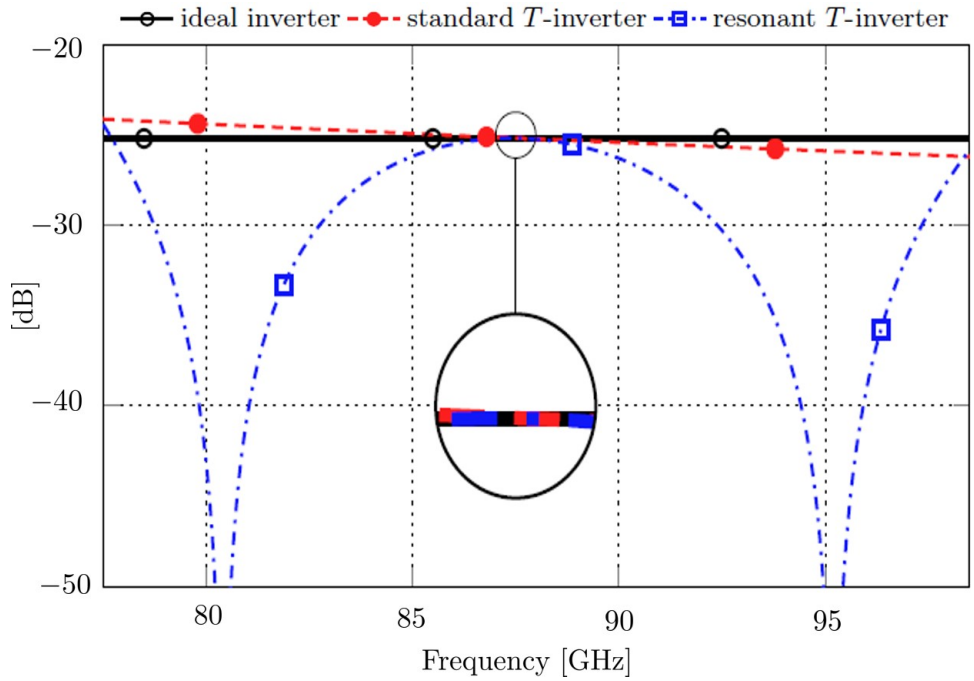

Figure 6.8: Comparison of the S_{21} parameter for the different inverters (ideal, standard and proposed one respectively).

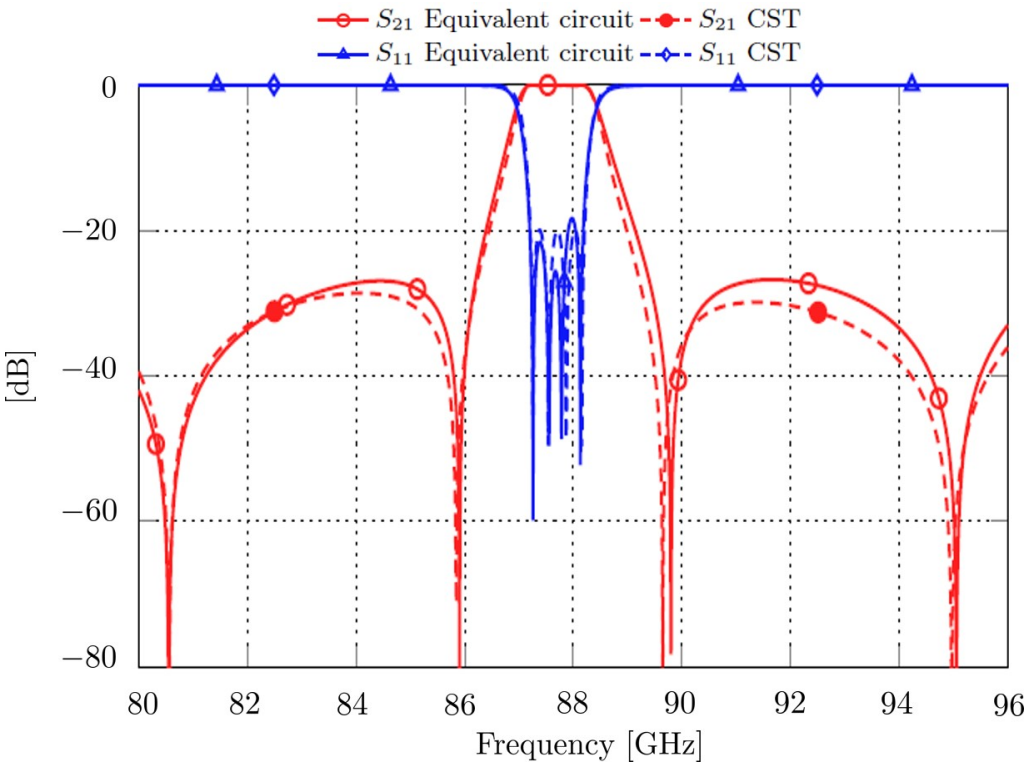

Figure 6.9: Comparison between the full-wave results obtained from CST MWS and the circuital ones obtained in ADS with the proposed equivalent circuit.

6.3.2 H-plane filter with mixed TE_{101} and TE_{102} resonators

This subsection aims at studying the dispersive behaviour in the H-plane counterpart. In order to implement the coupling matrix given on the right column of Figure 6.3b), which describes a filter with four real transmission zeros at angular normalized frequencies $\omega_{1,2} = \pm 1.722$ and $\omega_{3,4} = \pm 2.387$, a negative coupling must be realized between cavities one and four.

This negative sign in a filter based on the TE_{101} mode can be implemented by a capacitive slot [127], however, this strategy may lead to a thin iris difficult to manufacture. Another well known technique is to use one TE_{102} cavity [128]. A quasi-elliptical prototype designed following this strategy in the W-band has been recently presented [129]. However, only the four expected transmission zeros associated to the fully-canonical structure are obtained. The outer transmission zeros are present in the out of band region, but the possibility of achieving extra ones is not studied.

A prototype based on mixed TE_{101} and TE_{102} cavities is designed in this paper. In the presented prototype half of the cavities are based on the TE_{102} mode and the other half on the TE_{101} mode. The proposed structure is shown in Figure 6.10, where it can be seen that all the coupling windows correspond to vertical full-height H-plane inductive irises. Figures 6.11, 6.12 and 6.13 show the associated full-wave responses of three different set-ups simulated by the commercial software CST MWS. The two parameters that have been varied in these set-ups are only w_{SL} and l_0, and thus the simulated responses evidence that it is possible to obtain extra transmission zeros by varying the position and width of the source to load coupling aperture without significantly deteriorating the passband response. A further optimization step should be carried out to improve the in-band return-loss in a real application.

Figure 6.11 shows a set-up similar to the ones presented in [129], where no extra (more than $N = 4$) transmission zeros are achieved, although the outer ones are present far away from the passband at around 80 and 96 GHz. This result is achieved with $w_{SL} = 0.72$ mm, $l_0 = 1.25$ mm. The second set-up shown in Figure 6.12, where $w_{SL} = 0.76$ mm and $l_0 = 1.95$ mm, provides one extra transmission zero below the passband at around 83 GHz. Finally the simulated results of the third set-up are given in Figure 6.13, where two extra transmission zeros above the passband are achieved at around 93 and 96.6 GHz respectively, using $w_{SL} = 0.58$ mm and $l_0 = 3.05$ mm for the source to load coupling window.

Finally a prototype is manufactured in brass as a proof of concept. In this case only two halves are needed, as it is shown in Figure 6.14. The associated dimensions are given in the caption, and correspond to an additional proposed set-up to improve the out-of-band rejection in the lower band. The measured results are given in Figure 6.15, where the capability of this well-known structure to generate additional transmission zeros by designing the longitudinal position and aperture of the source to load coupling is validated and the sensitivity to the manufacture tolerances is evidenced.

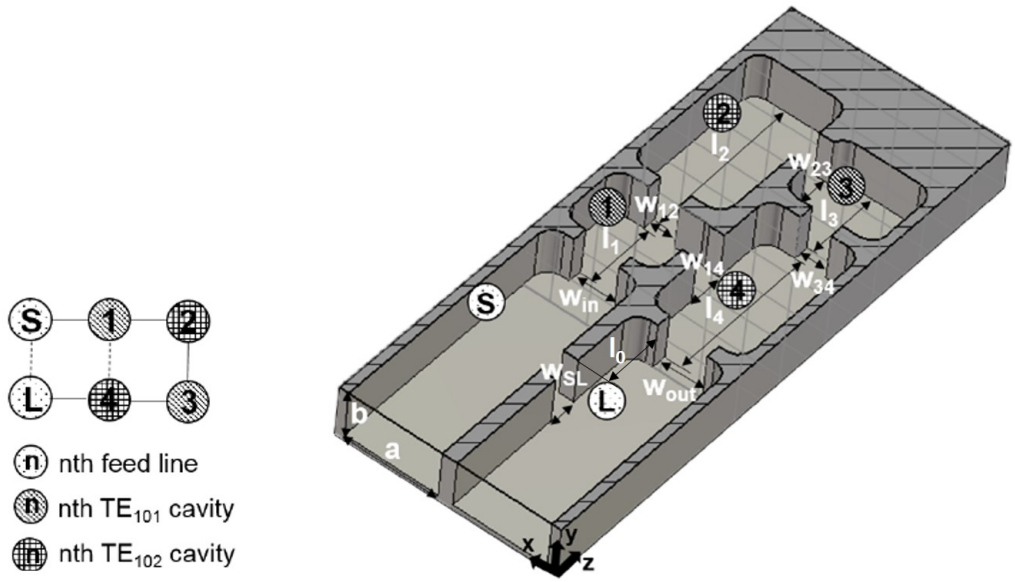

Figure 6.10: a) Structure of proposed H plane filter sliced at the height $y = b$ and simulated responses of different set-ups with dimensions (all in mm): $a = 2.54$, $b = 1.27$, $l_1 = 1.925$, $l_2 = 4.465$, $l_3 = 2.145$, $l_4 = 4.200$, $w_{in} = 1.225$, $w_{out} = 1.332$, $w_{12} = 0.840$, $w_{23} = 0.970$, $w_{34} = 0.835$ and $w_{14} = 0.95$. The dimensions of w_{SL} and l_0 for the different set-ups shown in Figures 6.11, 6.12 and 6.13.

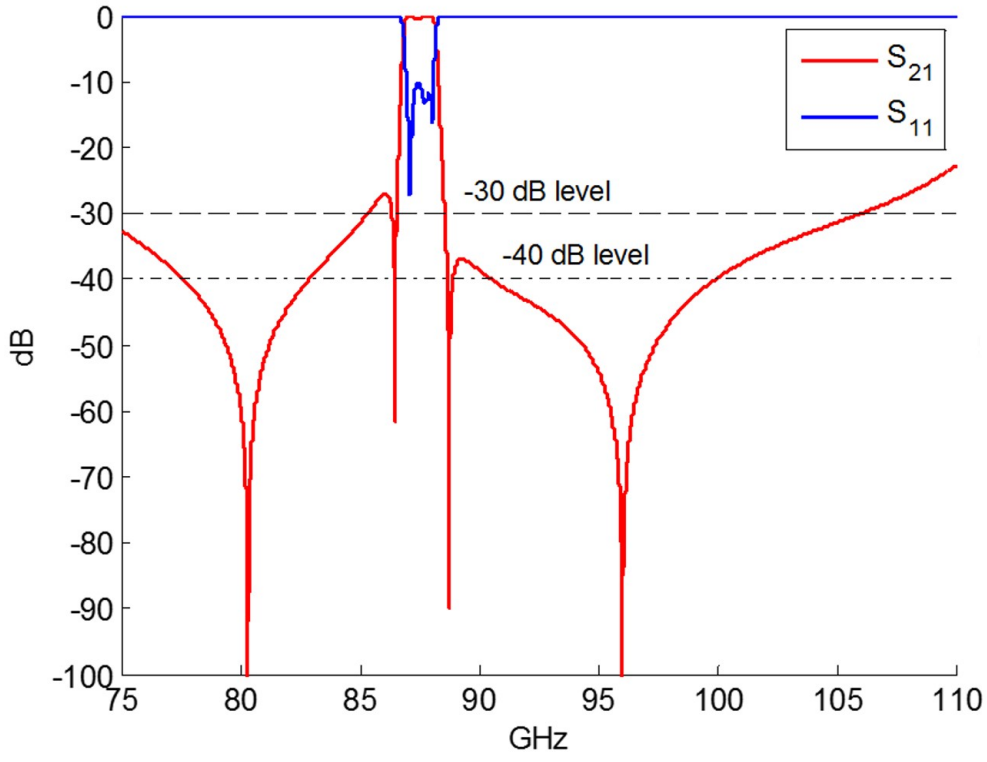

Figure 6.11: a) Simulated response of the first set-up proposed for the H plane filter shown in Figure 6.10 with dimensions associated to the source to load coupling $w_{SL} = 0.72$ mm and $l_0 = 1.25$ mm.

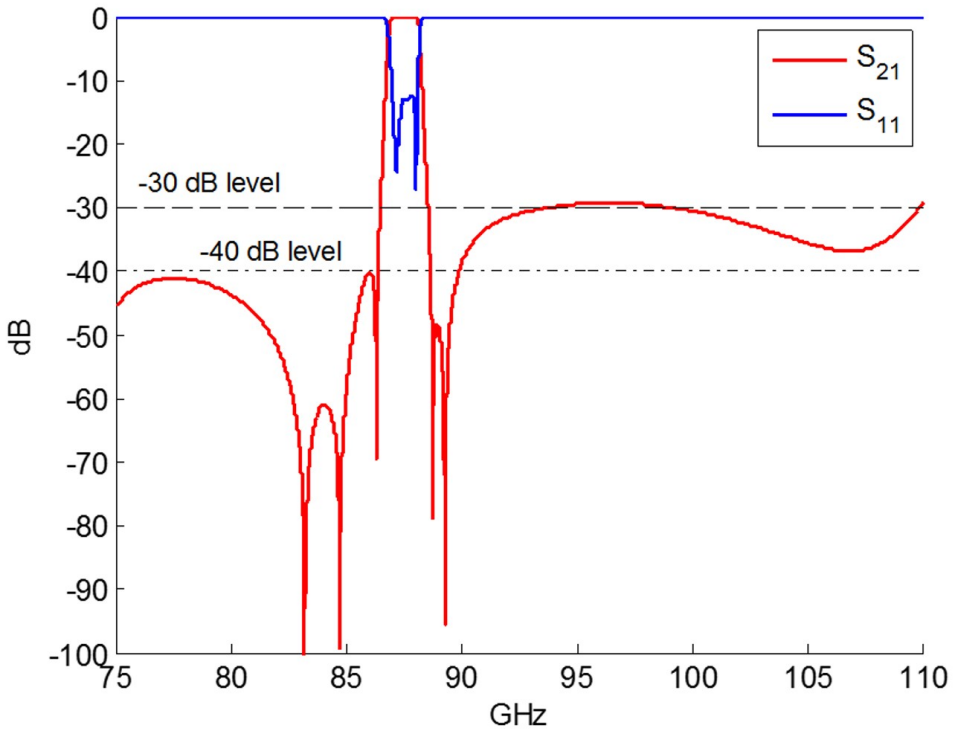

Figure 6.12: a) Simulated response of the first set-up proposed for the H plane filter shown in Figure 6.10 with dimensions associated to the source to load coupling $w_{SL} = 0.76$ mm and $l_0 = 1.95$ mm.

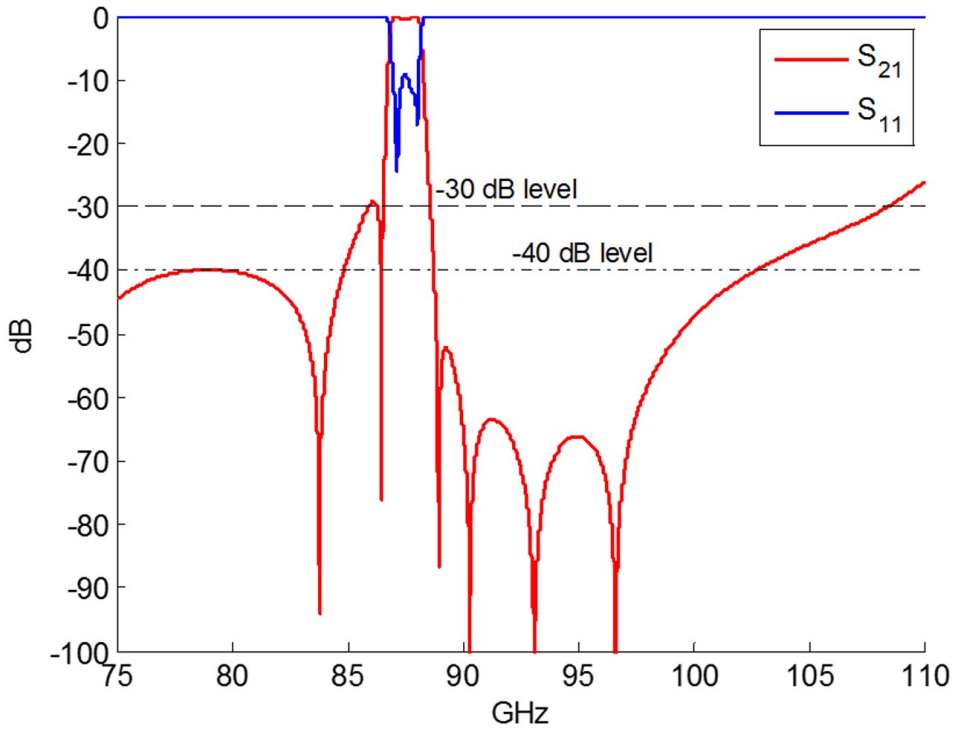

Figure 6.13: a) Simulated response of the first set-up proposed for the H plane filter shown in Figure 6.10 with dimensions associated to the source to load coupling $w_{SL} = 0.58$ mm and $l_0 = 3.05$ mm.

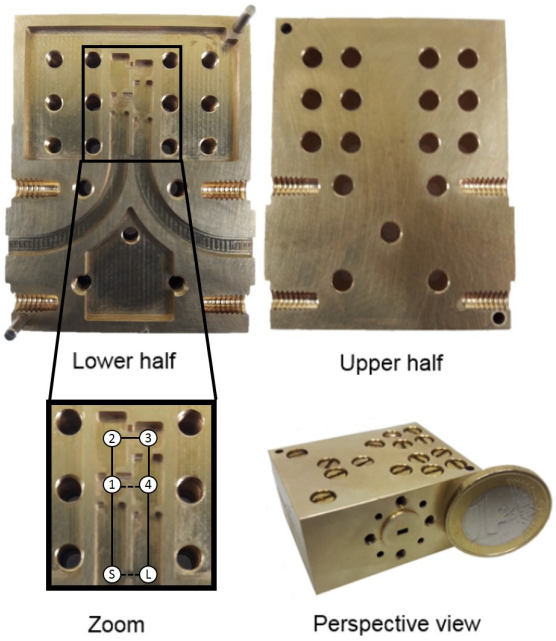

Figure 6.14: Parts of the manufactured H-plane prototype (courtesy of the group Lehrstuhl für Hochfrequenztechnik from the Christian Albrechts University of Kiel) with $w_{SL} = 0.68$, $l_0 = 4.75$, $a = 2.54$, $b = 1.27$, $l_1 = 1.925$, $l_2 = 4.465$, $l_3 = 2.145$, $l_4 = 4.200$, $w_{in} = 1.225$, $w_{out} = 1.332$, $w_{12} = 0.840$, $w_{23} = 0.970$, $w_{34} = 0.835$ and $w_{14} = 0.95$ (all dimensions in mm).

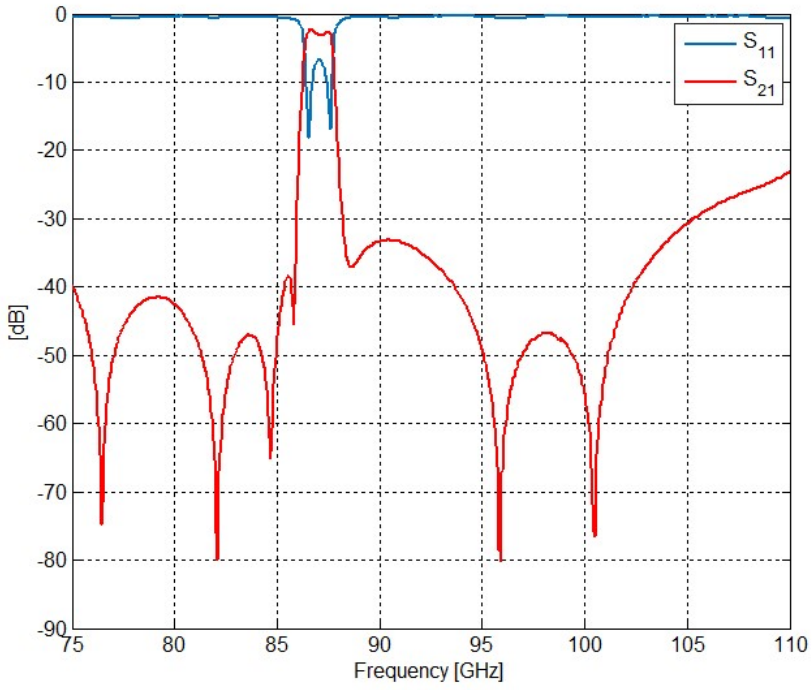

Figure 6.15: Measurement results for the manufactured H-plane prototype of Figure 6.14 (courtesy of the group Lehrstuhl für Hochfrequenztechnik from the Christian Albrechts University of Kiel).

6.4 New compact dielectric topologies

Dielectric resonator filters were first reported in [130–132] and traditionally have taken part of input multiplexers in satellite communication systems [133] or of mobile base stations [134, 135]. This kind of filters have a limited power handling capability and spurious-free window, but in contrast offer a compact size compared to other well-known technologies and high quality-factor [5].

The first dielectric resonators used a cylindrical rod and made use of the $TE_{10\delta}$ or the TM_{010} modes [131, 136–138]. Since then, dual-mode schemes of very diverse shapes have arisen to reduce the size and mass of the prototypes [117–121, 124, 125]. The use of quarter cut resonators with metallic plates or the use of half-cut resonators has also been proposed [122, 123].

The dielectric resonator of equilateral triangular shape has already been reported in the field of antennas, as one of the possible geometries of interest [139, 140]. This shape has also been reported at hundreds of THz in the field of optical nanoantennas [141, 142]. However, to the best of the author's knowledge, it has not been exploited in the filter domain yet, where perhaps the Δ-resonator shape of [70] is the most similar proposal to the one presented here.

In this Thesis the use of the equilateral triangular dielectric resonator is proposed as a possible shape to reduce the footprint of filter designs. Several topologies that can benefit from this particular shape are proposed in Figure 6.16. In particular, the proposal developed in the next Section is made up of equilateral triangular resonators working on single-mode. However, it would be possible to study the multimode capabilities of this kind of resonator or even to use half-cuts of it as in other designs [122, 123].

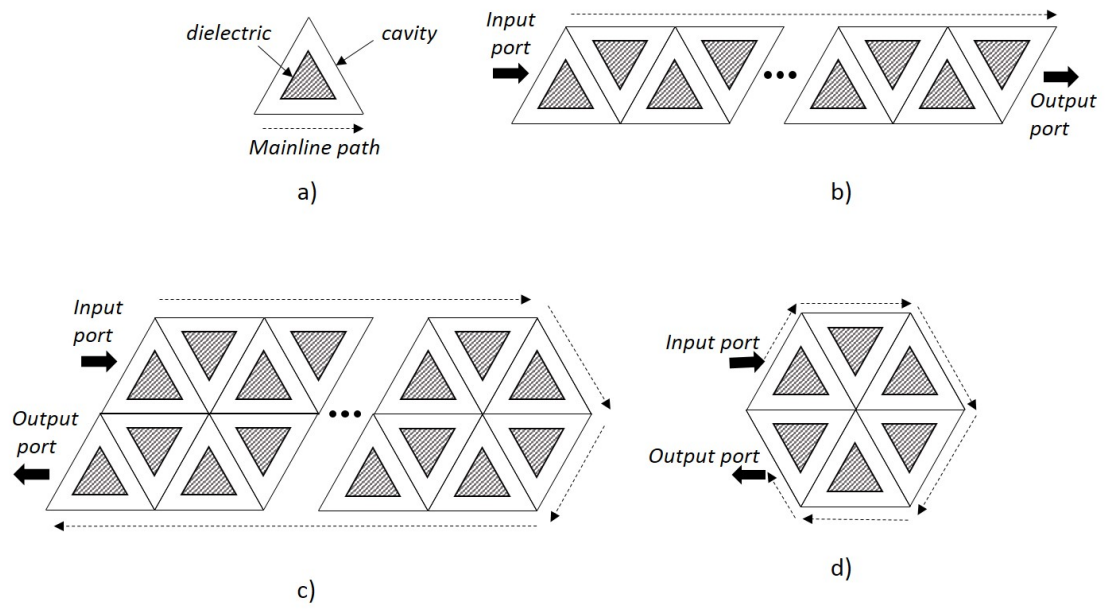

Figure 6.16: a) Scheme of dielectric resonator, enclosing cavity and signal path, b) inline topology, b) folded topology and c) hexagonal inline topology for equilateral triangular dielectric resonators.

6.5 Filter design

Among all the proposed topologies presented in the previous Section, the one shown in Figure 6.16d) has been selected in this Thesis to develop a prototype at the Ku band, exploiting its compactness. In particular, the proposed sixth order filter is designed at 12.5 GHz with 100 MHz of bandwidth (0.8% of fractional bandwidth) and 20 dB of return loss. The dielectric material chosen for the supports has a relative permittivity of $\varepsilon_r = 9.8$ and for the equilateral triangular resonators of $\varepsilon_r = 24$.

Figure 6.17a) shows an equilateral triangular dielectric resonator, whose height h_r is varied in Figure 6.17b) to obtain the desired resonant frequency. The next resonant mode is also plotted in Figure 6.17b), having a resonant frequency between 400 and 600 MHz higher than the fundamental mode within the range of the study. This study of the cavity suggests that the initial height of the resonators must be of 4.48 mm.

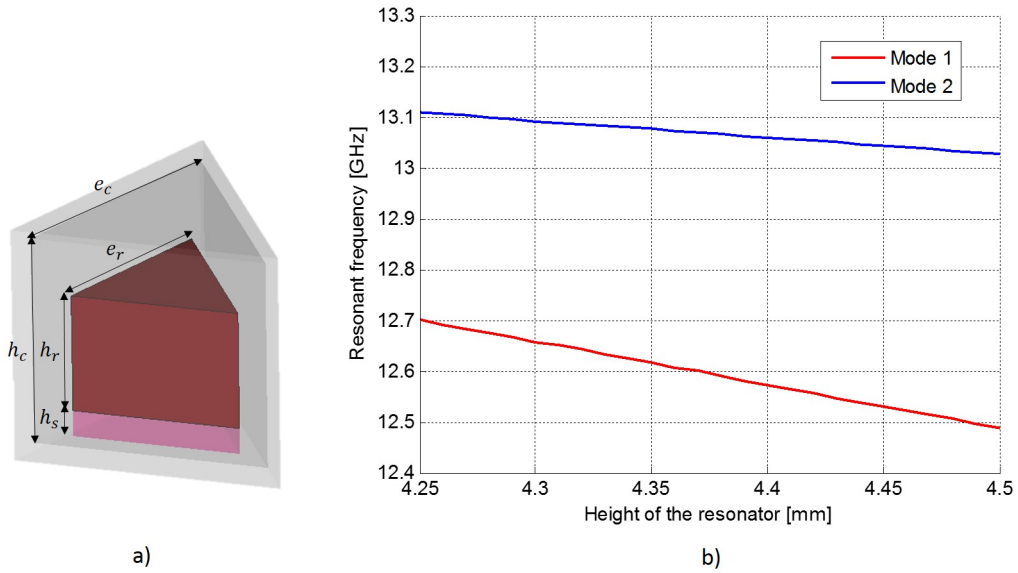

Figure 6.17: a) Proposed equilateral triangular dielectric resonator made up of ceramic material of $\varepsilon_r = 24$, placed over an alumina support of $\varepsilon_r = 9.8$. Resonator dimensions (in mm) : $h_c = 8$, $e_c = 8.42$, $h_s = 1$ and $e_r = 6$. b) Variation of the two first resonant frequencies with the height of the resonator h_r.

With the previous dimensions, the resonant mode of the cavity chosen for this design is shown in Figure 6.18, where different views of the corresponding field patterns numerically obtained are shown. Each subfigure includes a schematic representation of the field. It can be seen that the selected resonant modes resembles the $TM_{01\delta}$ mode of the cylindrical dielectric resonator [143]. The selected mode has PMW symmetry with respect to the plane xy, indicated with a black dotted line between points A-C in Figures 6.18a) and c). The distance between points A-B, defined as v_d in these Figures, is introduced as an additional degree of freedom to design, keeping the mentioned symmetry. In the final design, this distance has been set to $v_d = 1.30$ mm. The obtained Q-factor for the resonant cavity used as a proof of concept is 4450 (using copper, with $5.8 \cdot 10^7$ S/M for the outer box, and a ceramic of very high Q_d with a loss tangent of $\tan(\delta) = 4 \cdot 10^{-5}$). This value can be improved in a final design for practical applications.

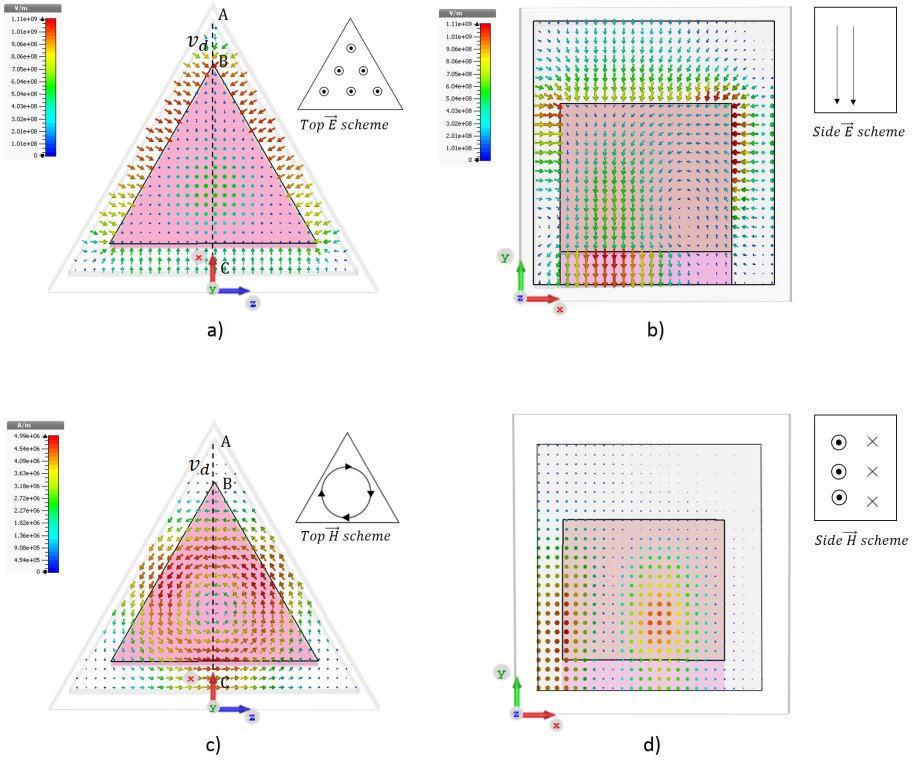

Figure 6.18: Resonant mode used to implement the 6-th order Chebychev response: a) top view and b) side view of the $\vec{E}$ field; c) top view and d) side view of the $\vec{H}$ field. The fundamental mode has PMW symmetry in the xy plane, indicated with a dotted black line between points A-C in a) and c). The distance between points A-B, v_d, is set to 1.30 mm.

The proposed sixth order Chebychev filter is designed with the resonator presented in Figures 6.17 and 6.18. The classical techniques to evaluate the inter-resonator coupling and the input/output couplings are here used [6, 7, 126]. For the input and output couplings the filter is fed by 50Ω SMA connectors. Regarding the interresonator couplings, the irises are placed at the bottom of the cavity due to the position of the SMA connectors. In particular, with the proposed location the coupling between source and load is avoided, which would be undesired for the objective response.

Figure 6.19a) shows the inner resonators, the outer box and the coupling windows of the filter. Figure 6.19b) shows the simulated response obtained with the commercial software CST MWS, where f.w. stands for full-wave, together with the ideal response given by the normalized coupling values shown in the coupling scheme on the right. A good agreement between responses has been achieved.

With this design, it has been evidenced that the equilateral triangular resonator may be a promising geometry yet to be exploited in the design of compact microwave filters, and in general for microwave devices as it has been shown throughout this whole Thesis from the initial Chapter. Finally, Figure 6.19c) shows the wideband response, where it can be seen that the next higher resonant mode of Figure 6.17 is just slightly excited, and the first significant spurious frequency is located at around 14.2 GHz. If this spurious frequency could be suppressed, a wide free-spurious window up to 18 GHz would be obtained. This could be studied in the near future, as well as the possibility to open an additional iris between resonators 1 and 6. The dimensions of the designed filter are given at the end of this Section in Figures 6.20-6.24.

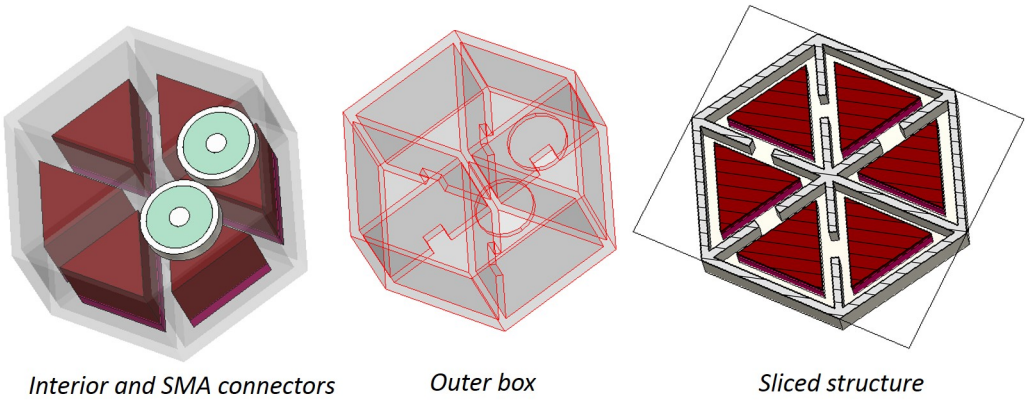

a)

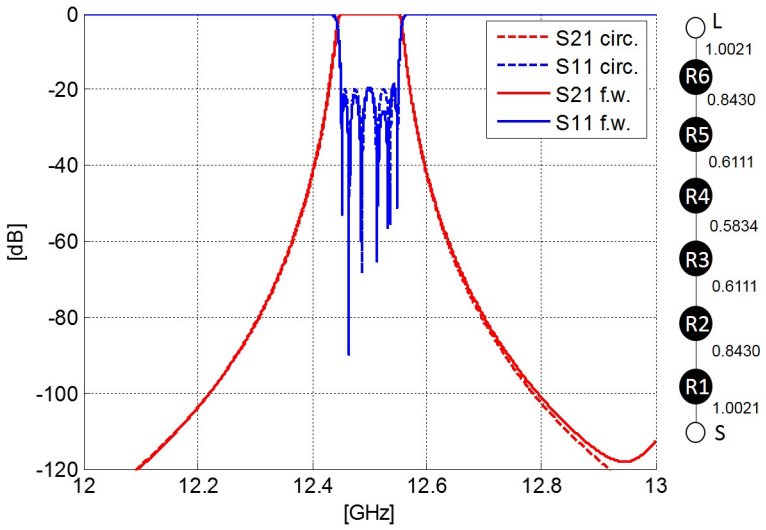

b)

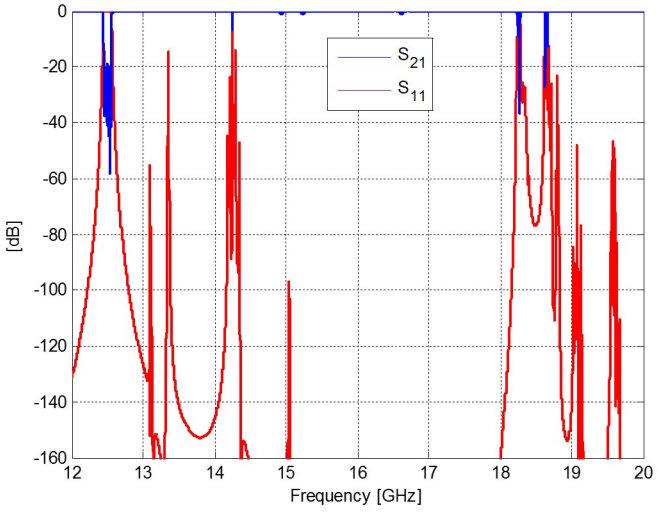

c)

Figure 6.19: a) Proposed structure (inner resonators as in Figure 6.17 and SMA connectors, outer box, and whole structure sliced at the bottom), b) Simulated response compared to the circuital response given by the coupling topology on the right.

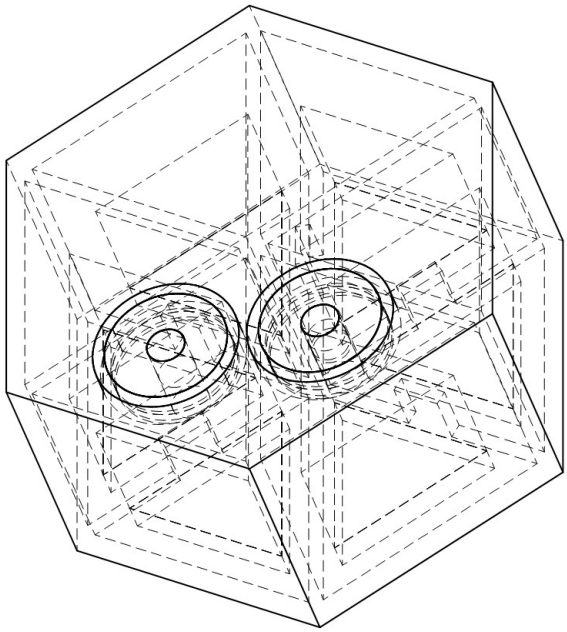

Figure 6.20: Perspective view of the designed dielectric resonator filter of 6-th order at 12.5 GHz with 0.8% of fractional bandwidth and 20 dB of return-loss. The box is made of perfect electric conductor, the relative permittivity of the ceramic is $\varepsilon_r = 24$ and relative permittivity of the support is $\varepsilon_r = 9.8$.

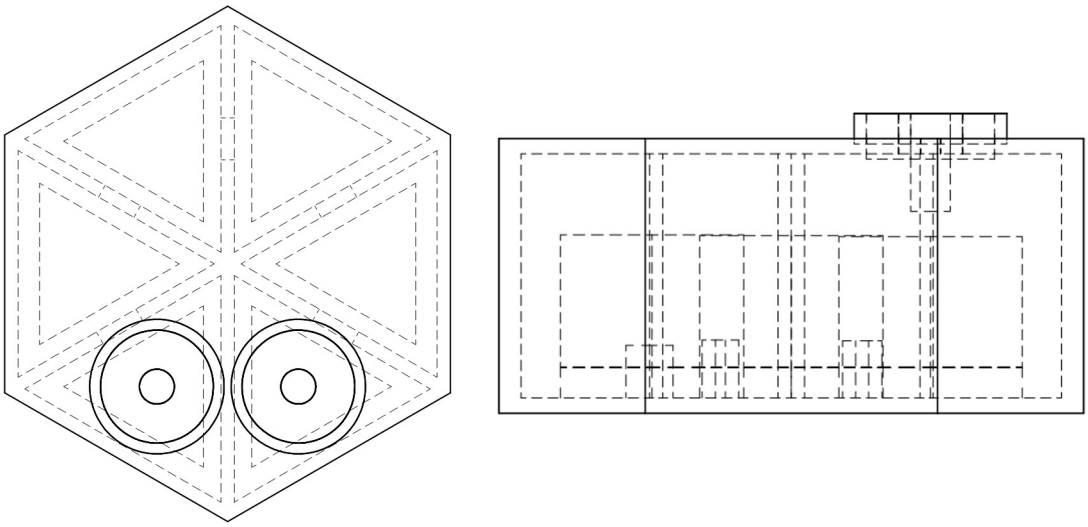

Figure 6.21: Top view and side view of the designed prototype shown in Figure 6.20.

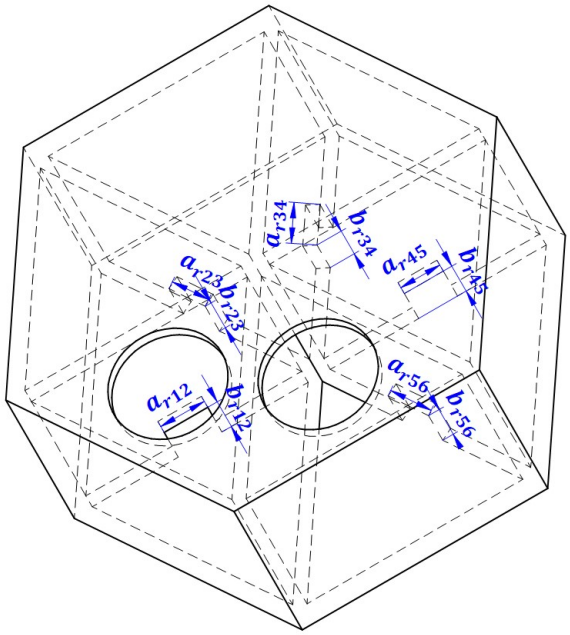

Figure 6.22: Box of the designed prototype shown in Figure 6.20. Final dimensions of the irises (all in mm): $a_{r12} = 1.70$, $b_{r12} = 1.87$, $a_{r23} = 1.52$, $b_{r23} = 1.89$, $a_{r34} = 1.54$, $b_{r34} = 1.72$, $a_{r45} = 1.52$, $b_{r45} = 1.89$, $a_{r56} = 1.70$ and $b_{r56} = 1.87$.

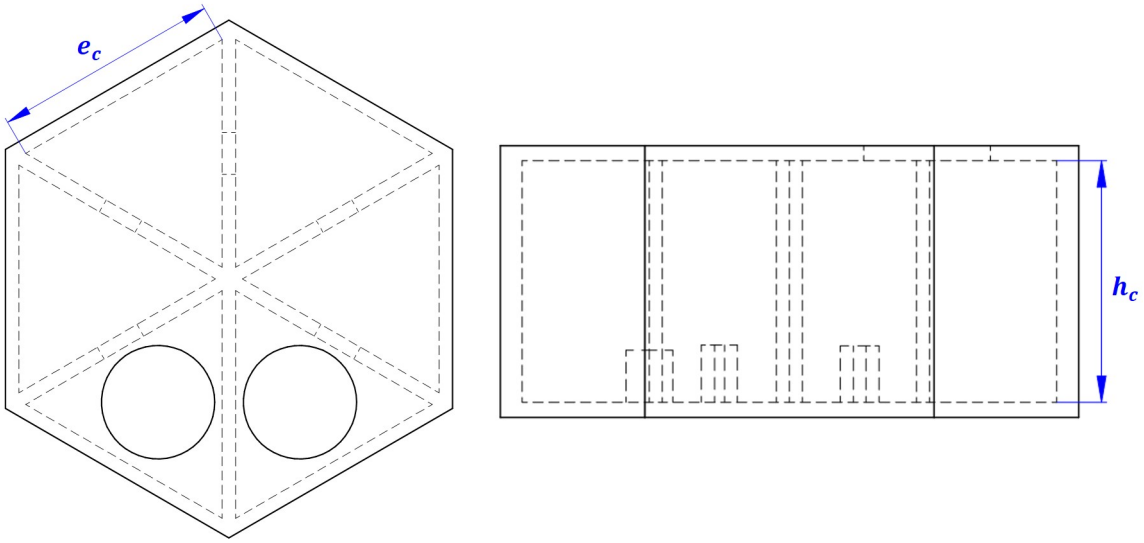

Figure 6.23: Box of the designed prototype shown in Figure 6.20. Final dimensions of the side and height of the cavities respectively (all in mm): $e_c = 8.42$ and $h_c = 8$.

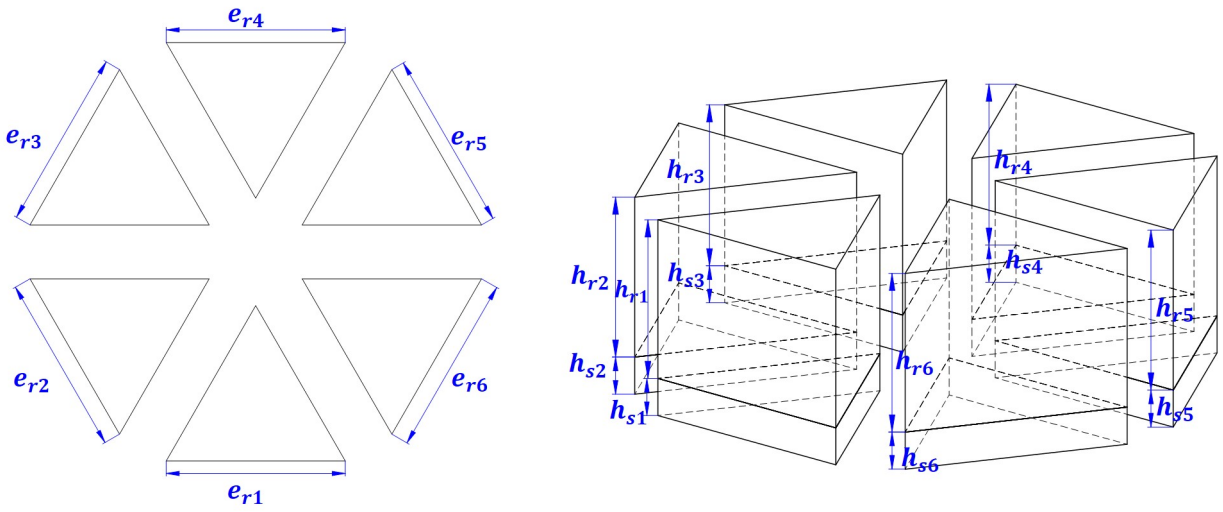

Figure 6.24: Ceramic resonators and alumina supports of the designed prototype shown in Figure 6.20. Final dimensions for the ceramic resonators (all in mm): $e_{ri} = 6$ (the same for all the resonators, with $i = 1, \ldots, 6$), $h_{r1} = h_{r6} = 4.28$, $h_{r2} = h_{r5} = 4.31$, $h_{r3} = h_{r4} = 4.34$. Final dimensions for the alumina supports (all in mm): $e_{si} = 6$ and $h_{si} = 1$ (the same for all the supports, with $i = 1, \ldots, 6$)).

7 Conclusions

This Chapter is divided into three sections and gathers all the original ideas, contributions and publications arisen from this Thesis. Section 7.1 summarizes the original ideas proposed in this dissertation, whose development has been detailed in Chapters 2 to 6. The general conclusions derived from the work carried out are also outlined. Section 7.2 enumerates the contributions of this Thesis to the efficient modelling of unconventional geometries, as well as the contributions to the design of microwave filters. Finally, the list of publications attained within the period of this 3-year Thesis is given in Section 7.3, separated to those previously obtained.

7.1 Original ideas and general conclusions

Modern telecommunication systems, and specially those for satellite communications, are subjected to restrictive specifications to provide the high quality of service demanded by final users. Complex devices are designed by microwave practitioners, who demand efficient and accurate Computer-Aided-Design (CAD) tools. Such tools have been developed over the last decades for those canonical geometries popular for on-board devices, such as the rectangular, circular or elliptical waveguides. However, with the development of the 3D printing techniques the design possibilities have been undoubtedly widened. Thus, robust CAD tools capable of analyzing the prospective geometries are key to their integration into modern devices, and it is in this scenario where the work developed in this Thesis has found the perfect spot.

In this context, the first part of this Thesis aims to contribute to the efficient analysis and modelling of two unconventional geometries: the equilateral triangular and the parabolic cylinder waveguides. In particular, Chapter 2 is devoted to the equilateral triangular waveguide, whose complete set of modes has been recently derived in [40, 41]. Due to the recent availability of this set, the application of the Mode-Matching method over this geometry has been proposed in this Thesis. To the best of the author's knowledge, it had not been applied yet. A flexible mathematical formulation based on well-known plane waves is given, which simplifies the surface integrals and allows a very easy generalization to other problems that involve canonical geometries (*i.e.*, rectangular, circular and elliptical cross-sections). Several test cases have been proposed to validate the formulation, and the attained results are in good agreement with those obtained with commercial software. Furthermore, this tool is later on used for efficiently designing challenging filters.

The parabolic cylinder waveguide, whose modal spectra was addressed long time ago, is studied in Chapter 3. The analytical resolution of the electromagnetic field in this

kind of geometry is far from being trivial, as it involves a cumbersome problem where two variables in the real domain are sought. Before the publication of the work developed in this Thesis, this kind of waveguide had to be solved by numerical CAD tools, since the analytical techniques available resorted to graphical means of resolution. This dissertation has proposed to combine the analytic continuation techniques available in the literature to approximate the corresponding basis functions [50], with a recently published algorithm for the resolution of bivariate systems of equations [52]. The proposed procedure has been tested with numerical software, and large number of modes have been successfully obtained with proved accuracy for both symmetric and asymmetric contours.

It is obvious that the present Thesis can not address all the candidate geometries that may arise with the modern 3D printing techniques. For this reason Chapter 4 is included for completeness. This Chapter proposes an efficient formulation based on nested 2D finite-element function-spaces to hybridate the 2D Finite Element and the Mode-Matching methods, which are an excellent alternative to solve problems based on cascaded blocks made up of waveguides with translation symmetry. Several measured devices from already published articles [107–111] have been used as a reference to test the software tool developed in this Thesis, proving that a large class of microwave devices can be efficiently analyzed by the proposed formulation.

The second part of this Thesis is devoted to the design of microwave filters. In first place two inline devices have been designed in equilateral triangular and in asymmetric parabolic cylinder waveguides, since the integration of any unconventional geometry into future telecommunication systems begins with the study of the performance of proof-of-concept designs. In second place, this Thesis focuses on compactness, which is a desirable feature in satellite communication systems as it has a direct impact on the launching cost [63]. In this context, it has been straightforward to propose a dual mode prototype based on equilateral triangular resonators, which exploits the mode degeneracy inherent to this unconventional geometry and allows to reduce the size and weight achieving the same desired full-wave response.

Following this line of research focused on the enhancement of compactness of microwave filters, additional strategies have been proposed in this Thesis. In the context of waveguide filters, the use of dispersive source to load coupling holes is addressed in this work. These frequency-dependent holes allow to obtain out-of-band transmission zeros, which improve the rejection achieved without increasing the number of resonators. This strategy is specially suited for high bands where the attainment of resonators with high Q-factor is difficult. Among all the possible waveguide filters, the well-known fully-canonical waveguide filters [5] are the selected ones to benefit from dispersive source to load couplings, due to the ease of implementation compared to other topologies. This part of the Thesis arose in the context of a three-month stay in the group Lehrstuhl für Hochfrequenztechnik of Kiel, which led to a deeper collaboration in the subsequent months. In this context, the equivalent circuits that model the resonant behaviour of the source to load coupling holes were proposed by this doctoral candidate, with which up to to N + 2 transmission zeros can be achieved, one extra apart from the one achievable in the literature so far [113, 114]. Two prototypes exploiting these dispersive holes have been proposed, the E-plane and its H-plane counterpart at the W-band. The two proposed prototypes have been manufactured and measured in the Lehrstuhl für Hochfrequenztechnik group, the E-plane prototype being proposed by the same group, whereas the H-plane prototype being fully-designed by this doctoral candidate.

Finally, another type of filters have been studied in this dissertation: the dielectric resonators. These filters are also usual in satellite communications, in particular taking part of the input multiplexers as they have enough power handling capabilities at this point of the chain of communications [5, 63]. One of the main benefits of the dielectric resonator technology is the size reduction that they can offer. In this context, in this Thesis the use of the equilateral triangular dielectric resonator has been proposed, whose advantageous geometrical shape to reduce the overall footprint has not been exploited yet in microwave filters to the best of the author's knowledge. Several topologies have been proposed, and among them one has been selected to show a proof-of-concept design in the Ku band showing very good performance and significant small footprint.

7.2 Original contributions of this work

The main contributions of this Thesis are summarized in this Section, organised according to two main objectives identified along this dissertation:

1. Contributions to the efficient electromagnetic analysis of unconventional geometries in waveguide technology:

    1.1. Development of a complete software tool based on the Mode-Matching method for the analysis of waveguide devices made up of cascaded blocks of equilateral triangular cross-sections. The tool includes a package to allow rotated cases and a routine that tests the fulfilment of the boundary conditions.

    1.2. Development of a CAD tool based on the use of plane waves in the Mode-Matching method for the efficient analysis of waveguide devices where the cascaded blocks integrate other canonical geometries (rectangular, circular, elliptical) together with the equilateral triangular geometry.

    1.3. Development of a quasi-analytical CAD tool for the systematic resolution of the modal spectra in the parabolic cylinder waveguide, with symmetric or asymmetric contour.

    1.4. Development of a software tool where the 2D-Finite Element and the Mode-Matching methods are efficiently hybridated for waveguide devices made up of cascaded waveguide blocks where arbitrary geometries may take part as well. An additional package for the efficient orthonormalization of multiconductor waveguides has been developed as well.

2. Contributions to the integration of novel geometries and coupling structures in microwave filters:

    2.1. Design of three filters made up of unconventional geometries as proofs of concept to boost their integration into future communication systems. Two inline prototypes of 7-th and 9-th order respectively have been designed in the K band, one based on equilateral triangular resonators and the other one in asymmetric parabolic resonators.

    2.2. Design of a Ku-band prototype based on dual mode cavities of equilateral triangular cross-section to evidence the advantage that the mode degeneracy inherent to this geometry represents in the area of microwave filters. The designed

prototype has been manufactured, tuned and measured, proving to be a good alternative to other conventional dual-mode filters.

2.3. Study of dispersive source to load couplings and their integration into fully canonical waveguide filters. Several equivalent circuits have been proposed to model the full-wave response observed, easing the integration of this behaviour into the classical canonical folded network by means of a single resonant source to load inverter.

2.4. Design, manufacture and measurement of two prototypes in the W-band with dispersive source to load coupling holes. One prototype is a 4-th order filter designed in rectangular waveguide with E-plane configuration, capable of generating two additional symmetrical out-of-band transmission zeros and phase equalization. The other prototype is a 4-th order filter designed in H-plane configuration with mixed TE_{101} and TE_{102} cavities, capable of generating asymmetrical responses with additional out-of band transmission zeros.

2.5. Design of a 6-th order filter based on dielectric resonators in the Ku band. This design exploits the size reduction achievable by the equilateral triangular geometry and is presented among several alternative topologies with reduced footprint.

7.3 List of publications

The publications related to the research carried out in this Thesis are listed below:

7.3.1 International journals

[1] A. Morán-López, J. Córcoles, J. A. Ruiz-Cruz, J. R. Montejo-Garai, and J. M. Rebollar, "Robust calculation of the modes in parabolic cylinder metallic waveguides by means of a root-finding method for bivariate functions," *IEEE Transactions on Microwave Theory and Techniques*, vol. 66, no. 2, pp. 623–632, 2018. DOI: 10.1109/TMTT.2017.2777969.

[2] J. Córcoles, A. Morán-López, and J. A. Ruiz-Cruz, "Nested 2D finite-element function-spaces formulation for the mode-matching problem of arbitrary cross-section waveguide devices," *Applied Mathematical Modelling*, vol. 60, pp. 286–299, 2018. DOI: 10.1016/j.apm.2018.03.019.

[3] A. Morán-López, J. Córcoles, J. A. Ruiz-Cruz, J. R. Montejo-Garai, and J. M. Rebollar, "Electromagnetic scattering at the waveguide step between equilateral triangular waveguides," *Advances in Mathematical Physics*, pp.1-16, vol. 2016, 2016. DOI: 10.1155/2016/2974675.

7.3.2 International referred conference papers

[1] D. Miek, A. Morán-López, J. A. Ruiz-Cruz, and M. Höft, "Ku-Band waveguide filter with multiple transmission zeros by resonant source to load and bypass cross-coupling," in *2019 49th European Microwave Conference (EuMC)*. Accepted.

[2] D. Miek, A. Morán-López, J. A. Ruiz-Cruz, and M. Höft, "Improved fully canonical phase equalized W-band waveguide filter with dispersive coupling inverter," in *2018 48th*

European Microwave Conference (EuMC). IEEE, 2018, pp. 166–169. DOI: 10.23919/EuMC.2018.8541743.

[3] A. Morán-López, J. Córcoles, J. A. Ruiz-Cruz, J. R. Montejo-Garai, and J. M. Rebollar, "Dual-mode filters in equilateral triangular waveguides with wide spurious-free response," in *2017 IEEE MTT-S International Microwave Symposium (IMS).* IEEE, 2017, pp. 1192–1195. DOI: 10.1109/MWSYM.2017.8058816.

[4] A. Morán-López, J. Córcoles, J. A. Ruiz-Cruz, J. R. Montejo-Garai, and J. M. Rebollar, "Direct computation of parabolic waveguide modes via a bivariate root-finding algorithm," in *2017 IEEE MTT-S International Conference on Numerical Electromagnetic and Multiphysics Modeling and Optimization for RF, Microwave, and Terahertz Applications (NEMO).* IEEE, 2017, pp. 152–154. DOI: 10.1109/NEMO.2017.7964217.

[5] A. Morán-López, J. Córcoles, and J. A. Ruiz-Cruz, "Efficient computation and orthonormalization of multiple TEM numerical modes arising from FEM for microwave computer-aided-design," in *2017 IEEE MTT-S International Conference on Numerical Electromagnetic and Multiphysics Modeling and Optimization for RF, Microwave, and Terahertz Applications (NEMO).* IEEE, 2017, pp. 197–199. DOI: 10.1109/NEMO.2017.7964232.

[6] A. Morán-López, J. Córcoles, J. A. Ruiz-Cruz, J. R. Montejo-Garai, and J. M. Rebollar, "Generalized scattering matrix of the discontinuity between an equilateral triangular waveguide and a rectangular, circular or elliptical waveguide," in *2016 Asia-Pacific Microwave Conference (APMC).* IEEE, 2016, pp. 1–4. DOI: 10.1109/APMC.2016.7931283.

7.3.3 Ongoing work

This subsection contains the journal and conference papers already sent or in preparation:

[1] A. Morán-López, J. Córcoles, J. A. Ruiz-Cruz, J. R. Montejo-Garai, and J. M. Rebollar, "Closed-form solution for the unloaded q-factor of the equilateral triangular cavity," *Sent to the journal Electronic Letters.*

[2] D. Miek, A. Morán-López, J. A. Ruiz-Cruz, and M. Höft, "Extra transmission zeros in h-plane W-band waveguide filter configurations," *Sent to the journal IEEE Microwave and Wireless Components Letters (manuscript ID: MWCL-19-0207).*

7.3.4 Other conferences

This subsection contains the conference papers of the research work related to the content of this document (Chapter 5) carried out before this Thesis:

[1] A. Morán-López, and J. A. Ruiz-Cruz, "Diseño de un filtro combline en banda S por subdivisión y optimización en etapas," in *XXXI Simposium Nacional de la Union´ Cient´ifica Internacional de Radio (URSI).* Madrid, 2016, pp. 1–4.

[2] A. Morán-López and J. A. Ruiz-Cruz, "Optimization method for the design of microwave filters based on sequential stages," in *Congress on Numerical Methods (CMN).* Lisbon, 2015, pp. 1–4.

8 Conclusiones

Este capítulo se divide en tres secciones y recoge las ideas originales, las contribuciones y las publicaciones surgidas de la presente Tesis. La Sección 8.1 resume las ideas originales que se han propuesto en este trabajo y cuyo desarrollo se ha detallado en los Capítulos 2 a 6, así como las principales conclusiones extraídas del trabajo de investigación llevado a cabo. La Sección 8.2 enumera las contribuciones de esta Tesis al modelado electromagnético eficiente de geometrías no convencionales, así como al diseño de filtros de microondas. Finalmente, las publicaciones obtenidas como resultado del desarrollo de tres años de Tesis se listan en la Sección 8.3.

8.1 Ideas originales y conclusiones generales

Los modernos sistemas de telecomunicaciones, y en particular los sistemas de comunicación por satélite, están sujetos a especificaciones muy restrictivas para garantizar la calidad de servicio demandada por los usuarios. Los ingenieros de microondas llevan a cabo el diseño de dispositivos complejos, para los cuales requieren herramientas de diseño asistido por ordenador que sean eficientes y precisas. En las últimas décadas dichas herramientas se han desarrollado para el análisis de aquellas geometrías canónicas típicas en los sistemas satelitales, como las guías de onda rectangular, circular o elíptica. Sin embargo, el desarrollo de las técnicas de impresión 3D ha abierto las puertas a nuevas posibilidades de diseño, y con ello se han hecho necesarias herramientas de diseño asistido por ordenador capaces de analizar las futuras geometrías. Es precisamente este escenario el que ha posibilitado el desarrollo del presente trabajo de investigación.

En particular, la primera parte de esta Tesis se desarrolla para contribuir al modelado electromagnético eficiente de dos geometrías no convencionales: la guía triangular equilátera y la guía cilíndrico-parabólica. El modelado de la guía triangular equilátera se presenta en el Capítulo 2, cuyo análisis por medio de herramientas de análisis modal se ha posibilitado recientemente gracias a la resolución del conjunto completo de modos de esta guía en [40, 41]. En el capítulo 2 de la presente Tesis se propone por primera vez la aplicación del método de análisis modal conocido como método de ajuste modal (*Mode-Matching method*) en la geometría triangular equilátera. La formulación propuesta en el capítulo se basa en el uso de ondas planas, y permite abordar la integración de discontinuidades formadas por esta guía y otra canónica (rectangular, circular, elíptica) de manera unificada. Se desarrolla una herramienta software de análisis de campos electromagnéticos, y se aplica sobre distintos casos de estudio que tienen por objeto su validación obteniéndose resultados excelentes. Además, la herramienta desarrollada se usa en capítulos posteriores para el diseño de filtros. El análisis electromagnético de la guía parabólico-

cilíndrica se lleva a cabo en el Capítulo 3. La resolución analítica del espectro modal de esta guía no es trivial, requiriéndose la resolución de un sistema de ecuaciones de dos variables en el dominio de los números reales. Antes de la publicación del trabajo desarrollado en esta Tesis, los modos de esta guía debían resolverse por medio de herramientas de análisis numérico, debido a que los métodos analíticos disponibles requerían en última instancia del uso de intersecciones gráficas para la resolución del sistema de ecuaciones. En esta Tesis se ha propuesto la resolución cuasi-analítica de esta guía combinando el uso de técnicas de continuación analítica para aproximar las funciones base [50] con el uso de un algoritmo de publicación reciente para resolver sistemas de ecuaciones [52]. La herramienta de análisis electromagnético desarrollada se valida a través de distintos casos de estudio que incluye casos simétricos y asimétricos, resolviéndose un elevado número de modos con gran precisión.

Resulta obvio que el trabajo de investigación desarrollado en esta Tesis no puede abordar todas las posibles geometrías que puedan surgir de la mano de las novedosas técnicas de impresión 3D. Por esta razón se desarrolla el Capítulo 4, por completitud. Este Capítulo propone una formulación de hibridización eficiente entre los métodos de elementos finitos en 2D (*2D-Finite Element method*) y de ajuste modal (*Mode-Matching method*), para lo cual se emplean funciones base anidadas del métodos de elementos finitos en 2D, dando lugar a matrices que pueden emplearse de modo directo en el cálculo de las integrales requeridas por el método de ajuste modal. La formulación propuesta se puede emplear para el análisis eficiente de aquellos dispositivos de microondas formados por la sucesión de guías de onda con espectro modal analítico y numérico. Para validar la herramienta de análisis desarrollada, se proponen varios dispositivos ya publicados en la literatura, obteniéndose muy buenos resultados.

En la segunda parte de esta Tesis, correspondiente a los Capítulos 5 y 6, se aborda el diseño de filtros de microondas. Dado que la integración de nuevas geometrías en los futuros dispositivos de comunicaciones depende no sólo de la disponibilidad de herramientas de análisis electromagnético eficiente, sino también de la existencia de prototipos funcionales, se desarrollan dos filtros *inline* diseñados en cavidades triangulares equiláteras y cilíndrico-parabólicas, respectivamente. En aras de la consecución de diseños cada vez más compactos, se propone también un filtro *dual-mode* en cavidades triangulares equiláteras, el cual se fabrica, sintoniza y mide, obteniéndose resultados satisfactorios.

Siguiendo esta última línea de investigación en la que se busca proponer ideas novedosas para la consecución de dispositivos compactos, en esta Tesis se han propuesto alternativas tanto para filtros en guía de onda como para filtros basados en resonadores dieléctricos. Para los primeros se ha propuesto hacer uso de acoplos dispersivos fuente-carga, los cuales permiten generar ceros de transmisión adicionales fuera de la banda de paso. De esta forma, se mejora el rechazo de las frecuencias indeseadas sin incrementar el número de resonadores del filtro. Esta estrategia es especialmente adecuada en bandas altas de frecuencia, donde resulta complejo obtener resonadores de alto factor Q. La aplicación de acoplos dispersivos fuente carga se propone en los conocidos filtros *folded* en guía de onda rectangular dada su facilidad de implementación. En este contexto, se proponen varios circuitos equivalentes que modelan el comportamiento resonante de dichos acoplos, y se diseñan, fabrican y miden dos prototipos en banda W, uno en plano E y otro en plano H. El trabajo desarrollado a este respecto se realiza en el contexto de una estancia de investigación de 3 meses en el grupo Lehrstuhl für Hochfrequenztechnik de Kiel, donde se realiza la fabricación de los prototipos en banda W. Por otro lado, los circuitos equivalentes

propuestos, así como el prototipo en plano H se diseñan por la estudiante de doctorado de la presente Tesis.

Finalmente, en relación con los filtros de resonadores dieléctricos, en esta Tesis se propone hacer uso del resonador dieléctrico con forma triangular equilátera, ya publicado en el contexto de antenas basadas en resonadores dieléctricos pero no en el diseño de filtros de microondas. En concreto, se proponen varias topologías posibles, de las cuales se selecciona una, de planta hexagonal, para realizar el diseño de un prototipo a modo de prueba de concepto en la banda Ku. Los resultados obtenidos son prometedores, obteniéndose la respuesta deseada con un diseño de reducidas dimensiones.

8.2 Contribuciones originales de esta Tesis

Las principales contribuciones del trabajo desarrollado en esta Tesis se resumen en esta sección, organizadas de acuerdo a dos objetivos principales:

1. Contribuciones al análisis electromagnético eficiente de geometrías no convencionales en guía de onda:

    1.1. Desarrollo de una herramienta completa de análisis asistido por ordenador basada en el método de ajuste modal (*Mode-Matching method*) para dispositivos en guía de onda formados por bloques de guías triangulares equiláteras. Esta herramienta incluye un paquete software que permite analizar casos de geometrías rotadas e incluye una rutina de validación de cumplimiento de condiciones de contorno.

    1.2. Desarrollo de una herramienta de análisis asistido por ordenador basada en el uso de ondas planas para analizar mediante la técnica de ajuste modal (*Mode-Matching*) dispositivos en guía de onda formados por bloques de guías triangulares equiláteras y otras geometrías canónicas en guía rectangular, circular y elíptica.

    1.3. Desarrollo de una herramienta de análisis asistido por ordenador para la resolución cuasi-analítica del espectro modal de la guía parabólico-cilíndrica de contorno simétrico y asimétrico.

    1.4. Desarrollo de una herramienta de análisis asistido por ordenador de hibridación eficiente entre los métodos de elementos finitos en 2D (*2D-Finite Element method*) y de ajuste modal (*Mode-Matching method*) basada en el uso de funciones base anidadas de elementos finitos, para dispositivos de microondas formados por la sucesión de guías de onda con espectro modal analítico y numérico.

2. Contribuciones a la integración de nuevas geometrías y estructuras de acoplo en filtros de microondas:

    2.1. Diseño de tres filtros en guías de onda no convencionales, diseñados como prueba de concepto para su futura integración en sistemas de telecomunicación futuros. Se han diseñado dos prototipos de orden 7 y 9, el primero en cavidades triangulares equiláteras y el segundo en cavidades asimétricas cilíndrico-parabólicas respectivamente en la banda K.

2.2. Diseño de un filtro dual-mode en banda Ku en cavidades triangulares equiláteras. Este prototipo, diseñado, fabricado y medido, hace uso de la degeneración modal presente en este tipo de geometría para la obtención de un prototipo compacto, y ha demostrado ser una buena alternativa a otros prototipos dual-mode convencionales.

2.3. Estudio de acoplos fuente-carga dispersivos y de su integración en los conocidos como fully canonical folded filters. Se han propuesto varios circuitos equivalentes para modelar la respuesta electromagnética observada, facilitando así la integración de este comportamiento por medio de un único inversor fuente-carga resonante.

2.4. Diseño, fabricación y medida de dos prototipos en guía de onda rectangular, en banda W y con acoplos fuente-carga dispersivos. Uno de los prototipos de orden 4 se diseña en plano E con dos ceros de transmisión fuera de la banda de paso y ecualización de fase. El otro prototipo, también de orden 4, se diseña en plano H haciendo uso de cavidades mixtas, unas basadas en el modo TE_{101} y otras en el modo TE_{102}, siendo capaz de generar respuestas asimétricas con ceros de transmisión adicionales.

2.5. Diseño de un filtro de resonadores dieléctricos de forma triangular equilátera en banda Ku. El prototipo diseñado tiene orden 6 y planta hexagonal, presentando un tamaño significativamente reducido gracias a la geometría empleada. Se proponen otras topologías alternativas muy compactas que hacen uso de este resonador para futuros diseños.

8.3 Lista de publicaciones

A continuación de detalla la lista de publicaciones de la presente Tesis:

8.3.1 Artículos en revistas internacionales

[1] A. Morán-López, J. Córcoles, J. A. Ruiz-Cruz, J. R. Montejo-Garai, and J. M. Rebollar, "Robust calculation of the modes in parabolic cylinder metallic waveguides by means of a root-finding method for bivariate functions," *IEEE Transactions on Microwave Theory and Techniques*, vol. 66, no. 2, pp. 623–632, 2018. DOI: 10.1109/TMTT.2017.2777969.

[2] J. Córcoles, A. Morán-López, and J. A. Ruiz-Cruz, "Nested 2D finite-element function-spaces formulation for the mode-matching problem of arbitrary cross-section waveguide devices," *Applied Mathematical Modelling*, vol. 60, pp. 286–299, 2018. DOI: 10.1016/j.apm.2018.03.019.

[3] A. Morán-López, J. Córcoles, J. A. Ruiz-Cruz, J. R. Montejo-Garai, and J. M. Rebollar, "Electromagnetic scattering at the waveguide step between equilateral triangular waveguides," *Advances in Mathematical Physics*, pp.1-16, vol. 2016, 2016. DOI: 10.1155/2016/2974675.

8.3.2 Publicaciones en congresos internacionales

[1] D. Miek, A. Morán-López, J. A. Ruiz-Cruz, and M. Höft, "Ku-Band waveguide filter with multiple transmission zeros by resonant source to load and bypass cross-coupling," in *2019 49th European Microwave Conference (EuMC)*. Aceptado.

[2] D. Miek, A. Morán-López, J. A. Ruiz-Cruz, and M. Höft, "Improved fully canonical phase equalized W-band waveguide filter with dispersive coupling inverter," in *2018 48th European Microwave Conference (EuMC)*. IEEE, 2018, pp. 166–169. DOI: 10.23919/EuMC.2018.8541743.

[3] A. Morán-López, J. Córcoles, J. A. Ruiz-Cruz, J. R. Montejo-Garai, and J. M. Rebollar, "Dual-mode filters in equilateral triangular waveguides with wide spurious-free response," in *2017 IEEE MTT-S International Microwave Symposium (IMS)*. IEEE, 2017, pp. 1192–1195. DOI: 10.1109/MWSYM.2017.8058816.

[4] A. Morán-López, J. Córcoles, J. A. Ruiz-Cruz, J. R. Montejo-Garai, and J. M. Rebollar, "Direct computation of parabolic waveguide modes via a bivariate root-finding algorithm," in *2017 IEEE MTT-S International Conference on Numerical Electromagnetic and Multiphysics Modeling and Optimization for RF, Microwave, and Terahertz Applications (NEMO)*. IEEE, 2017, pp. 152–154. DOI: 10.1109/NEMO.2017.7964217.

[5] A. Morán-López, J. Córcoles, and J. A. Ruiz-Cruz, "Efficient computation and orthonormalization of multiple TEM numerical modes arising from FEM for microwave computer-aided-design," in *2017 IEEE MTT-S International Conference on Numerical Electromagnetic and Multiphysics Modeling and Optimization for RF, Microwave, and Terahertz Applications (NEMO)*. IEEE, 2017, pp. 197–199. DOI: 10.1109/NEMO.2017.7964232.

[6] A. Morán-López, J. Córcoles, J. A. Ruiz-Cruz, J. R. Montejo-Garai, and J. M. Rebollar, "Generalized scattering matrix of the discontinuity between an equilateral triangular waveguide and a rectangular, circular or elliptical waveguide," in *2016 Asia-Pacific Microwave Conference (APMC)*. IEEE, 2016, pp. 1–4. DOI: 10.1109/APMC.2016.7931283.

8.3.3 Artículos y contribuciones en desarrollo

Esta subsección contiene artículos y contribuciones ya enviados para su revisión o en preparación para su envío:

[1] A. Morán-López, J. Córcoles, J. A. Ruiz-Cruz, J. R. Montejo-Garai, and J. M. Rebollar, "Closed-form solution for the unloaded q-factor of the equilateral triangular cavity," *Enviado a la revista Electronic Letters.*

[2] D. Miek, A. Morán-López, J. A. Ruiz-Cruz, and M. Höft, "Extra transmission zeros in h-plane W-band waveguide filter configurations," *Enviado a la revista IEEE Microwave and Wireless Components Letters (manuscript ID: MWCL-19-0207).*

8.3.4 Otras publicaciones

Esta subsección contiene dos publicaciones en conferencias (una nacional y otra internacional) desarrolladas en relación con el contenido del Capítulo 5 de esta Tesis, con anterioridad a la misma:

[1] A. Morán-López, and J. A. Ruiz-Cruz, "Diseño de un filtro combline en banda S por subdivisión y optimización en etapas," in *XXXI Simposium Nacional de la Union´ Cient´ıfica Internacional de Radio (URSI)*. Madrid, 2016, pp. 1–4.

[2] A. Morán-López and J. A. Ruiz-Cruz, "Optimization method for the design of microwave filters based on sequential stages," in *Congress on Numerical Methods (CMN)*. Lisbon, 2015, pp. 1–4.

A Electromagnetic field in a homogeneous waveguide

The electric and magnetic field of a waveguide with translation symmetry along the propagation axis with arbitrary cross-section surrounded by perfect electric conductor and filled with isotropic and homogeneous dielectric, can be described by a modal series [105]:

$$\vec{E} = \sum_{p=1}^{\infty} \left(a_p e^{-\gamma_p z} + b_p e^{\gamma_p z}\right)\vec{e}_p + \left(a_p e^{-\gamma_p z} - b_p e^{\gamma_p z}\right)e_{zp}\hat{z} \tag{A.1}$$

$$\vec{H} = \sum_{p=1}^{\infty} \left(a_p e^{-\gamma_p z} - b_p e^{\gamma_p z}\right)\vec{h}_p + \left(a_p e^{-\gamma_p z} + b_p e^{\gamma_p z}\right)h_{zp}\hat{z}. \tag{A.2}$$

Each modal solution identified by subindex p in (A.1)-(A.2) is obtained from the resolution of the scalar Helmholtz equation:

$$\Delta_t \Phi_p + k_{cp}^2 \Phi_p = 0. \tag{A.3}$$

In order to solve the previous equation, Neumann and Dirichlet conditions must be imposed, from which TE modes (Transversal Electric) and TM modes (Transversal Magnetic) arise. For TEM modes, Laplace equation is involved.

A.1 TE modes

TE modes are the solution to (A.3), when Neumann-type boundary conditions are applied, that is when:

$$\left.\frac{\partial \Phi_p}{\partial n}\right|_{\zeta} = 0, \tag{A.4}$$

where ζ is the contour of the waveguide.

Once the pairs of eigenfunctions Φ_p and corresponding eigenvalues k_{cp} of (A.3) have been solved after imposing (A.4), the electromagnetic field of a TE mode that takes part of the modal series in (A.1)-(A.2) can be computed as:

$$e_{zp} = 0, \tag{A.5}$$

$$h_{zp} = -\frac{\sqrt{Y_p}k_{cp}^2}{\gamma_p}\sqrt{N_p}\Phi_p, \tag{A.6}$$

$$\vec{e}_p = \sqrt{Z_p}\sqrt{N_p}\nabla_t\Phi_p \times \hat{z}, \tag{A.7}$$

$$\vec{h}_p = \sqrt{Y_p}\sqrt{N_p}\nabla_t\Phi_p. \tag{A.8}$$

In these expressions the wave impedance (admittance) Z_p (Y_p) is defined as

$$Z_p = Y_p^{-1} = \frac{j\omega\mu}{\gamma_p}, \tag{A.9}$$

and the normalization constant N_p is obtained from

$$N_p = [\iint_{A_s} |\nabla_t\Phi_p|^2\, dS]^{-1} \;=\; [\, k_{cp}^2 \iint_{A_s} \Phi_p^2 dS\,]^{-1}. \tag{A.10}$$

This normalizing constant guarantees that the modes fulfill:

$$\iint_{A_s} \vec{e}_p \times \vec{h}_p \cdot \hat{z}\, dS = 1. \tag{A.11}$$

A.2 TM modes

TM modes are the solution to (A.3), when Dirichlet-type boundary conditions are applied, that is when:

$$\Phi_p\big|_\zeta = 0, \tag{A.12}$$

where ζ is the contour of the waveguide.

After imposing (A.12), the electromagnetic field of a TM mode that takes part of the modal series in (A.1)-(A.2) can be computed as:

$$e_{zp} = -\frac{\sqrt{Z_p}k_{cp}^2}{\gamma_p}\sqrt{N_p}\Phi_p \tag{A.13}$$

$$h_{zp} = 0, \tag{A.14}$$

$$\vec{e}_p = \sqrt{Z_p}\sqrt{N_p}\nabla_t\Phi_p, \tag{A.15}$$

$$\vec{h}_p = \sqrt{Y_p}\sqrt{N_p}\hat{z} \times \nabla_t\Phi_p. \tag{A.16}$$

In these expressions the wave impedance (admittance) Z_p (Y_p) is defined as

$$Z_p = Y_p^{-1} = \frac{\gamma_p}{j\omega\varepsilon}, \tag{A.17}$$

and the normalization constant N_p is analogous to the TE mode family:

$$N_p = [\iint_{A_s} |\nabla_t\Phi_p|^2\, dS]^{-1} \;=\; [\, k_{cp}^2 \iint_{A_s} \Phi_p^2 dS\,]^{-1}. \tag{A.18}$$

A.3 TEM modes

TEM modes arise in multiconductor waveguides, and are the solution to the Laplace equation:

$$\Delta_t \Phi_p = 0, \tag{A.19}$$

which is the same as (A.3) with $k_{cp} = 0$. In a structure with $N+1$ unconnected conductors, each one with contour ζ_n, N linearly independent TEM modes fulfil equation (A.19) with non-homogeneous Dirichlet boundary conditions:

$$\Phi_p\big|_{\zeta_n} = v_{pn}, \tag{A.20}$$

where v_{pn} are the potentials from $n = 1, \ldots, N+1$ for each TEM mode p. The chosen values of v_{pn} for a TEM mode must be a linearly independent set from the chosen values of the rest of TEM modes to be computed. Then, the electromagnetic field of a TEM mode that takes part of the modal series in (A.1)-(A.2) can be computed as:

$$\vec{e}_p = \sqrt{Z_p}\sqrt{N_p}\nabla_t \Phi_p, \tag{A.21}$$

$$\vec{h}_p = \sqrt{Y_p}\sqrt{N_p}\,\hat{z} \times \nabla_t \Phi_p, \tag{A.22}$$

with $e_{zp} = 0$ and $h_{zp} = 0$. In these expressions the wave impedance (admittance) Z_p (Y_p) is defined as:

$$Z_p = Y_p^{-1} = \sqrt{\frac{\mu}{\varepsilon}}. \tag{A.23}$$

Finally, the normalization constant N_p is computed as:

$$N_p = [\iint_{A_s} |\nabla_t \Phi_p|^2 \, dS]^{-1}. \tag{A.24}$$

Bibliography

[1] M. R. Palattella, M. Dohler, A. Grieco, G. Rizzo, J. Torsner, T. Engel, and L. Ladid, "Internet of things in the 5G era: Enablers, architecture, and business models," *IEEE Journal on Selected Areas in Communications*, vol. 34, no. 3, pp. 510–527, 2016.

[2] "Space-enabled internet of things shown in Berlin," available at the ESA website: https://www.esa.int/Our_Activities/Telecommunications_Integrated_Applications/Space-enabled_Internet_of_Things_shown_in_Berlin, last access: 2019-03-01.

[3] "Satellite for 5G overview," available at the ESA website: https://artes.esa.int/satellite-5g/overview, last access: 2019-03-01.

[4] "Space and SATCOM for 5G : European transport and connected mobility," available at the ESA website: https://artes.esa.int/esaespi-conference-%E2%80%98space-and-satcom-5g-european-transport-and-connected-mobility, last access: 2019-03-01.

[5] R. J. Cameron, C. M. Kudsia, and R. Mansour, *Microwave filters for communication systems*. John Wiley & Sons, 2015.

[6] J.-S. G. Hong and M. J. Lancaster, *Microstrip filters for RF/microwave applications*. John Wiley & Sons, 2004, vol. 167.

[7] I. Hunter, *Theory and design of microwave filters*. The Institution of Engineering and Technology, 2001.

[8] A. Wexler, "Solution of waveguide discontinuities by modal analysis," *IEEE Transactions on Microwave Theory and Techniques*, vol. 15, no. 9, pp. 508–517, 1967.

[9] T. Itoh, *Numerical techniques for microwave and millimeter-wave passive structures*. Wiley-Interscience, 1989.

[10] F. Arndt, R. Beyer, J. M. Reiter, T. Sieverding, and T. Wolf, "Automated design of waveguide components using hybrid mode-matching/numerical EM building-blocks in optimization-oriented CAD frameworks-state of the art and recent advances," *IEEE Transactions on Microwave Theory and Techniques*, vol. 45, no. 5, pp. 747–760, 1997.

[11] M. Guglielmi, R. Sorrentino, and G. Conciauro, *Advanced Modal Analysis: CAD Techniques for Waveguide Components and Filter*. John Wiley & Sons, Inc., 1999.

[12] F. Arndt, J. Brandt, V. Catina, J. Ritter, I. Rullhusen, J. Dauelsberg, U. Hilgefort, and W. Wessel, "Fast CAD and optimization of waveguide components and aperture antennas by hybrid MM/FE/MoM/FD methods-state-of-the-art and recent advances," *IEEE Transactions on Microwave Theory and Techniques*, vol. 52, no. 1, pp. 292–305, 2004.

[13] "CST Microwave Studio," https://www.cst.com/, last access: 2019-03-01.

[14] "Ansys High Frequency Structure Simulator," https://www.ansys.com, last access: 2019-03-01.

[15] "Mician," https://www.mician.com/, last access: 2019-03-01.

[16] "WASP-NET," http://www.wasp-net.com, last access: 2019-03-01.

[17] N. Marcuvitz, *Waveguide handbook*. The Institution of Engineering and Technology, 1951.

[18] G. Matthaei, L. Young, and E. Jones, "Microwave filters, impedance-matching networks, and coupling structures, artech house," *Artech House Book*, 1980.

[19] R. Levy and S. B. Cohn, "A history of microwave filter research, design, and development," *IEEE Transactions on Microwave Theory and Techniques*, vol. 32, no. 9, pp. 1055–1067, 1984.

[20] J. Uher, J. Bornemann, and U. Rosenberg, *Waveguide components for antenna feed systems: Theory and CAD*. Artech House Publishers, 1993.

[21] Y.-B. Jung, S. Eom, J. Yun, S. Jeon, and C. Kim, "A horn antenna design with novel waveguide polarizer for mobile satellite communications applications," in *2009 IEEE 70th Vehicular Technology Conference Fall*. IEEE, 2009, pp. 1–3.

[22] A. El Kamili, A. Tribak, J. Terhzaz, Á. Mediavilla Sánchez *et al.*, "A dual band orthomode transducer in K/Ka bands for satellite communications applications," *Progress In Electromagnetics Research Letters*, vol. 73, pp. 73–82, 2018.

[23] L. Pelliccia, C. Tomassoni, F. Cacciamani, P. Vallerotonda, R. Sorrentino, J. Galdeano, and C. Ernst, "Very-compact waveguide bandpass filter based on dual-mode TM cavities for satellite applications in Ku-band," in *2018 48th European Microwave Conference (EuMC)*. IEEE, 2018, pp. 93–96.

[24] H. Hu, K.-L. Wu, and R. J. Cameron, "Stepped circular waveguide dual-mode filters for broadband contiguous multiplexers," *IEEE Transactions on Microwave Theory and Techniques*, vol. 61, no. 1, pp. 139–145, 2013.

[25] U. Rosenberg, J. Bornemann, and S. Amari, "Design of dual-band waveguide transformers," in *IEEE MTT-S International Microwave Symposium Digest, 2005.* IEEE, 2005, pp. 1215–1218.

[26] E. Canessa, C. Fonda, and M. Zennaro, "Low-cost 3D printing for science," *Education & Sustainable Development*, 2013.

[27] I. O. for Standardization (ISO), "Additive manufacturing - General principles - Terminology," 2015.

[28] C. Barnatt, *3D Printing Third Edition.* CreateSpace Independent Publishing Platform, 2016.

[29] I. O. Saracho-Pantoja, J. R. Montejo-Garai, J. A. Ruiz-Cruz and J. M. Rebollar, "Low-cost additive manufacturing: A new approach to microwave waveguide engineering education through 3D printing," *International Journal of Engineering Education*, vol. 33, pp. 741–750, 2017.

[30] H. Kodama, "A scheme for three-dimensional display by automatic fabrication of three-dimensional model," *IEICE Trans. on Electronics*, pp. 237–241, 1981.

[31] W. Otter and S. Lucyszyn, "3D printing of microwave components for 21st century applications," in *2016 IEEE MTT-S International Microwave Workshop Series on Advanced Materials and Processes for RF and THz Applications (IMWS-AMP).* IEEE, 2016, pp. 1–3.

[32] O. A. Peverini, G. Addamo, R. Tascone, G. Virone, P. Cecchini, R. Mizzoni, F. Calignano, E. P. Ambrosio, D. Manfredi, and P. Fino, "Enhanced topology of E-plane resonators for high-power satellite applications," *IEEE Transactions on Microwave Theory and Techniques*, vol. 63, no. 10, pp. 3361–3373, 2015.

[33] J. R. Montejo-Garai, I. O. Saracho-Pantoja, C. A. Leal-Sevillano, J. A. Ruiz-Cruz, and J. M. Rebollar, "Design of microwave waveguide devices for space and ground application implemented by additive manufacturing," in *2015 International Conference on Electromagnetics in Advanced Applications (ICEAA).* IEEE, 2015, pp. 325–328.

[34] G. Addamo, O. A. Peverini, F. Calignano, D. Manfredi, F. Paonessa, G. Virone, and G. Dassano, "3D printing of high-performance feed horns from Ku to V bands," *IEEE Antennas and Wireless Propagation Letters*, vol. 17, no. 11, pp. 2036–2040, 2018.

[35] G. Addamo, O. A. Peverini, D. Manfredi, F. Calignano, F. Paonessa, G. Virone, R. Tascone, and G. Dassano, "Additive manufacturing of Ka-Band dual-polarization waveguide components," *IEEE Transactions on Microwave Theory and Techniques*, vol. 66, no. 8, pp. 3589–3596, 2018.

[36] G. Lamé, *Leçons sur la théorie analytique de la chaleur.* Mallet-Bachelier, 1861.

[37] S. Schelkunoff, *Electromagnetic Waves.* Van Nostrand, 1943.

[38] P. Overfelt and D. White, "TE and TM modes of some triangular cross-section waveguides using superposition of plane waves (short paper)," *IEEE Transactions on Microwave Theory and Techniques*, vol. 34, no. 1, pp. 161–167, 1986.

[39] C. Wang, "Exact solution of equilateral triangular waveguide," *Electronics Letters*, vol. 46, no. 13, pp. 925–927, 2010.

[40] B. J. McCartin, "Eigenstructure of the equilateral triangle, Part I: The Dirichlet problem," *Siam Review*, vol. 45, no. 2, pp. 267–287, 2003.

[41] B. J. McCartin, "Eigenstructure of the equilateral triangle, Part II: The Neumann problem," *Mathematical Problems in Engineering*, vol. 8, no. 6, pp. 517–539, 2002.

[42] O. Asfar, "The symmetric and antisymmetric eigenvalue problem for electromagnetic equilateral triangular waveguides via plane wave reconstruction," *Multidisciplinary Digital Publishing Institute Proceedings*, vol. 2, no. 1, p. 13, 2018.

[43] R. E. Collin, *Foundations for microwave engineering*. John Wiley & Sons, 2007.

[44] D. M. Pozar, *Microwave engineering*. John Wiley & Sons, 2009.

[45] C. G. Montgomery, R. H. Dicke, and E. M. Purcell, *Principles of microwave circuits*. The Institution of Engineering and Technology, 1987.

[46] J. Zagrodzinski, "Electromagnetic fields in parabolic waveguides and resonators," in *Proc. Third Colloquium on Microwave Communications, Academiai Kiado, Budapest*, 1968, pp. 457–465.

[47] J. C. P. Miller, *Tables of Weber Parabolic Cylinder Functions Giving Solutions of the Differential Equation* $d^2y/dx^2 + (1/4x^2 - a)y$. HM Stationery Office, 1955.

[48] A. Gil, J. Segura, and N. M. Temme, "Fast and accurate computation of the weber parabolic cylinder function w (a, x)," *IMA journal of numerical analysis*, vol. 31, no. 3, pp. 1194–1216, 2011.

[49] J. S. Amparo Gil and N. M. Temme, "Algorithm 914: parabolic cylinder function w (a, x) and its derivative," *ACM Transactions on Mathematical Software (TOMS)*, vol. 38, no. 1, p. 6, 2011.

[50] C. S. Kenney and P. Overfelt, "A simple approach to mode analysis for parabolic waveguides," *IEEE Transactions on Microwave Theory and Techniques*, vol. 39, no. 3, pp. 405–412, Mar. 1991.

[51] P. Morse and H. Feshbach, *Methods of Theoretical Physics*. McGraw-Hill, New York, 1953.

[52] Y. Nakatsukasa, V. Noferini, and A. Townsend, "Computing the common zeros of two bivariate functions via Bézout resultants," *Numerische Mathematik*, vol. 129, no. 1, pp. 181–209, Jan. 2015.

[53] J.-M. Jin, *The finite element method in electromagnetics*. John Wiley & Sons, 2002.

[54] G. Pelosi, R. Coccioli, and S. Selleri, *Quick finite elements for electromagnetic waves*. Artech House, 2009.

[55] J. Zapata and J. Garcia, "Analysis of passive microwave structures by a combined finite element generalized scattering matrix method," in *Proc. of the 1991 North American Radio Science Meeting*, 1991, p. 146.

[56] J. Zapata, J. Garcia, L. Valor, and J. Garai, "Field-theory analysis of cross-iris coupling in circular waveguide resonators," *Microwave and Optical Technology Letters*, vol. 6, no. 16, pp. 905–907, 1993.

[57] J. Montejo-Garai, L. Valor, J. Garcia, and J. Zapata, "A full-wave analysis of tuning and coupling posts in dual-mode circular waveguide filters," *Microwave and Optical Technology Letters*, vol. 7, no. 11, pp. 505–507, 1994.

[58] R. Beyer and F. Arndt, "Efficient modal analysis of waveguide filters including the orthogonal mode coupling elements by an MM/FE method," *IEEE Microwave and Guided Wave Letters*, vol. 5, no. 1, pp. 9–11, 1995.

[59] L. Wray, G. Van Ommering, and B. Kosinski, "Commercial communications satellites: A unique business model for space programs," in *First International Technology Management Conference*. IEEE, 2011, pp. 368–378.

[60] A. E. Williams, "A four-cavity elliptic waveguide filter," *IEEE Transactions on Microwave Theory and Techniques*, vol. 18, no. 12, pp. 1109–1114, 1970.

[61] M. Kunes, "Microwave multiplexers for space applications," *Electronics & communication engineering journal*, vol. 10, no. 1, pp. 29–35, 1998.

[62] M. Yu, D. J. Smith, A. Sivadas, and W. Fitzpatrick, "A dual mode filter with trifurcated iris and reduced footprint," in *2002 IEEE MTT-S International Microwave Symposium Digest (Cat. No. 02CH37278)*, vol. 3. IEEE, 2002, pp. 1457–1460.

[63] E. Doumanis, G. Goussetis, and S. Kosmopoulos, *Filter design for satellite communications: helical resonator technology*. Artech House, 2015.

[64] M. Politi and A. Fossati, "Direct coupled waveguide filters with generalized chebyshev response by resonating coupling structures," in *The 40th European Microwave Conference*. IEEE, 2010, pp. 966–969.

[65] L. Szydlowski, A. Lamecki, and M. Mrozowski, "Coupled-resonator waveguide filter in quadruplet topology with frequency-dependent coupling–a design based on coupling matrix," *IEEE Microwave and Wireless Components Letters*, vol. 22, no. 11, pp. 553–555, 2012.

[66] L. Szydlowski and M. Mrozowski, "A self-equalized waveguide filter with frequency-dependent (resonant) couplings," *IEEE Microwave and Wireless Components Letters*, vol. 24, no. 11, pp. 769–771, 2014.

[67] S. Amari, J. Bornemann, W. Menzel, and F. Alessandri, "Diplexer design using pre-synthesized waveguide filters with strongly dispersive inverters," in *IEEE MTT-S International Microwave Symposium Digest*. IEEE, 2001, pp. 1627–1630.

[68] S. Fiedziuszko, D. Doust, and S. Holme, "Satellite L-band output multiplexer utilizing single and dual mode dielectric resonators," in *IEEE MTT-S International Microwave Symposium Digest*. IEEE, 1989, pp. 683–686.

[69] S. Lundquist, M. Mississian, M. Yu, and D. Smith, "Application of high power output multiplexers for communications satellites," in *18th International Communications Satellite Systems Conference and Exhibit*, 2000, p. 1191.

[70] Y. Latouche, D. Gasperoni, and J. J. Herren, "High power C-band dielectric resonator filters for output multiplexers," in *2001 IEEE MTT-S International Microwave Symposium Digest (Cat. No. 01CH37157)*, vol. 3. IEEE, 2001, pp. 1607–1610.

[71] A. Panariello, M. Yu, and C. Ernst, "Ku-band high power dielectric resonator filters," *IEEE Transactions on Microwave Theory and Techniques*, vol. 61, no. 1, pp. 382–392, 2013.

[72] M. Ruggieri, S. De Fina, M. Pratesi, E. Saggese, and C. Bonifazi, "The W-band data collection experiment of the david mission," *IEEE Transactions on Aerospace and Electronic Systems*, vol. 38, no. 4, pp. 1377–1387, 2002.

[73] S. De Fina, M. Ruggieri, and A. V. Bosisio, "Exploitation of the W-band for high capacity satellite communications," *IEEE Transactions on Aerospace and Electronic Systems*, vol. 39, no. 1, pp. 82–93, 2003.

[74] J. A. Ruiz-Cruz, J. R. Montejo-Garai, and J. M. Rebollar, "Computer aided design of waveguide devices by mode-matching methods," in *Passive Microwave Components and Antennas*. IntechOpen, 2010.

[75] H. Patzelt and F. Arndt, "Double-plane steps in rectangular waveguides and their application for transformers, irises, and filters," *IEEE Transactions on Microwave Theory and Techniques*, vol. 30, no. 5, pp. 771–776, 1982.

[76] J. Esteban and J. M. Rebollar, "Generalized scattering matrix of generalized two-port discontinuities: application to four-port and nonsymmetric six-port couplers," *IEEE Transactions on Microwave Theory and Techniques*, vol. 39, no. 10, pp. 1725–1734, 1991.

[77] C. Sabatier, "Scattering at an offset circular hole in a rectangular waveguide," *IEEE Transactions on Microwave Theory and Techniques*, vol. 40, no. 3, pp. 587–592, 1992.

[78] R. H. MacPhie and K.-L. Wu, "Scattering at the junction of a rectangular waveguide and a larger circular waveguide," *IEEE Transactions on Microwave Theory and Techniques*, vol. 43, no. 9, pp. 2041–2045, 1995.

[79] P. Matras, R. Bunger, and F. Arndt, "Mode-matching analysis of the step discontinuity in elliptical waveguides," *IEEE Microwave and Guided Wave Letters*, vol. 6, no. 3, pp. 143–145, 1996.

[80] K.-L. Chan and S. Judah, "Modal analysis at the junction formed by a circular or an elliptic waveguide and a translated and rotated elliptic waveguide," *IEE Proceedings-Microwaves, Antennas and Propagation*, vol. 145, no. 6, pp. 501–507, 1998.

[81] A. P. Orfanidis, G. A. Kyriacou, and J. N. Sahalos, "A mode-matching technique for the study of circular and coaxial waveguide discontinuities based on closed-form coupling integrals," *IEEE Transactions on Microwave Theory and Techniques*, vol. 48, no. 5, pp. 880–883, 2000.

[82] M. Mongiardo and C. Tomassoni, "Modal analysis of discontinuities between elliptical waveguides," *IEEE Transactions on Microwave Theory and Techniques*, vol. 48, no. 4, pp. 597–605, 2000.

[83] G. Figlia and G. Gentili, "On the line-integral formulation of mode-matching technique," *IEEE Transactions on Microwave Theory and Techniques*, vol. 50, no. 2, pp. 578–580, 2002.

[84] J. Córcoles, M. González de Aza, and J. Zapata, "Full-wave analysis of finite periodic cylindrical conformal arrays with floquet spherical modes and a hybrid finite element–generalized scattering matrix method," *Journal of Electromagnetic Waves and Applications*, vol. 28, no. 1, pp. 102–111, 2014.

[85] J. Rubio, J. Corcoles, and M. G. de Aza, "Inclusion of the feeding network effects in the generalized-scattering-matrix formulation of a finite array," *IEEE Antennas and Wireless Propagation Letters*, vol. 8, pp. 819–822, 2009.

[86] F. Arndt, B. Koch, H.-J. Orlok, and N. Schroder, "Field theory design of rectangular waveguide broad-wall metal-insert slot coulplers for millimeter-wave applications," *IEEE Transactions on Microwave Theory and Techniques*, vol. 33, no. 2, pp. 95–104, 1985.

[87] F. Arndt, J. Dittloff, U. Papziner, D. Fasold, N. Nathrath, and H. Wolf, "Rigorous field theory design of compact and lightweight broadband diplexers for satellite communication systems," in *1989 19th European Microwave Conference*. IEEE, 1989, pp. 1214–1219.

[88] J. Esteban and J. M. Rebollar, "Field theory CAD of septum OMT-polarizers," in *IEEE Antennas and Propagation Society International Symposium 1992 Digest*. IEEE, 1992, pp. 2146–2149.

[89] M. Abramowitz and I. A. Stegun, *Handbook of mathematical functions: with formulas, graphs, and mathematical tables*. Courier Corporation, 1965, vol. 55.

[90] J. A. Stratton, *Electromagnetic theory*. John Wiley & Sons, 2007.

[91] N. W. McLachlan, *Theory and application of Mathieu functions*. Dover Pub., New York, 1951.

[92] S. Zhang and J.-M. Jin, *Computation of special functions*. Wiley Interscience, 1996.

[93] P. Moon and D. E. Spencer, *Field theory handbook: including coordinate systems, differential equations and their solutions*. Springer, 2012.

[94] R. D. Spence and C. Wells, "The propagation of electromagnetic waves in parabolic pipes," *Physical Review*, vol. 62, no. 1-2, p. 58, 1942.

[95] O. Wada and M. Nakajima, "Circular to rectangular waveguide mode conversion through a parabolic cylinder waveguide–TE_{on} incident," *Electronics and Communications in Japan (Part II: Electronics)*, vol. 70, no. 9, pp. 20–31, 1987.

[96] P. Daly, "Finite element approach to propagation in elliptical and parabolic waveguides," *International Journal for Numerical Methods in Engineering*, vol. 20, no. 4, pp. 681–688, Apr. 1984.

[97] R. J. Noriega-Manez and J. C. Gutiérrez-Vega, "Mode structure and attenuation characteristics of hollow parabolic waveguides," *JOSA B*, vol. 24, no. 9, pp. 2273–2278, 2007.

[98] T. Larsen, *Odd an even parabolic cylinder functions. A FORTRAN subroutine*. Lab. Electromagnet. Theory, Tech. Univ. of Denmark, Lyngby, Rep. R 89, 1971.

[99] M. Alnaes *et al.*, "The FEniCS project version 1.5," *Archive of Numerical Software*, vol. 3, no. 100, pp. 9–23, 2015.

[100] V. Hernández, J. E. Román, and V. Vidal, "SLEPc: A scalable and flexible toolkit for the solution of eigenvalue problems," *ACM Trans. Math. Softw.*, vol. 31, no. 3, pp. 351–362, Sep. 2005.

[101] J. A. Ruiz-Cruz and J. M. Rebollar, "Eigenmodes of waveguides using a boundary contour mode-matching method with an FFT scheme," *International Journal of RF and Microwave Computer-Aided Engineering*, vol. 15, no. 3, pp. 286–295, 2005.

[102] T. Larsen, "On the relation between modes in rectangular, elliptical, and parabolic waveguides and a mode-classifying system," *IEEE Transactions on Microwave Theory and Techniques*, vol. 20, no. 6, pp. 379–384, Jun. 1972.

[103] S. Amari and M. Bekheit, "A new class of dual-mode dual-band waveguide filters," *IEEE Transactions on Microwave Theory and Techniques*, vol. 56, no. 8, pp. 1938–1944, 2008.

[104] J. A. Ruiz-Cruz, Y. Zhang, J. R. Montejo-Garai, J. M. Rebollar, and K. A. Zaki, "Longitudinal dual-mode filters in rectangular waveguide," in *2008 IEEE MTT-S International Microwave Symposium Digest*. IEEE, 2008, pp. 631–634.

[105] R. E. Collin, *Field theory of guided waves*. Wiley-IEEE Press, 1960.

[106] G. H. Golub and C. F. Van Loan, *Matrix computations*. JHU press, 2012, vol. 3.

[107] J. A. Ruiz-Cruz, Y. Zhang, K. A. Zaki, A. J. Piloto, and J. Tallo, "Ultra-wideband LTCC ridge waveguide filters," *IEEE Microwave and Wireless Components Letters*, vol. 17, no. 2, pp. 115–117, 2007.

[108] N. Yoneda, R. Miyazaki, I. Matsumura, and M. Yamato, "A design of novel grooved circular waveguide polarizers," *IEEE Transactions on Microwave Theory and Techniques*, vol. 48, no. 12, pp. 2446–2452, 2000.

[109] A. Mediavilla, J. L. Cano, and K. Cepero, "On the octave bandwidth properties of octagonal-shaped waveguide mode transformers," *IEEE Transactions on Microwave Theory and Techniques*, vol. 59, no. 10, pp. 2447–2451, 2011.

[110] J. A. Ruiz-Cruz, Y. Zhang, J. M. Rebollar, K. A. Zaki, J. R. Montejo-Garai, and A. J. Piloto, "TEM Mode-Matching analysis of multi-coupled strip-line filters," in *2007 IEEE/MTT-S International Microwave Symposium*. IEEE, 2007, pp. 541–544.

[111] J. A. Ruiz-Cruz, J. R. Montejo-Garai, and J. M. Rebollar, "Multi-section bow-tie steps for full-band waveguide polarization rotation," *IEEE Microwave and Wireless Components Letters*, vol. 20, no. 7, pp. 375–377, 2010.

[112] J. R. Montejo-Garai and J. Zapata, "Full-wave design and realization of multicoupled dual-mode circular waveguide filters," *IEEE Transactions on Microwave Theory and Techniques*, vol. 43, no. 6, pp. 1290–1297, 1995.

[113] C.-L. Hsu and J.-T. Kuo, "Microstrip realization of trisection synthesis with frequency-dependent admittance inverter," *Progress In Electromagnetics Research*, vol. 113, pp. 195–210, 2011.

[114] L. Szydlowski, A. Lamecki, and M. Mrozowski, "Coupled-resonator filters with frequency-dependent couplings: Coupling matrix synthesis," *IEEE Microwave and Wireless Components Letters*, vol. 22, no. 6, pp. 312–314, 2012.

[115] A. Haidar, H. Ezzeddine, and S. Bila, "Design of a dual-bandpass filter with dispersive coupling," in *2017 IEEE MTT-S International Microwave Symposium (IMS)*. IEEE, 2017, pp. 730–732.

[116] S. Amari and J. Bornemann, "Maximum number of finite transmission zeros of coupled resonator filters with source/load-multiresonator coupling and a given topology," in *Asia-Pacific Microwave Conference. Proceedings (Cat. No. 00TH8522)*. IEEE, 2000, pp. 1175–1177.

[117] K. Wakino, T. Nishikawa, and Y. Ishikawa, "Miniaturization technologies of dielectric resonator filters for mobile communications," *IEEE Transactions on Microwave Theory and Techniques*, vol. 42, no. 7, pp. 1295–1300, 1994.

[118] Y. Ishikawa, H. Wada, H. Nishida, and S. Hidaka, "TE_{101} triple mode dielectric resonator apparatus," Jun. 28 1994, US Patent 5,325,077.

[119] D. Fernando, I. Hunter, and V. Postoyalko, "A novel dual-mode $TE_{01\delta}$ dielectric resonator," in *MTT/ED/AP/LEO Societies Joint Chapter United Kingdom and Republic of Ireland Section. 1999 High Frequency Postgraduate Student Colloquium (Cat. No. 99TH8409)*. IEEE, 1999, pp. 48–53.

[120] T. Kurisu and S. Abe, "Multiple-mode dielectric resonator and method of adjusting characteristic of the resonator," Aug. 21 2001, US Patent 6,278,344.

[121] M. Hoft, "Y-shape dielectric dual-mode resonator," *IEEE Transactions on Microwave Theory and Techniques*, vol. 56, no. 12, pp. 3066–3071, 2008.

[122] M. Memarian and R. Mansour, "Dual-mode half-cut dielectric resonator filters," in *2009 IEEE MTT-S International Microwave Symposium Digest*. IEEE, 2009, pp. 1465–1468.

[123] M. Memarian and R. Mansour, "Dual-band half-cut dielectric resonator filters," in *2009 European Microwave Conference (EuMC)*. IEEE, 2009, pp. 555–558.

[124] M. Höft, "Dielectric TE dual-mode resonator filters," in *German Microwave Conference Digest of Papers*. IEEE, 2010, pp. 206–209.

[125] P. Rezaee and M. Höft, "A new class of compact dual-mode dielectric resonator filters," in *2016 IEEE MTT-S International Microwave Symposium (IMS)*. IEEE, 2016, pp. 1–3.

[126] R. J. Cameron, "Advanced coupling matrix synthesis techniques for microwave filters," *IEEE Transactions on Microwave Theory and Techniques*, vol. 51, no. 1, pp. 1–10, 2003.

[127] J. A. Ruiz-Cruz, K. A. Zaki, J. R. Montejo-Garai, and J. M. Rebollar, "Rectangular waveguide elliptic filters with capacitive and inductive irises and integrated coaxial excitation," *IEEE MTT-S International Microwave Symposium Digest*, pp. 269–272, 2005.

[128] U. Rosenberg, "New planar waveguide cavity elliptic function filters," in *Microwave Conference, 1995. 25th European.* IEEE, 1995, pp. 524–527.

[129] J.-Q. Ding, S.-C. Shi, K. Zhou, Y. Zhao, D. Liu, and W. Wu, "WR-3 band quasi-elliptical waveguide filters using higher order mode resonances," *IEEE Transactions on Terahertz Science and Technology*, vol. 7, no. 3, pp. 302–309, 2017.

[130] S. Cohn and E. Targow, "Investigation of microwave dielectric resonator filters, Rantec Corporation," Internal report, Tech. Rep., 1965.

[131] S. B. Cohn, "Microwave bandpass filters containing high-Q dielectric resonators," *IEEE Transactions on Microwave Theory and Techniques*, vol. 16, no. 4, pp. 218–227, 1968.

[132] W. H. Harrison, "A miniature high-Q bandpass filter employing dielectric resonators," *IEEE Transactions on Microwave Theory and Techniques*, vol. 16, no. 4, pp. 210–218, 1968.

[133] I. Hidalgo-Carpintero and M. J. Padilla-Cruz, "Moderate bandwidth filter for multiplexer applications," in *2003 33rd European Microwave Conference.* IEEE, 2003, pp. 1243–1246.

[134] V. E. G. Walker, "Dielectric resonators and filters for cellular base-stations," Ph.D. dissertation, University of Leeds, 2003.

[135] R. R. Mansour, "Filter technologies for wireless base stations," *IEEE Microwave Magazine*, vol. 5, no. 1, pp. 68–74, 2004.

[136] K. Wakino, T. Nishikawa, S. Tamura, and Y. Ishikawa, "Microwave bandpass filters containing dielectric resonators with improved temperature stability and spurious response," in *1975 IEEE-MTT-S International Microwave Symposium.* IEEE, 1975, pp. 63–66.

[137] J. Plourde and D. Linn, "Microwave dielectric resonator filters utilizing $Ba_2Ti_9O_{20}$ ceramics," in *1977 IEEE MTT-S International Microwave Symposium Digest.* IEEE, 1977, pp. 290–293.

[138] Y. Kobayashi and S. Yoshida, "Bandpass filters using TM_{010} dielectric rod resonators," in *1978 IEEE-MTT-S International Microwave Symposium Digest.* IEEE, 1978, pp. 233–235.

[139] A. K. Nidhi and F. Khatoon, "Stacked equilateral triangular dielectric resonator antenna excited with coaxial feeding," *IOSR Journal of Electronics and Communication Engineering*, vol. 9, no. 3, pp. 1–7, 2014, doi: 10.9790/2834-09360107.

[140] A. A. Kishk, "A triangular dielectric resonator antenna excited by a coaxial probe," *Microwave and Optical Technology Letters*, vol. 30, no. 5, pp. 340–341, 2001.

[141] W. T. Sethi, H. Vettikalladi, H. Fathallah, and M. Himdi, "Equilateral triangular dielectric resonator nantenna at optical frequencies for energy harvesting," *International Journal of Antennas and Propagation*, vol. 2015, 2015.

[142] W. Tariq-Sethi, H. Vettikalladi, H. Fathallah and M. Himdi, "1× 2 equilateral triangular dielectric resonator nantenna array for optical communication," in *2016 7th International Conference on Sciences of Electronics, Technologies of Information and Telecommunications (SETIT)*. IEEE, 2016, pp. 7–9.

[143] M. Ene-Dobre, M. Banciu, L. Nedelcu, G. Stoica, C. Busuioc, and H. Alexandru, "Microwave antennas based on $Ba_{1-x}Pb_xNd_2Ti_5O_{14}$," *Journal of Optoelectronics and Advanced Materials*, vol. 13, no. 9, p. 1298, 2011.